

**Fault zones in potential geothermal reservoir rocks  
in the Upper Rhine Graben:  
Characteristics, permeability implications,  
and numerical stress field models**

---

Dissertation  
zur Erlangung des mathematisch-naturwissenschaftlichen Doktorgrades  
"Doctor rerum naturalium"  
der Georg-August-Universität Göttingen  
  
im Promotionsprogramm Geowissenschaften  
der Georg-August University School of Science (GAUSS)

vorgelegt von

Silke Meier

aus Hildesheim

Göttingen 2016

## **Betreuungsausschuss**

Prof. Dr. Sonja L. Philipp  
Abteilung Strukturgeologie und Geodynamik  
Geowissenschaftliches Zentrum der Georg-August-Universität Göttingen

Prof. Dr. Martin Sauter  
Abteilung Angewandte Geologie  
Geowissenschaftliches Zentrum der Georg-August-Universität Göttingen

## **Mitglieder der Prüfungskommission**

### Referentin:

Prof. Dr. Sonja L. Philipp  
Abteilung Strukturgeologie und Geodynamik  
Geowissenschaftliches Zentrum der Georg-August-Universität Göttingen

### Korreferent:

Prof. Dr. Martin Sauter  
Abteilung Angewandte Geologie  
Geowissenschaftliches Zentrum der Georg-August-Universität Göttingen

### weitere Mitglieder der Prüfungskommission

Prof. Dr. Jonas Kley  
Abteilung Strukturgeologie und Geodynamik  
Geowissenschaftliches Zentrum der Georg-August-Universität Göttingen

Prof. Dr. Sharon Webb  
Abteilung Experimentelle und Angewandte Mineralogie  
Geowissenschaftliches Zentrum der Georg-August-Universität Göttingen

Dr. John Reinecker  
GeoThermal Engineering GmbH, Baischstraße 8, 76133 Karlsruhe

Dr. Kristian Bär  
Fachgebiet Angewandte Geothermie  
Institut für Angewandte Geowissenschaften - Technische Universität Darmstadt

Tag der mündlichen Prüfung: 03. Mai 2016

## Abstract

Fault zones in carbonate successions of the Middle Triassic Muschelkalk are potential target structures of hydrothermal projects in the Upper Rhine Graben (URG). A mixed-method approach was applied to make assumptions on fault-zone permeability structures, stress states and local stress fields. This thesis contributes to exploration of fault-related Muschelkalk reservoirs in the URG and draws comparison with the already successfully tested hydrothermal reservoir of the Lower Triassic Bunter sandstone. To define fault-zone characteristics and estimate related permeability structures in Muschelkalk rocks, fault zones of different types (e.g., normal, inverted, oblique-slip) and different scales (displacement: medium-scale: 1-10 m; large-scale >10 m) were analyzed in detail. The outcrop analogue study of one large-scale fault zone in thick-bedded sandstones of Bunter age provided the opportunity for comparison. Special emphasis in both sedimentary successions was given to damage-zone and fault-core characteristics as well as to characteristics of associated fracture systems (e.g., density, aperture distribution, connectivity, vertical extension).

Fracture systems formed in rather homogenous units have a positive effect on reservoir permeability. They may provide, in particular in proximity to the fault core, potential fluid pathways across multiple layers and enhanced fracture connectivity of comparatively short fractures. In contrast, fracture systems in strongly mechanically layered units may have less impact on reservoir permeability. Fault cores show partially significant complexity, comprising mainly sealing, but also conductive structures. Large-scale fault zones, i.e., in reservoir-scale, in both potential reservoir units are best described as combined conduit-barrier systems. They show potentially conductive fracture systems in damage zones (and additionally in Bunter: transition zone) and a low-permeable to sealing fault core.

To improve knowledge about fault-zone local stress fields within the layered Muschelkalk reservoir (reservoir depth: 2.900 m) 3D-numerical models were developed, using the finite element software COMSOL Multiphysics®. Pronounced differences in local stress fields occur, depending on (1) orientation, (2) impact of maximum horizontal stress  $S_H$ , (3) fault-zone scale and (4) contrasts in rock-mechanical properties. Clear dependency of fault-zone orientation on stress magnitude and displacement follows for stress regimes with high horizontal compression. In particular, large-scale fault-zones at  $30^\circ$  to  $S_H$  may be favorable for  $S_H$ -induced horizontal displacement within soft fault-zone units since highest displacement-values occur. Decrease of stress magnitudes in soft fault rocks diminishes towards fault zones oriented perpendicular to  $S_H$ . Impact of mechanical layering increases with increasing horizontal compression, resulting in vertically heterogeneous stress fields. To make assumptions on the hydraulic activities of fault zones, analytical estimations on slip and dilation tendencies for analyzed fault zones at reservoir conditions are presented. Results reveal stress state variations of each fault zone, attributed to the current transitional stress regime and varying orientations of the maximum horizontal stress  $S_H$ .

Results of presented outcrop analogue studies help to make profound assumptions on fault-zone permeability structures and thus to define promising drilling targets in the URG. In this context, sedimentary successions were found which can be excluded as potential geothermal reservoirs. Findings of 3D-numerical models could help to support the strategy of possibly needed stimulation treatments in the Muschelkalk reservoir. Moreover, results of this thesis gain insights on potential problems during the drilling operation in Muschelkalk reservoirs, e.g., the likelihood of a vertically heterogeneous stress field.

## Kurzfassung

Störungszonen in den karbonatischen Wechselfolgen des Muschelkalks (Mittlere Trias) sind potenzielle Ziele für hydrothermale Projekte im Oberrheingraben (ORG). Es wurden verschiedene Methoden miteinander kombiniert, um die Permeabilitäts-Strukturen solcher Störungszonen, deren Spannungszustände und lokale Spannungsfelder abzuschätzen. Diese Arbeit kann damit zur Exploration von störungsgebundenen Muschelkalk-Reservoirien im ORG beitragen. Sie vergleicht diese mit einem bereits erfolgreich getesteten (störungsgebundenen) hydrothermalen Reservoir, den Sandsteinen des Buntsandsteins.

Um für den Muschelkalk die Charakteristika von Störungszonen zu definieren und die zugehörige Permeabilitätsstruktur abzuschätzen, wurden verschiedene Störungszonentypen (z.B. Abschiebungen, invertierte Störungszonen, Schrägabschiebung) mit unterschiedlichen Maßstäben (Versatz: mittel-skalig 1-10 m, groß-skalig >10 m) detailliert untersucht. Eine Aufschlussanalogstudie zu einer groß-skaligen Störungszone (Schrägabschiebung) in dickbankigen Sandsteinen (Buntsandstein, Untere Trias) wurde zum Vergleich herangezogen. Der besondere Schwerpunkt lag jeweils auf der Charakterisierung von Bruchzone und Störungskern sowie des assoziierten Bruchsystems (Bruchdichte, Öffnungsweitenverteilung, Vernetzungsgrad, vertikale Ausdehnung).

Die Daten zeigen, dass Bruchsysteme in eher homogenen Einheiten einen positiven Effekt auf die Reservoir-Permeabilität haben. Sie bieten, vor allem in der Nähe des Störungskerns, potenzielle Fließwege auch über mehrere Schichten und zeigen eine starke Vernetzung zwischen vergleichsweise kurzen Brüchen. Im Gegensatz dazu scheinen störungsgebundene Bruchsysteme in Einheiten mit einer starken mechanischen Schichtung einen geringeren Einfluss auf die Reservoirpermeabilität zu haben. Störungskerne zeigen stellenweise eine signifikante Komplexität, da sie vor allem abdichtende aber stellenweise auch durchlässige Strukturen aufweisen. Groß-skalige Störungszonen (im Reservoir-Maßstab) lassen sich für beide potenzielle Reservoirhorizonte am besten als kombinierte Barriere-Leiter-Systeme beschreiben. Diese Barriere-Leiter-Systeme zeichnen sich durch ein potenziell hydraulisch durchlässiges Bruchsystem in der Bruchzone (und im Buntsandstein zusätzlich in der Übergangszone) sowie einen schwach durchlässigen bis abdichtenden Störungskern aus.

Um die Kenntnisse zum lokalen Spannungsfeld in Störungszonen im geschichteten Muschelkalk (Reservoirtiefe: 2.900 m) zu verbessern, wurden mit der Finite-Elemente-Software COMSOL Multiphysics® numerische 3D-Modelle erstellt. Es wurden deutliche Unterschiede des lokalen Spannungsfelds in Abhängigkeit von (1) der Orientierung, (2) dem Einfluss der maximalen Horizontalspannung  $S_H$  im Spannungsregime, (3) Störungszonen-Maßstab und (4) den Kontrasten der mechanischen Eigenschaften festgestellt. In Spannungsregimen mit starker horizontaler Kompression wurde für Spannungsmagnituden und Versatz eine deutliche Abhängigkeit von der Orientierung der Störungszone festgestellt. Vor allem groß-skalige Störungszonen mit einem  $30^\circ$ -Winkel zu  $S_H$  scheinen einen  $S_H$ -induzierten Horizontalversatz innerhalb weicher Störungszoneneinheiten zu begünstigen; in dieser wurden die höchsten Versatzbeträge festgestellt. Die typische Abnahme von Spannungsmagnituden in weicheren Störungszoneneinheiten verringert sich in Richtung von Störungszonen, die senkrecht zu  $S_H$  streichen. Der Einfluss der mechanischen Schichtung steigt mit zunehmender horizontaler Kompression, was zu einem vertikal heterogenen Spannungsfeld führt. Um Annahmen zu einer möglichen hydraulischen Aktivität einer Störungszone zu treffen, werden für die untersuchten Störungszonen analytische Abschätzungen zu Bewegungs-

und Dehnungstendenzen unter Reservoir-Bedingungen präsentiert. Die Ergebnisse zeigen unterschiedliche Spannungszustände der analysierten Störungzonen, die auf das rezente Übergangsregime sowie unterschiedliche Orientierungen der maximalen Horizontalspannungen  $S_H$  zurückzuführen sind.

In dieser Arbeit präsentierte Ergebnisse von Aufschlussanalogstudien helfen dabei, fundierte Annahmen zur Permeabilitätsstruktur von Störungzonen zu treffen und damit vielversprechende Bohrziele im ORG zu definieren. In diesem Zusammenhang konnten sedimentäre Wechselfolgen identifiziert werden, die als potenzielle geothermische Reservoirs ausgeschlossen werden können. Die Ergebnisse der numerischen 3D-Modellierungen können dazu beitragen, möglicherweise nötige Stimulationsmaßnahmen im Muschelkalk Reservoir optimal auszulegen. Darüber hinaus bieten die Ergebnisse die Möglichkeit, Einblick in potenzielle Probleme während der Bohrungsherstellung in Muschelkalk-Reservoirs zu bekommen, wie zum Beispiel die Wahrscheinlichkeit eines vertikal heterogenen Spannungsfeldes.

## Preface

This thesis was drawn up as part of the joint project "*Outcrop Analogue Studies in Geothermal Exploration*" within the component project "*Investigation of fault zones in outcrop analogues and investigation of drilling targets*". Participating project partners of the joint project have been the Geothermal Engineering GmbH, GeoEnergy GmbH, Ruprecht-Karls-University Heidelberg, Friedrich-Alexander University of Erlangen-Nürnberg, and Georg-August University of Göttingen. The project was launched in 2011 and completed in 2015.

The objective of the joint project was to develop a standardized workflow to explore potential geothermal reservoirs. This project is based on a multi-method approach applied in outcrop analogues of potential reservoir rocks within the Upper Rhine Graben in Southwest Germany. It combines the analysis of lithofacies, diagenetic processes and petrophysical properties, LIDAR-based 3D-modelling of the outcrops, analysis of geophysical well data, and, such as in the present work, the characterization of fault zones in view of their hydromechanical properties and determination of potential drilling targets.

This cumulative thesis includes the following three manuscripts, two of which have already been published in peer-reviewed scientific journals; the third one is submitted to a peer-reviewed scientific journal:

- **Meier, S.**, Bauer, J.F., Philipp, S.L., 2015. Fault zone characteristics, fracture systems and permeability implications of Middle Triassic Muschelkalk in Southwest Germany. *Journal of Structural Geology* 70, 170-189. Chapter 2.
- **Meier, S.**, Bauer, J.F., Philipp, S.L., submitted. Fault zones in layered carbonate successions: From field data to stress field models. Submitted to *Geomechanics and Geophysics for Geo-Energy and Geo-Resources*. Chapter 3.
- Bauer, J.F., **Meier, S.**, Philipp, S.L., 2015. Architecture, fracture system, mechanical properties and permeability structure of a fault zone in Lower Triassic sandstone, Upper Rhine Graben. *Tectonophysics* 647-648, 132-145. Chapter 4.

## Table of Contents

Abstract .....	2
Kurzfassung .....	3
Preface.....	5
1 General Introduction .....	7
1.1 Motivation .....	7
1.2 Fault zones and reservoir permeability .....	8
1.3 Study area .....	9
1.4 Aims and approach.....	10
1.5 Thesis outline .....	12
2 Fault zone characteristics, fracture systems and permeability implications of Middle Triassic Muschelkalk in Southwest Germany.....	17
3 Fault zones in layered carbonate successions: From field data to stress field models ..	50
4 Architecture, fracture system, mechanical properties and permeability structure of a fault zone in Lower Triassic sandstone, Upper Rhine Graben .....	90
5 Rock samples of the Muschelkalk: Facies and diagenesis.....	116
6 Summarizing Discussion .....	121
6.1 Fault-zone related permeability in potential hydrothermal reservoirs of the Upper Rhine Graben .....	121
6.1.1 Fault-zone permeability structures in Muschelkalk rocks.....	121
6.1.2 Fault-zone permeability structure in Lower Bunter – A comparison .....	123
6.1.3 Mineralizations within the fault damage zones.....	124
6.2 Stress state and fault-zone permeability .....	125
6.3 Enhancing hydrothermal reservoirs – Stimulation treatments in sedimentary successions.....	126
7 Conclusions and Outlook.....	130
Appendix.....	135
Acknowledgments / Danksagung .....	139
CV / Lebenslauf .....	140

# 1 General Introduction

## 1.1 Motivation

In recent years the exploitation of renewable energy sources such as geothermal heat has gained high attention. In contrast to petrothermal reservoirs which utilize geothermal energy stored in tight and dry crystalline or sedimentary rocks (hot dry rock *HDR*), hydrothermal reservoirs mainly use thermal water available in deep aquifers through natural fluid paths and potentially in context with fault zones (DiPippo, 2005; Stober et al., 2011). Usage as a low-enthalpy hydrothermal reservoir for electric power generation is possible at aquifer temperatures above 100°C (DiPippo, 2005; Stober et al., 2011). A successfully operating geothermal site is at best characterized by (1) high temperature and (2) high flow rate (DiPippo, 2005).

Comparatively good conditions for the utilization of deep geothermal energy in Germany have been stated to low-enthalpy hydrothermal reservoirs within the Upper Rhine Graben (URG), Southwest Germany (Stober et al., 2011; Agemar et al., 2014a). Despite a considerably high geothermal gradient (i.e., relative increase of temperature with depth) in the URG (45-50 °C/km; Stober and Bucher, 2015), however, only few hydrothermal projects are established in the German sector, i.e., Landau, Insheim and Bruchsal (Agemar et al., 2014b). This is particularly due to a tectonically very complex structure and a manifold fault-zone pattern that exists within the URG: As central part of the Cenozoic European Rift System the URG was formed since Eocene and subjected to several tectonic stages during its formation. As a result, the URG shows significant tectonic complexity, where potential reservoir formations are located at various depths (Illies, 1972; Brun and Wenzel, 1991; Ziegler, 1992; Schumacher, 2002; Paschen et al., 2003; Ziegler and Dèzes, 2005).

Following examples of geothermal sites in Landau and Insheim, exploration concepts of current geothermal projects target fault zones and associated fracture systems as zones of possibly enhanced permeability (fractured reservoirs; Nelson, 1985). Since other fault zones, however, may impede fluid flow instead (e.g., Caine et al., 1996) this results in significant permeability anisotropies in fault-related potential hydrothermal reservoirs (Stober and Bucher, 2015). This leads to the necessity of detailed exploration concepts.

Reservoir characterization and exploration are commonly accomplished by geophysical exploration methods such as seismic surveys. These methods clearly display large-scale structures such as main fault zones and prominent seismic reflectors and thus provide reservoir models; small-scale fractures cannot be identified due to the low spatial resolution of seismic data. In hydrothermal reservoirs, however, knowledge about these small-scale structures, which may strongly affect fluid flow and thus have an immense impact on reservoir permeability, is of great importance. In this context, studies of fault zones exposed in outcrop analogues may be an appropriate tool to characterize even small-scale structures and variations of mechanical properties. Outcrop analogues expose rocks similar to those at depth, i.e. rocks of similar stratigraphy, facies, and lithology (e.g., Philipp et al., 2010). Thus, outcrop analogues offer the opportunity to analyze fault zones and associated structural features at highest possible resolution.

The Middle Triassic Muschelkalk is a prominent hydrothermal reservoir in the URG (e.g., Stober and Bucher, 2015). Although Muschelkalk rocks are located at geothermally relevant depth (i.e., sufficiently high temperatures can be expected), successful

geothermal projects in the URG exploit deeper aquifers such as the crystalline basement, Rotliegend (Lower Permian), and Bunter (Lower Triassic) (Agemar et al., 2014b). One reason is as follows: Exploring the Muschelkalk as a potential reservoir is very challenging due to a strong mechanical layering in these limestone-marl-alternations. This mechanical layering affects fracture propagation and thus the formation of interconnected and hydraulically active fracture networks. Thus, an increased exploration risk regarding sufficient fluid flow exists in general for a Muschelkalk potential reservoir, also in connection with fault zones. Changes of lithology and mechanical properties in mechanically layered rocks affect fault-zone structure, fracture-system connectivity and thus reservoir permeability.

This thesis has been motivated to make assumptions on fault-zone permeability structure, fracture-system characteristics and impact of mechanical layering on fracture propagation in a high resolution. The study is (1) focused on fault zones hosted in carbonate successions of the Middle Triassic Muschelkalk and (2) draws comparison to sandstones of Lower Triassic Bunter which are already successfully exploited in the URG.

## **1.2 Fault zones and reservoir permeability**

In general, knowledge of three fault-zone properties is of particular importance in hydrothermal reservoirs: (1) permeability structure, (2) stress state, and (3) local stress field:

(1) A simple model of the fault-zone internal structure in brittle and low-porous rocks describes a fault core enclosed by damage zones (Fig. 1.1a). In this model, fault damage zones have an enhanced fracture density which increases towards the fault core (Chester and Logan, 1986; Caine et al., 1996; Faulkner et al., 2010). This may lead to an enhanced permeability due to the formation of fluid pathways (e.g., Caine et al., 1996), but to a decrease in effective Young's modulus  $E$  and uniaxial compressive strength UCS (e.g., Priest, 1993). The fault core is commonly composed of material either with low Young's moduli (low stiffness) such as fault gouge or with high Young's moduli (high stiffness) such as mineralizations. Both materials may provide a relatively high sealing capacity for inactive fault zones. Caine et al. (1996) proposed four endmembers to describe the permeability structure of fault zones in brittle rocks (conduit vs. barrier) based on the relative percentage of damage zone (conductive) and fault core (sealing) structures (Fig 1.1b). However, it has proved difficult to apply this model on fault zones in layered sedimentary successions: Fault zones may be formed by linkage of already existing fault segments resulting in a very complex fault-zone structure, in particular of the fault core (Bastesen and Braathen, 2010; Bastesen et al., 2013). Moreover, in porous sedimentary rocks, deformation bands may be formed rather than fractures, having contrasting effects on permeability (sealing structures) and rock mechanical properties (increasing rock strengths) (Antonellini and Aydin, 1994; Tondi et al., 2006; Fossen et al., 2007).

(2) The hydraulic activity of fault zones clearly depends on the stress state and on their orientation in the given remote stress field respectively (Fig. 1.1c; Barton et al., 1995; Zoback, 2007). Hydraulic activity is particularly ascribed to extensional fault zones (open structures; high dilation tendency  $T_D$ ) and critically stressed fault zones close to reactivation (high slip tendency  $T_S$ ). In contrast, compressive structures show reduced permeability since potential fluid pathways are closed (Barton et al., 1995; Morris et al., 1995; Sibson, 1994; Zoback, 2007).

(3) Contrasting mechanical properties within fault zones lead to the development of local stress fields with stress magnitudes differing from those in the undisturbed host rock (Fig. 1.1d). These local stress fields affect fracture formation and fracture propagation within fault zones and are thus directly linked to their permeability evolution (Gudmundsson et al., 2010).

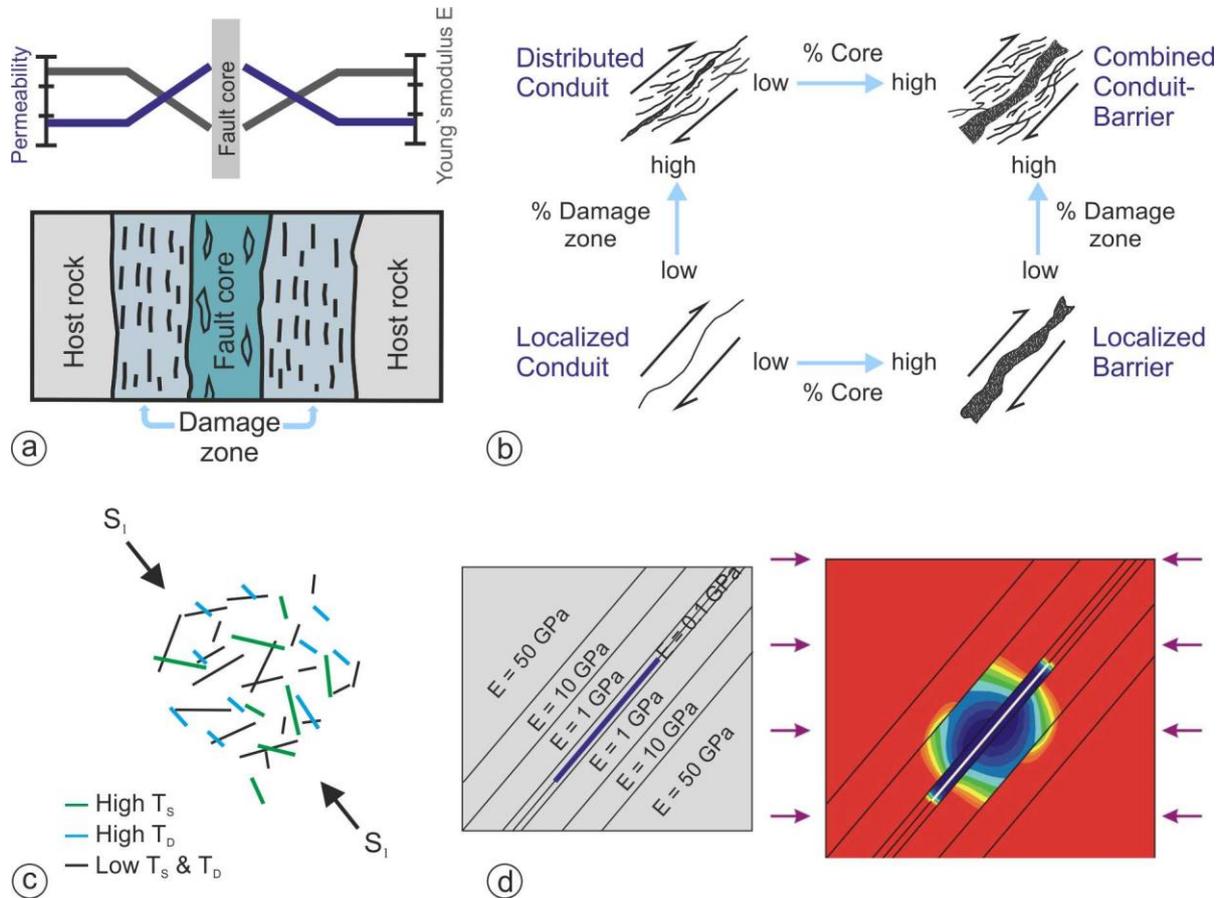


Fig. 1.1. Impact of fault zones on reservoir permeability. a) Sketch of a typical fault-zone structure separated to fault core, damage zone, and host rock (modified from Gudmundsson et al., 2010). The diagram above illustrates typical trends of fracture related permeability and Young's modulus  $E$  across fault zones assuming an increase of fracture density towards the fault core. Fractures in the high-strain fault core are rare or difficult to define, the Young's modulus may be low (fault gouge) or high (mineralizations), respectively. b) Definition of fault-zone permeability structures based on the relative percentage of fault core and damage zone (modified from Caine et al., 1996). c) Sketch of deviating slip tendencies and dilation tendencies in a fault-zone pattern in the earth crust in context with a given stress field (map view; modified from Zoback, 2007). Color code indicating fault-zone stress state see key ( $T_s$  slip tendency,  $T_D$  dilation tendency). The arrows indicate the orientation of the maximum horizontal stress  $S_H (=S_1)$ . d) Development of a local stress field within a fault zone under compression due to contrasting Young's moduli (modified from Gudmundsson et al., 2010). This local stress field affects fracture formation and propagation.

### 1.3 Study area

Due to its particular structure the URG provides the opportunity to study potential geothermal reservoir rocks, for example sedimentary successions of Triassic age, which are either buried deep within the graben or may be exposed in outcrop analogues on the uplifted graben shoulders. The four outcrop analogues of the Middle Triassic Muschelkalk selected for this study are located on the eastern graben shoulder in the Kraichgau-Syncline (IL Illingen; IT Ittlingen; KN Knittlingen; NL Nussloch), having a maximum distance of approximately 40 km to the eastern main boundary fault zone. The outcrop analogue selected for comparison, exposing sandstones of the Lower Triassic Bunter, is situated on the western graben shoulder near Cleebourg, very close to the western main

boundary fault zone (CL; Alsace, France). A detailed description of the URG geological setting is given in Chapters 2, 3, and 4.

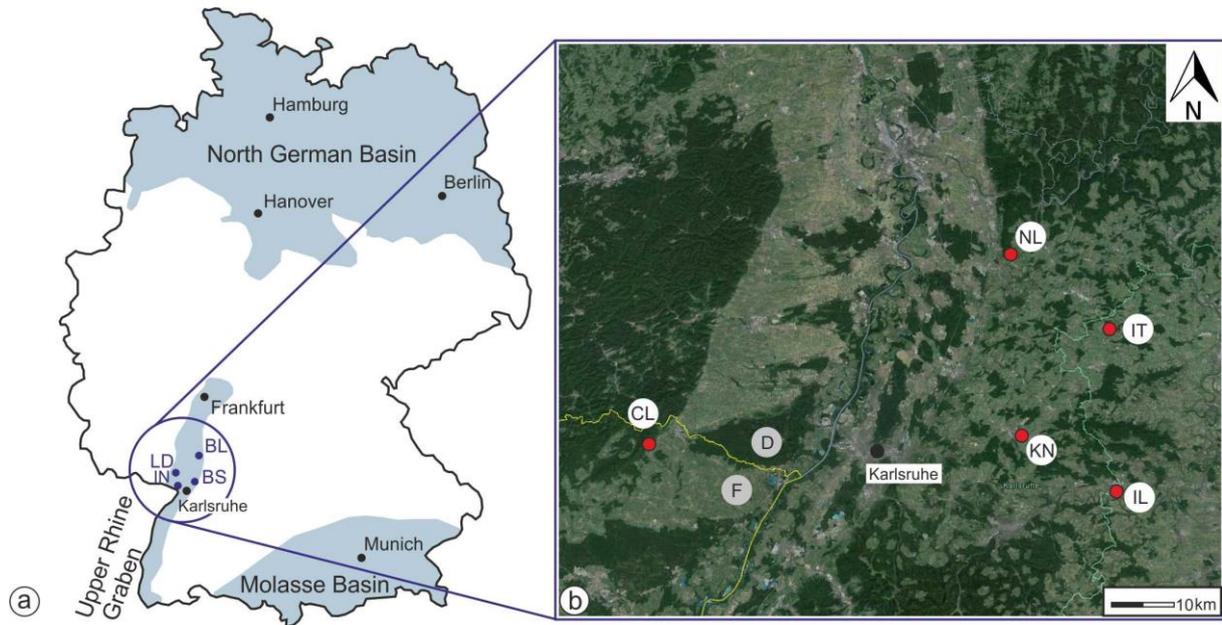


Fig. 1.2. a) Regions in Germany with proven hydrothermal potential modified from Stober et al. (2011): Upper Rhine Graben, North German Basin, and Molasse Basin; section shown in (b) indicated by the blue circle. This thesis focuses on the Upper Rhine Graben. The locations of established hydrothermal projects are indicated by blue dots (LD Landau; IN Insheim; BS Bruchsal). Another hydrothermal site (BL Brühl) is currently under construction, the deep wellbore Brühl GT1 has already been drilled. b) Locations of selected outcrop analogues are indicated by red dots ('Google Earth' map). Outcrop analogues of the Middle Triassic Muschelkalk are located in Germany (D) on the eastern graben shoulder (Kraichgau-Syncline; IL Illingen; IT Ittlingen; KN Knittlingen; NL Nussloch). The outcrop analogue of the Lower Triassic Bunter is located in France (F) on the western graben shoulder very close to the western main boundary fault zone (CL; Alsace).

## 1.4 Aims and approach

This thesis aims at characterizing fault zones and associated fracture systems since they may have huge impact on hydrothermal reservoir permeability. The main objectives are to identify permeability structures of fault zones and to estimate resulting fault-related permeability in sedimentary successions and in particular for Muschelkalk potential reservoirs. Along with estimations on fault-zone stress state at reservoir conditions this shall lead to the proposal of possible or, in contrast, inappropriate drilling targets of deep wellbores for reservoir exploitation. Therefore, this study is also set out to examine to what extent outcrop analogue studies of fault zones can contribute to exploration concepts for hydrothermal reservoirs in the URG. In order to achieve these main objectives, this thesis particularly focuses on the following key topics.

### *(1) Defining fault-zone characteristics and estimating their permeability structure at different fault-zone scales:*

This thesis aims at analyzing fault zones and their associated structural features in layered carbonate successions, i.e., fault-zone structure, fracture system, and minor faults at the highest possible resolution in the field. The aim is to identify differences in fault zones of different scales. Thus, this thesis aims at investigating whether the simplified fault-core-damage-zone model is applicable to define permeability structures of fault zones hosted in carbonate successions of the Muschelkalk.

In this context special attention shall be given to fault-core complexity, i.e., structural elements and faulted material. To estimate fracture-related permeability, information on selected fracture-system parameters such as orientation, fracture density, aperture, connectivity, and vertical extension is needed. In addition, special emphasis shall be placed on indicators of hydraulic activity within fault damage zone and fault core during fault-zone evolution.

*(2) Improving knowledge of fault-zone local stress field within the potential hydrothermal reservoir Muschelkalk in the Upper Rhine Graben:*

It is well known that contrasting mechanical properties in fault zones cause stresses which differ from those in the surrounding host rock and therefore induce a local stress field (e.g., Gudmundsson et al., 2010). Furthermore, it is understood that strong mechanical layering leads to a vertically very heterogeneous stress field affecting fracture propagation and thus fracture-system connectivity and permeability (e.g., Philipp et al., 2013). Based on this, this thesis aims at investigating local stress fields within fault zones hosted in layered carbonate successions of the Muschelkalk at reservoir depth for fault zones of (1) differing scale and (2) with differing orientation. For this purpose, three-dimensional (3D) numerical models on fault-zone local stress fields at stress conditions similar to those in the potential Muschelkalk reservoir need to be developed.

Based on results of outcrop analogue studies it is intended to generate model geometries (fault-zone displacements and internal-structure characteristics) as realistic as possible and to estimate rock-mechanical input parameters. Data on mechanical properties are needed, i.e., their variations in both vertical direction (across the carbonate succession) and horizontal direction (across damage zone and host rock). If no data on in-situ stress magnitudes are available, it is common practice to use analytical models to estimate allowable horizontal stress magnitudes at reservoir depth defined by the frictional equilibrium theory (stress polygon; Peška and Zoback, 1995).

*(3) Identifying fault zones with preferable orientation for fluid flow in the Upper Rhine Graben:*

The fact that potentially active fluid pathways exist in extensional fault zones and critically stressed fault zones, respectively, is well understood. These fault-zone stress states depend on the fault-zone orientation in the given stress field (Barton et al., 1995; Morris et al., 1995; Sibson, 1994; Zoback, 2007).

Hence, fault-zone orientations preferable for fluid flow, i.e., high dilation tendency or high slip tendency, respectively, shall be identified within the URG, crosscut by a complex fault zone pattern. Orientation data of fault zones exposed in the investigated outcrop analogues shall be used to estimate their stress states with analytical models, at stress conditions equal to those used in 3D-numerical models and based on rough estimate of stress orientations using the world stress map (Heidbach et al., 2008).

*(4) Comparing fault zones within different potential hydrothermal reservoirs in the URG. Fault zones in layered carbonate successions versus fault zones in thick bedded sandstone:*

The Lower Triassic Bunter, composed of thick bedded sandstones alternating with shale, is another potential hydrothermal reservoir in the URG. It is well understood that fault

zones in layered and low-porous carbonate successions and fault zones in thick-bedded and porous sandstones show pronounced differences in their characteristics: both the fault-zone structure (characteristics of the fault-zone units fault core and damage zones or additional mixed or transition zones) and the structural features (fractures vs. deformation bands) may be different. Therefore, this thesis aims at pointing out possible differences of fault zones hosted in Middle Triassic Muschelkalk and Lower Triassic Bunter and, if possible, suitable drilling targets within the URG.

The approach of this study is summarized in Fig. 1.3, the crucial point being detailed structural geological field studies in outcrop analogues of Muschelkalk and Bunter. In addition, this approach is supported by analytical models which focus on the in-situ stress field and fault-zone stress states within the potential Muschelkalk reservoir. Finally, results of this integrative approach are combined in 3D-numerical models of fault-zone local stress fields in layered carbonate successions.

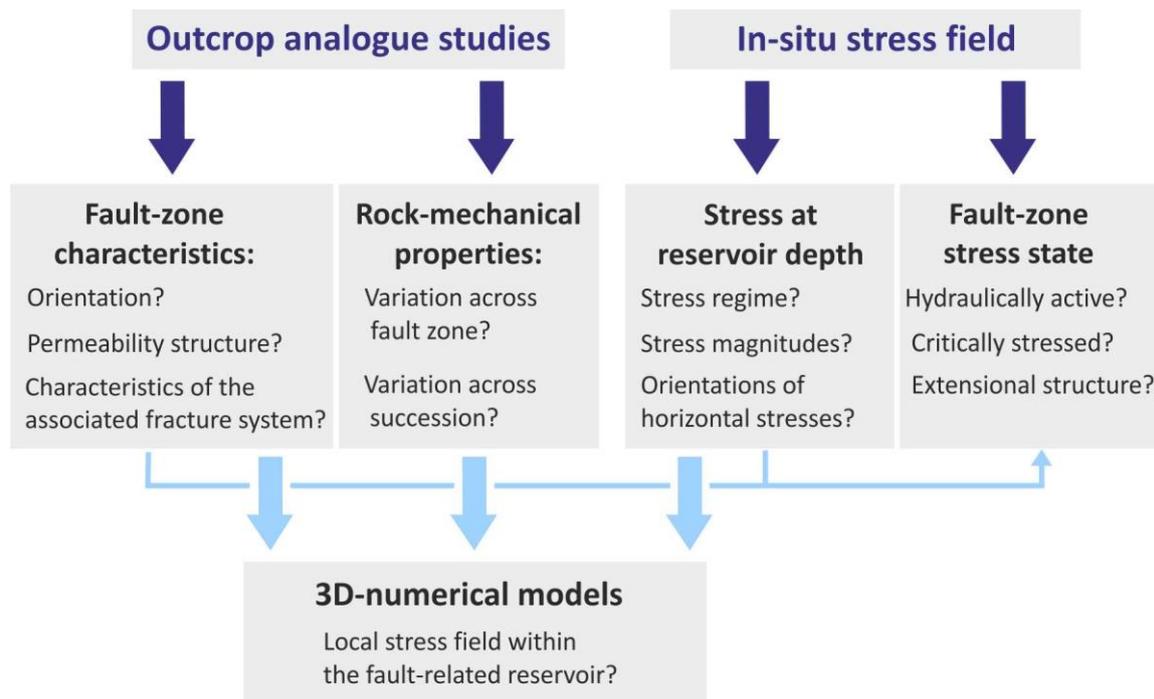


Fig. 1.3. Overview of the integrative approach to characterize fault zones in potential hydrothermal reservoir rocks in the Upper Rhine Graben. This approach comprises detailed outcrop analogue studies of fault zones in the Middle Triassic Muschelkalk and Lower Triassic Bunter, estimations on the in-situ stress field and stress state of fault zones, and finally 3D-numerical models on the local stress field of fault zones in the potential Muschelkalk reservoir.

## 1.5 Thesis outline

This thesis has a cumulative structure. Chapters 2, 3, and 4 are built from three self-contained manuscripts, two of which have already been published in peer-reviewed scientific journals; the third one is submitted to a peer-reviewed scientific journal.

Chapter 2: Meier, S., Bauer, J.F., Philipp, S.L., 2015. Fault zone characteristics, fracture systems and permeability implications of Middle Triassic Muschelkalk in Southwest Germany. *Journal of Structural Geology* 70, 170-189.

Chapter 3: Meier, S., Bauer, J.F., Philipp, S.L., submitted. Fault zones in layered carbonate successions: From field data to stress field models. Submitted to *Geomechanics and Geophysics for Geo-Energy and Geo-Resources*.

Chapter 4: Bauer, J.F., Meier, S., Philipp, S.L., 2015. Architecture, fracture system, mechanical properties and permeability structure of a fault zone in Lower Triassic sandstone, Upper Rhine Graben. *Tectonophysics* 647–648, 132–145.

Brief overview of the applied methods is given in each manuscript according to the main topic (structural geological outcrop analogue studies, laboratory measurements, 3D-numerical models, analytical models). A separate reference list is provided at the end of each chapter. The citation style corresponds to the respective scientific journal.

*Chapter 2* represents a detailed outcrop analogue study on the characteristics of eight faults zones hosted in the carbonate succession of the Middle Triassic Muschelkalk (Lower, Middle, and Upper Muschelkalk; mu-mo). Analyzed fault zones are of different type (normal fault zones, reverse fault zones, inverted fault zones, oblique-slip fault zones), and different scale (displacement: medium-scale 1-10 m; large-scale >10 m). This paper focuses on fault-zone orientations, characteristics of fault-zone units (structures, fault rocks, width), and data of the associated fracture systems (orientation, density, aperture, connectivity, length and vertical extension in context with mechanical layering). Furthermore, special emphasis is given on indications on previous hydraulic activity of the fault zones (mineralizations in fractures and fault cores). This study gains insights in the permeability and permeability evolution of fault-related and mechanically layered Muschelkalk rocks. Furthermore it describes an integration of fault-zone formation and reactivation of the described fault zones in context with the regional stress-field changes in the URG.

I am the first author of this paper, did field work, did field data evaluation and interpretation, prepared and selected figures, and wrote the text. The contribution of the co-authors includes collaboration in the data acquisition in the field, an early discussion of the results, and revision of the manuscript in the pre-submission state.

*Chapter 3* describes the setup and results of 3D-numerical models of fault-zone local stress fields using the software COMSOL Multiphysics® (Version 5.0). This paper focuses on the Upper Muschelkalk reservoir (mo). The model geometry is based on fault-zone internal structure characteristics of a large-scale and a medium-scale fault zone (described in Chapter 2) and lithological profiles of the Upper Muschelkalk. This manuscript illustrates in detail the steps to gain information on input parameters, i.e., changes of Young's modulus  $E$  across the fault zone and across the carbonate succession. Firstly, laboratory measurements of static Young's modulus  $E$  were performed. Secondly, variations of  $E$  were estimated with Rebound hardness measurements: (1) Schmidt-hammer tests in outcrop analogues and (2) Equotip tests along core samples. Boundary loads are applied, representing horizontal stress magnitudes and vertical stress magnitudes which are realistic for the fault-related Muschelkalk potential reservoir (reservoir depth of approx. 2.900 m). Results of the numerical models include magnitudes of principal stresses, shear stresses, and displacements within fault zones for four fault-zone orientations relative to the orientation of the maximum horizontal stress  $S_H$ : (1)  $S_H = 0^\circ$ , (2)  $S_H = 30^\circ$ , (3)  $S_H = 60^\circ$ , and (4)  $S_H = 90^\circ$  to the fault zone. Furthermore, this chapter provides estimations on slip tendencies and dilation tendencies of fault zones analyzed in Chapter 2 at stress conditions as in the 3D-numerical models (equal stress regimes and stress magnitudes of  $S_V$ ,  $S_H$ , and  $S_h$ ).

I am the first author of this paper, did field work and laboratory measurements, did data evaluation and interpretation, used analytical models to gain information on model input parameters and fault-zone stress states, developed 3D-numerical models, prepared and selected figures and wrote the text. The co-authors contributed on the one hand to

sampling of Muschelkalk rocks in order to determine rock mechanical properties in the laboratory. On the other hand the contribution includes a discussion on the model setup at an early stage and critical reviews of the manuscript.

*Chapter 4* draws a comparison with fault zones in sandstones and presents a detailed study of one fault zone hosted in thick bedded porous sandstones of the Lower Triassic Bunter. This work describes characteristics of the fault-zone units (defined as damage zone, transition zone, and fault core) in detail and presents data of the associated discontinuity system (particularly fractures; orientation, density, length, aperture, connectivity, mineralization). Rock mechanical properties of 12 rock samples were determined in the laboratory and supported by in-situ Schmidt-hammer Rebound hardness tests to make assumptions on their variations across the fault zone. This study provides assumptions on the fault-zone type, displacement and indications on the fault-zone permeability structure.

This publication was written by Johanna F. Bauer. My contribution was the collaboration in the data acquisition and sampling in the field as well as an early discussion of the results and revision of the manuscript before submission.

*Chapter 5* shortly provides descriptions of thin sections of Muschelkalk rock samples taken in the outcrop analogues. Particular emphasis is given on facies and diagenesis.

*Chapter 6* provides a summarizing discussion of outcomes presented in Chapters 2 to 5 with special attention on comparison of fault-zone permeability structures in the potential hydrothermal reservoirs in Muschelkalk carbonate successions and Bunter thick-bedded-sandstones.

*Chapter 7* provides summarizing conclusions drawn from the findings of previous chapters and an outlook with regard to hydrothermal exploration in faulted sedimentary successions.

The *Appendix* contains additional large-scale 3D-numerical models with a homogeneous fault core (homogeneous Young's modulus) instead of a heterogeneous fault core presented in Chapter 3.

## References

- Agemar, T., Alten, J., Ganz, B., Kuder, J., Kühne, K., Schumacher, S., Schulz, R., 2014a. The Geothermal Information System for Germany – GeotIS. ZDGG 165 (2), 129–144.
- Agemar, T., Weber, J., Schulz, R., 2014b. Deep Geothermal Energy Production in Germany. *Energies* 2014 7 (7), 4397–4416.
- Antonellini, M., Aydin, A., 1994. Effect of faulting on fluid-flow in porous sandstones: Petrophysical properties. *AAPG Bulletin - American Association of Petroleum Geologists* 78 (3), 355-377.
- Barton, C.A., Zoback, M.D., Moos, D., 1995. Fluid flow along potentially active faults in crystalline rock. *Geology* 23, 683–686.
- Bastesen, E., Braathen, A., 2010. Extensional faults in fine grained carbonates – analysis of fault core lithology and thickness-displacement relationships. *Journal of Structural Geology* 32, 1609-1628.
- Bastesen, E., Braathen, A., Skar, T., 2013. Comparison of scaling relationships of extensional fault cores in tight carbonate and porous sandstone reservoirs. *Petroleum Geoscience* 19, 385-398.

- Billi, A., Salvini, F., Storti, F., 2003. The damage zone-fault core transition in carbonate rocks: implications for fault growth, structure and permeability. *Journal of Structural Geology* 25, 1779-1794.
- Caine, J.S., Evans J.P., Forster, C.B., 1996. Fault zone architecture and permeability structure. *Geology* 24, 1025-1028.
- Chester, F.M., Logan, J.M., 1986. Implications for mechanical properties of brittle faults from observations of the punchbowl fault zone, California. *Pure and Applied Geophysics* 124, 79-106.
- DiPippo, R., 2005. *Geothermal Power Plants: Principles, Applications and Case Studies*. Elsevier, Oxford.
- Faulkner, D.R., Jackson, C.A.L., Lunn, R.J., Schlische, R.W., Shipton, Z.K., Wibberley, C.A.J., Withjack, M.O., 2010. A review of recent developments concerning the structure, mechanics and fluid flow properties of fault zones. *Journal of Structural Geology* 32, 1557-1575.
- Fossen, H., Schultz, R.A., Shipton, Z.K., Mair, K., 2007. Deformation bands in sandstone: a review. *Journal of the Geological Society* 164, 755-769.
- Gudmundsson, A., Simmenes, T.H., Larsen, B., Philipp, S.L., 2010. Effects of internal structure and local stresses on fracture propagation, deflection, and arrest in fault zones. *Journal of Structural Geology* 32, 1643-1655.
- Heidbach, O., Tingay, M., Barth, A., Reinecker, J., Kurfeß, D., Müller, B., 2008. The World Stress Map database release 2008, doi:10.1594/GFZ.WSM.Rel2008.
- Morris, A., Ferrill, D.A., Henderson, D.B., 1996. Slip-tendency analysis and fault reactivation. *Geology* 24 (3), 275-278.
- Nelson, R.A., 1985. *Geologic Analysis of Naturally Fractured Rocks*. Gulf Publishing Company, Houston, Texas.
- Péška, P., Zoback, M.D., 1995. Compressive and tensile failure of inclined wellbores and determination of in situ stress and rock strength. *Journal of Geophysical Research* 100 (B7), 12791-12811.
- Philipp, S.L., Reyer, D., Meier, S., 2010. Strukturgeologische Geländestudien in Aufschlussanaloge und Permeabilitätsentwicklung in potentiellen geothermischen Reservoiren. *Zeitschrift für geologische Wissenschaften* 38, 49-59.
- Philipp, S.L., Afşar, F., Gudmundsson, A., 2013. Effects of mechanical layering on hydrofracture emplacement and fluid transport in reservoirs. *Frontiers in Earth Science* 1(4), 1-19, doi: 10.3389/feart.2013.00004.
- Priest, S.D., 1993. *Discontinuity Analysis for Rock Engineering*. Chapman and Hall, London.
- Ramsay, J.G., Lisle, R.J., 2000. *Modern Structural Geology, Volume 3: Applications of Continuum Mechanics in Structural Geology*. Academic Press, London.
- Sibson, R.H., 1994. Crustal stress, faulting and fluid flow. In Parnell, J. (Ed.), *Geofluids: Origin, Migration, and Evolution of Fluids in Sedimentary Basins*. Geological Society Special Publications 78, 69-84.
- Stober, I., Bucher, K., 2015. Hydraulic and hydrochemical properties of deep sedimentary reservoirs of the Upper Rhine Graben, Europe. *Geofluids* 15, 464-482.

Stober, I., Fritzer, T., Obst, K., Schulz, R., 2011. Tiefe Geothermie – Nutzungsmöglichkeiten in Deutschland. BMU, Bundesministerium für Umwelt, Naturschutz und Reaktorsicherheit (Ed.), Berlin.

Tondi, E., Antonellini, M., Aydin, A., Marchegiani, L., Cello, G., 2006. The role of deformation bands, stylolites and sheared stylolites in fault development in carbonate grainstones of Majella Mountain, Italy. *Journal of Structural Geology* 28, 376-391.

Zoback, M.D. 2007. *Reservoir Geomechanics*. Cambridge University Press, Cambridge.

## **2 Fault zone characteristics, fracture systems and permeability implications of Middle Triassic Muschelkalk in Southwest Germany.**

Silke Meier, Johanna F. Bauer, Sonja L. Philipp

Published in *Journal of Structural Geology* 70 (2015) 170-189. doi: 10.1016/j.jsg.2014.12.005

### **Abstract**

Fault zone structure and lithology affect permeability of Triassic Muschelkalk limestone-marl-alternations in Southwest Germany, a region characterized by a complex tectonic history. Field studies of eight fault zones provide insights into fracture system parameters (orientation, density, aperture, connectivity, vertical extension) within fault zone units (fault core, damage zone). Results show decreasing fracture lengths with distances to the fault cores in well-developed damage zones. Fracture connectivity at fracture tips is enhanced in proximity to the slip surfaces, particularly caused by shorter fractures. Different mechanical properties of limestone and marl layers obviously affect fracture propagation and thus fracture system connectivity and permeability. Fracture apertures are largest parallel and subparallel to fault zones and prominent regional structures (e.g., Upper Rhine Graben) leading to enhanced fracture-induced permeabilities. Mineralized fractures and mineralizations in fault cores indicate past fluid flow. Permeability is increased by the development of hydraulically active pathways across several beds (non-stratabound fractures) to a higher degree than by the formation of fractures interconnected at fracture tips. We conclude that there is an increase of interconnected fractures and fracture densities in proximity to the fault cores. This is particularly clear in more homogenous rocks. The results help to better understand permeability in Muschelkalk rocks.

## 1 Introduction

Since fault zones show a different permeability structure compared with their host rocks, they may control crustal fluid flow (Chester and Logan, 1986; Caine et al., 1996; Sibson, 1996; Caine and Forster, 1999; Sibson, 2000; Agosta and Kirschner, 2003; Micarelli et al., 2006a; Caine et al., 2010; Faulkner et al., 2010; Gudmundsson et al., 2010; Agosta et al., 2012; Philipp, 2012; Reyer et al., 2012). They can either act as conduits or barriers, depending on their infrastructure and the local stress field (e.g., Caine et al., 1996; Agosta et al., 2010; Gudmundsson et al., 2010). In general, fault zones consist of distinct units with different properties. Namely, the fault core in the fault zone center, comprising fault gouge, brecciated material and mineral precipitations, and the surrounding damage zone, characterized by an increased fracture density and minor faults (Chester and Logan, 1986; Caine et al., 1996; Berg and Skar, 2005), where preexisting structures such as bedding are commonly preserved (e.g., Billi et al., 2003). The increased fracture densities in the damage zones may lead to an enhanced permeability (Caine et al., 1996; Faulkner et al., 2010; Gudmundsson et al., 2010). In contrast, fault gouge with reduced grain sizes as well as mineral precipitation within the fault core decrease permeability in many cases. During slip in active fault zones, however, fractures or pores may get interconnected and provide an enhanced permeability within this unit (e.g., Sibson, 1994; Caine et al. 1996).

The damage-zone/fault-core model based on of fault zones in brittle rock, however, is not applicable to all fault zones due to their formation in different rock types with various mechanical properties (e.g., porous sedimentary rocks). Some authors therefore describe additional units in high porosity or unconsolidated sediments, such as mixed zones embedded between fault core and damage zone (Heynekamp et al., 1999), or a distal fault core at the margins of the fault core (Clausen et al., 2003). Furthermore, additional structures in porous rocks may form which show contrary effects on permeability compared to fractures: deformation bands (sandstones, carbonates) or stylolites (carbonate rocks), with enhanced sealing capacities (Aydin, 1978; Antonellini and Aydin, 1994; Tondi et al., 2006). These structures are the result of either grain movement, grain rotation or grain fracturing in narrow bands of localized strain (deformation bands), and pressure solution (stylolites) (Aydin, 1978; Antonellini and Aydin, 1994; Tondi et al., 2006), and may lead to a decreased permeability (Antonellini and Aydin, 1994; Fossen et al., 2007).

In fractured reservoirs fractures may have great effects on fluid flow, since they can either increase reservoir permeability or increase permeability anisotropy (Nelson, 1985; Gudmundsson, 2011; Philipp et al., 2013). Because matrix permeability in geothermal reservoir rocks is negligible in most cases and high flow rates are needed for successful geothermal projects, the characterization of fault zones and associated fracture systems is of particular importance (Paschen et al., 2003; Philipp et al., 2010; Stober et al., 2011; Reyer et al., 2012). In the present study we use outcrop analogues to analyze the effect of fault zones on fracture system parameters and permeability in fault-related and fractured geothermal reservoirs.

Outcrop analogues expose rocks similar to those found at geothermally relevant depths (in terms of stratigraphy, lithology, facies) and therefore provide an opportunity to study fracture-induced permeability of potential geothermal reservoir rocks (Philipp et al., 2010). We focus on the Middle Triassic Muschelkalk which forms one potential geothermal reservoir in a region with comparatively high geothermal gradient in Germany: the Upper Rhine Graben (URG; Paschen et al., 2003; Stober and Jodocy, 2009; Stober et al., 2011). We investigate whether the simplified fault core-/damage

zone model is applicable to define the permeability structure of fault zones crosscutting more or less brittle carbonates. In particular we focus on the fracture systems associated with the fault zones. Deformation bands or stylolites were not visible macroscopically in the field and therefore are not taken into account.

We present results of eight fault zones crosscutting Muschelkalk rocks of the Kraichgau-Syncline located on the eastern graben shoulder of the URG (Fig. 1) aiming at characterizing fault zones and associated fracture systems. First, we show preferred orientations of fault zones and associated main fracture sets in the Kraichgau-Syncline. Here we aim at integrating fault zone developments in the context of the regional stress field evolution. Second, we characterize three selected fault zones in detail. We examine selected fracture system parameters (orientation, density, aperture, connectivity, vertical extension) within defined fault zone units and their distributions across the fault zones. Special attention is given to record mineral precipitations within the fault zone units and in particular within fractures to highlight preferred orientations of past fluid flow. With the studies we gain insights into the development of fracture-associated permeability of Muschelkalk rocks.

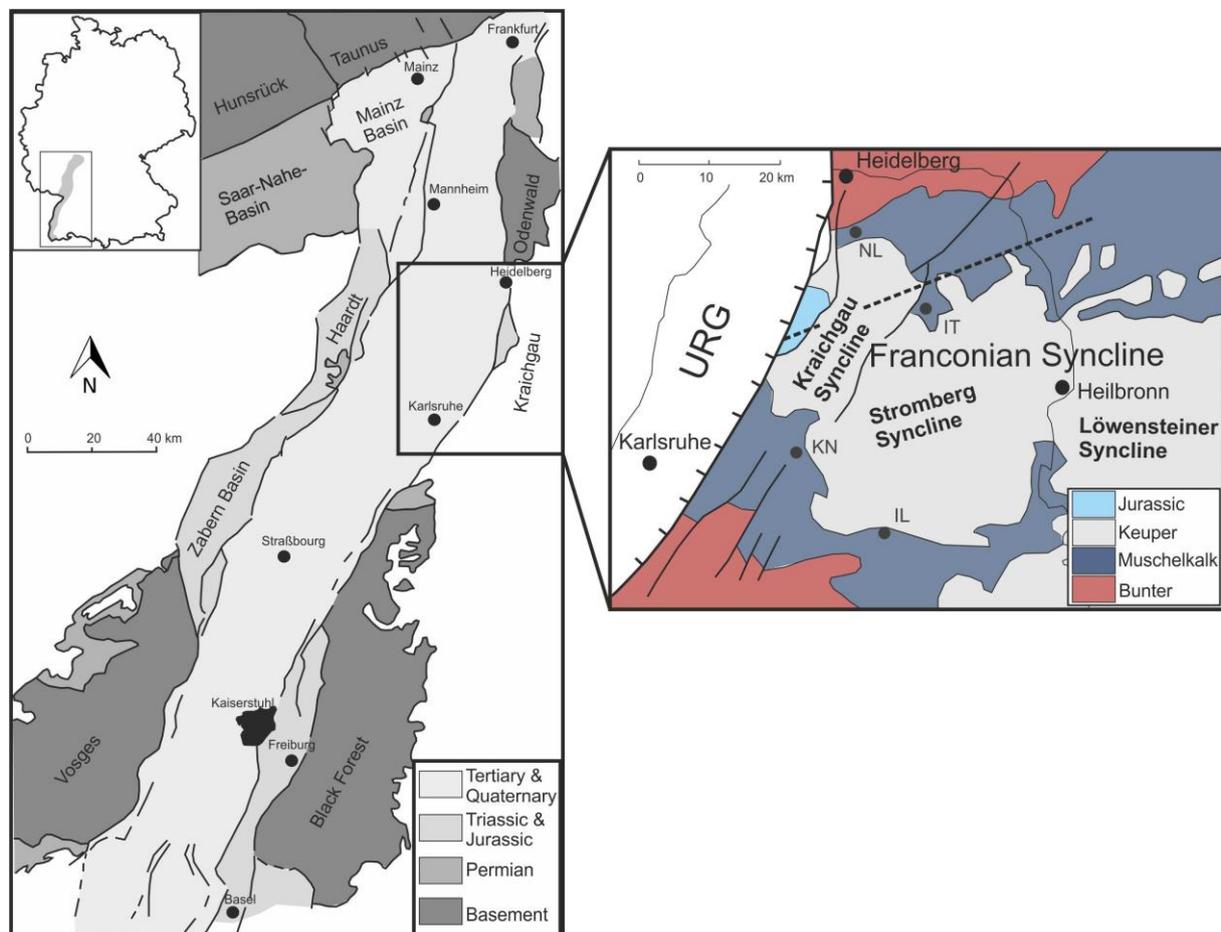


Fig. 1. Simplified geological maps (modified from Walter, 2007) of the Upper Rhine Graben (URG; left) and the Kraichgau study area (right). The locations of the quarries are marked by dark-gray dots (IL - Illingen; IT - Ittlingen; KN - Knittlingen; NL - Nussloch). The axis of the Kraichgau-Syncline is marked by a dashed line.

## 2 Geological setting

The URG forms the central part of the Cenozoic European Rift System, which extends from the North Sea to the Mediterranean Sea (Illies, 1972; Ziegler, 1992; Schumacher, 2002; Ziegler and Dèzes, 2005). This extensional structure, margined by master normal

faults, was formed since Eocene in a weakened region, due to a thinned crust and a thermal anomaly, and exhibits a displacement of approximately 4 km (Illies, 1972; Illies and Greiner, 1978, Ziegler and Dèzes, 2005). The graben interior is filled with Tertiary and Quaternary sediments. The Variscan basement as well as Permian and Mesozoic formations crop out at the eastern and western graben shoulders (Illies, 1972; Walter, 2007), which were uplifted during subsidence within the graben (Schweitzer and Kraatz, 1982; Trunkó, 1984; Ziegler, 1992).

The URG shows an asymmetric setting with larger displacement at the eastern graben margin (Illies, 1972; Eisbacher and Fielitz, 2010). Due to a complex fault block structure within the graben and variations in displacement, lithological changes are common and an irregular graben floor is developed (Illies, 1972; Trunkó, 1984).

The URG evolution is marked by repeated stress field changes, for example in Oligocene and Miocene (Illies, 1972; Trunkó, 1984; Schuhmacher, 2002). In the Pliocene, the URG was reactivated again, resulting in strike-slip movements from changes in the regional stress field (Illies and Greiner, 1978; Schumacher, 2002). The shear components led to reactivations of primary normal faults as oblique-reverse faults in particular at the eastern graben margin (Illies, 1972; Ziegler, 1992). The recent stress field provides a strike-slip stress regime parallel to the graben axis as well (e.g., Ziegler, 1992, and references therein; Schumacher, 2002; Heidbach et al., 2008).

Our study area, the Kraichgau-Syncline (Fig. 1), is located on the eastern graben shoulder of the URG and part of the Franconian-Syncline (Walter, 2007). This syncline belongs to a system of ENE-WSW trending intramontane basins, which developed during the Stephanium and Early Permian due to reactivations of Variscan structures (Schuhmacher, 2002; Ziegler and Dèzes, 2005). In context of the URG tectonics the Kraichgau-Syncline was mildly uplifted compared with the adjacent highs of Odenwald and Black Forest on the eastern graben shoulder (Schweitzer and Kraatz, 1982; Engesser and Leiber, 1991). Various fault zones crosscut the Kraichgau-Syncline with preferred orientations of SSW-NNE, SW-NE and NW-SE (Trunkó, 1984).

The Middle Triassic Muschelkalk, divided into Lower, Middle and Upper Muschelkalk, has a total thickness of 200 m to 230 m. The succession is composed of alternating carbonates and evaporates (Schweitzer and Kraatz, 1982; Engesser and Leiber, 1991). These alternations are the results of sea-level-changes during their deposition in the epicontinental sea (Engesser and Leiber, 1991).

The Lower Muschelkalk shows a total thickness of approximately 75 m to 78 m and comprises carbonates, i.e., limestones, marly limestones, marls and dolomites, which were deposited under shallow marine conditions (Schweitzer and Kraatz, 1982; Engesser and Leiber, 1991). The thickness of Middle Muschelkalk rocks is varying but shows a maximum of 100 m (Engesser and Leiber, 1991; Eisbacher and Fielitz, 2010). These alternating carbonates and evaporites (dolomite, gypsum, anhydrite, rock salt) were formed under a shallow marine environment in a marine basin that repeatedly became isolated and experienced significant evaporation. Leaching of these evaporates has led to the aforementioned thickness variations, and only residual clay is commonly present (Engesser and Leiber, 1991). The 85 m to 100 m thick formation of the Upper Muschelkalk can be further subdivided into three main subunits, named as *Trochiten-Kalk* (mo1), *Nodosus-Schichten* (mo2) and *Semipartitus-Schichten* (mo3). They are characterized by micritic limestones, which are low on fossils, alternating with fossil-rich carbonates, marls and clay (Schweitzer and Kraatz, 1982; Engesser and Leiber, 1991). Deposition has been ascribed to a shallow marine environment characterized by changing

water conditions (micritic limestones versus tempestites; Schweitzer and Kraatz, 1982; Engesser and Leiber, 1991).

### 3 Field studies

To obtain information on fault zone infrastructures, well exposed fault zones with distinct fault zone units are needed. The selected quarries, where the Muschelkalk rocks are crosscut by various fault zones, are located in the northern and southern part of the Kraichgau-Syncline (Fig. 1). The Nussloch-quarry is situated near the URG master-fault, whereas the Illingen-quarry shows the maximum distance of approximately 30 km to the graben margin. Due to the tectonic history of the study area, including changes in the regional stress field resulting in reactivations (cf., Sections 2. and 5.1.), the fault zones are of different types and show various displacements (cf., Table 1, Section 5.1.). The damage zones of some main fault zones include minor faults, as is expected by progressive fault growth (e.g., Childs et al., 2009).

Table 1. Analyzed fault zones. The fault zone types refer to the reflections in the discussion (Sections 5.1.1. to 5.1.3.).

Quarry	Number of fault zones	Fault zone type	Displacement
Nussloch (NL)	1	Normal fault zone with associated minor fault	~ 40 m, minor fault unknown
Knittlingen (KN)	1	Reactivated reverse fault zone	unknown
Knittlingen (KN)	2	Normal fault zone, reactivated as reverse fault	~ 4 m
Illingen (IL)	1	Oblique-slip fault zone with minor fault	Horizontal unknown, vertical ~ 0.15 m, minor fault unknown
Illingen (IL)	1	Normal fault zone	0.30 m
Illingen (IL)	1	Reverse fault zone	0.57 m
Ittlingen (IT)	1	Normal fault zone	~ 3 m

In order to characterize the fault zone infrastructures, we determined the thicknesses and lithological features of the fault cores as well as the damage zone characteristics (damage zone widths and properties of the fracture systems within the damage zones; see below). According to previous studies we define the boundary between fault core and damage zone as the boundary between faulted rock (e.g., fault gouge or breccia, lenses, dragged bedding) and pronounced original bedding where the fracture density is higher than the background density (cf., Braathen et al., 2009; Bastesen and Braathen, 2010; Bastesen et al., 2013; Schueller et al., 2013).

Kinematically and mechanically, fractures can be distinguished in extension fractures and shear fractures, depending on their relative movement to the fracture plane (Fossen, 2010; Gudmundsson, 2011). Extension fractures show a relative movement normal to the fracture plane (opening/extension mode, for example joints and veins) and shear fractures in direction parallel to it (shear modes; eg., Twiss and Moores, 2007;

Gudmundsson, 2011). Since there is not always the possibility to obtain clear evidence for fracture kinematics in the field, we use the general term fracture for a surface across which the rock has lost cohesion.

To determine the damage zone width, the fracture density distribution (number of fractures per unit length) normal to the slip surface was detected, if possible, in several limestone beds of these limestone-marl-alternations, using the scanline-method (e.g., Priest, 1981; Berg and Skar, 2005; Micarelli et al., 2006a). The selected limestone beds are well exposed and traceable over several meters. In rare cases of covered beds we used beds with comparable thicknesses for continued scanlines. Each scanline starts at the boundary of the fault core and damage zone (the fault core thickness was measured at this zero point) and runs towards the damage-zone-/host-rock transition of the hanging wall and footwall, except for the scanline across the Illingen oblique-slip fault (cf., Sections 4.1., 4.2.2.). Additional scanlines within the undisturbed host rock give information on background fractures. We define the outer boundary of the damage zone as the point where the fracture density clearly decreases towards background fracturing (e.g., Childs et al., 2009; Schueller et al., 2013). Besides the fracture orientations (strike direction and dip angle), the properties of each fracture within the defined fault zone units were examined as follows.

One important fracture parameter in terms of reservoir permeability is the fracture aperture. Few open fractures with larger apertures may enhance the permeability, because the flow rate depends on the cube of the fracture aperture (cubic law; De Marsily, 1986; Odling et al., 1999) and fluid flow may be channeled along the widest parts of a fracture (Odling and Roden, 1997; Philipp et al., 2013, and references therein). We show the maximum values of fracture apertures, that is the maximum fracture dimension measured perpendicular to the fracture walls (Philipp et al., 2013). However, we have to consider that measurements under surface conditions are not directly applicable for permeability calculations for example due to uplift induced expansion and erosion as well as weathering effects such as karstification. It is intended that our measurements provide indications for fracture aperture distributions within fault zones, but no absolute values.

Additionally, it is necessary to distinguish between open fractures and fractures sealed with mineral precipitations. Open fractures include no filling material between the fracture walls (Nelson, 1985). We name fractures showing mineral precipitations, for example deposits of calcite or silica, mineralized fractures. They are indicators for past fluid flow, whereas they could act as barriers for recent fluid flow in potential geothermal reservoirs (Nelson, 1985; De Marsily, 1986; Philipp, 2012). Thus, the fracture orientations and distance to the fault core of mineralized fractures were noted during the field studies. Due to sealing of these fractures the fracture thickness was measured instead of fracture aperture.

Furthermore, the fracture system connectivity is of great importance in our investigation, because only interconnected fractures could form a hydraulically active fracture network (Stauffer and Aharony, 1994; Odling et al., 1999; Ortega and Marrett, 2000; Micarelli et al., 2006a; Philipp et al., 2013). We distinguish between connected and unconnected fractures, that is, between fractures whose tips terminate against other fractures, and unconnected fractures with no visible connection. These observations indicate the degree of physical connection of the fracture system.

Additionally, we take the fracture vertical extension into account. First, the fracture length was investigated as the distance of a straight line connecting the two fracture tips

in vertical direction (also referred to as fracture height). Second, we considered how far the fractures propagate through the mechanically layered rocks, distinguishing 'stratabound' and 'non-stratabound' fractures (Odling et al., 1999). Stratabound fractures are restricted to only one limestone bed. Non-stratabound fractures, however, expand across several beds and therefore may create a hydraulically relevant flow path between multiple layers.

## 4 Field results

In this section, first a short overview of the orientations of all analyzed fault zones and of the fracture systems within the quarries is presented. Second, detailed results of fault zone infrastructures and associated fracture system properties of selected, well exposed fault zones are shown to analyze their complex structures and discuss their most likely specific tectonic development.

### 4.1 Fault zone and fracture system orientations

We show the orientation of the fracture system (all fracture data of fault zones and host rock) as well as the fault zone orientations within the quarries Nussloch (NL), Illingen (IL), Knittlingen (KN) and Ittlingen (IT) (Fig. 2; the color code refers to the fault zone classifications in the discussion, Section 5.1.). Despite the Knittlingen-quarry exposes additional fault zones, we only present results of three fault zones due to the best accessibility in the outcrop.

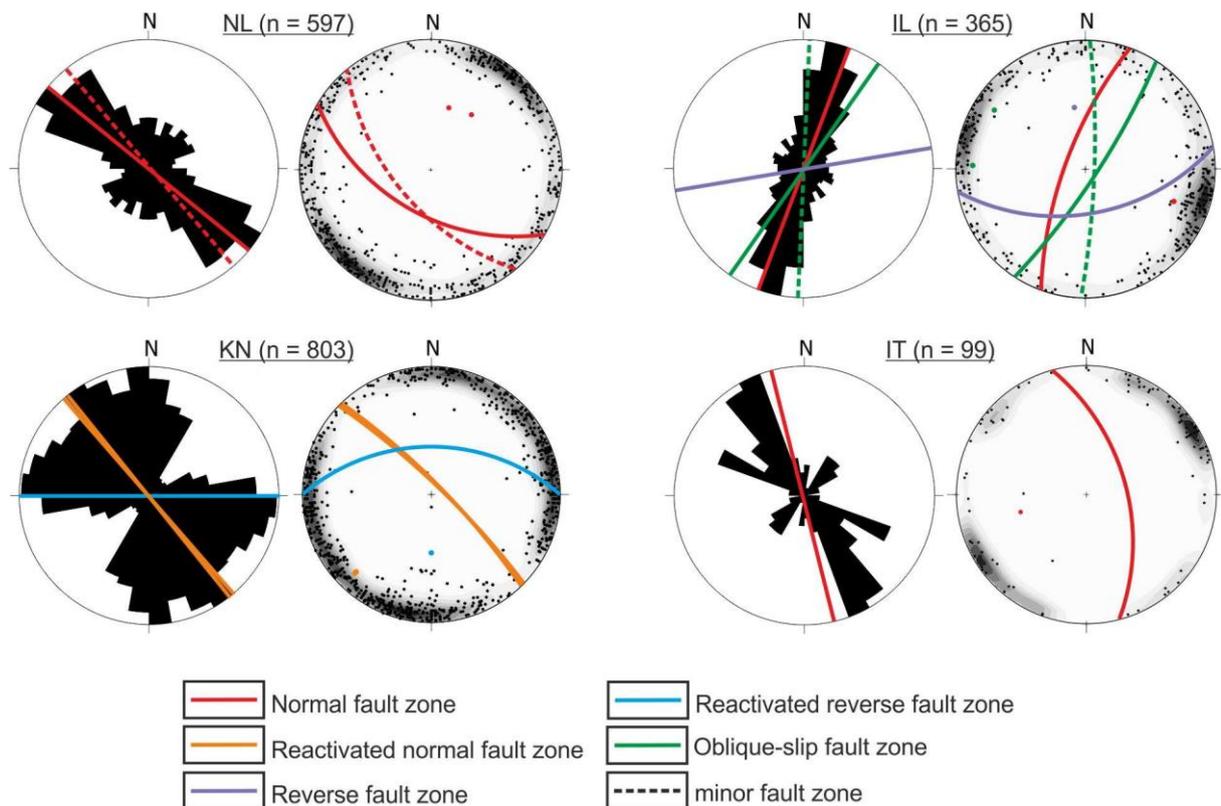


Fig. 2. Orientation of fracture systems and fault zones ( $n$  = number of fractures) in the quarries Nussloch (NL), Illingen (IL), Knittlingen (KN) and Ittlingen (IT). Left: Symmetrical Rose Diagram ( $10^\circ$ -classes), the fault zones are plotted as lines. Right: Schmidt Diagram, equal area projection, lower hemisphere. The fractures are marked by poles (black), the fault zones by great circles and poles. Color code indicating fault zone type see key. These definitions refer to the reflections in the discussion (Sections 5.1.1. to 5.1.3.).

The analyzed fault zones are formed parallel to regional structures of the URG and the Kraichgau-Syncline in NNE-SSW- to N-S-direction, NW-SE-direction and E-W-direction.

The individual fracture systems are clearly affected by the fault zones: main fracture sets are formed parallel or subparallel to the fault zone strikes, except for the Knittlingen-quarry, where a wider scatter in fracture orientations occurs.

Since footwall and hanging wall show an asymmetric deformation behavior resulting in different fracture patterns within these fault blocks (e.g., Berg and Skar, 2005; Reyer et al., 2012), detailed fracture data are separated in fractures in footwalls versus fractures in hanging walls of the fault zones (Fig. 3; the color code refers to the fault zone classifications in the discussion, Section 5.1). The main fracture set is developed parallel to the fault zone strike in almost all hanging walls. In the footwalls, however, the fracture sets are formed either subparallel to or exhibit an angle of approximately 30° to the fault zone strike. These fractures may be shear fractures (Riedel shears) associated with the fault zone. Some of these fractures, however, may be not directly fault-related, but rather background fractures associated with the main regional stress field. Differing fracture orientations within the defined fault zone units are developed particularly in the Knittlingen-quarry.

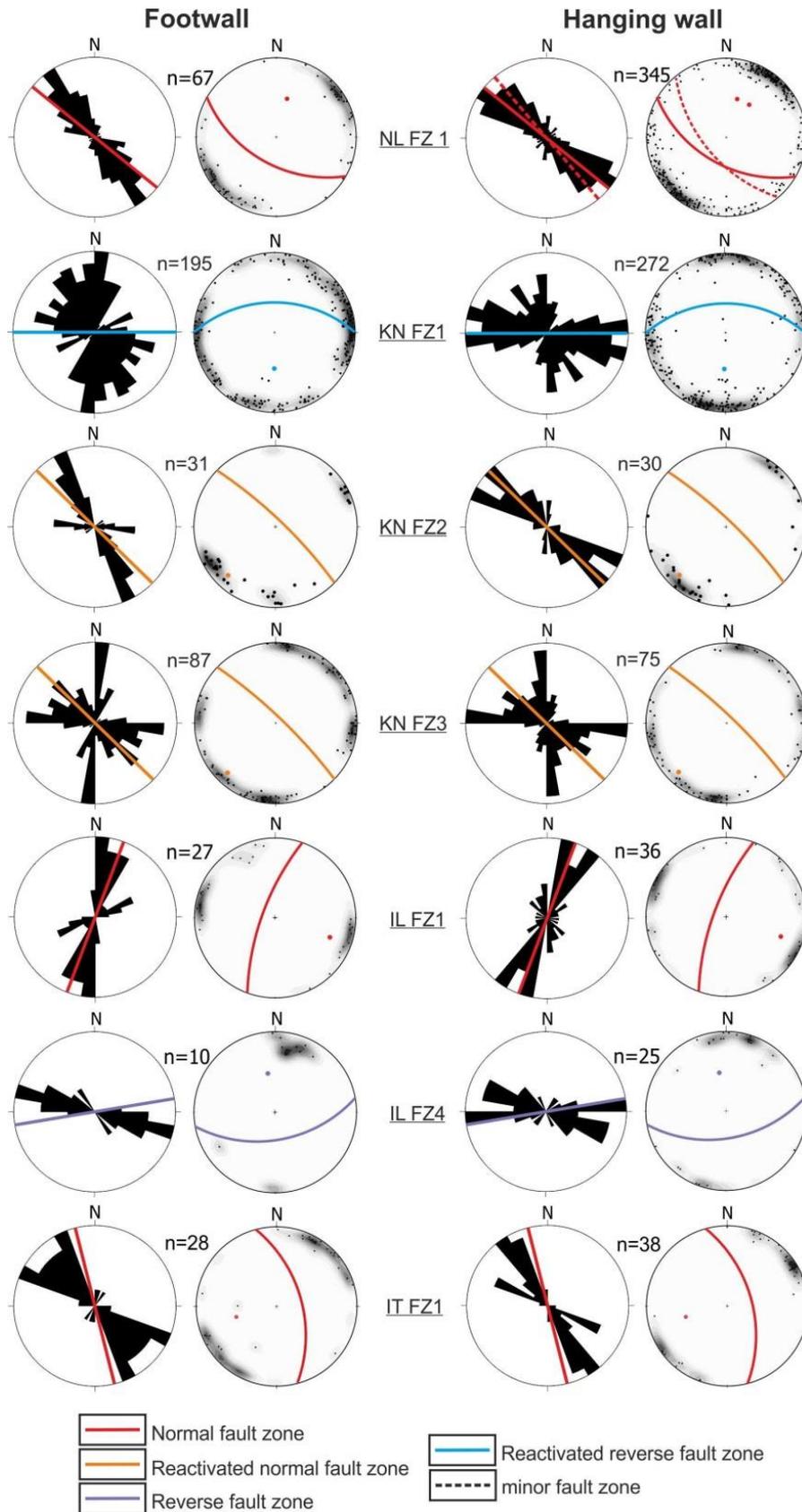


Fig. 3. Fracture orientations of the fractures in footwall and hanging wall of the fault zones (FZ) analyzed in Nussloch (NL), Knittlingen (KN), Illingen (IL) and Ittlingen (IT). Left: Symmetrical Rose Diagram ( $10^\circ$ -classes), the fault zones are plotted as lines. Right: Schmidt Diagram, equal area projection, lower hemisphere. The fractures are marked by poles (black), the fault zones by great circles and poles. Color code indicating fault zone type see key. These definitions refer to the reflections in the discussion (Sections 5.1.1. to 5.1.3.).

Figure 4 shows the fracture system orientation within the fault zone in Illingen. Due to the steep dip of this fault zone, we distinguish between eastern fault block, western fault block and fault core only. The fracture systems in the eastern and western fault blocks contain main fracture sets parallel to main and minor (western fault block) slip surfaces. Fractures with differing orientation in the eastern fault block are interpreted as background fractures associated with main regional structures. The main fracture set in the fault core is different with strike NNE-SSW.

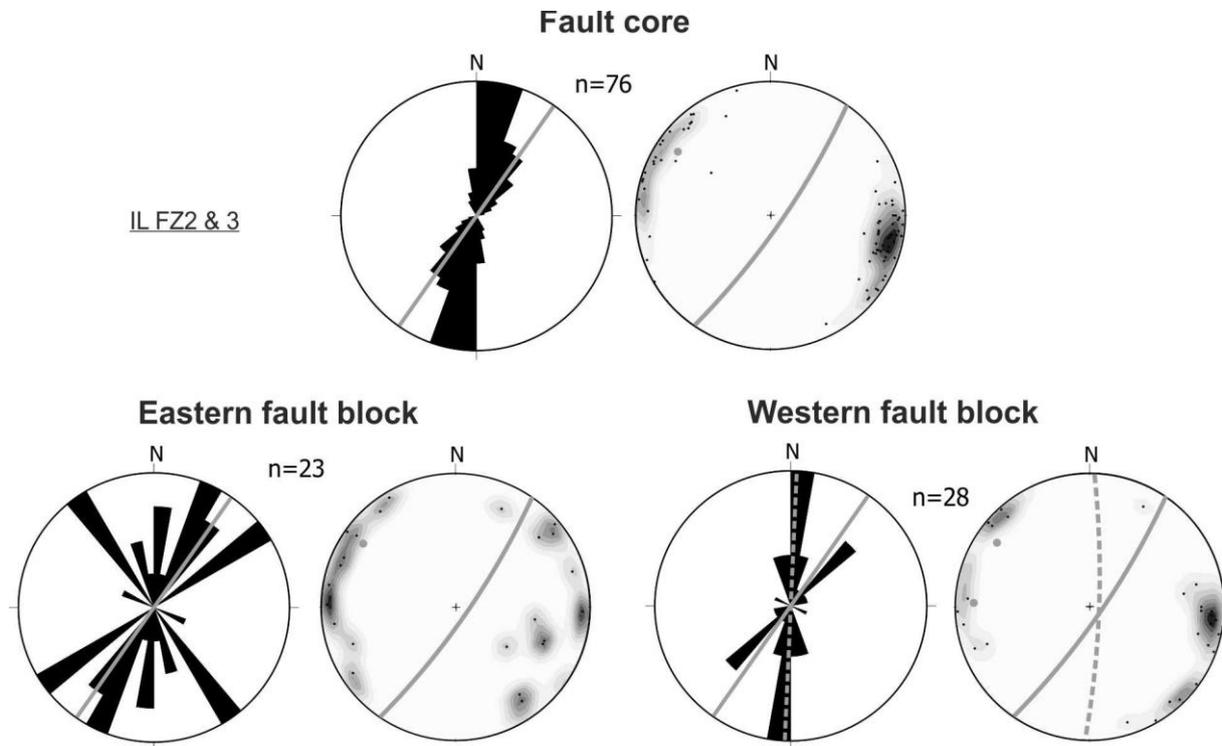


Fig. 4. Fracture system orientation in the main fault zone in Illingen (IL) separated in eastern fault block, fault core and western fault block: Fault zone (FZ) 2 as main fault and FZ 3 as minor fault within the western fault block (marked by dashed lines). Left: Symmetrical Rose Diagram ( $10^\circ$ -classes), the fault zones are plotted as gray lines. Right: Schmidt Diagram, equal area projection, lower hemisphere. The fractures are marked by poles (black), the fault zones by great circles and poles in each case (gray).

## 4.2 Detailed fault zone analyses

### 4.2.1 Nussloch

The steep-dipping fault zone cropping out in the Nussloch-quarry (northern Kraichgau; cf., Fig. 1) is hosted in parts of the entire succession of the Muschelkalk. The first slip surface (SP 1; NE) juxtaposes Middle Muschelkalk rocks, mainly residual clay and dolomite, and limestone-marl-alternations of the Lower Muschelkalk in the lower outcrop-level as well as Middle Muschelkalk rocks in the upper level. Another adjacent slip surface (SP 2; SW) juxtaposes these Middle Muschelkalk rocks and the Upper Muschelkalk (Fig. 5). A synthetic minor fault zone located in the hanging wall (Upper Muschelkalk) intersects with this main slip surface SP 2. The triangularly shaped area embedded between the slip surfaces of main and minor fault is highly fractured at their intersection (named as fractured zone, Fig. 5b).

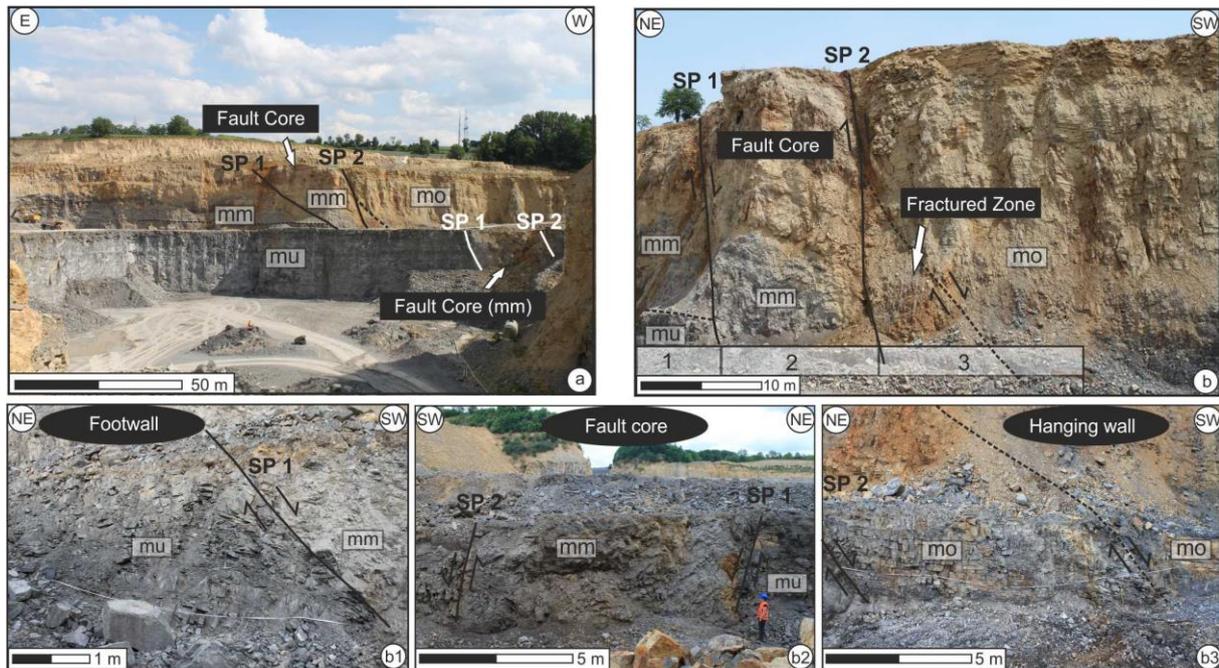


Fig. 5. Field pictures of the analyzed fault zone in the Nussloch-quarry (SP = slip surface, also referred to as slip plane). a) Outcrop overview. View S. b) Fault zone overview, fault zone parts 1 to 3 are shown in detail in the lower section. View SE (b1 and b3) or to NW, respectively (b2). The trace of the minor fault is marked by a dashed line.

The up to 13 m wide fault core is embedded between the main slip surfaces and consists of inclined Middle Muschelkalk rocks and underlying Lower Muschelkalk rocks (Figs. 5 and 6). In general, this fault core comprises deformed rock, fault breccia and isolated host rock lenses, particularly at the fault core/hanging-wall-transition. In the Middle Muschelkalk part, gray colored residual clay is dragged downwards in an s-shape. Minor slip surfaces within the fault core displace the rocks at several locations. At the fault core-hanging-wall-boundary the fault core is characterized by red-colored, up to 1.5 m wide mineralizations (Fig. 6).

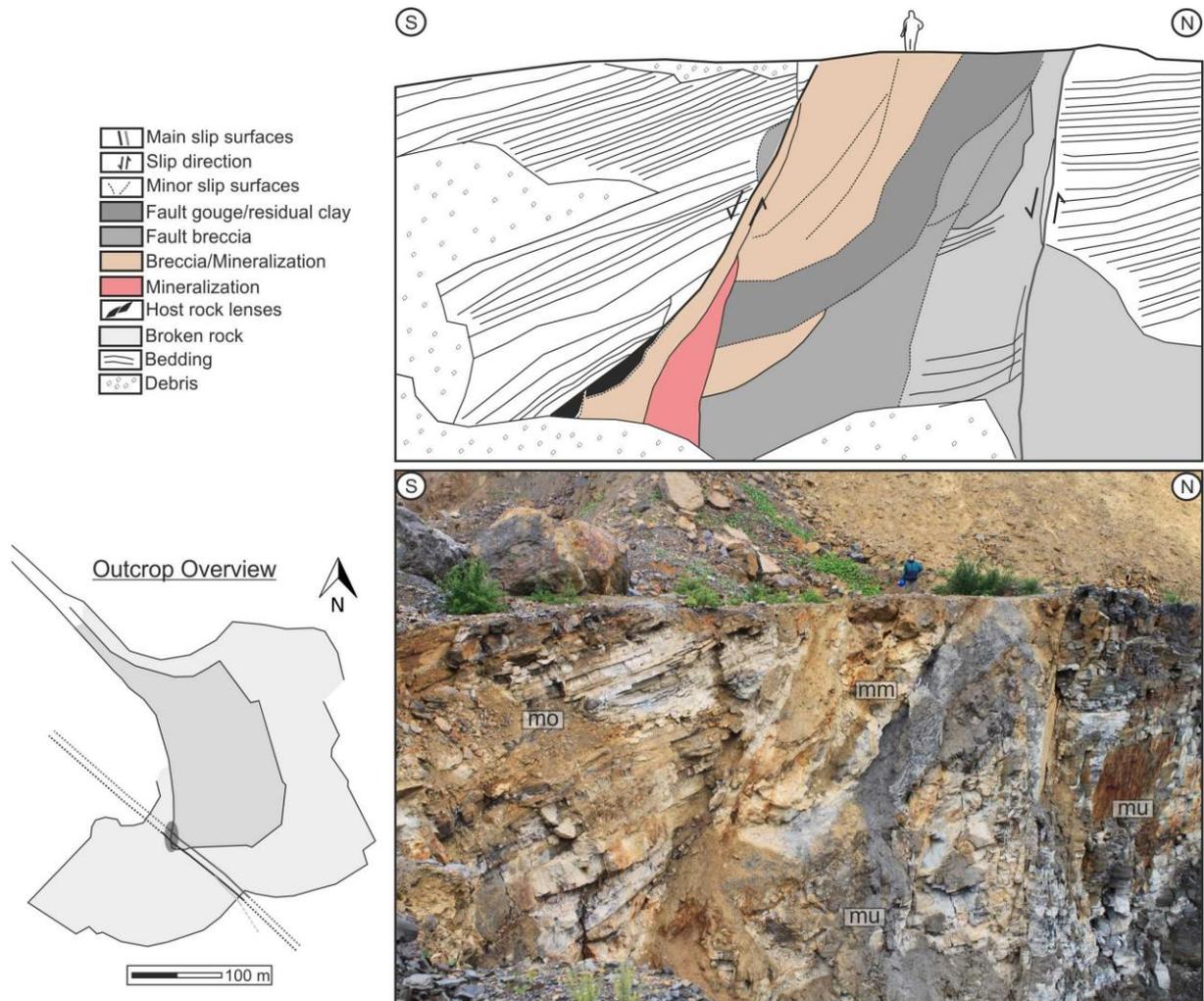


Fig. 6. Sketch and field picture of the analyzed fault zone in the Nussloch-quarry (view W). See person for scale. Outcrop overview: Picture location is displayed by the gray shaded ellipse, the fault zone trace by gray and black lines (dashed lines - assumed fault zone trace).

The fracture density distribution normal to the fault zone was examined in several scanlines. The highest fracture density occurs at contact to the slip surface (Fig. 7). However, there is no decrease to background fracturing with rising distance to the fault core. We assume that the outer damage zone boundary is not reached in the analyzed fault zone section and that our measurements were exclusively performed within the damage zone. Two scanlines cut the minor fault zone within the hanging wall damage zone and therefore their minor damage zone as well (Fig. 7b).

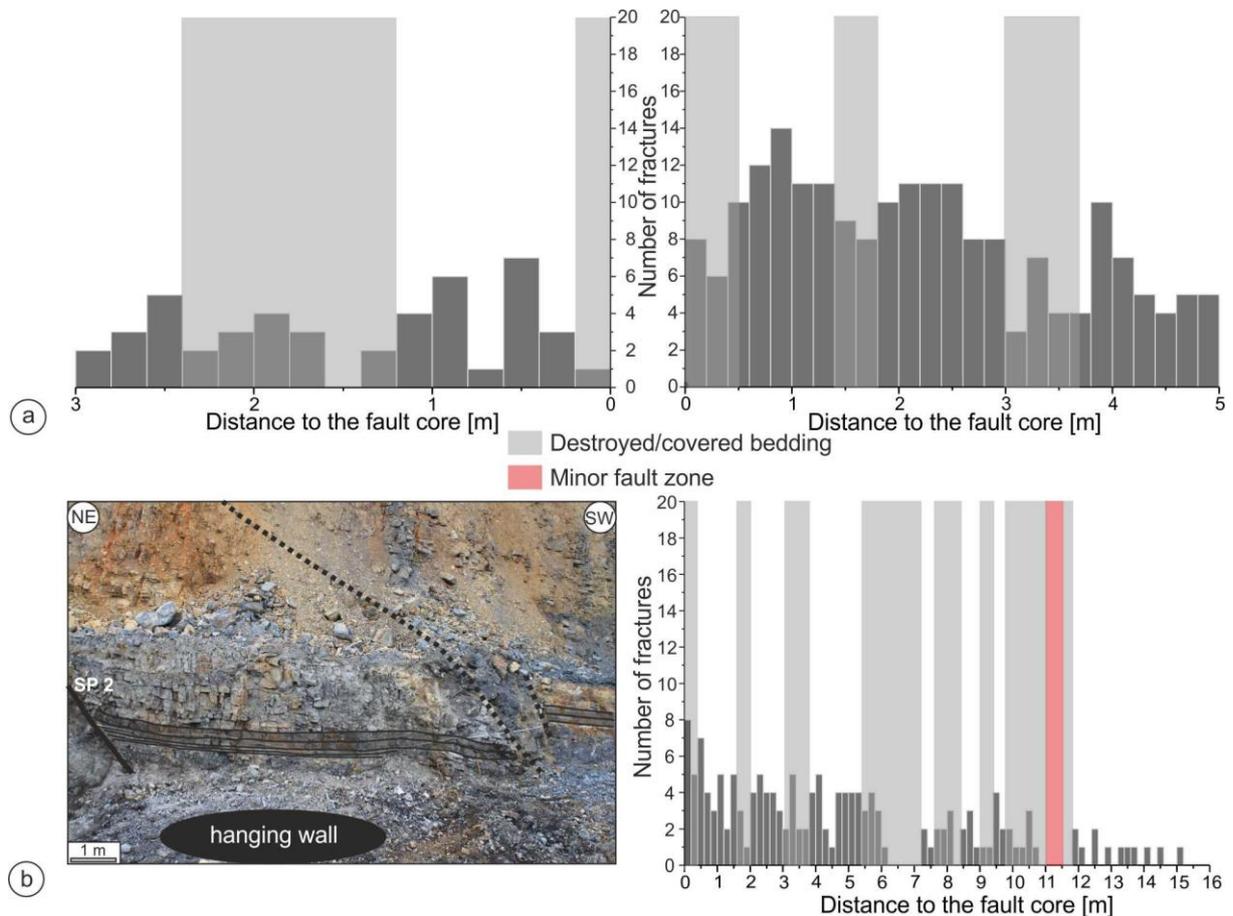


Fig. 7. Fracture density distribution normal to the main fault zone in the Nussloch-quarry. a) Data from all scanlines in the footwall up to 3 m (left) and hanging wall up to 5 m (right) distance to the fault core. b) Overview-picture of the hanging wall including one minor fault zone (left, view SE; scanline locations are traced) and fracture density distribution in the longest profiles 1 and 2 (up to 16 m). These profiles cut the minor fault zone in the SW (marked by the red bar) and therefore their damage zone. In the gray labeled zones the rock mass is destroyed or covered, not every fracture was detected individually.

#### 4.2.2 Illingen

The steep fault zone in Illingen shows slight changes in strike-direction (see above; Fig. 8). The quarry provides the possibility to study both the fault core in the South (Figs. 8a and 8b) and one slip surface in the North (Fig. 8c). Various structures are hosted on the undulating slip surface exposed in the North such as slickenlines and slip fibers. Additionally we observed limestone beds rotated and truncated against each other (Fig. 8c).

The fault core in the South, embedded within the two main slip surfaces, comprises fault breccias at contact to the main slip surfaces, limestone beds folded to an anticline in the upper center, flexures at contact to the western slip surface, and limestone lenses (Fig. 8a). Minor slip surfaces juxtapose the rocks at the bottom of the wall with a normal displacement of approximately 15 cm (Fig. 8b). The dip-direction and dip-angle of the bedding changes within the fault core, with a steeper angle towards the western main slip surface (Fig. 8b). Similar flexures are formed in the eastern fault block at contact to the slip surface, whereas the bedding in the western fault block is more or less horizontal. The western fault block is crosscut by one minor fault zone.

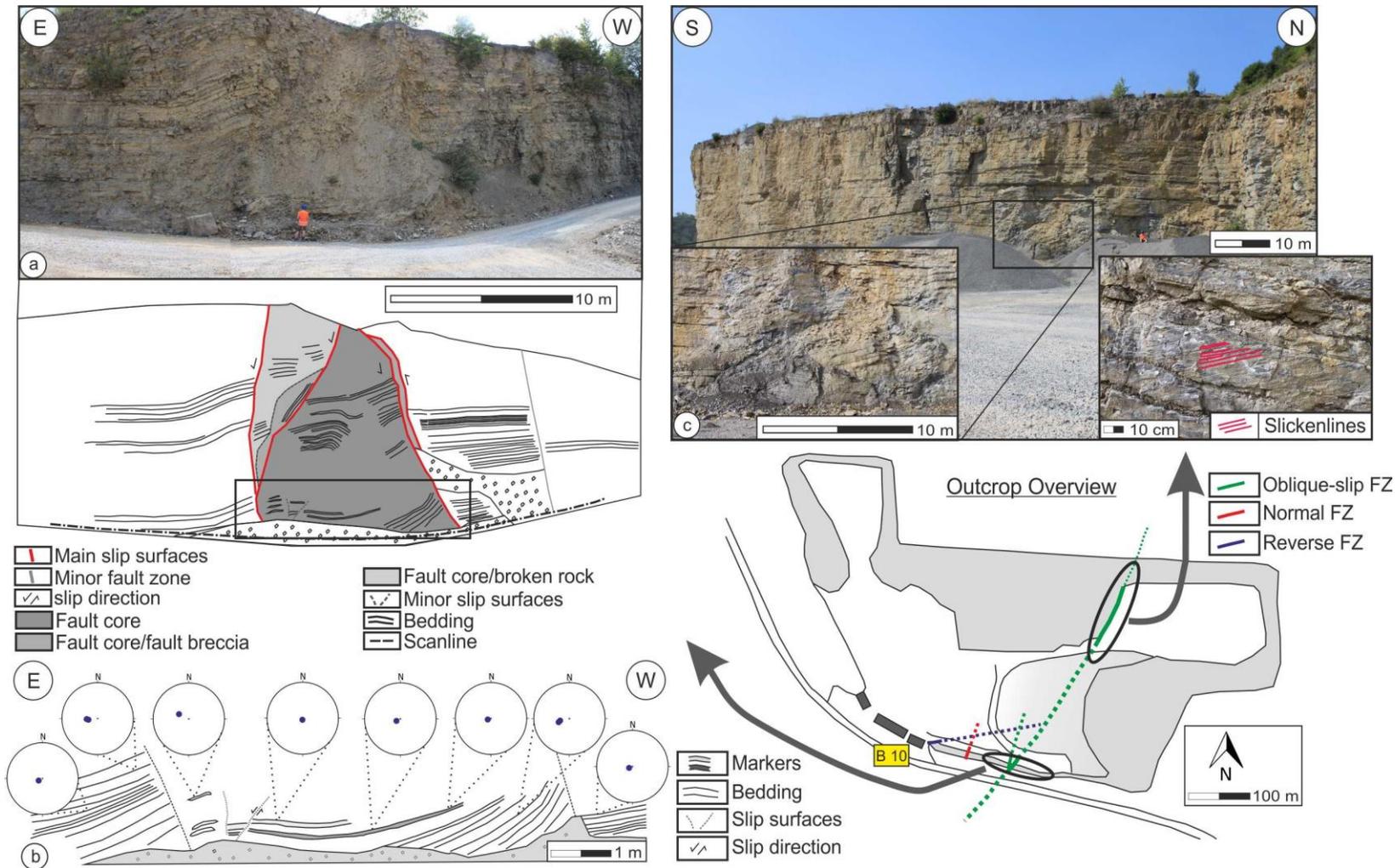


Fig. 8. Overview of the main fault zone in Illingen: Trace of main and minor fault zones are displayed by lines in the outcrop overview (color code indicating fault zone type see key; these definitions are based on the reflections in the discussion in Sections 5.1.1. to 5.1.3.; dashed lines - assumed fault zone trace). a) Fault core at the southern quarry border (view S). b) Detailed sketch of the lower fault core part with lower hemisphere projection of the poles (bedding). c) Field pictures of the exposed fault plane in the northern outcrop part (view W).

### 4.2.3 Knittlingen

The low-angle fault zone in Knittlingen with unknown displacement because of lacking visible marker horizons shows various deformation structures in hanging wall and footwall in particular (Fig. 9). The most conspicuous structure in the footwall is a synthetic minor fault. Between main and minor slip surface thin and softer layers are folded, but the thick and competent bed underneath is broken and shows a counterclockwise rotation. Another noticeable structure in the footwall is one water-bearing antithetic discontinuity, which intersects with the aforementioned minor slip surface. The hanging wall, where a flexure is formed, is less deformed than the footwall.

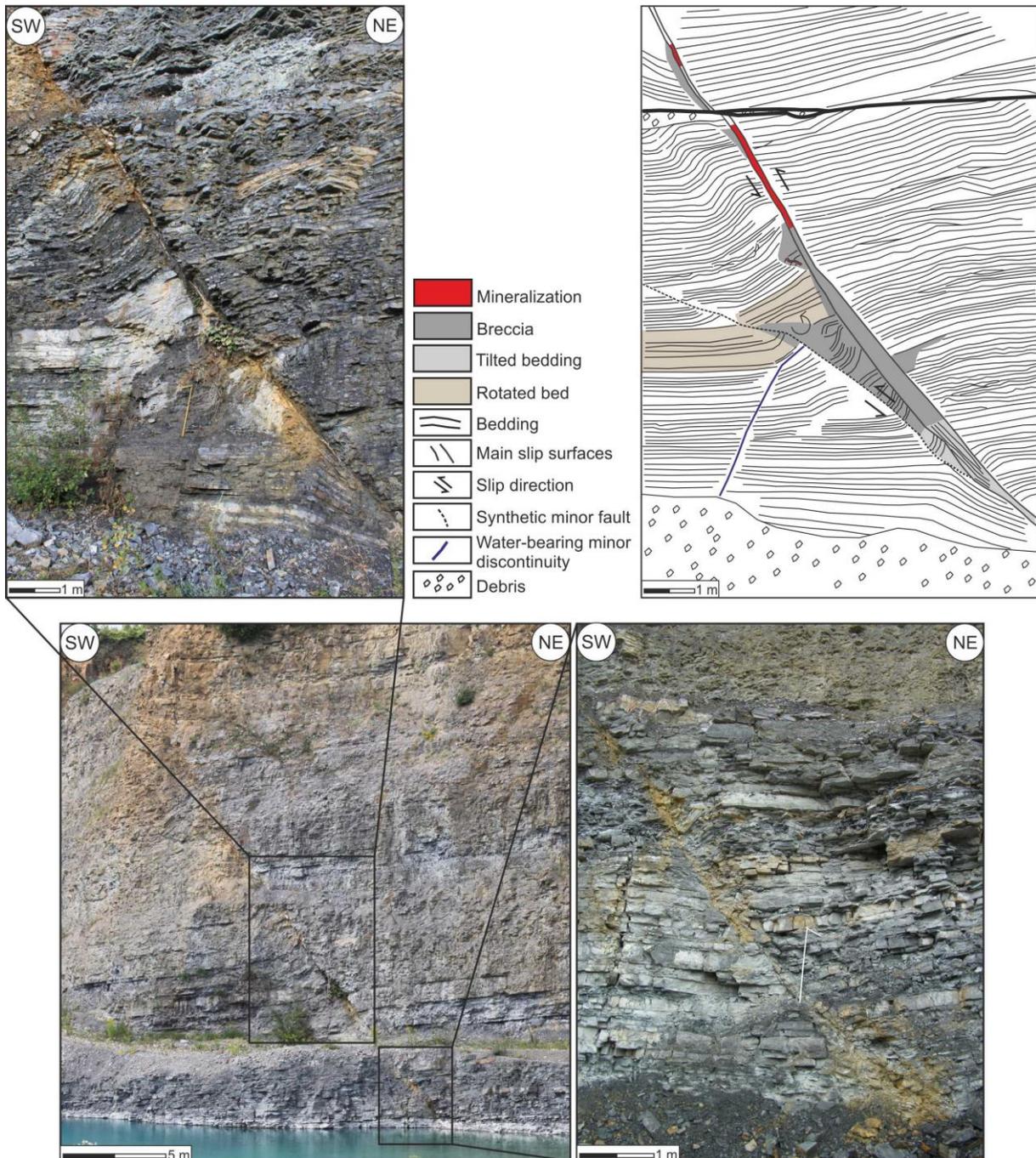


Fig. 9. Overview pictures and sketch of the described fault zone (FZ 1) cropping out in the Knittlingen-quarry (view NW). The sketch shows the soft and thin folded layers as well as the broken and rotated competent bed.

The fault core comprises various structures like lenses and both upwards and downwards dragged, tilted, and folded bedding. Other fault core parts are completely mineralized or comprise brecciated rock.

One outcrop-level beneath, where decimeter-thick limestone beds crop out, a differing deformation behavior is observable in the footwall. The competent beds are compressed, but not folded. In contrast, flexures occur in the hanging wall. The fault core in this fault zone part is brecciated and comprises discolored zones. Some limestone beds are dragged upwards in the fault core, similar to the upper section of this fault zone.

We determined the fracture density distribution normal to the fault zone (Fig. 10). Our results show no clear decrease to background fracturing with rising distance to the fault core. In addition to the high fracture density at contact to the slip surface an increased fracture density was detected at a distance of 2 to 3 m in the hanging wall.

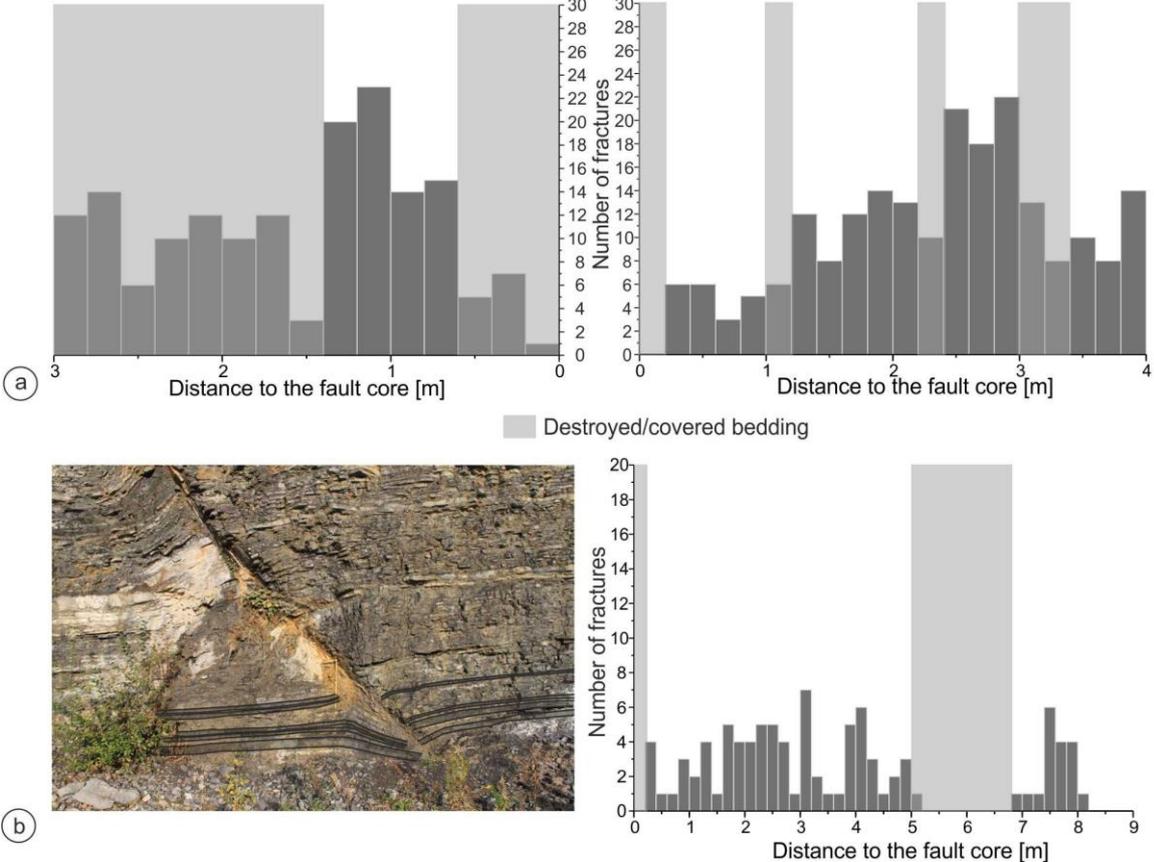


Fig. 10. Fracture density distribution normal to the described fault zone (FZ 1) in the Knittlingen-quarry. a) Data from all scanlines in the footwall up to 3 m (left) and hanging wall up to 4 m (right) distance to the fault core. b) Overview-picture of this fault zone (left, view NW; scanline locations are traced; scale: see folding rule expanded to 1 m) and fracture density distribution in the longest profile (right, up to 8.5 m). In the gray labeled zones the rock mass is covered or destroyed, not every fracture was detected individually.

### 4.3 Fracture connectivity

As mentioned in Section 3, the fracture connectivity is one important parameter in terms of reservoir permeability (Stauffer and Aharony, 1994; Odling et al., 1999; Micarelli et al., 2006a). We plot the fracture length versus fracture orientation (scale: 0°-180°; Fig. 11), and fault core distance [m] (Fig. 12) respectively, where we distinguish between connected (connected at either one or both tips) and unconnected fractures. Some fractures are marked by a star, because only the minimum length could be detected when one fracture tip was visible.

We plot the fracture length [m] of all fractures within the fracture systems vs. fracture orientation (Fig. 11a). In general, shorter fractures (up to a fracture length of 1 m) are more common within the quarries. Due to this huge number of comparatively shorter fractures, we show the data of fractures up to a fracture length of 1 m (Fig. 11b), in addition, to get a higher resolution on their fracture connectivity. The percentage of fractures with great length is generally higher for fractures parallel or subparallel to major slip surfaces and to regional structures (i.e., URG, axis of the Kraichgau-Syncline).

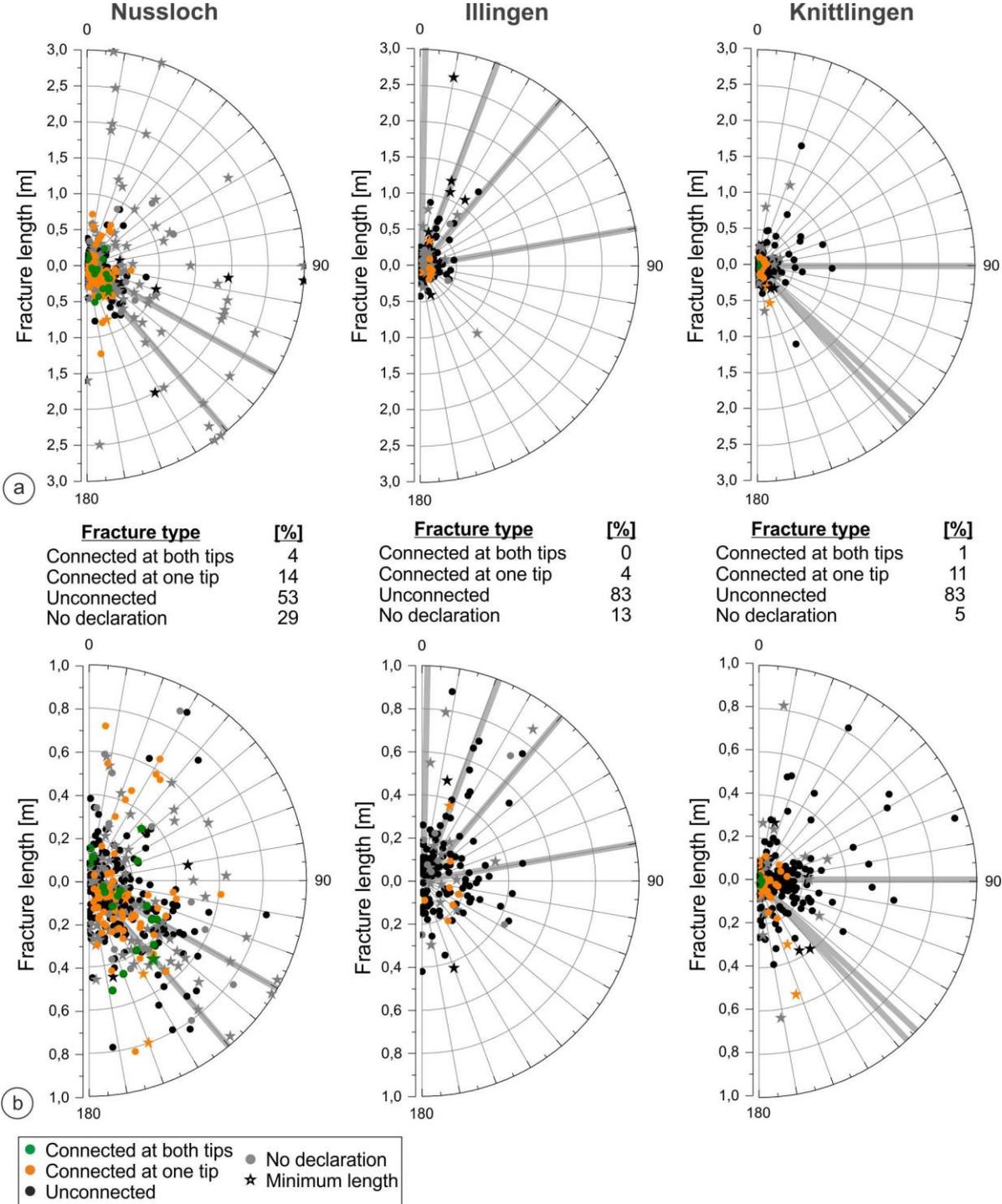


Fig. 11. Fracture connectivity of the fracture systems in the quarries Nussloch, Illingen and Knittlingen (color code see key; classified fracture types: percentage is shown for the entire dataset). Fracture length [m] vs. strike (scale: 0°-180°). a) All fracture data. b) Fracture data for shorter fractures up to 1 m length. The fault zone orientations are marked by a gray line. Fractures, from which only the minimum length was determined because only one tip was visible, are labeled with a star.

Most of the fractures are unconnected, whereby especially shorter fractures formed parallel to the fault zones provide a better connectivity within the fracture system. The highest percentage of interconnected fractures, and fractures connected at both fracture tips in particular, occurs within the Nussloch fracture system.

To show the connectivity of the fracture system within the fault zones, we plot the fracture length [m] and connectivity vs. fault core distance [m]. Individual long fractures are formed up to 6 m distance to the fault core of the fault zone in Nussloch, whereby the fracture length decreases with distance to this unit. Very few fractures (up to 0.5 m in length) are connected at both tips in the hanging wall of this fault zone, mainly up to a maximum distance of 3 m to the fault core (Fig. 12a). In the footwall fewer fractures with lengths up to 0.3 m are connected at one fracture tip.

The fracture system within the fault zone in Illingen contains mostly unconnected fractures, apart from individual fractures in the eastern fault block (Fig. 12b). Within the separated fault zone units of the fault zone in Knittlingen some fractures show connectivity at one fracture tip (Fig. 12c). These fractures, however, do not exceed a fracture length of 0.2 m, with one exception in the footwall (0.6 m).

In general, the data show a decreasing fracture length with increasing distance to the fault cores but a better connectivity of fractures with lengths up to 0.5 m (Fig. 12). That implies an improvement of fracture system vertical connectivity based on these comparatively shorter fractures in the fault zone units, as mentioned above.

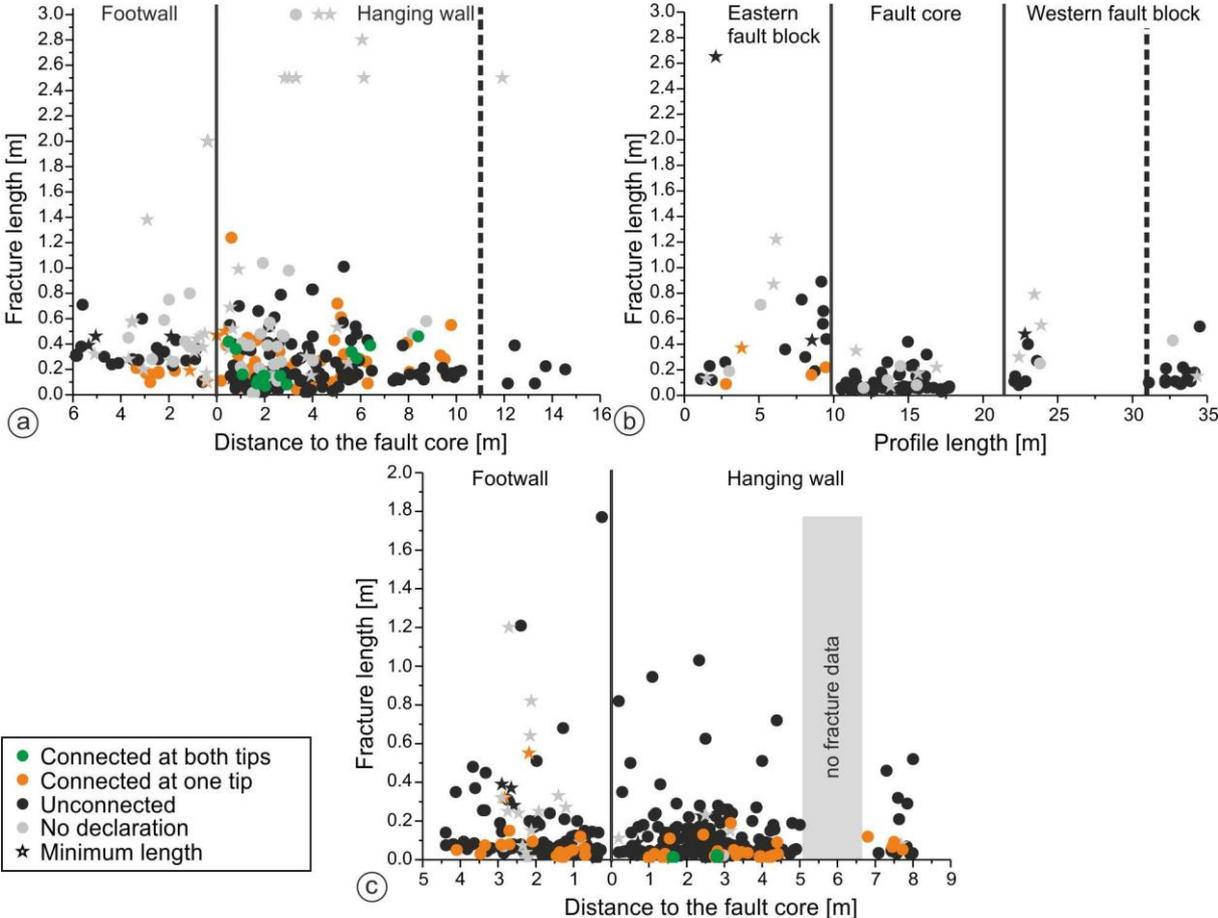


Fig. 12. Fracture connectivity of the fractures within the main fault damage zones (color code see key): a) Nussloch. b) Illingen. c) Knittlingen. In the gray labeled zone the rock formation is covered or destroyed, not every fracture was detected individually. The positions of fault core and minor fault zones are marked by dark-gray or by black dashed lines, respectively. Fractures, from which only the minimum length was determined because only one tip was visible, are labeled with a star.

#### 4.4 Fracture vertical extension

Fractures extending over multiple limestone beds (i.e., non-stratabound fractures) may increase the reservoir permeability across the mechanically layered Muschelkalk rocks in vertical direction. Stratabound fractures, however, are restricted to one bed (cf., Section 3.; Odling et al., 1999). Therefore, we plot the percentage of stratabound to non-stratabound fractures determined in the quarries separately for the units fault zone and host rock and the same data in relation to the fault core distance of the detailed fault zones (cf., Section 4.2.; Figs. 13b, 13d, and 13f). Due to isolated limestone beds within the fault core of the fault zone in Illingen and a resulting rare dataset compared with the other outcrops, the fracture system within this fault zone is separated to eastern fault block, fault core and western fault block (Fig. 13d). In Figure 13 the fault zone types refer to the definitions in the discussion (Section 5.1.).

The percentage of non-stratabound fractures in the Nussloch-quarry is higher for all separated units, with a slightly increased value in the analyzed fault zone and a lowest value in the host rock of Upper Muschelkalk (HR mo, Fig. 13a). Within the fault zone, non-stratabound fractures clearly increase with proximity to the core zone (Fig. 13b). At the minor fault crosscutting the hanging wall of the main fault zone, the amount of non-stratabound fractures is enhanced in the minor fault hanging wall.

In contrast, the general percentages of stratabound fractures in Illingen and Knittlingen are higher (Figs. 13c and 13e), except for fractures within one fault zone in Knittlingen (FZ 3; Fig. 13e). The fault zone in Illingen contains a higher percentage of non-stratabound fractures within the eastern and western fault blocks, but a smaller value within the core zone of this main fault.

Within one fault zone in Knittlingen, described in detail in Section 4.2.3. (FZ 1), the percentage of stratabound fractures at contact to the fault core is high (Fig. 13f), particularly in the footwall. Non-stratabound fractures, however, increase in direction to the aforementioned antithetic discontinuity crosscutting the footwall (cf., Section 4.2.3.).

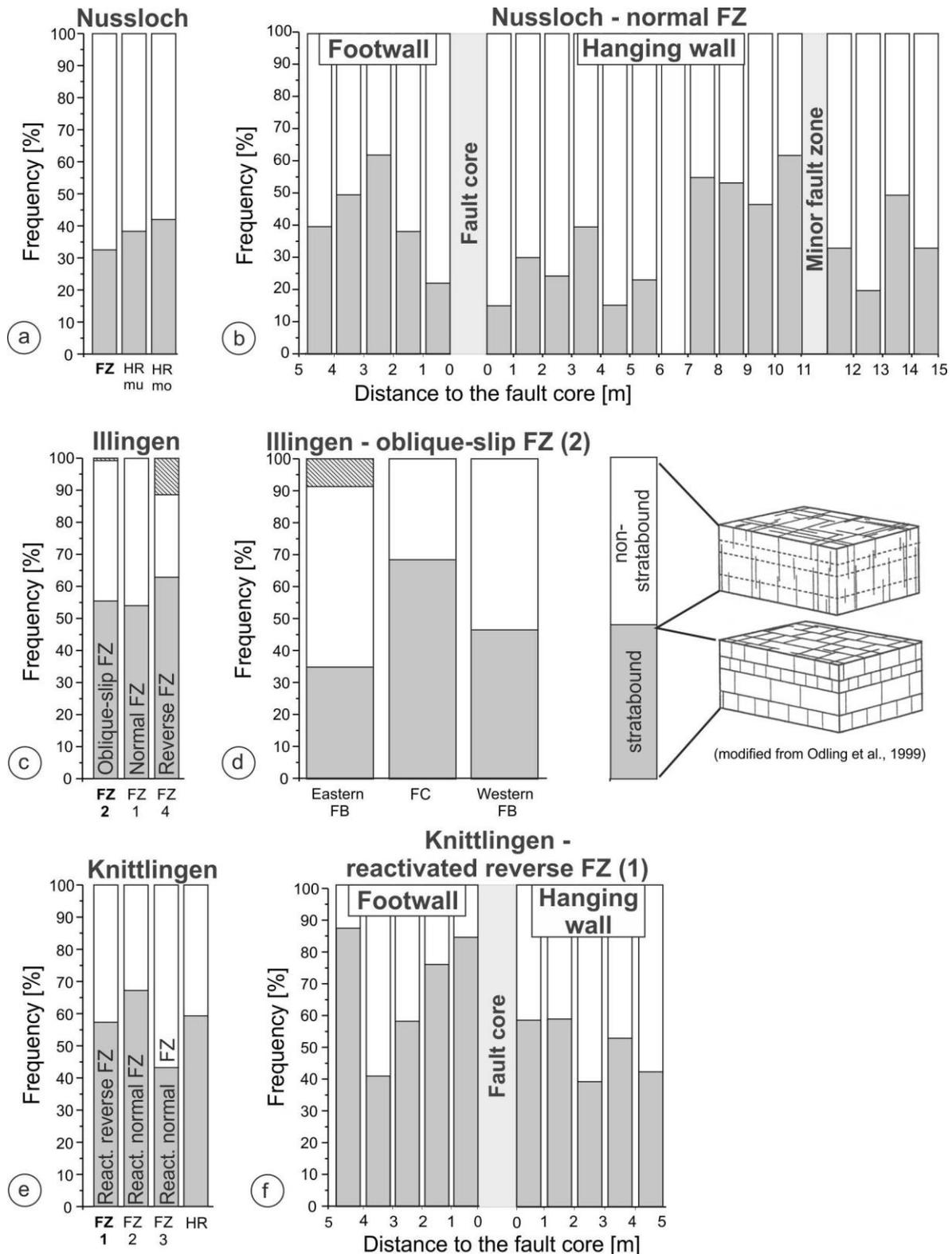


Fig. 13. Percentage of stratabound vs. non-stratabound fractures. a) Fracture data of the Nussloch-quarry separated to the main fault zone (FZ), host rock of the Lower Muschelkalk (HR mu) and of the Upper Muschelkalk (HR mo). b) Fracture data determined normal to the main fault zone in the Nussloch-quarry (cf., Section 4.2.1.). c) Fracture data of the Illingen-quarry separated to FZ 2 (main fault zone), FZ 1, and FZ 4. d) Fracture data determined normal to the main fault zone (FZ 2) in the Illingen-quarry (cf., Section 4.2.2.) separated to eastern fault block (FB), fault core (FC) and western fault block. The percentage of fractures with no declaration in Illingen is marked by a shaded signature. e) Fracture data of the Knittlingen-quarry separated in FZ 1, FZ 2, FZ 3 and host rock (HR). f) Fracture data determined normal to FZ 1 in the Knittlingen-quarry (cf., Section 4.2.3.). The definition of stratabound and non-stratabound fractures is illustrated with a sketch (modified from Odling et al., 1999). The fault zone types refer to the reflections in the discussion (Sections 5.1.1. to 5.1.3.).

#### 4.5 Mineralized and open fractures

We show the fracture aperture data to describe the fracture aperture distribution within the fault zones. Preferred fracture orientations and fracture locations for past fluid flow are highlighted by recording mineral-precipitations within the fracture system (cf., Section 3.). We plot the fracture aperture or thickness [mm] versus fracture orientation (Fig. 14, left) as well as the percentages of mineralized fractures (Fig. 14, center). Finally, we plot the fracture aperture or thickness [mm] in relation to the fault core distance (Fig. 14, right). In all plots we distinguish between mineralized and open fractures. Mineralized fractures with unknown thicknesses (e.g., due to only one visible fracture plane) are plotted with a fracture thickness of 0.1 mm in order to represent the fracture location in relation to the fault core distance.

The fracture systems in the quarries Nussloch, Illingen and Knittlingen contain mainly open fractures. The highest amounts of mineralized fractures were observed in the host rock of the Upper Muschelkalk and within the damage zone of the main fault zone in Nussloch. In Knittlingen and Illingen a minor amount of mineralized fractures was detected, where the few mineralized fractures are developed mainly within the fault zones.

In general, our data show a preferred orientation of fractures sealed with minerals parallel and subparallel to the analyzed fault zones and to regional structures like the URG, variscan and hercynian structures (Fig. 14), that is in NNE-SSW-, NE-SW- and NW-SE- direction. Fractures with comparatively larger apertures or thicknesses up to 4 mm (Illingen) are accumulated in these main directions as well. Several of these thicker fractures show mineral-precipitations, particularly in the Nussloch quarry (Fig. 14a).

In all described fault zones the fracture apertures or thicknesses decrease with increasing distance to the slip surfaces. By contrast, no clear relation between mineralization and fault core distance becomes apparent. In Nussloch and Knittlingen (Figs. 14a and 14c) many fractures located close to the fault core show mineralizations, but also at distance up to a few meters. In the Illingen oblique-slip fault zones (Fig. 14b), however, only few fractures, located in the fault core, are mineralized.

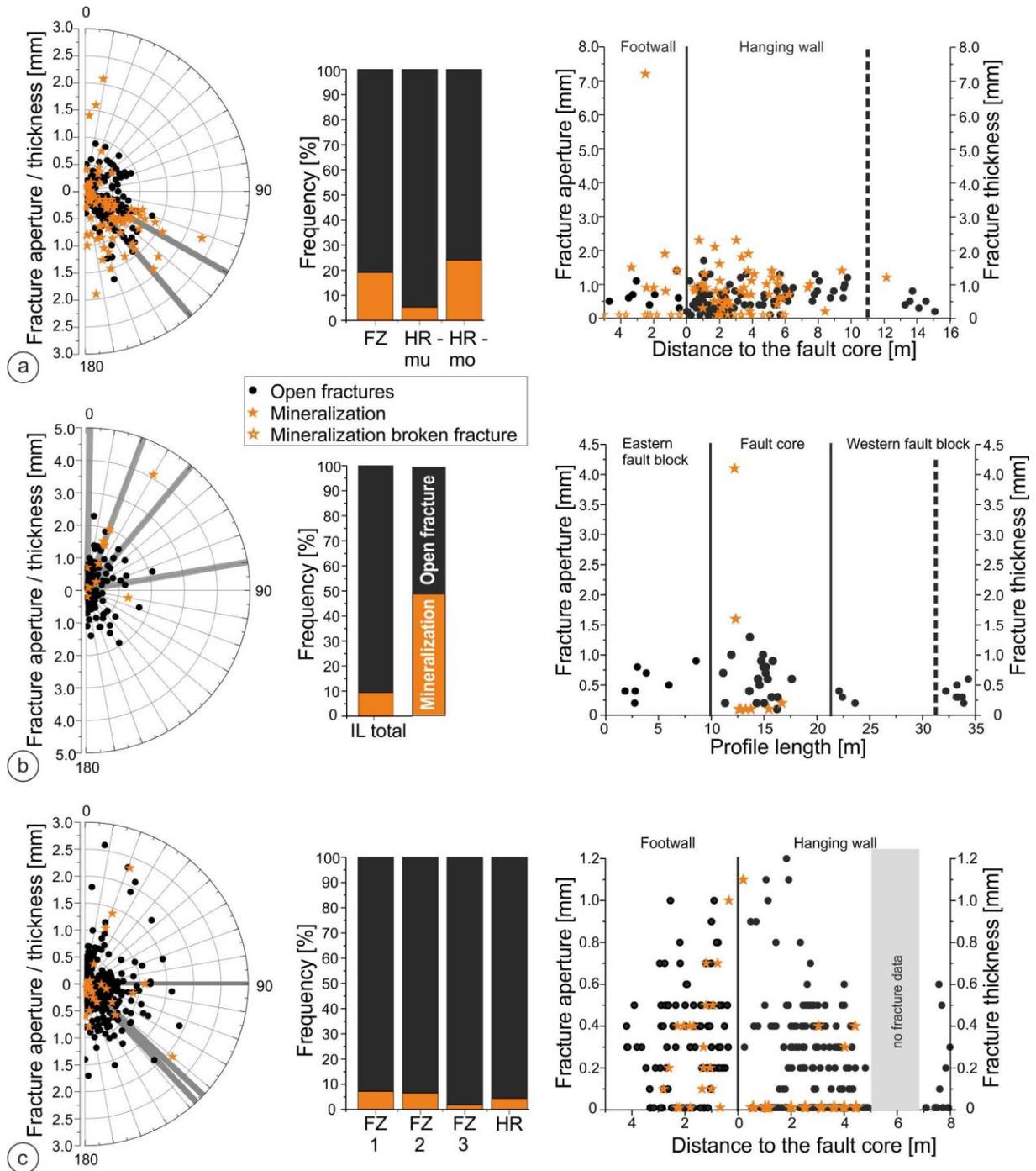


Fig. 14. Mineralized and open fractures: a) Nussloch. b) Illingen. c) Knittlingen. Left: Fracture aperture and thickness [mm] vs. strike. The fault zone orientations are marked by a gray line. Center: Percentage of mineralized fractures separated in fault zones and host rock (except for Illingen (b) due to the minor database). Right: Fracture aperture and thickness [mm] in relation to the fault core distance [m], the positions of fault core and minor fault zones are marked by dark-gray or by black dashed lines, respectively. The positions of mineralized fractures with unknown aperture are marked by open stars.

## 5 Discussion

### 5.1 Kinematics and tectonic evolution of the fault zones

The described fault zones show different geometric features and dissect this area in different blocks. In this section, we aim at explaining the evolution of the analyzed fault zones, regarding to the different stress field phases and interpreting fault zone kinematics.

Schumacher (2002) discusses the evolution of the URG within a changing regional stress field environment in detail and names four main evolution phases:

1. Late Eocene: N-S- to NNE-SSW-oriented compression ( $\sigma_1$ -direction: NNE) resulting in left lateral strike-slip. Primary ENE-WSW- and NNE-SSW- oriented faults were reactivated as normal faults or strike-slip faults, respectively.
2. Early Oligocene: WNW-ESE- to E-W-oriented extension ( $\sigma_3$ -direction: WNW) within the main rifting phase with regional normal faulting.
3. Late Oligocene: NE-SW-oriented compression ( $\sigma_1$ -direction: NE) resulting in right lateral strike-slip (also reactivation of URG-parallel faults as right lateral strike-slip faults).
4. Miocene (to recent): NW-SE-oriented compression ( $\sigma_1$ -direction: NW) resulting in left-lateral strike-slip.

Beside extensional and shear induced elements, structures indicating a compressional regime in the study area also are described in previous studies. Illies and Greiner (1978) for example mention primary normal faults of the eastern graben rim, which had been overprinted by younger reverse faults and small scale up-thrusts are described formed north of Karlsruhe (Ziegler, 1992).

The fault zones analyzed in the present study reflect the aforementioned stress field changes and are clearly related to the formations of main regional structures, in particular URG and Kraichgau-Syncline. Like the URG, the Kraichgau-Syncline consists of a block mosaic, separated by various fault zones, caused by extension, left lateral strike-slip or compression within the stress field of the URG formation (e.g., Kleinschnitz, 2009, and references therein).

#### 5.1.1 Nussloch

We define the Nussloch fault zone as a normal fault zone with a total displacement of at least 40 m, distributed on step faults. This extension structure is located close to the graben master fault and most probably part of a fault system described in literature: Kleinschnitz (2009) mentions a stepwise fault zone induced subsidence of the Kraichgau east of Nussloch. One of these fault zones crosscutting the Kraichgau east of Nussloch juxtaposes the Upper Muschelkalk and the Lower Muschelkalk formation. Both strike direction (NW-SE) and displacement coincide with the analyzed Nussloch normal fault zone. The stress field of this normal fault zone formation is in good accordance with the stress field characterized by left-lateral strike-slip and NE-SW-extension in Miocene (cf., Schumacher, 2002).

#### 5.1.2 Illingen

Based on the flexures in the fault core and the eastern fault block at contact to the main slip surfaces of the Illingen fault zone (southern quarry-part) we assume a step fault induced normal displacement from western towards eastern fault block. Due to the exposed slickenlines which show a strike-slip and a dip-slip component (northern quarry-part) and the minor slip surfaces within the fault core (southern quarry-part) we define the Illingen fault zone as an oblique-slip fault zone. The aforementioned structures and the high deformation grade of the slip surface exposed in the North indicate also a reactivation of the fault zone.

We assume that the tectonic elements within the Illingen quarry are affected by a strike-slip regime, but also by E-W-extension, probably caused by  $\sigma_1$  oriented NNW-SSW, resulting in the formation of the main oblique-slip fault zone. Due to the orientation parallel to the URG, this fault zone can be linked to the regional stress field of the URG.

Beside the normal dip-slip component within the main oblique-slip fault zone another extension induced structure occurs in the formation of one NNE-SSW-oriented normal fault zone. We define a third fault zone as an ENE-WSW-oriented reverse fault zone due to exposed markers which indicate a reverse displacement and therefore a compression induced structure. The associated stress fields of fault zones formation and reactivation are in line with the regional stress field in late Eocene or Oligocene (cf., Schumacher, 2002).

### 5.1.3 Knittlingen

Both extension and compression structures are exposed in Knittlingen and indicate a complex local tectonic history. Compression induced structures, i.e., reverse faults and folds (particularly flexures) are the most prominent structures in this quarry.

The rock formation within the characterized fault zone (FZ 1) in Knittlingen shows a high deformation grade. We assume repeated slip events on the fault plane and a formation of this fault zone by fault linkage within these rocks characterized by alternating mechanical properties. Fault linkage could explain the variety in fault core characteristics along the fault plane (lenses, tilted bedding or fault breccia) (Bastesen et al., 2009; Childs et al., 2009; Bastesen and Braathen, 2010; Bastesen et al., 2013). Flexures in the hanging wall indicate a main upward movement of this fault block. Furthermore, flexure monoclines of softer limestone and marl beds as well as one broken and rotated competent bed hosted in the footwall are clearly caused by compression, where different mechanical properties of limestone and marl obviously have led to different deformation of the limestone beds.

However, it seems that this fault zone was subjected to an extensional regime to a minor degree since some fault zone parts locally show extension structures (downward tilted bedding at contact and within the fault core). We propose a partially reactivation of this fault zone due to changes in dip angle where some fault core parts (probably with lower dip angle) were reactivated first. However, compressional structures predominate and thus we characterize this fault zone as reactivated reverse fault zone. Within this quarry, additional structures of compressive deformation occur in form of flexure monoclines (strike direction NW-SE), which show beginning fracturing and fault development along the axial surface (fold propagation fault).

Two other exposed fault zones (strike direction: NW-SE) show both a normal displacement and compressional structures like flexures or compressed limestone beds indicating a reactivation (inversion) of these primary normal faults.

A changing local stress field is common in regions characterized by a complex fault block structure due to rotation of  $\sigma_1$ -direction at fault zones. The formation may be related to the regional stress field of the URG in Miocene (cf., Schumacher, 2002) with slight changes of the local stress field. It is, however, difficult to classify the local stress field at fault zone formation and reactivation. The fracture system, characterized by a wide scatter in fracture orientation, is affected by this complex local stress field as well.

## 5.2 Past fluid flow

### 5.2.1 Past fluid flow within the study area

Mineralized fractures and mineralizations within fault zones crosscutting the study area are described in several previous studies. Illies (1972) mentions tertiary mineral veins (e.g., barite, fluorite and various ore minerals), which are developed at both graben shoulders as consequence of mineralization through open fissures, but absent within the

graben fill due to a differing stress regime. In addition, Eisbacher and Fielitz (2010) refer to NW-oriented fault zone and fractures, which are sealed by mineralizations.

Our data show that fractures formed in this NW-SE-direction are mineralized within the fracture systems of the studied quarries as well, particularly in the Nussloch-quarry. Furthermore, mineralized fractures accumulate in directions parallel and subparallel to the graben master fault and may therefore be related to the graben formation.

In the present study the comparatively high amount of mineralized fractures within the Nussloch-quarry is conspicuous. We conclude that these mineralizations may be connected to the formation of the well-known Pb-Zn-deposit of Wiesloch (e.g., Walter, 2007; Kleinschnitz, 2009), which is located close to the Nussloch-quarry. This Pb-Zn-deposit was formed in context of the URG development, as hydrothermal metal-bearing fluids circulated through the fractures and faults (Kleinschnitz, 2009).

### *5.2.2 Past fluid flow with regard to fault zone permeability evolution*

The permeability structure within fault zones and thereby associated fluid flow is changing during fault zone evolution and depends on their individual infrastructure (e.g., Caine et al., 1996; Agosta and Kirschner, 2003; Billi et al., 2003). The fault core of active faults zones may act as a conduit for fluid flow, if fractures or pores get interconnected during slip, whereas this unit acts as a barrier in inactive fault zones due to reduced grain sizes (cf., Section 1.; e.g., Sibson, 1994; Caine et al., 1996).

Billi et al. (2003) discuss fault zone permeability development during their evolution in carbonate rocks in detail, including the following two main stages. First, they define a conduit stage, which precedes the formation of the fault core. When fracturing starts, the fault zone permeability increases and the fault zone acts as a self-enhancing conduit. In the second stage, the fault zone permeability structure is changing, due to the beginning of particle rotation and particle fracturing. The fine-grained matrix increases within the particle population and reduces the fracture connectivity and permeability (Billi et al., 2003; Micarelli et al., 2006b). As a result, the fault core starts to seal and may become a barrier for fluid flow. Fluid flow is limited to the fault damage zone at this stage, particularly in proximity to the fault core, where the rock is still highly fractured (Billi et al., 2003).

This evolutionary model of fault zone permeability is applicable to our study. The fault cores of all analyzed fault zones show mineralizations and therefore signs of fluid flow within this fault zone unit, independently of their type, particularly the up to 1.5 m wide mineralizations at the fault core-hanging-wall-boundary in Nussloch. Both fractures within the fault core (Illingen oblique-slip fault zone) and the whole fault core unit of smaller scale fault cores (Knittlingen reactivated reverse fault zone) are sealed by minerals as well. Additionally, red colored areas and zones of discolorations indicate fluid flow within the fault cores in Nussloch and Knittlingen.

During fault zone evolution, this fluid flow, but also a grain size reduction, led to sealing of the fault cores and barrier formation within this fluid circulation system. As proposed by Billi et al. (2003) we assume that fluid flow was then localized within the fault zone damage zones characterized by an enhanced fracture density. In the present study several fractures are sealed with minerals within this unit, particularly with orientations parallel and subparallel to the fault zones.

### 5.3 Fracture system characterization within the fractured reservoir

In order to enable fluid flow in a fractured reservoir, the fracture system and the individual beds have to be hydraulically connected (e.g., Odling et al., 1999; Ortega and Marrett, 2000; Micarelli et al., 2006a, b; Reyer et al., 2012). Previous studies show enhanced percentages of interconnected fractures within damage zones and an increase in fracture connectivity from the protolith-damage zone boundary towards the fault plane (Micarelli et al., 2006b; Agosta et al., 2010). Despite our data show that most of the fractures are not connected with other fractures at fracture tips we conclude improved fracture vertical connectivity in proximity to slip surfaces of the fault zones, particularly caused by comparatively shorter fractures up to a length of 0.5 m. The Nussloch normal fault zone with a displacement of some tens of meters, which was formed under an extensional regime in context of the URG and Kraichgau tectonics, exhibits the best fracture connectivity within the damage zone fracture system of all analyzed fault zones since fractures connected at both fracture tips are included in particular.

It has long been recognized that the average fracture density in thinner beds is typically higher compared with thicker beds due to the formation of a stress shadow (Hobbs, 1967; Narr and Suppe, 1991; Gross et al., 1995; Van der Pluijm and Marshak, 2004). In general, our data show a similar behavior, with highest fracture densities in comparatively thinner limestone beds. Figure 15 exemplary shows the bed thickness [cm] versus fracture density (number of fractures per meter) of all fracture data in Nussloch, separately for fault zone and host rock. In addition we observe that limestone beds with similar thicknesses show higher fracture densities within the fault damage zone compared with the host rock. As proposed in previous studies (Caine et al., 1996; Berg and Skar, 2005; Micarelli et al., 2006b; Reyer et al., 2012), we observed a further enhanced fracture density in proximity to the slip surface. Thus, the probability of the formation of interconnected fractures in horizontal direction increases in this fault zone part.

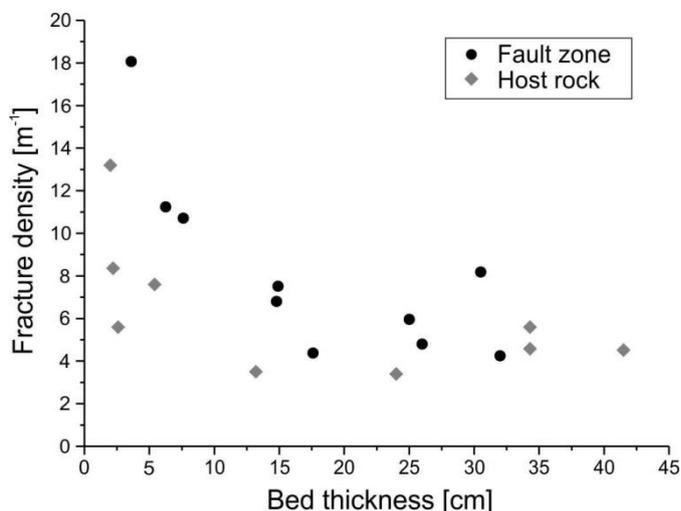


Fig. 15. Nussloch-quarry: Bed thickness [cm] vs. fracture density [m<sup>-1</sup>], separately for fault zone and host rock.

Our data generally show the significance of mechanical layering for fracture propagation and fracture arrest at contacts, as shown in several previous studies (Narr and Suppe, 1991; Odling et al., 1999; Gross and Eyal, 2007; Larsen et al., 2010; Reyer et al., 2012; Boro et al., 2013; Philipp et al., 2013; Afşar et al., 2014). Reyer et al. (2012), for example, propose that the number of stratabound fractures is generally higher in mechanically layered sedimentary rocks, which are characterized by abrupt lithological changes (Narr and Suppe, 1991; Gross et al., 1995), such as the Lower Muschelkalk of the North German Basin, compared with more homogeneous units. The mechanical

layering of these limestone-marl-alternations affects the fracture propagation and fracture arrest respectively due to stiffness variations and stress field changes (Gross and Eyal, 2007; Larsen et al., 2010; Reyer et al., 2012). For example Larsen et al. (2010) and Philipp et al. (2013) describe the effects of fracture arrest at contacts such as stylolites, zones of multilayers, welded layers, and cavities which induce a mechanical layering that does not coincide with clear lithological changes. In the limestone-marl-alternations of the Middle Triassic Muschelkalk, however, the mechanical contrasts match with lithological contacts: stiff limestone beds alternate with soft marl layers. Despite this effect of mechanical layering is obvious, non-stratabound fractures may be formed as result of linkage processes of preexisting fractures induced by faulting (Agosta et al., 2010). Therefore we focus on the distribution of non-stratabound fractures in relation to the fault core distance for further reservoir characterization in the present study and summarize fracture data of all scanlines, neglecting the limestone bed thicknesses.

Our data of the Knittlingen-quarry show that the comparatively thick marl layers ( $\sim 10$  cm) which induce a strong mechanical layering clearly act as stress barriers for fracture propagation. Many fractures become arrested at contacts to marl layers due to the changing stress field, regardless of the fracture locations (close to the slip surface or at distance).

In both other quarries (marl thickness 0.5 to 2 cm) a better connectivity between multiple limestone beds is caused by non-stratabound fractures, particularly at contact to the fault core in the Nussloch-quarry, where the fractures propagate across the thinner marl layers in the more homogenous rock formation. Therefore we assume that the effects of mechanical layering on fracture propagation in fault zones are significant.

Philipp et al. (2013) propose that diagenetic processes (cementation, pressure solution, mechanical compaction) in reservoirs lead to stiffness homogenizations of adjacent layers where a formerly mechanically layered succession may behave mechanically as a single layer. Thus, this effect is of particular importance for fracture propagation and permeability in a fractured reservoir and should be taken into account.

In general our data show that the possibility of interconnected fracture formation increases with increasing fracture densities in proximity to the fault core, particularly in more homogenous rocks. The reservoir permeability is enhanced by the development of hydraulically active pathways across several beds (non-stratabound fractures) to a higher degree compared with the improvement caused by the formation of fractures interconnected at the fracture tips

The best fracture induced reservoir permeability in the present study is proposed for the Nussloch normal fault. The enhanced permeability in this normal fault is caused by a high percentage of non-stratabound fractures, which may provide a hydraulically active pathway across several limestone beds (e.g., Odling et al., 1999) and supported by improved fracture vertical connectivity.

#### *5.4 Permeability implications on the analyzed fracture systems*

Open fractures are of particular importance in terms of reservoir permeability. In the present study many fractures remained open. These open fractures are potential pathways for recent fluid flow in fractured reservoirs associated with the characterized fault zones.

As an extension of the cubic law (cf., Section 3.) we use calculations of the hydraulic conductivity  $k_f$  [m/s] for sets including parallel and open fractures [m/s] after Bear 1993

(Eq. (1)) to show fracture orientations of fractures which enhance the permeability of the fracture system:

$$k_f = \frac{\rho_f \cdot g}{12 \mu \cdot L} (\sum_{i=1}^m b^3), \quad (1)$$

where  $\rho_f$  is the fluid density [kg/m<sup>3</sup>],  $g$  the acceleration due to gravity [m/s<sup>2</sup>],  $\mu$  the dynamic viscosity [Pa s],  $L$  the profile length [m] and  $b$  the fracture aperture [m].

Since fracture data of surface measurements in the outcrop analogues are used for our calculations, for fluid reservoirs we have to consider that fracture parameters change with increasing depth, resulting for example in reduced fracture apertures and densities (Lee and Farmer, 1993). Therefore, we aim at highlighting fracture orientations with enhanced permeabilities, but no absolute values.

We show permeability calculations based on the surface measurements exemplary for the quarries Nussloch and Knittlingen. We conclude that increased fracture frequencies in the damage zones and larger fracture apertures parallel and subparallel to fault zone strike and to regional structures like the URG and Variscan structures may lead to enhanced permeability compared with other orientations (Fig. 16).

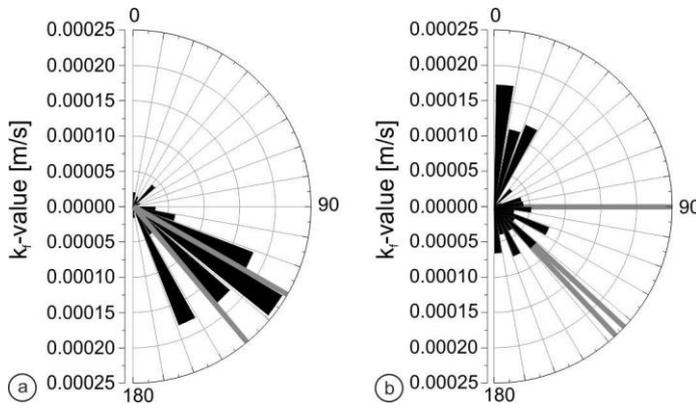


Fig. 16. Based on surface measurements calculated hydraulic conductivity ( $k_f$ -value) [m/s] versus fracture orientation (scale: 0°-180°): a) Nussloch. b) Knittlingen. The fault zone orientations are marked by gray lines.

We propose that surface data may be used for estimations of fault zone characteristics at depth. Several fault zone and fracture system characteristics or at least relationships should be applicable to reservoir conditions. Also at depth the fracture density would be enhanced at contact to the slip surfaces. Furthermore we assume that the distribution of fractures with largest apertures at contact to the slip surface and parallel and subparallel to fault zone strikes remains the same. Thus, estimations on reservoir permeability are generally possible based on surface measurement in outcrop analogues. In order to obtain realistic permeability estimations it is essential to vary fracture system parameters such as aperture and density to adapt these parameters to reservoir conditions in further investigations. The received fracture data of the present study serve as a basis of future numerical models for example of fluid and heat transport in fault zones.

## 6 Conclusions

Based on outcrop analogue studies of eight fault zones crosscutting limestone-marl-alternations of the Middle Triassic Muschelkalk in the Kraichgau-Syncline (Southwest Germany) we conclude:

1. Fault zone formation and reactivation in the Kraichgau-Syncline is clearly affected by regional stress field changes of the Upper Rhine Graben development. Fault zones and associated main fracture sets have orientations similar to prominent regional structures, such as the NNE-SSW-oriented oblique-slip fault zone parallel

- to the URG or the NW-SE-oriented normal fault zone parallel to the step faults which induced the subsidence of the Kraichgau-Syncline.
2. Fractures extending across multiple limestone beds of the exposed limestone-marl alternations may create pathways for fluid flow across these beds in the reservoir, but different mechanical properties of limestone and marl obviously also affect fracture propagation. An enhanced fracture density and fracture connectivity of shorter fractures within the fracture system in the fault damage zones at contact to the fault core may improve reservoir permeability.
  3. Increased fracture frequencies in fault damage zones and largest fracture apertures in direction of fault zone strike and of prominent regional structures may lead to enhanced permeability compared with other orientations. Fractures formed in these directions which are sealed by minerals as well as mineralizations within fault cores indicate hydraulic activity during fault zone evolution.
  4. The fault damage zones in the Middle Triassic Muschelkalk may be potential drilling targets of geothermal wellbores in the adjacent Upper Rhine Graben although in many cases the hydraulic connectivity of the natural fracture network may need to be improved. Well-developed fault cores may be potential barriers for fluid flow in inactive fault zones.

### **Acknowledgments**

The authors appreciate the support of the German Federal Ministry for Economic Affairs and Energy (BMWi), previously of the German Federal Ministry for the Environment, Nature Conservation and Nuclear Safety (BMU) as part of the Research and Development Project AuGE (Outcrop Analogue Studies in Geothermal Exploration) within the framework of the 5<sup>th</sup> Energy Research Program (FKZ 0325302). We thank our AuGE-project partners Geothermal Engineering GmbH, GeoEnergy GmbH, University of Heidelberg, and University of Erlangen for their support. Thanks to the owners of the quarries for the permission to perform the field studies (Sämann Stein- und Kieswerke GmbH & Co. KG and HeidelbergCement). Careful reviews by Alvar Braathen and Agust Gudmundsson helped improve the manuscript.

### **References**

- Afşar, F., Westphal, H., Philipp, S.L., 2014. How facies and diagenesis affect fracturing of limestone beds and reservoir permeability in limestone-marl alternations. *Marine and Petroleum Geology* 57, 418-432.
- Agosta, F., Kirschner, D.L., 2003. Fluid conduits in carbonate-hosted seismogenic normal faults of central Italy. *Journal of Geophysical Research* 108 (B4), 2221, <http://dx.doi.org/10.1029/2002JB002013>.
- Agosta, F., Alessandroni, M., Antonellini, M., Tondi, E., Giorgioni, M., 2010. From fractures to flow: A field-based quantitative analysis of an outcropping carbonate reservoir. *Tectonophysics* 490, 197-213.
- Agosta, F., Ruano, P., Rustichelli, A., Tondi, E., Galindo-Zaldívar, J., Sanz de Galdeano, C., 2012. Inner structure and deformation mechanisms of normal faults in conglomerates and carbonate grainstones (Granada Basin, Betic Cordillera, Spain): Inferences on fault permeability. *Journal of Structural Geology* 45, 4-20.
- Antonellini, M., Aydin, A., 1994. Effect of faulting on fluid-flow in porous sandstones: Petrophysical properties. *American Association of Petroleum Geologists Bulletin* 78, 355-377.

- Aydin, A., 1978. Small faults formed as deformation bands in sandstone. *Pure and Applied Geophysics* 116, 913-930.
- Bastesen, E., Braathen, A., Nøttveit, H., Gabrielsen, R.H., Skar, T., 2009. Extensional fault cores in micritic carbonate – Case studies from the Gulf of Corinth, Greece. *Journal of Structural Geology* 31, 403-420.
- Bastesen, E., Braathen, A., 2010. Extensional faults in fine grained carbonates – analysis of fault core lithology and thickness-displacement relationships. *Journal of Structural Geology* 32, 1609-1628.
- Bastesen, E., Braathen, A., Skar, T., 2013. Comparison of scaling relationships of extensional fault cores in tight carbonate and porous sandstone reservoirs. *Petroleum Geoscience* 19, 385-398.
- Bear, J., 1993. Modeling Flow and Contaminant Transport in Fractured Rocks. In: Bear, J., Tsang, C.F. and De Marsily, G. (Eds.), *Flow and Contaminant Transport in Fractured Rocks*. Academic Press, New York, 1-37.
- Berg, S.S., Skar, T., 2005. Controls on damage zone asymmetry of a normal fault zone: outcrop analyses of a segment of the Moab fault, SE Utah. *Journal of Structural Geology* 27, 1803-1822.
- Billi, A., Salvini, F., Storti, F., 2003. The damage zone-fault core transition in carbonate rocks: implications for fault growth, structure and permeability. *Journal of Structural Geology* 25, 1779-1794.
- Boro, H., Bertotti, G., Hardebol, N.J., 2013. Distributed fracturing affecting isolated carbonate platforms, the Latemar platform natural laboratory (Dolomites, North Italy). *Marine and Petroleum Geology* 40, 69-84.
- Braathen, A., Tveranger, J., Fossen, H., Skar, T., Cardozo, N., Semshaug, S.E., Bastesen, E., Sverdrup, E., 2009. Fault facies and its application to sandstone reservoirs. *AAPG Bulletin - American Association of Petroleum Geologists* 93, 891-917.
- Caine, J.S., Evans J.P., Forster, C.B., 1996. Fault zone architecture and permeability structure. *Geology* 24, 1025-1028.
- Caine, J.S., Forster, C.B., 1999. Fault zone architecture and fluid flow: insights from field data and numerical modeling. In: Haneberg, W.C., Mozley, P.S., Moore, J.C., Goodwin, L.B. (Eds.), *Faults and Sub-surface Fluid Flow in the Shallow Crust*. AGU Geophysical Monograph 113, 101-127.
- Caine, J.S., Bruhn, R.L., Forster, C.B., 2010. Internal structure, fault rocks, and inferences regarding deformation, fluid flow, and mineralization in the seismogenic Stillwater normal fault, Dixie Valley, Nevada. *Journal of Structural Geology* 32, 1576-1589.
- Chester, F.M., Logan, J.M., 1986. Implications for mechanical properties of brittle faults from observations of the punchbowl fault zone, California. *Pure and Applied Geophysics* 124, 79-106.
- Childs, C., Manzocchi, T., Walsh, J.J., Bonson, C.G., Nicol, A., Schöpfer, M.P.J., 2009. A geometric model of fault zone and fault rock thickness variations. *Journal of Structural Geology* 31, 117-127.
- Clausen, J.A., Gabrielsen, R.H., Johnsen, E., Korstgård, J.A., 2003. Fault architecture and clay smear distribution. Examples from field studies and drained ring-shear experiments. *Norwegian Journal of Geology* 83, 131-146.
- De Marsily, G., 1986. *Quantitative Hydrogeology: groundwater hydrology for engineers*. Academic Press, New York.
- Eisbacher, G.H., Fielitz, W., 2010. Karlsruhe und seine Region, Nordschwarzwald, Kraichgau, Neckartal, Oberrein-Graben, Pfälzerwald und westliche Schwäbische Alb. In: Rothe, P. (Ed.), *Sammlung geologischer Führer* 103. Gebr. Borntraeger, Stuttgart.

- Engesser, W., Leiber, J., 1991. Geologischer Bau und Landschaftsgeschichte. In: Schütz, J. (Ed.), *Der Rhein-Neckar-Kreis*. Theiss, Stuttgart, 17-49.
- Faulkner, D.R., Jackson, C.A.L., Lunn, R.J., Schlische, R.W., Shipton, Z.K., Wibberley, C.A.J., Withjack, M.O., 2010. A review of recent developments concerning the structure, mechanics and fluid flow properties of fault zones. *Journal of Structural Geology* 32, 1557-1575.
- Fossen, H., Schultz, R.A., Shipton, Z.K., Mair, K., 2007. Deformation bands in sandstone: a review. *Journal of the Geological Society* 164, 755-769.
- Fossen, H., 2010. *Structural Geology*, second ed.. Cambridge University Press, New York.
- Gross, M.R., Fischer, M.P., Engelder, T., Greenfield, R.J., 1995. Factors controlling joint spacing in interbedded sedimentary rocks: Integrating numerical models with field observations from the Monterey Formation, USA. In: Ameen, M.S., (Ed.), *Fractography: Fracture topography as a tool in fracture mechanics and stress analysis*. Geological Society Special Publication 92, 215-233.
- Gross, M.R., Eyal, Y., 2007. Throughgoing fractures in layered carbonate rocks. *GSA Bulletin* 119, 1387-1404.
- Gudmundsson, A., Simmenes, T.H., Larsen, B., Philipp, S.L., 2010. Effects of internal structure and local stresses on fracture propagation, deflection, and arrest in fault zones. *Journal of Structural Geology* 32, 1643-1655.
- Gudmundsson, A., 2011. *Rock Fractures in Geological Processes*, first ed.. Cambridge University Press, New York.
- Heidbach, O., Tingay, M., Barth, A., Reinecker, J., Kurfeß, D., Müller, B., 2008. The World Stress Map database release 2008, doi:10.1594/GFZ.WSM.Rel2008.
- Heynekamp, M.R., Goodwin, L.B., Mozley, P.S., Haneberg, W.C., 1999. Controls on fault-zone architecture in poorly lithified sediments, Rio Grande Rift, New Mexico: implications for fault-zone permeability and fluid flow. In: Haneberg, W.C., Mozley, P.S., Casey Moore, J., Goodwin, L.B. (Eds.), *Faults and Subsurface Fluid Flow in the Shallow Crust*.
- Hobbs, D.W., 1967. The formation of tension joints in sedimentary rocks: An explanation. *Geological Magazine* 104, 550-556.
- Illies, J.H., 1972. The Rhine Graben Rift System – Plate tectonics and transform faulting. *Geophysical Surveys* 1, 27-60.
- Illies, J.H., Greiner, G., 1978. Rhinegraben and the Alpine system. *Geological Society of America Bulletin* 89, 770-782.
- Kleinschnitz, M., with one contribution of Engesser, W., 2009. Erläuterungen zu Blatt L 6718 Heidelberg-Süd. In: *Regierungspräsidium Freiburg, Landesamt für Geologie, Rohstoffe und Bergbau* (Ed.), *Karte der mineralischen Rohstoffe von Baden-Württemberg*, 1 : 50 000. Freiburg i. Br..
- Larsen, B., Grunnaleite, I., Gudmundsson, A., 2010. How fracture systems affect permeability development in shallow-water carbonate rocks: An example from the Gargano Peninsula, Italy. *Journal of Structural Geology* 32, 1212-1230.
- Lee, C. H, Farmer, I., 1993. *Fluid Flow in Discontinuous Rocks*. Chapman and Hall, London.
- Micarelli, L., Moretti, I., Jaubert, M., Moulouel, H., 2006a. Fracture analysis in the south-western Corinth rift (Greece) and implications on fault hydraulic behavior. *Tectonophysics* 426, 31-59.
- Micarelli, L., Benedicto, A., Wibberley, C.A.J., 2006b. Structural evolution and permeability of normal fault zones in highly porous carbonate rocks. *Journal of Structural Geology* 28, 1214-1227.

- Narr, W., Suppe, J., 1991. Joint spacing in sedimentary rocks. *Journal of Structural Geology* 13, 1037-1048.
- Nelson, R.A., 1985. *Geologic Analysis of Naturally Fractured Rocks*. Gulf Publishing Company, Houston, Texas.
- Odling, N.E., Roden, J.E., 1997. Contaminant transport in fractured rocks with significant matrix permeability, using natural fracture geometries. *Journal of Contaminant Hydrology* 27, 263-283.
- Odling, N.E., Gillespie, P., Bourguin, B., Castaing, C., Chiles, J.P., Christensen, N.P., Fillion, E., Genter, A., Olsen, C., Thrane, L., Trice, R., Aarseth, E., Walsh, J.J., Watterson, J., 1999. Variations in fracture system geometry and their implications for fluid flow in fractured hydrocarbon reservoirs. *Petroleum Geoscience* 5, 373-384.
- Ortega, O., Marrett, R., 2000. Prediction of macrofracture properties using microfracture information, Mesaverde Group sandstones, San Juan basin, New Mexico. *Journal of structural Geology* 22, 571-588.
- Paschen, H., Oertel, D., Grünwald, R., 2003. Möglichkeiten geothermischer Stromerzeugung in Deutschland. TAB Arbeitsbericht 84.
- Philipp, S.L., Reyer, D., Meier, S., 2010. Strukturgeologische Geländestudien in Aufschlussanaloge und Permeabilitätsentwicklung in potentiellen geothermischen Reservoiren. *Zeitschrift für geologische Wissenschaften* 38, 49-59.
- Philipp, S.L., 2012. Fluid overpressure estimates from aspect ratios of mineral veins. *Tectonophysics* 581, 35-47.
- Philipp, S.L., Afşar, F., Gudmundsson, A., 2013. Effects of mechanical layering on hydrofracture emplacement and fluid transport in reservoirs. *Frontiers in Earth Science* 1:4.
- Priest, S.D., Hudson, J.A., 1981. Estimation of discontinuity spacing and trace length using scanline surveys. *International Journal of Rock Mechanics and Mining Sciences & Geomechanics Abstracts* 18, 183-197.
- Reyer, D., Bauer, J.F., Philipp, S.L., 2012. Fracture systems in normal fault zones crosscutting sedimentary rocks, Northwest German Basin. *Journal of Structural Geology* 45, 38-51.
- Schueller, S., Braathen, A., Fossen, H., Tveranger, J., 2013. Spatial distribution of deformation bands in damage zones of extensional faults in porous sandstones: Statistical analysis of field data. *Journal of Structural Geology* 52, 148-162.
- Schumacher, M.E., 2002. Upper Rhine Graben: Role of preexisting structures during rift evolution. *Tectonics* 21, doi: 10.1029/2001TC900022.
- Schweitzer, V., Kraatz, R., 1982. Kraichgau und südlicher Odenwald. In: Gwinner, M.P. (Ed.), *Sammlung geologischer Führer* 72. Gebr. Borntraeger, Berlin-Stuttgart.
- Sibson, R.H., 1994. Crustal stress, faulting and fluid flow. In Parnell, J. (Ed.), *Geofluids: Origin, Migration, and Evolution of Fluids in Sedimentary Basins*. Geological Society Special Publications 78, 69-84.
- Sibson, R.H., 1996. Structural permeability of fluid-driven fault-fracture meshes. *Journal of Structural Geology* 18, 1031-1042.
- Sibson, R.H., 2000. Fluid involvement in normal faulting. *Journal of Geodynamics* 29, 469-499.
- Stauffer, D., Aharony, A., 1994. *Introduction to Percolation Theory*, second ed.. Taylor and Francis, London.
- Stober, I., Jodocy, M., 2009. Eigenschaften geothermischer Nutzhorizonte im baden-württembergischen und französischen Teil des Oberrheingrabens. *Grundwasser* 14(2), 127-137.

- Stober, I., Fritzer, T., Obst, K., Schulz, R., 2011. Tiefe Geothermie – Nutzungsmöglichkeiten in Deutschland. BMU, Bundesministerium für Umwelt, Naturschutz und Reaktorsicherheit (Ed.), Berlin.
- Tondi, E., Antonellini, M., Aydin, A., Marchegiani, L., Cello, G., 2006. The role of deformation bands, stylolites and sheared stylolites in fault development in carbonate grainstones of Majella Mountain, Italy. *Journal of Structural Geology* 28, 376-391.
- Trunkó, L., 1984. Karlsruhe und Umgebung, Nördlicher Schwarzwald, südlicher Kraichgau, Rheinebene, Ostrand des Pfälzer Waldes und der Nordvogesen. In: Gwinner, M.P. (Ed.), *Sammlung geologischer Führer* 78. Gebr. Borntraeger, Berlin-Stuttgart.
- Twiss, R.J., Moores, E.M., 2007. *Structural Geology*, second ed.. W.H. Freeman, New York.
- Van Der Pluijm, B.A., Marshak, S., 2004. *Earth Structure*, second ed.. W.W. Norton & Company Inc., New York.
- Walter, R., 2007. *Geologie von Mitteleuropa*, seventh ed.. Schweizerbarth, Stuttgart.
- Ziegler, P.A., 1992. European Cenozoic rift system. *Tectonophysics* 208, 91-111.
- Ziegler, P.A., Dèzes, P., 2005. Evolution of the lithosphere in the area of the Rhine Rift System. *International Journal of Earth Science (Geol. Rundschau)* 94, 594-614.

### **3 Fault zones in layered carbonate successions: From field data to stress field models**

Silke Meier, Johanna F. Bauer, Sonja L. Philipp

Submitted to Geomechanics and Geophysics for Geo-Energy and Geo-Resources

#### **Abstract**

We present a field-study based workflow to develop 3D-numerical models on local stress fields within fault zones hosted in layered rocks at reservoir depths. As an example we use the carbonate successions of the Upper Muschelkalk (Middle Triassic) in the Upper Rhine Graben, Southwest Germany, that form a reservoir for deep geothermal energy. Steps of the workflow include (A) characterization of fault-zone units and mechanical layering, (B) estimations of rock mechanical properties and (C) assumptions on the in-situ stress regime. Results of 3D-numerical models of fault-zone local stress fields at reservoir depth of 2.900 m show pronounced differences depending on (1) fault-zone orientation, (2) impact of maximum horizontal stress  $S_H$  in the given stress regime (normal faulting, strike-slip faulting or transitional normal to strike-slip faulting), (3) fault-zone scale and (4) contrast in mechanical properties. Soft fault damage zones and fault cores trending at a minor angle to  $S_H$  ( $0^\circ$  to  $30^\circ$ ) concentrate less stress than comparable units at higher angles to  $S_H$  ( $60^\circ$  to  $90^\circ$ ), in particular in the strike-slip regime. The impact of mechanical layering increases with horizontal compression. This may result, for example, in formation of barriers to fracture propagation and thus lower probability of forming well-interconnected fracture networks necessary for fluid flow in reservoirs. Comparisons to estimated fault-zone stress states such as dilation and slip tendencies, show that their prediction in the study area is difficult because of the current transitional stress regime (normal to strike-slip faulting) and, in addition, varying orientations of  $S_H$ .

## 1 Introduction

Fault zones, due to their prominent effects on fluid flow and rock mechanical properties in the upper crust, have been the focus of numerous studies. Since fault zones form mechanically heterogeneous discontinuities and may behave as sealing or conductive structures, they lead to strong anisotropy of the rock mass (e.g., Caine et al. 1996; Caine and Forster 1999; Faulkner et al. 2010; Bense et al. 2013). Widely accepted is a simple fault-zone structure with a high-strain fault core consisting of gouge, breccia, and mineral precipitations enclosed by damage zones comprising high fracture density and minor faults reflecting the fault growth (Chester and Logan 1986; Caine et al. 1996; Faulkner et al. 2010). Particularly in layered rocks, however, the fault-zone internal structure can be very complex due to formation of a very heterogeneous fault core and an asymmetric damage zone, affecting rock mechanical properties and permeability (Agosta et al. 2010; Bastesen and Braathen 2010; Jeanne et al. 2012; Reyer et al. 2012; Bastesen et al. 2013; Bauer et al. 2015).

The hydro-mechanical behavior of a fault zone depends on various rock properties within the different fault-zone units. Of particular importance are the presence of a less permeable (in inactive fault zones) and often soft (low Young's modulus) fault core, the width and characteristics of the damage zone, i.e., characteristics of the associated fracture system in non- or low-porous rocks, and the formation of stylolites or deformation bands in porous rocks (Caine et al. 1996; Tondi et al. 2006; Fossen et al. 2007; Agosta et al. 2010). Such discontinuities affect not only the permeability (potential fluid flow vs. sealing structures), but also the effective rock mechanical properties Young's Modulus  $E$  and uniaxial compressive strength UCS: in low-porous rocks a significant decrease of  $E$  and UCS with increasing fracture density has been shown (Priest 1993; Caine et al. 1996; Tondi et al. 2006; Fossen et al. 2007; Agosta et al. 2010; Jeanne et al. 2012).

In a given regional stress field, the contrasting rock mechanical properties compared with the host rock (Fig. 1a) lead to the development of local stress fields within fault zones which is directly related to the permeability evolution of the rock mass, since either favorable or non-favorable local stresses for fracture propagation are developed and most of the fractures remain short (Gudmundsson et al. 2010). Moreover, a strong link has been ascribed between the fault-zone stress state and the hydraulic activity along fault zones (Sibson 1994; Barton et al. 1995; Gudmundsson 2000). Potential fluid pathways within the current stress field are formed in critically stressed fault zones that are close to slip and in extensional fault zones with a high tendency to dilate (Fig. 1b; Morris et al. 1995; Ferrill et al. 1999; Zoback 2007, Gudmundsson 2000, 2011).

The Middle Triassic Muschelkalk in the Upper Rhine Graben (URG; Fig. 2) in Southwest Germany is an example of a potential (low enthalpy) geothermal reservoir in layered carbonate successions (Paschen et al. 2003; Stober and Jodocy 2009; Stober and Bucher 2015), where due to low matrix porosities and permeabilities, fault zones and fractures are of particular importance (fractured reservoir; cf. Nelson 1985). Therefore, fault zones crosscutting Middle Triassic Muschelkalk in Germany are the focus of recent studies concerning the characteristics, permeability structure, and rock mechanical properties (Reyer et al. 2012 - Northwest German Basin; Meier et al. 2015 - URG).

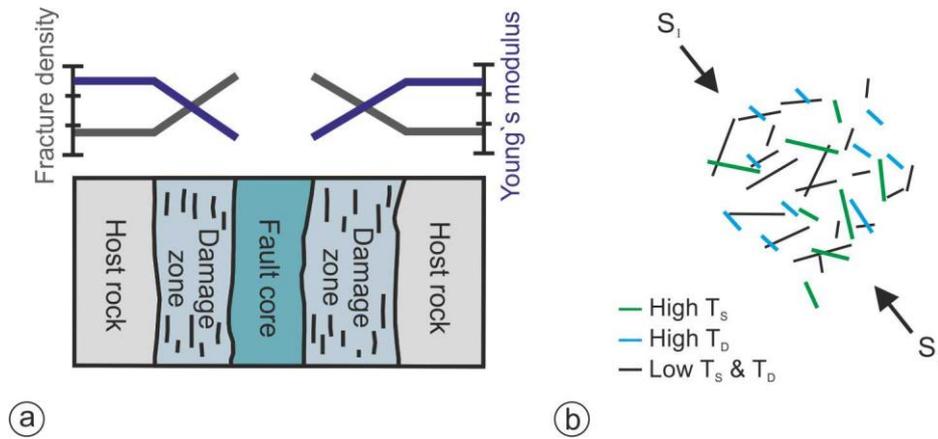


**Fig. 1** Sketch of a typical fault-zone internal structure (modified from Gudmundsson et al. 2010). The diagram above illustrates typical distributions of fracture density and Young's modulus  $E$  across the host rock and fault damage zone. In the fault core fracture density is commonly difficult to define.  $E$  may be very low due to soft fault rocks, or may be very high due to mineralizations, respectively. b) Symbolic fault-zone traces in the earth's crust (map view) with deviating slip tendencies  $T_s$  and dilation tendencies  $T_D$  due to their different orientations (modified from Zoback 2007). The arrows indicate the orientation of the maximum horizontal stress  $S_H$  ( $S_1$ )

In this paper we present three-dimensional (3D)-numerical models using the finite element software COMSOL Multiphysics® (Version 5.0) to gain insights on local stress fields and displacements of fault zones in the Muschelkalk potential geothermal reservoir in the given remote stress field within the URG. Fault zones in the 3D-numerical models are based on a field study by Meier et al. (2015), who worked in Muschelkalk outcrop analogues located in the Kraichgau-Syncline on the eastern graben shoulder (Fig. 2).

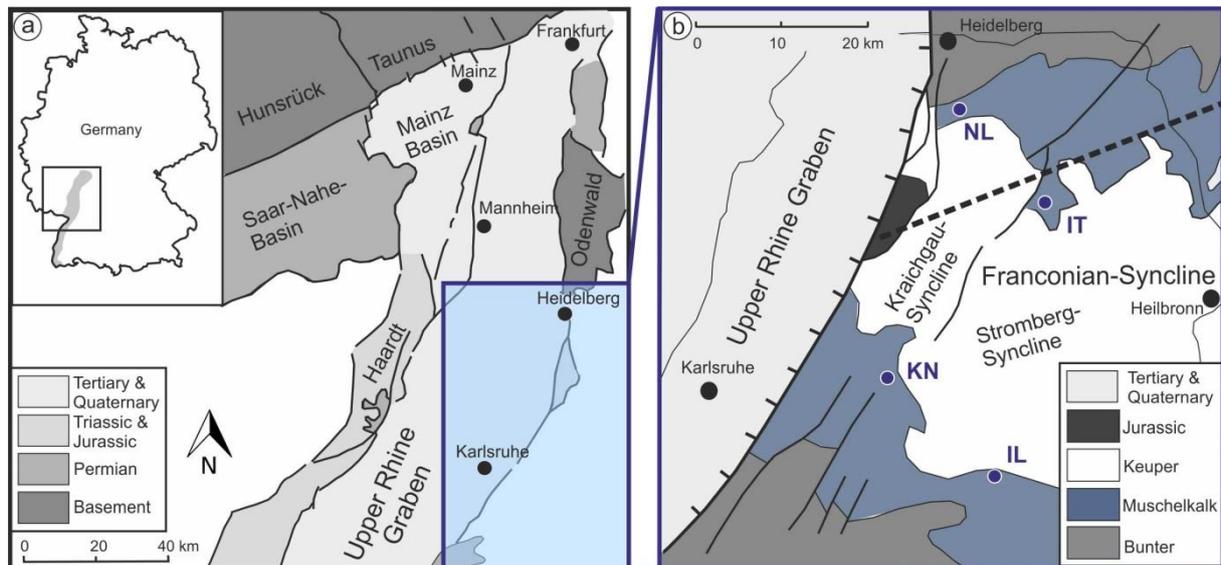


**Fig. 2** Simplified geological maps of the study area, for stratigraphic units see key (modified from Walter 2007). a) Northern Upper Rhine Graben (URG), section shown in (b) indicated in blue. b) Enlarged view of the section in (a), showing the Kraichgau-Syncline located on the eastern graben shoulder of the URG. The locations of the quarries studied as outcrop analogues of the Muschelkalk buried deep within the graben are marked by blue dots (IL Illingen; IT Ittlingen; KN Knittlingen; NL Nussloch). The axis of the Kraichgau-Syncline is marked by a dashed line

In the following we first discuss special features of fault zones in layered rocks and second give a brief introduction to Muschelkalk reservoir geology. Third we estimate the stress state of fault zones in the URG (using the fault zones in Meier et al. 2015 as a basis). Here we include slip tendencies and dilation tendencies for fault zones in the given stress regimes since they control the hydraulic activity of the fault zones (Barton et al. 1995, Morris et al. 1995; Ferrill et al. 1999; Sibson 2000). Fourth we explain our approach to develop 3D-numerical models in several steps based on field data,

laboratory tests and analytical models. Finally, we discuss numerical modelling results in context with estimations on slip- and dilation tendencies of fault zones and draw conclusions.

## **2 Fault zones in layered rocks**

Fault-zone characteristics, i.e., fault-zone structure and width, vary for different fault-zone scales and different lithologies. In general, the fault-zone width is related to the fault-zone growth. Several authors describe a relationship of displacement and fault-zone width, both damage-zone width and fault-core width, which is related to fault-core complexity. In particular, however, there is a relationship of fault segment linkage and fault-zone geometry (e.g., Childs et al. 2009; Bastesen and Braathen 2010; Faulkner et al. 2010; Faulkner et al. 2011; Bastesen et al. 2013). Fault zones in layered rocks are particularly complex in their internal structure. One reason is that they commonly form through linkage of fault-zone segments. This process leads to varying dip angles of the main slip surfaces. Also, the fault cores become heterogeneous and comprise minor slip surfaces, fault lenses, breccia, shale smear, tilted bedding, and mineralizations (Bastesen et al. 2009; Childs et al. 2009; Bastesen and Braathen 2010; Bastesen et al. 2013; Meier et al. 2015).

Layered rocks are commonly characterized by lithological and mechanical property changes that significantly affect fault-zone structure, fracture-system development and permeability. These effects occur not only because of varying layer thicknesses (fracture density correlates inversely with bed thickness; Hobbs 1967; Narr and Suppe 1991; Gross et al. 1995). The described effects also occur due to changes of rock mechanical properties, i.e., strong mechanical layering (fracture arrest, fracture offset or fracture propagation at contacts; Narr and Suppe 1991; Gross et al. 1995; Odling et al. 1999; Gross and Eyal 2007; Larsen et al. 2010; Philipp et al. 2013). It is common to characterize mechanical layers based on their individual Young's moduli  $E$ , which is a measure of the rock's stiffness (e.g., Zoback 2007; Gudmundsson 2011; Philipp et al. 2013). Therefore, we use the following nomenclature: rocks with high Young's moduli are referred to as stiff and those with low Young's moduli as soft.

In layered rocks with alternating mechanical properties such as the limestone-marl-alternations considered in this study, the effects of contrasting mechanical properties on fault-zone units are significant. Reyer et al. (2012), for example, describe a correlation of fault-core widths and amounts of soft marl layers within normal faults crosscutting carbonate successions. Furthermore, the characteristics of layered rocks such as bed thicknesses and strongly varying mechanical properties may affect not only fracture-system characteristics (see below) but also the damage-zone width. The latter may increase in limestone-marl-alternations characterized by small bed thicknesses and high stiffness contrasts between individual layers (Reyer et al. 2012).

In layered rocks it is particularly difficult to predict characteristics of the damage-zone fracture system. Here we use 'fracture' as a general term and do not distinguish extension fractures and shear fractures (fracture kinematics are difficult to define accurately in the field; cf. Meier et al. 2015) but rather stratabound fractures, i.e., fractures restricted to individual layers and non-stratabound fractures, i.e., fractures not affected by layering (Odling et al. 1999). This distinction is used because non-stratabound fractures extend across multiple layers in vertical direction and may increase reservoir permeability. In contrast, stratabound fractures do rarely form vertically interconnected networks and contribute less to reservoir permeability (cf. Philipp et al. 2013).

Formation of stratabound fractures caused by fracture arrest at contacts between mechanical layers can be explained by stress field rotations and the formation of stress concentrations versus stress barriers resulting in heterogeneous local stress fields (Gudmundsson 2011; Philipp et al. 2013). Both soft and stiff layers may act as stress barriers depending on the remote stress field. Soft layers tend to form stress barriers in horizontal tension, but stiff layers tend to form stress barriers in horizontal compression (Philipp et al. 2013).

Fault zones crosscutting Upper Muschelkalk are hosted in carbonate successions clearly characterized by alternating layers with contrasting mechanical properties: stiff limestones and dolomites alternate with soft marl. The mechanical layering is particularly strong in the Nodosus-Schichten (subunit mo2; Meier et al. 2015; cf., section 3): there are stiff limestone beds and partially thick units of soft carbonates. Throughout the entire analyzed fault-zone section, even at contact to the fault core, fractures terminate at comparatively thick marl layers and thus are stratabound. In contrast, fractures persist across thinner marl layers (non-stratabound) in more homogeneous rocks exposed in Nussloch (Trochiten-Kalk; subunit mo1), especially at contact to the fault core (Meier et al. 2015). Based on the aforementioned field observations we (1) analyze the entire Upper Muschelkalk and (2) focus on the Nodosus-Schichten (mo2) in addition.

### **3 Muschelkalk reservoir geology in the Upper Rhine Graben**

The URG is part of the European Cenozoic Rift System which extends across Central Europe (Fig. 2). It has undergone different tectonic stages of extensional and strike-slip regimes since its formation in Eocene (Illies 1972; Ziegler 1992; Schumacher 2002; Ziegler and Dèzes 2005). The present-day maximum horizontal stress in the URG is oriented approximately NW-SE to NNW-SSE (Plenefisch and Bonjer 1997; Schumacher 2002; Heidbach et al. 2008; Homuth et al. 2014). The regional stress regime in the URG is transitional from normal faulting to strike-slip faulting whereas local stress regimes are commonly difficult to define (Plenefisch and Bonjer 1997; Homuth et al. 2014).

The URG, bounded by two main fault systems, offers the opportunity to study rocks of the Variscan basement and of Permian and Triassic age. These rocks were either uplifted and may now be exposed on the graben shoulders or were buried deep in the graben and overlain by thick Cenozoic sediments, respectively. Cross sections show an asymmetric graben geometry and a complex fault-zone pattern within the graben. This leads to complex displacements between stratigraphic units. Therefore the Middle Triassic Muschelkalk, discussed here, can be located at various depths (Illies 1972; Illies 1977; Brun and Wenzel 1991; Paschen et al. 2003). For example it occurs at depths of approximately 1.000 m in the Landau Oilfield in the western graben area (Illies 1977), at 3.000 m at the eastern boundary fault near Heidelberg (Jodocy and Stober 2010) and at 4.200 m in the graben center (Paschen et al. 2003). Here, we use a depth of approximately 2.900 m as top of the Muschelkalk potential reservoir as it occurs in a deep geothermal wellbore drilled in the URG.

The successions of the Muschelkalk consist of three units, Lower, Middle, and Upper Muschelkalk and comprise alternating carbonates (limestones, dolomites and marls) and evaporates (gypsum, anhydrite, rock salt) (Schweizer and Kraatz 1982; Engesser and Leiber 1991). Because the Upper Muschelkalk (mo) is a prominent hydrothermal reservoir in the URG (Paschen et al. 2003; Stober and Jodocy 2009; Stober and Bucher 2015) we focus on this unit.

The Upper Muschelkalk (mo) consists of the main subunits *Trochiten-Kalk* (mo1), *Nodosus-Schichten* (mo2), and *Semipartitus-Schichten* (mo3) with a total thickness of 85-100 m in the outcrop analogue exposed in the Kraichgau-Syncline (Schweizer and Kraatz 1982; Engesser and Leiber 1991) and 60-85 m in the geothermal reservoir at depth (Stober and Bucher 2015). According to Engesser and Leiber (1991) the sequence of the *Trochiten-Kalk* (mo1) is mainly characterized by micritic limestones alternating with fossil-rich and stiff tempestites, and subordinated marls and clay especially in the *Hassmersheimer Schichten*. In contrast, the softer *clay zones a-ζ* within the *Nodosus-Schichten* (mo2), dominated by marl beds, form main parts in this subunit and alternate with stiff limestone beds. This characteristic is continued in the *Semipartitus-Schichten* (mo3) comprising limestones, fossil-rich carbonates, and marl interbeds.

## 4 Muschelkalk reservoir in-situ stress regime

### 4.1 General considerations

To consider the in-situ stress regime in the faulted Muschelkalk reservoir, the magnitude of the vertical stress ( $S_V$ ) compared with the range of possible horizontal stresses  $S_h$  (minimum horizontal stress) and  $S_H$  (maximum horizontal stress) are important. In a normal faulting regime  $S_V$  is the maximum principle stress ( $S_1$ ), the intermediate and minimum principal stress directions,  $S_2$  and  $S_3$ , respectively, are horizontal ( $S_H$  and  $S_h$ ) according to Anderson's theory of faulting. In contrast,  $S_V$  is equal to  $S_H$  in a transitional regime from normal to strike-slip faulting ( $S_1 = S_2$ ). In a strike-slip regime  $S_H$  ( $S_1$ ) has a higher magnitude compared with  $S_V$  ( $S_2$ ).

For this study, only stress orientations reported in the world stress map are used (Heidbach et al. 2008), no measurements on in-situ stress magnitudes are available. For  $S_V$  the weight of the overburden (calculated as average rock density multiplied by the depth and the acceleration due to gravity) can be used for estimation.

For  $S_H$  and  $S_h$  we apply a method known as frictional equilibrium theory to define the range of possible stress ratios within the reservoir. This approach assumes that the state of stress in the crust is in frictional equilibrium, i.e., the stress magnitudes of  $S_H$  and  $S_h$  are limited by the frictional strength of favorably-oriented faults (Peška and Zoback 1995; Jaeger et al. 2007; Zoback 2007). Shear failure of fault zones depends on the (static) coefficient of friction  $\mu$  which is the ratio of shear stress  $\tau$  and normal stress  $S_N$  (Morris et al. 1996; Jaeger et al. 2007; Zoback 2007). This is also referred to as "frictional sliding criterion" for existing planes of weakness when cohesion is absent (Twiss and Moores 1992). When the ratio of  $\tau$  and  $S_N$  reaches  $\mu$ , slip on the fault plane is likely so that further increase of stress magnitudes is impossible (Morris et al. 1996; Zoback 2007). Therefore, pre-existing faults limit the stress magnitudes at depths (Peška and Zoback 1995; Jaeger et al. 2007; Zoback 2007).

The ratio of effective principal stresses is given by Jaeger et al. (2007) as

$$\frac{S_1 - P_p}{S_3 - P_p} = \left( \sqrt{\mu^2 + 1} + \mu \right)^2 \quad (1)$$

where  $\mu$  is the coefficient of friction and  $P_p$  the in-situ pore pressure. Using the aforementioned assumptions it is possible to draw a stress polygon for frictionally stable areas in different stress regimes and thus to estimate the range of possible horizontal stress magnitudes at any given depth, pore pressure, and  $\mu$  (Peška and Zoback 1995; Zoback 2007). According to Byerlee (1978)  $\mu$  lies within a relative small range ( $0.6 \leq \mu \leq 1.0$ ), independent from the rock type but depending on the normal stress magnitude on

the failure plane. For intermediate normal stress below 200 MPa, equivalent to a shallow crustal depth less than 5 km, hence for the potential geothermal reservoir in this study (top reservoir: 2.900m),  $\mu$  of 0.85 can be applied (Byerlee 1978).

The stress polygon in Fig. 3 is illustrated for a depth of 2.900 m, an assumed average overburden density of 2.300 kg/m<sup>3</sup> for the overlain Cenozoic sediments (Rousset et al. 1993, and references therein; Rotstein et al. 2006),  $\mu$  of 0.85, and hydrostatic pore pressure ( $P_p = 0.43S_v$ ). The stress polygon shows that the allowable horizontal stress magnitudes are between  $0.55 S_v \leq S_h$  and  $S_H \leq 3.10 S_v$ . We present stress magnitudes of  $S_H$  and  $S_h$  for a normal faulting regime, a transitional regime from normal faulting to strike-slip faulting (here referred to as transitional regime), and strike-slip faulting regime (cf. section 3; Plenefisch and Bonjer 1997; Homuth et al. 2014). The points on the periphery of the polygon indicate stress states in which the crust is at its frictional limit (Peška and Zoback 1995). The range of differential stress magnitudes between the principal stresses at depth may decrease for higher pore pressures or lower coefficients of friction, resulting in transitions from one stress regime to another at relatively small stress-field changes (Peška and Zoback 1995; Zoback 2007).

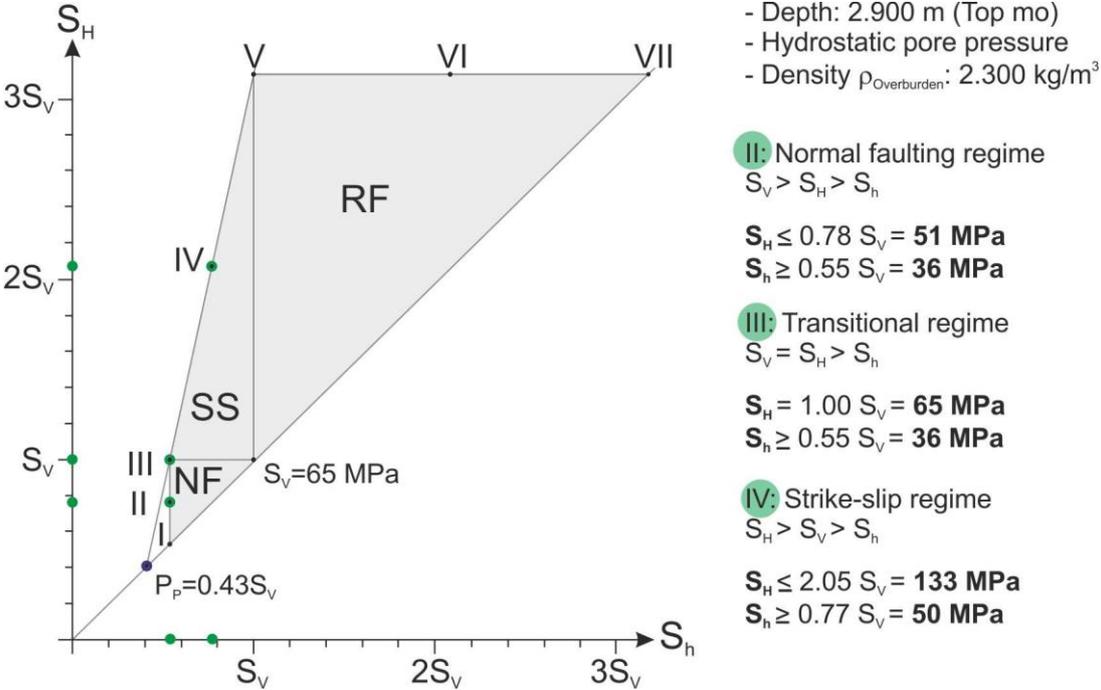


**Fig. 3** Stress polygon after Peška and Zoback (1995) showing the maximum horizontal stress  $S_H$  and the minimum horizontal stress  $S_h$  allowable by a frictional equilibrium of the crust. It is illustrated for a reservoir depth of 2.900 m, an assumed average overburden density of 2.300 kg/m<sup>3</sup>, and hydrostatic pore pressure  $P_p$ . The allowable horizontal stresses  $S_H$  and  $S_h$  are limited by the outer periphery of the polygon indicating frictional equilibrium. Vertical and horizontal lines within the stress polygon separate the stress fields according to Anderson’s theory of faulting: NF normal faulting, SS strike-slip, and RF reverse faulting. Stress states I-VII are defined by different stress ratios: I radial extension, II normal faulting, III transitional normal-faulting-strike-slip regime, IV, strike-slip faulting, V transitional strike-slip-reverse faulting, VI reverse faulting, VII radial compression. Values of  $S_h$  can be read on the x-axis and values of  $S_H$  on the y-axis, respectively. In the URG the normal faulting regime (II), the transitional normal-faulting-strike-slip regime (III, in this study referred to as transitional regime), and the strike-slip regime (IV) are of particular importance (Plenefisch and Bonjer 1997; Homuth et al. 2014). Allowable horizontal stresses  $S_H$  and  $S_h$  for the aforementioned stress regimes are highlighted by green markers on the x-axis and y-axis in the diagram. The associated calculated stress magnitudes are presented to the right of the stress polygon

## 4.2 Stress state of fault zones

In this section, we present analytical models of the fault-zone stress state, i.e., the slip tendency  $T_S$  and dilation tendency  $T_D$  of fault zones within the Muschelkalk potential reservoir in the URG, using data from nine fault zones exposed in outcrop analogues in the Kraichgau-Syncline (Meier et al. 2015).

First, we use the Mohr-diagram for three-dimensional stress to estimate possible normal stresses  $S_N$  and shear stresses  $\tau$  acting on the given fault planes at potential reservoir depth with stress magnitudes determined in section 4.1 for a normal faulting regime, a transitional regime, and a strike-slip regime. Our calculations of  $S_N$  and  $\tau$  are based on a detailed description by Ramsay and Lisle (2000) in which the orientation of the fault plane is considered by the definition of three angles ( $\alpha$ ,  $\beta$ ,  $\gamma$ ) and related direction cosines ( $l$ ,  $m$ ,  $n$ ) between the plane's normal and coordinate axes of the principal stresses  $S_1$ ,  $S_2$ , and  $S_3$ :

$$S_N = S_1 l^2 + S_2 m^2 + S_3 n^2 \quad (2)$$

$$\tau = [(S_1 - S_2)^2 l^2 m^2 + (S_2 - S_3)^2 m^2 n^2 + (S_3 - S_1)^2 n^2 l^2]^{1/2} \quad (3)$$

In this study, the principal stresses are defined by  $S_V$ ,  $S_H$ , and  $S_h$  and are assigned depending on the given stress regime (cf. section 4.1). As mentioned in section 3, the orientation of the maximum horizontal stress  $S_H$  within the URG varies between NW-SE and NNW-SSE (Plenefisch and Bonjer 1997; Schumacher 2002; Heidbach et al. 2008; Homuth et al. 2014). To cover these variations in the calculations, we define two possible  $S_H$ -orientations according to two deep wellbores drilled within the URG, published in the world stress map, i.e., Bruchsal (134°; eastern graben margin) and Soultz (approximately 160°; western graben margin) (Heidbach et al. 2008).

We plot  $S_N$  [MPa] versus  $\tau$  [MPa] acting on the fault planes (Fig. 4) at a  $S_H$ -orientation of 134° (Fig. 4a) and of 160° (Fig. 4b). For each fault zone an individual symbol has been assigned and related numbers are in accordance with the numbering of the fault zones in the Schmidt diagrams. For each fault zone three stress states for different faulting regimes are indicated with different gray shades: for normal faulting (black), transitional (gray), and strike-slip faulting regime (white) at reservoir depth of 2.900 m.

To estimate potential reactivation of a fault plane, Morris et al. (1996) introduced the slip tendency  $T_S$  from the ratio of  $\tau$  to  $S_N$  acting on the fault planes:

$$T_S = \tau / S_N \quad (4)$$

To assess critical  $T_S$  with regard to a potential reactivation of the fault plane, the coefficient of friction  $\mu$  (cf. section 4.1; Byerlee 1978) has to be considered since shear failure of a pre-existing fault plane (as an existing zone of weakness) is most likely when  $T_S$  reaches  $\mu$  (Morris et al. 1996). Therefore, the lines in the diagrams show the frictional sliding criterion (similar to the linearized Mohr-Coulomb criterion) for  $\mu = 0.6$ , 0.85 and 1.0 giving the slope of the line and zero cohesion (Twiss and Moores 1992; Zoback 2007).

In general, the data show that none of the fault zones would be critically stressed at reservoir depth and hydrostatic pore pressure since their ratios of  $\tau$  to  $S_N$  do not even reach a low friction coefficient of 0.6 (Fig. 4). However, the stress states of fault zones within the Muschelkalk potential reservoir in the URG are very difficult to define accurately and may differ due to varying impacts of  $S_V$ ,  $S_H$ , and  $S_h$  in the different stress regimes.

Stress regime	Normal faulting $S_v > S_H > S_h$	Transitional $S_v = S_H > S_h$	Strike-slip $S_H > S_v > S_h$
$S_v$ [MPa]	65	65	65
$S_H$ [MPa]	51	65	133
$S_h$ [MPa]	36	36	50

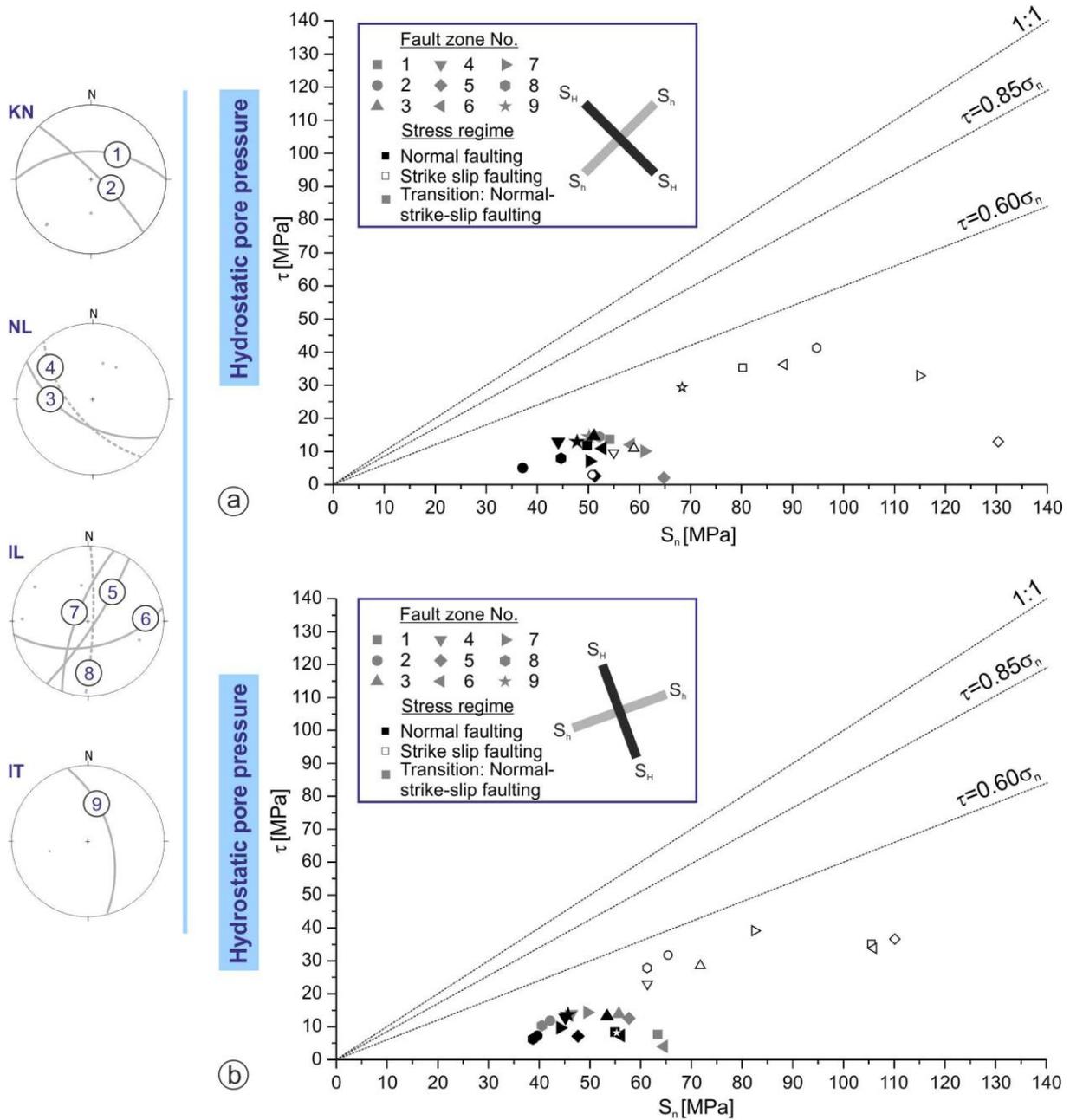


**Fig. 4** Mohr diagrams for three-dimensional stress states to estimate normal stress ( $S_N$ , equation 2) and shear stress ( $\tau$ , equation 3) [MPa] acting on fault planes presented in Meier et al. (2015), plotting effective  $S_N$  vs.  $\tau$  (i.e., for hydrostatic pore pressure), for varying  $S_H$ -orientations. The coefficient of friction  $\mu$  ranges between 0.6 and 1 for normal stress magnitudes below 200 MPa (Byerlee 1978; cf. section 4.1) and is an indicator of shear failure on pre-existing fault planes, solid lines show  $\mu$  of 0.6, 0.85, and 1, respectively. Schmidt diagrams (equal area projections, lower hemisphere) on the left show fault-zone orientations determined in the quarries KN Knittlingen, NL Nussloch, IL Illingen, and IT Ittlingen. These fault zones are labelled (1 - 9) in the Mohr diagrams. On the top we show allowable stress magnitudes of  $S_v$ ,  $S_H$ , and  $S_h$  for a normal faulting regime, a transitional regime or a strike-slip regime, respectively (cf. section 4.1). a)  $S_H$ -orientation  $134^\circ$  as determined in the deep wellbore in Bruchsal at the eastern graben margin. b)  $S_H$ -orientation  $160^\circ$  as determined in the deep wellbore in Soultz at the western graben margin (Heidbach et al. 2008). See key for numbering of the analyzed fault zones (1 - 9) and the stress regime. The sketches in the keys show the orientations of the horizontal stresses  $S_H$  and  $S_h$

Highest values of  $S_N$  and  $\tau$  acting on the fault planes are calculated for a strike-slip regime in which the fault-zone orientation has maximum impact by strongly different values of  $S_N$  and  $\tau$  for different fault planes (since  $S_H = S_1$ ). In contrast, lower values for  $S_N$  occur for the normal faulting regime in particular. Due to the impact of  $S_V$  ( $S_1$  in this stress regime) the fault-zone dip angle is of particular importance. Comparatively high magnitudes of  $\tau$  are determined for lower dip angles in the range of  $50^\circ$  that is approximately  $40^\circ$  to  $S_V$ . This can be explained by planes of maximum  $\tau$  which are oriented up to  $45^\circ$  to  $S_1$  (e.g., Twiss and Moores 1992). The steeply dipping fault zones (for example 2, 5, and 8) exhibit, in contrast, comparatively low  $\tau$ .

Furthermore, the orientation of  $S_H$  varies across the URG. This leads, particularly in the strike-slip regime, to partially pronounced differences in the stress state of similar fault planes at different locations within the URG due to varying angles to  $S_H$  ( $134^\circ$  vs.  $160^\circ$ ). Considering the strike-slip regime, fault zone 2 (KN) and 5 (IL) which show prominent angles to  $S_H$  at an orientation of  $134^\circ$  in the URG (Fig. 4a) are presented in more detail. Fault zone 2 is oriented parallel to  $S_H$  resulting in low  $S_N$  and low  $\tau$  acting on the fault plane. In contrast, fault zone 5 is oriented perpendicular to  $S_H$ . This leads to high  $S_N$  acting on the fault plane but low  $\tau$ . These stress states change at a  $S_H$ -orientation of  $160^\circ$  (Fig. 4b). In this case fault zone 5 exhibits higher  $\tau$  and lower  $S_N$  on the fault plane compared with the aforementioned example since this fault zone is oriented at a lower and more favorable angle for shear failure in relation to  $S_H$ . Stress magnitudes acting on the fault plane of fault zone 2 are higher for both  $S_N$  and  $\tau$ . Thus, considering the aforementioned differences, a general statement on the stress state of fault zones across the URG is not possible.

Besides  $T_S$ , the dilation tendency  $T_D$  of a fault zone, i.e., the probability of a fault zone or fracture to dilate in a given local stress field, is of particular importance for fluid flow (Barton et al. 1995; Morris et al. 1995; Ferrill et al. 1999). The dilation tendency can be defined by

$$T_D = \frac{(S_1 - S_N)}{(S_1 - S_3)} \quad (5)$$

(Ferrill et al. 1999). Values range between 0 and 1, the highest possibility for a fault zone to dilate given for  $T_D = 1$ . A high  $T_D$  for example can be estimated for a fault zone with low  $S_N$  and low  $\tau$  (Zoback 2007).

We plot  $T_S$  [-] versus  $T_D$  [-] calculated for the fault zones at  $S_H$ -orientation of  $134^\circ$  (Fig. 5a) and  $160^\circ$  (Fig. 5b). Fault-zone numbering, assigned symbols, and gray shades correspond to those in Fig. 4. As mentioned above, estimated  $T_S$  are highest for a strike-slip regime but below a friction coefficient  $\mu$  of 0.6, the analyzed fault planes not being critically stressed. However, some fault zones show high  $T_D$  and are therefore able to provide pathways for fluids within both examples. Furthermore,  $T_D$  of the fault zones clearly depends on the stress regime. Fault zone 2 (KN) and 5 (IL) show contrasting probabilities to dilate in the given local stress field at  $S_H$ -orientation of  $134^\circ$ . Fault zone 2 shows high  $T_D$  in all stress regimes due to its orientation parallel to  $S_H$  and low  $S_N$  and  $\tau$  acting on the fault plane (see above). In contrast,  $T_D$  of fault zone 5 decreases with increasing impact of  $S_H$ , i.e., towards the strike-slip regime since this fault zone is oriented perpendicular to  $S_H$ .

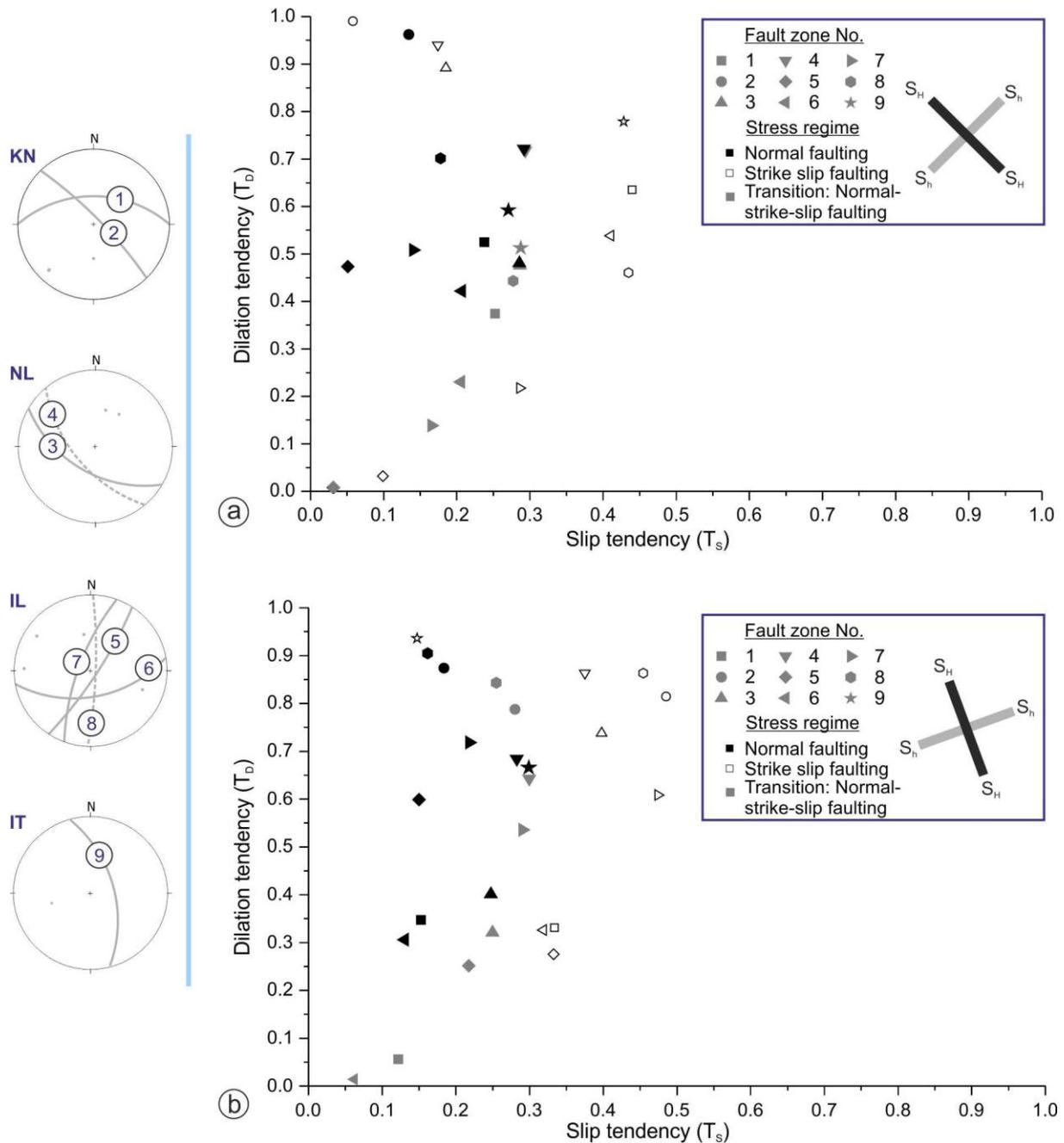


**Fig. 5** Slip tendency  $T_s$  (cf. equation 4) vs. dilation tendency  $T_D$  (cf. equation 5) for the fault zones and  $S_H$ -orientations presented in Fig. 4 (cf. Meier et al. 2015). a)  $S_H$ -orientation  $134^\circ$  (Bruchsal). b)  $S_H$ -orientation  $160^\circ$  (Soultz). See key for numbering of the analyzed fault zones (1 - 9) and the stress regime. The sketches in the keys show the orientations of the horizontal stresses  $S_H$  and  $S_h$

## 5 Numerical model setup

We used the finite element simulation software COMSOL Multiphysics® and the implemented *Structural Mechanics* module applying *Solid Mechanics* as physics interface in order to compute stresses and displacements within a number of three-dimensional (3D) numerical fault-zone models. As is common for models of upper crustal rocks (at low pressures, temperatures, and a gradual change in stress) a linear elastic behavior, i.e., Hooke's law, Young's modulus being the ratio of stress and strain, is applied (cf. Jaeger et al. 2007; Zoback 2007; Gudmundsson 2011). This means we used an isotropic and linear elastic material model so that only the elastic material properties Young's Modulus  $E$  [GPa] and Poisson's ratio  $\nu$  [-] need to be defined. Typical  $\nu$ -values of rocks lie

within a small range between 0.2 and 0.3, whereas  $E$  varies from less than 1 GPa to more than 100 GPa (Jaeger 1979; Gudmundsson 2011). In the models,  $\nu$  is constant at 0.25, and the varying material property is  $E$  following the estimations described below (sections 5.1 - 5.3).

Here we present two 3D-numerical model geometries of normal fault zones crosscutting the carbonate successions of the Upper Muschelkalk: (1) Large-scale normal fault zones hosted within the entire potential geothermal reservoir (mo1-mo3), and (2) medium-scale models of normal fault zones crosscutting the *Nodosus*-Schichten (mo2) only, because this succession is characterized by particularly strong mechanical layering (stiff limestone vs. thick softer marl units; cf. sections 2 and 3).

Fault-zone displacements and internal-structure characteristics are based on examples of fault zones exposed in outcrop analogues of the Muschelkalk described in Meier et al. (2015) (Fig. 6). In the following subsections we describe how we obtained reasonable in-situ Young's moduli, how the model geometries were simplified due to modelling limitations, and which boundary conditions and discretizations were applied in the model series.

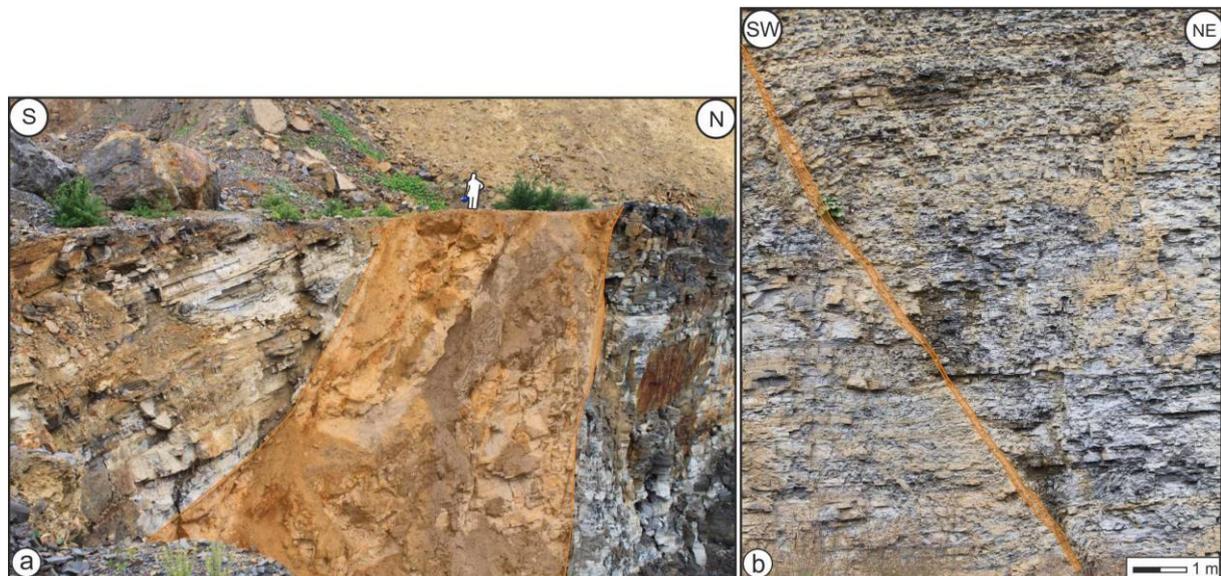


**Fig. 6** Outcrop examples of fault zones serving as base for the 3D-numerical models presented below. The fault cores are highlighted in orange. a) Nussloch normal fault zone with a displacement of tens of meters (hosted in the Lower, Middle and Upper Muschelkalk) as an example of a large-scale fault zone. The thick fault core (up to 13 m wide) is characterized by soft rocks (fault gouge, residual clay of the Middle Muschelkalk, fault breccia), but also by stiff material (mineralizations, host rock lenses) particularly at the fault-core to hanging-wall boundary. The characteristics of this fault zone are described in detail in Meier et al. (2015). b) Inverted normal fault zone in the Knittlingen quarry as an example of a small-scale fault zone. This fault core (0.2 - 0.5 m wide) is rather homogeneous and comprises soft rocks (fault breccia and marl that is dragged into the fault core due to shear movement along the slip plane)

### 5.1 *In-situ Young's moduli*

As described above, the only non-constant mechanical property assigned in the numerical models is  $E$ . Since in-situ  $E$  may vary horizontally between distinct fault-zone units and vertically between layers in the carbonate succession (cf. sections 5.2 and 5.3), we aim at estimating these variations. Because laboratory tests require a large number of specimens for each sample, they cannot be performed for every bed of the carbonate successions within each fault-zone unit and we use a combined approach for estimations on the relative variations of  $E$ .

As basis for the estimations we performed uniaxial compression tests (Mutschler 2004) to determine the Uniaxial Compressive Strength UCS [MPa] and static Young's Modulus  $E_s$  [GPa] of oriented rock samples taken in the quarries Nussloch (NL), Knittlingen (KN), Illingen (IL), and Ittlingen (IT) (Fig. 2). Due to strong lamination of the soft marl layers solely sampling of stiff limestone beds was possible. The cylindrical specimens were prepared both perpendicular and parallel to bedding with diameters of 40 mm and length-diameter ratios of 2.0 to 2.5. The specimens were loaded to failure at a constant rate (1000 N/s). After preload of the specimens (70% UCS),  $E_s$  was determined in the second load cycle as slope from the linear-elastic segment of the stress-strain curve. Volume and weight of the intact specimens were determined prior to the compression tests resulting in calculations of the bulk density [ $\text{kg/m}^3$ ]. Mean values of UCS,  $E_s$  and bulk density determined in the laboratory tests are summarized in Table 1.

**Table 1** Mean values and standard deviations of the rock-mechanical properties Uniaxial Compressive Strength (UCS [MPa]) and static Young's modulus ( $E_s$  [GPa]) as determined in laboratory tests as well as mean values of the bulk density [ $\text{kg/m}^3$ ]. Rock samples are from Upper Muschelkalk limestone beds in the quarries Nussloch (NL), Knittlingen (KN), Illingen (IL), and Ittlingen (IT)

Sample	Parallel to bedding		Perpendicular to bedding		Bulk density [ $\text{kg/m}^3$ ]
	UCS [MPa]	$E_s$ [GPa]	UCS [MPa]	$E_s$ [GPa]	
NL	126 ± 9	41 ± 4	120 ± 11	62 ± 28	2508 ± 50
KN	158 ± 21	60 ± 8	172 ± 21	59 ± 7	2703 ± 13
IL	159 ± 20	59 ± 7	170 ± 25	64 ± 8	2661 ± 77
IT	136 ± 17	54 ± 17	149 ± 15	57 ± 11	2706 ± 9

Due to scale effects,  $E_s$ -values measured in the laboratory tend to be higher than in-situ  $E$  of the rock mass in the field (small unfractured specimens vs. larger fractured rock volume; Heuze 1980). However, this difference decreases with increasing depth and  $E$  generally increases with depth (Gudmundsson 2011). Since the top of the Upper Muschelkalk potential reservoir is located at a depth of 2.900 m, but both increasing and decreasing effects are difficult to be quantified (cf. Philipp et al. 2013) we use the values from the laboratory tests as basis for estimations on the relative variations of  $E$  described in the following.

The approach for these estimations uses quick and non-destructive measurements of the Rebound hardnesses  $R$  [-] in the outcrops as a proxy for  $E$  (Fig. 7a). We used two types: (1) Schmidt hammer tests (Proceq SA, type LD; impact energy 0.735 Nm) in outcrops and (2) Equotip tests (Sensors standard type D; impact energy 1 Nmm) along core samples of one near-surface wellbore to prevent damage on the core samples (Fig. 8). In both tests the rebound of a guided mass load released on a rock mass is measured (cf. Viles et al. 2011).

We performed Schmidt hammer tests across fault zones exposed in the quarries Illingen as an example of a large-scale fault zone and Knittlingen as an example of a medium-scale fault zone. (cf. Meier et al. 2015). Although there is a very large scatter of  $R$ -values, even within individual limestone beds, different trends occur in different fault-zone blocks (Fig. 7a), indicating that the small-scale mechanical layering of the Upper Muschelkalk leads to the displacement of rocks with different mechanical properties against each other.

Several studies indicate correlations of Schmidt hammer R-values with E (Sachpazis 1990; Katz et al. 2000; Yagiz 2009; Aydin and Basu 2005). Yagiz (2009) provides a comprehensive summary of correlations between R and E for various rock types, the relevant for limestone being:

$$E = 0.0987R^{1.5545} \quad (6)$$

We applied this correlation on the measurements of R to obtain values on horizontally varying E in fault damage zones and host rocks (Fig. 7b).

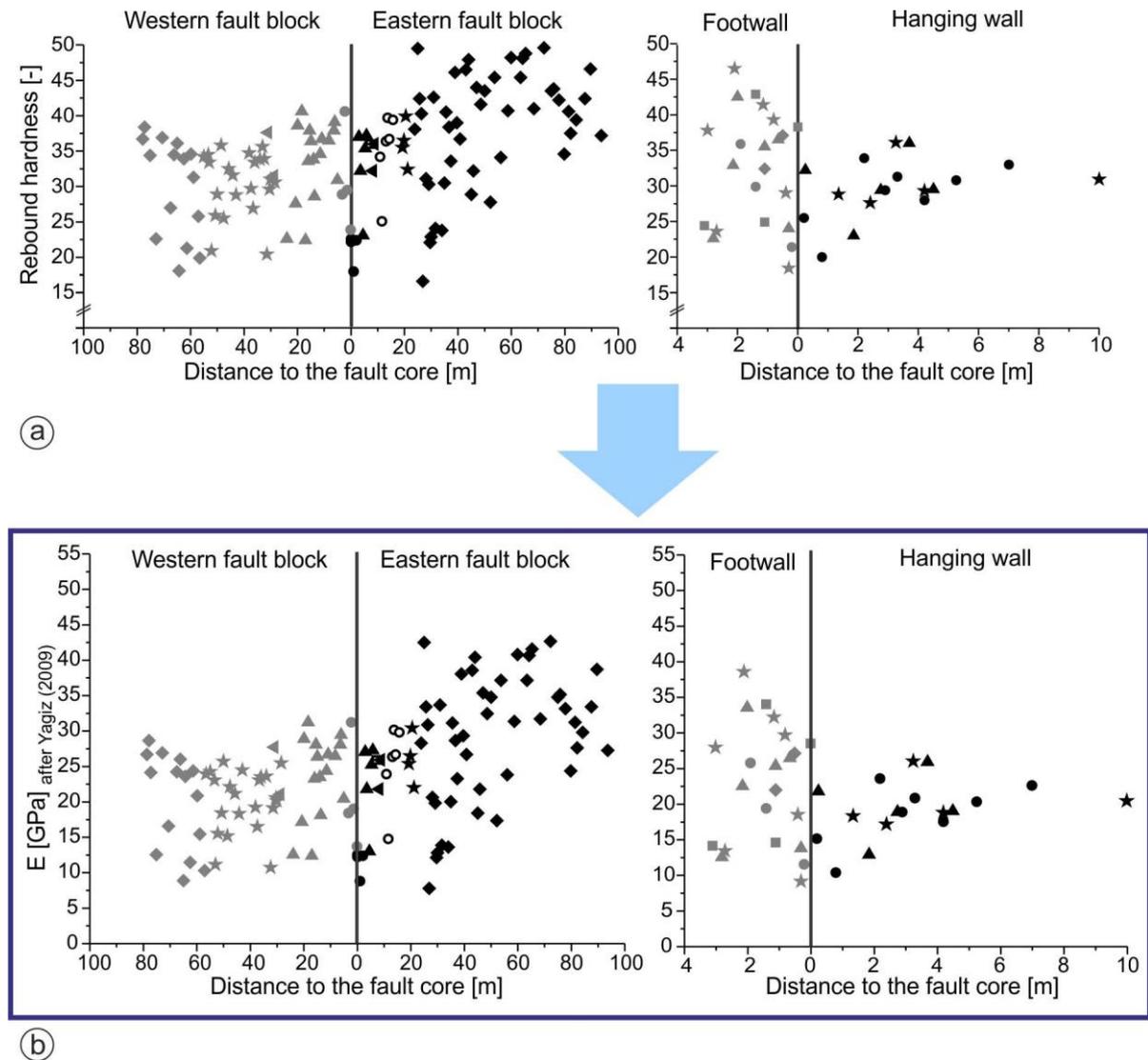


**Fig. 7** a) Rebound hardness R-values [-] determined by Schmidt hammer tests in relation to the fault-core distance within the Illingen fault zone (left) and the Knittlingen fault zone (right). Measurements taken in the same bed are indicated by equal symbols. b) E [GPa] across the fault zones calculated using correlations between R-values and E according to Equation 6 (Yagiz 2009)

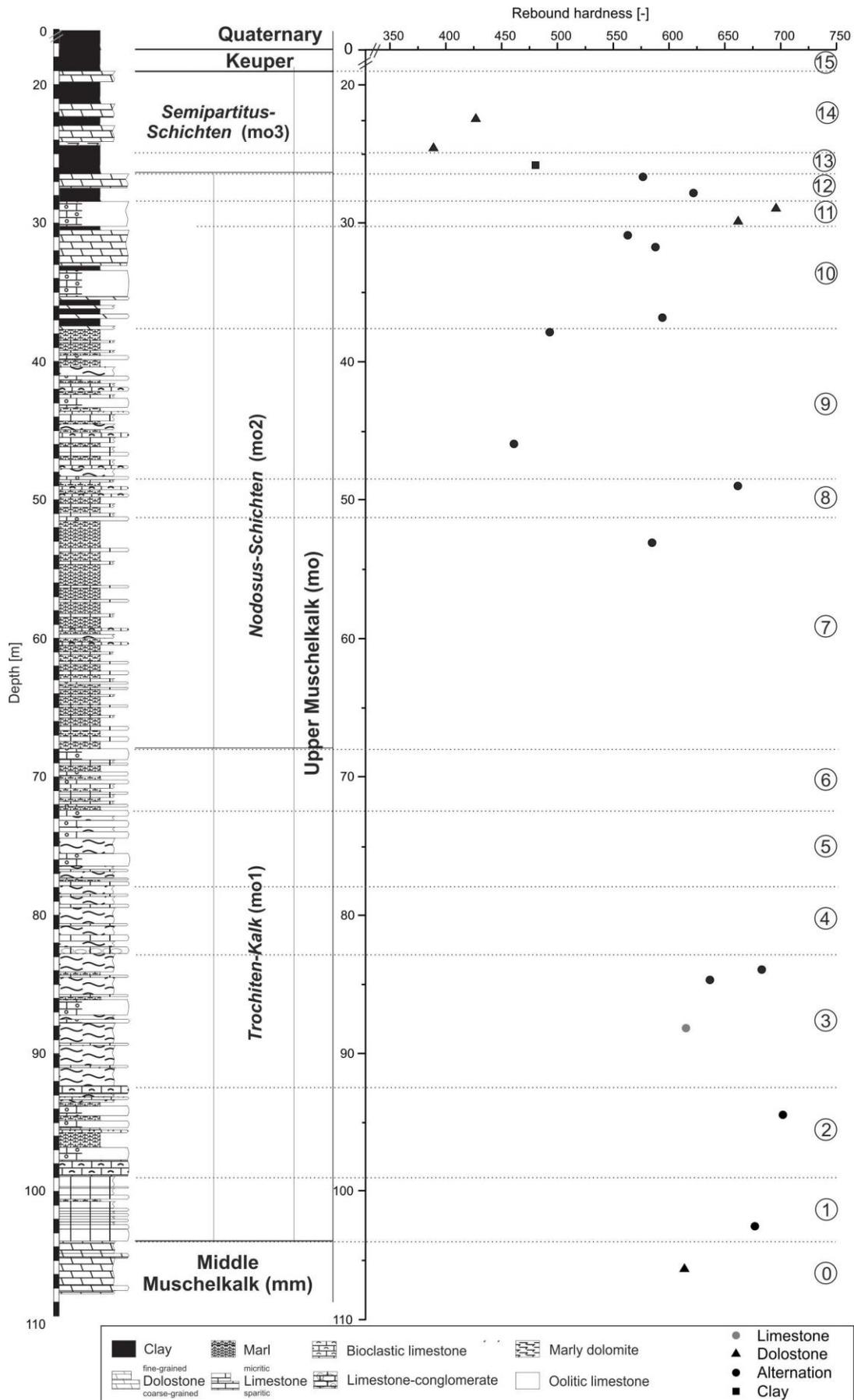


**Fig. 8** Lithological profile and Rebound hardness  $R [-]$  based on Equotip measurements along core samples of one near-surface wellbore in the Nussloch quarry (cf. Fig. 2). In this wellbore, rocks of Quaternary, Lower Keuper, Upper Muschelkalk, and top Middle Muschelkalk have been drilled through

To estimate vertical variations of  $E$  in the largest possible vertical extent we performed the aforementioned Equotip tests along core samples of one near surface wellbore. This wellbore was drilled in the Nussloch quarry to a depth of 107 m, in the first 19 meters through clastic sedimentary rocks of Quaternary and Keuper age and underneath through the carbonate successions of Upper Muschelkalk (mo3-mo1) to top Middle Muschelkalk (Fig. 8). Equotip R-value measurements were performed along the core samples in intervals of one meter. However, core samples of soft rocks such as marl are lacking partially over several meters. The R-values vary significantly in mo3 and mo2 with lowest R-values in subunit mo3. Highest R-values were measured in subunit mo1. Equotip values were used to refine  $E$  variations in the models as described in the next two subsections.

## 5.2 Large-scale 3D-numerical models: Geometry setup and Young's moduli assigned

The first model geometry is based on the large-scale Nussloch normal fault zone described in Meier et al. (2015) (Fig. 6a) with a total displacement in the range of tens of meters. Based on the Equotip R-values along the lithological profile of the near-surface wellbore we defined a total of 16 layers, mainly representing the Upper Muschelkalk (layers 1-14) (cf. section 5.1; Fig. 8) and, in addition, layers representing Middle Muschelkalk (layer 0) and Keuper (layer 15), which were introduced to compensate for displacement-induced gaps at top of the hanging wall and base of the footwall, respectively. To reduce complexity of the model and associated computing power, we simplified the succession by omitting some thin layers and layers with unknown parameters; to limit approximations on rock mechanical properties of rocks filling the displacement-induced gaps we assigned a fault-zone displacement of 10 m.

In the next step, the units 'host rock' and 'damage zone' were separated. The outer damage zone boundary of the Nussloch normal fault in the outcrop is probably not exposed within the analyzed fault-zone section, but must exceed 15m (Meier et al. 2015). We assigned a damage zone width of 20 m in both hanging wall and footwall as zone width in this model geometry (Fig. 9).

To obtain values for  $E$  in host rock and damage zone, we used 60 GPa, i.e., approximately the maximum  $E$  determined in laboratory tests (cf. Table 1) as a base value (100%). This value is set equivalent to the maximum Equotip R-value along the core samples of the near-surface wellbore, determined in subunit mo1 (layer 2;  $R=702$  [-]; Fig. 8). Following the correlations of Schmidt hammer R-values with  $E$  after Yagiz (2009) (cf. section 5.1; Fig. 7), we estimated 30 GPa as the base  $E$ -value within the damage zones.  $E$ -values of all remaining zones were estimated using a percentage factor of their R-value in relation to the maximum R-value of 702 [-].

The fault core in this model geometry is also based on the fault core hosted in the normal fault zone in Nussloch, characterized by high heterogeneity, comprising thick mineralizations and host rock lenses at contact to the hanging wall (Meier et al. 2015). The assigned fault core is 8 m wide with  $E$  of 5 GPa and 10 GPa in softer fault core parts and 30 GPa in stiffer parts, respectively.

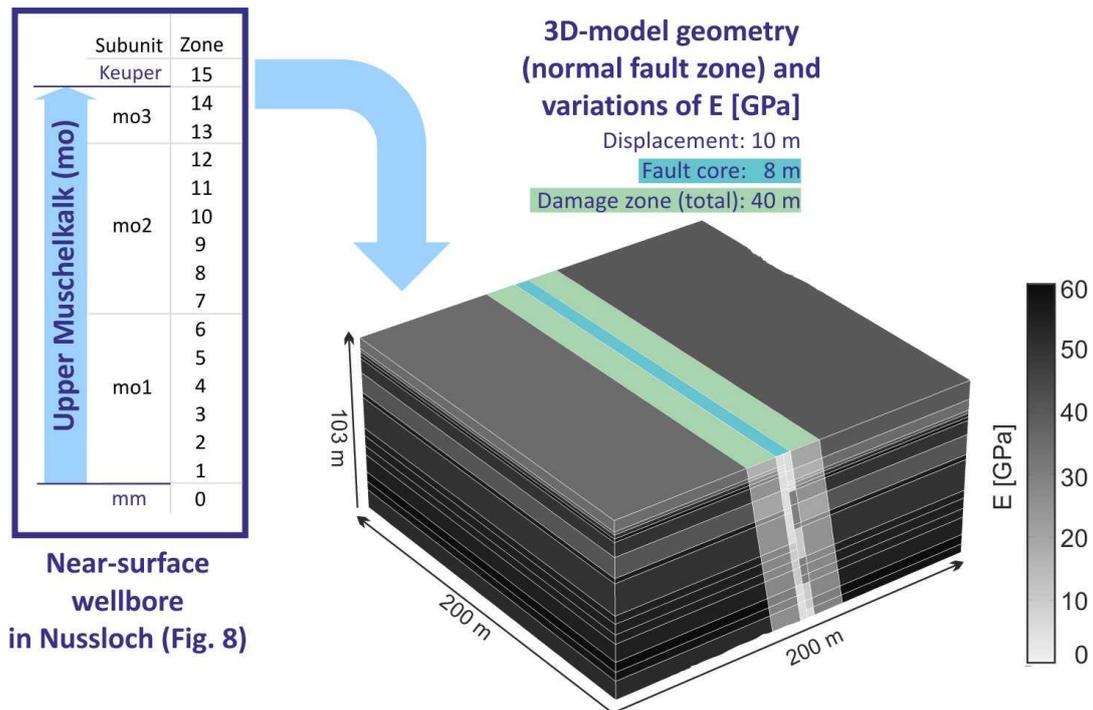


**Fig. 9** Geometry of the large-scale 3D-numerical models below, based on the Nussloch normal fault zone (Fig. 6) and the carbonate succession drilled through in the near-surface wellbore (Fig. 8). We assigned a normal displacement of 10 m, a fault core width of 8 m and a total damage zone width of 40 m. 16 layers with differing Young's moduli  $E$  are defined separately for host rock and damage zones, i.e., fault damage zone rocks are softer than equivalent layers in the host rock. The fault core is characterized by heterogeneous  $E$ , for example by stiffer mineralizations at parts of the contact to the hanging wall. See color scale for assigned  $E$

### 5.3 Medium-scale 3D-numerical models: Geometry setup and Young's moduli assigned

This model geometry is based on several fault zones with displacements in the range of a few meters, such as two inverted normal fault zones crosscutting the mo2 in the Knittlingen quarry (Fig. 6). The carbonate succession is characterized by limestone-marl-alternations showing a higher resolution of subunit mo2 compared with the large-scale models (limestone beds alternating with clay zone  $\alpha$  to  $\zeta$ ). We defined 17 layers along the lithological profile after Engesser and Leiber (1991) mainly along subunit mo2 (layers 1-14), but also along parts of mo1 (layer 0) and mo3 (layers 15 and 16) to fill up the gaps caused by the displacement of the normal fault zone, which was set to 3 m (Fig. 10).

In contrast to the large-scale models we defined similar  $E$  for each layer representing limestone and similar  $E$  for each layer representing a clay zone, whereas again all layers are separated in host rock and damage zones.  $E$  values within the damage zones are an approximation to correlations of Schmidt hammer R-values with  $E$  along the Knittlingen fault zone (Fig. 7b), in which softer rocks (hanging wall damage zone;  $E \approx 20$  GPa) are displaced against stiffer rocks (footwall damage zone;  $E \approx 30$  GPa).  $E$  values within the host rock are approximately the host rock maximum  $E$  and minimum  $E$  assigned in the carbonate succession of the large-scale model (host rock limestone: 60 GPa; host rock clay zone: 30 GPa) (Fig. 9).

The damage zone widths of the Knittlingen fault zones are difficult to define in the field. First, this is because of a high deformation grade in the fault-zone blocks resulting from repeated slip events on the fault plane. Second, this may be due to high background fracturing within thin beds in the host rock. Third, no clear decrease of the fracture density to background fracturing has been identified (Meier et al. 2015), what may be

due to the commonly wider damage zone in carbonate successions characterized by strong mechanical layering (cf. section 2; Reyer et al. 2012). In the numerical models of this geometry we assigned a damage-zone width of 5 m for each fault block.

The fault cores of the Knittlingen normal fault zones are 0.2 to 0.4 m wide. In the model geometry, however, the fault core has a width of 0.6 m due to meshing requirements. The fault-core rocks are rather soft, including breccia and marl dragged into. We assigned a homogeneous E of 5 GPa.

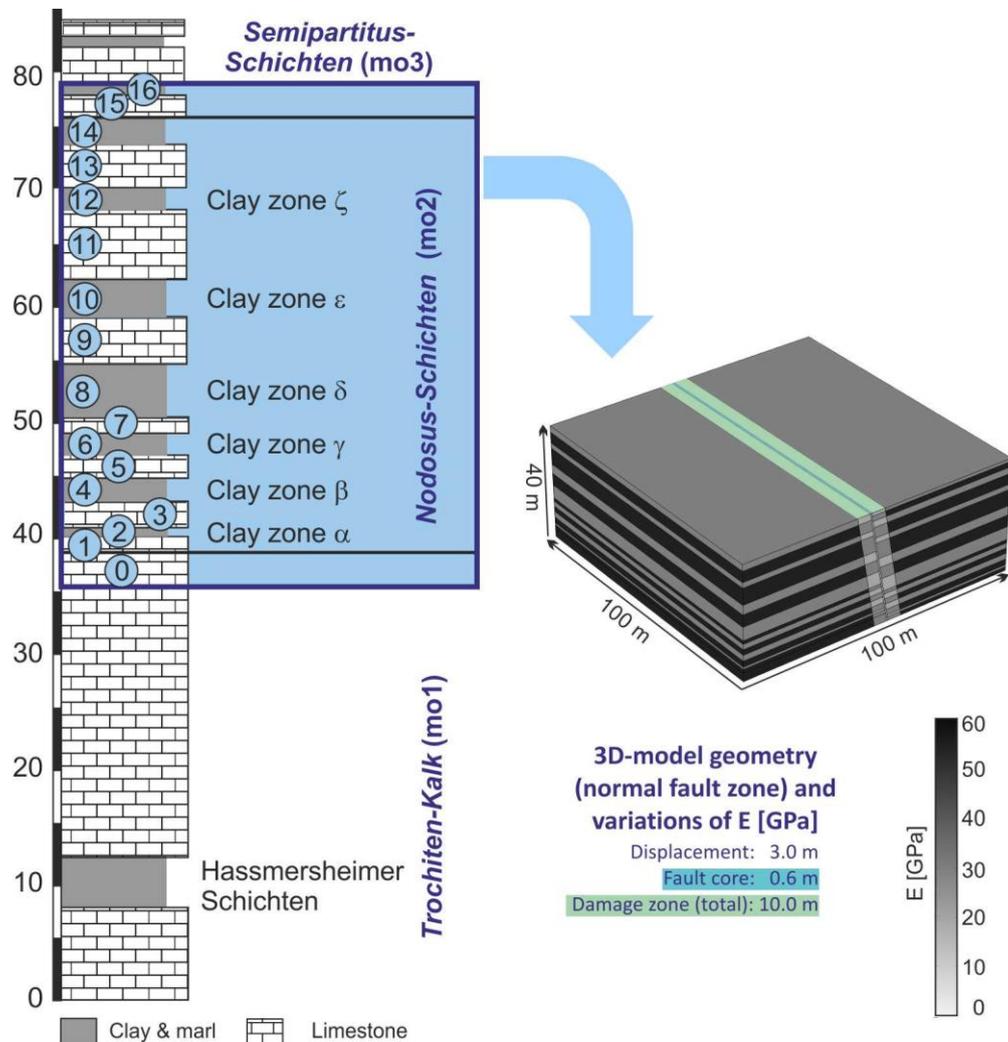


**Fig. 10** Geometry of the medium-scale 3D-numerical models below, based on a profile of the Upper Muschelkalk subunit mo2 in particular (cf. Engesser and Leiber 1991) and normal fault zones in Knittlingen (Fig. 6). We assigned a normal displacement of 3 m as well as a fault core width of 0.6 m and a total damage zone width of 10 m. We defined 17 layers along the lithological profile characterized by stiff limestones and soft clay zones  $\alpha$  to  $\zeta$ . As in the large-scale models (Fig. 9) fault damage zone rocks are softer than the equivalent layers in the host rock. Here, however, the fault core is homogeneous with a low Young's modulus E of 5 GPa. See color scale for assigned E

#### 5.4 Boundary conditions and model runs

To study the effects of varying fault-zone orientations in both 3D-numerical model geometries, we modeled four fault-zone strike directions relative to the orientation of the applied maximum horizontal stress (Fig. 11): (1)  $S_H = 0^\circ$ , (2)  $S_H = 30^\circ$ , (3)  $S_H = 60^\circ$ , and (4)  $S_H = 90^\circ$ . These angles were selected based on observations in analytical models (cf. section 4.2) and prominent angles to  $S_1$  described in literature. To simplify the discussion on the modelling results (section 6), the fault zones are referred to as parallel-

fault-zone (1), 30°-fault-zone (2), 60°-fault-zone (3), and 90°-fault-zone (4) according to their orientation. All fault zones dip steeply (dip angle 80°).

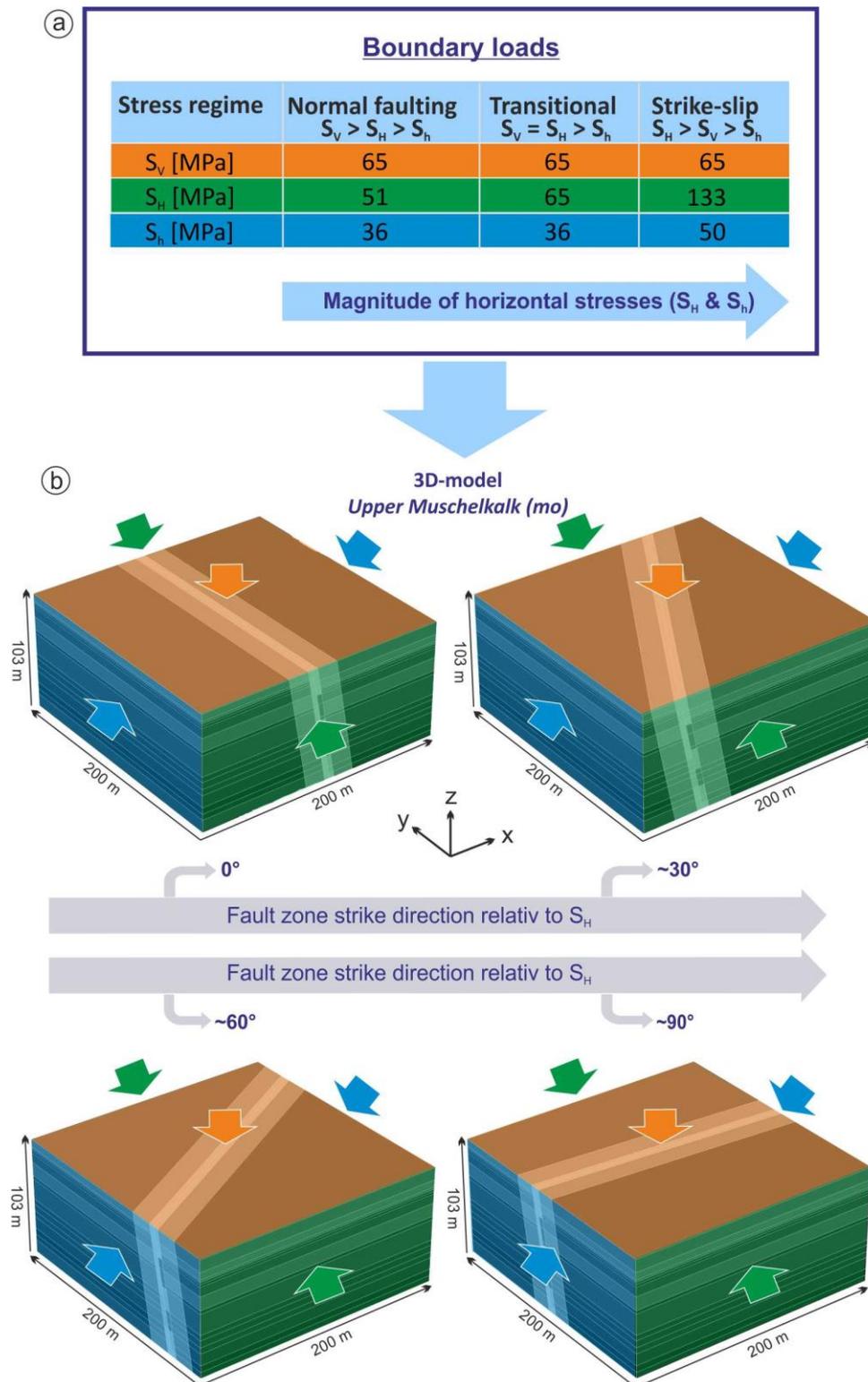


**Fig. 11** a) Magnitudes of the boundary loads according to  $S_v$ ,  $S_H$  and  $S_h$  obtained by the stress polygon described in Fig. 3 (Chapter 4.1) for the stress regimes normal faulting, transitional, and strike-slip faulting. The magnitudes of horizontal stresses increase towards the strike-slip faulting. b) Sketch of the applied boundary loads on the large-scale models (cf. Fig. 9) as an example of a 3D-numerical model.  $S_v$  is applied from the top parallel to the z-axis (orange),  $S_H$  parallel to the y-axis (green),  $S_h$  parallel to the x-axis (blue). Horizontal stresses are applied on two opposite boundaries to simulate a three-dimensional stress regime. A roller constraint was chosen for the boundary condition at the model base (see text for explanation). For each stress regime and model geometry (Figs. 9 and 10) we modeled four fault-zone orientations relative to the orientations of the applied maximum horizontal stress  $S_H$  (0°, 30°, 60°, and 90° to  $S_H$ )

Furthermore, we modeled three possible in-situ stress regimes within the Upper Muschelkalk potential geothermal reservoir in the Upper Rhine Graben (cf. section 3): i.e., (1) normal faulting regime, (2) transitional regime, and (3) strike-slip faulting regime. The magnitude of the vertical stress  $S_V$  is constant in all models but the magnitudes of the horizontal stresses  $S_H$  and  $S_h$  vary according to the calculated stress magnitudes (cf. section 4). Special attention is thereby given on the impact of the maximum horizontal stress  $S_H$  which is either the intermediate ( $S_2$ ) or the maximum principal stress ( $S_1$ ). The two geometries, four fault-zone orientations and three stress regimes result in a total of 24 different numerical models.

All models were run stationary, that is all loads and constraints are constant in time. For each stress regime the vertical stress  $S_V$  and the horizontal stresses  $S_H$  and  $S_h$  are applied as *boundary loads* at five of the six boundaries of the 3D-numerical models (Fig. 11). Additionally, we defined a *roller constraint* at the bases of the models as last required boundary condition. This boundary condition constrains the movement in the out-of-plane direction, but the boundary is free to move in the in-plane direction. The advantage of this roller constraint is that unrealistic stresses that would occur close to the bases of the models when the models are fastened using *fixed constraints* can be avoided.

In the last pre-processing step, we discretized the models into tetrahedron-shaped finite elements as is common in 3D-stress-analysis (e.g., Logan 2002). Finally, the models were run with an iterative linear solver that computed the displacements at all element nodes and stresses within the elements.

## 6 Results of 3D-numerical models

In the following we present the results of the 3D-numerical models (Figs. 13 - 18) in comparison to analytical estimations of stress states  $T_S$  and  $T_D$  (section 4.2). Each figure table presents an overview of the results for one of the two geometries described above: large-scale models (cf. section 5.2; Figs. 13, 15 and 17) and medium-scale models (cf. section 5.3; Figs. 14, 16 and 18). Displayed are trends throughout the 3D-numerical models in terms of the four fault-zone orientations (i.e., angle between fault-zone strike and maximum horizontal stress  $S_H$ :  $0^\circ$ ,  $30^\circ$ ,  $60^\circ$ ,  $90^\circ$ ; cf. section 5.4; displayed as downwards increasing angles) and the three stress regimes (i.e., normal faulting, transitional, and strike-slip faulting regime; cf. sections 4.1 and 5.4; displayed as rightwards increasing magnitudes of the applied horizontal stresses  $S_H$  and  $S_h$ ). Thereby each figure table presents surface plots of one resulting parameter for 12 numerical models (1) principal stresses (Figs. 13 and 14), (2) shear stresses (equivalent stresses; Figs. 15 and 16), and (3) displacements (total displacement and displacement in x-, y-, and z-direction; Figs. 17 and 18).

In addition to the surface plots for each parameter, 1D-diagrams of selected profiles (Fig. 12) that run from the footwall towards the hanging wall and parallel to the coordinate system axes are included. Due to boundary effects at the model margins we chose 1D-profile locations located at distance to the z-boundary (representing depth) and in the same distance to the horizontal boundary that is the boundary parallel to the x-axis (parallel-fault-zone and  $30^\circ$ -fault-zone) or y-axis ( $60^\circ$ -fault-zone and  $90^\circ$ -fault-zone) respectively, depending on fault-zone orientation. In each large-scale 3D-numerical model the 1D-profile cuts a softer layer in the footwall compared with a stiffer layer in the hanging wall. The fault core at 1D-profile depth is built heterogeneously: a soft fault-core unit at contact to the footwall and, in contrast, a mineralized unit at contact to the

hanging wall (Fig. 12a; profile depth: -25 m; x- or y-boundary distance: 15 m). In each medium-scale 3D-numerical model the 1D-profile cuts a stiff limestone layer in the footwall, the soft fault core, and a soft clay zone (clay zone  $\zeta$ ) in the hanging wall (Fig. 12b; profile depth: -10 m; x- or y-boundary distance: 10 m).

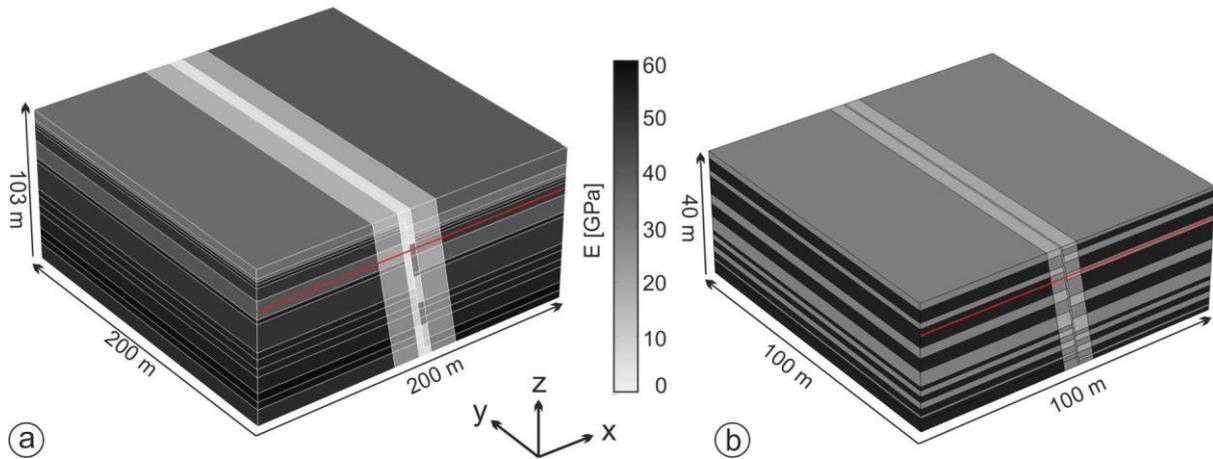


**Fig. 12** Locations of the 1D-diagram-profiles (indicated by red lines) within the large-scale 3D-numerical models and medium-scale 3D-numerical models at fault-zone orientation  $0^\circ$  to  $S_H$ . 1D-profiles in all models are parallel to the x-axis or y-axis, respectively, from the fault-zone footwall towards the hanging wall. a) Large-scale model. At 1D-profile depth of -25 m the layer in the footwall is softer than the layer in the hanging wall. Furthermore, the 1D-profile cuts a mineralized unit of the fault core at contact to the hanging wall. b) Medium-scale model. The 1D-profile cuts a stiff limestone layer in the footwall and soft clay zone  $\zeta$  in the hanging wall (profile depth: -10 m)

### 6.1 Principal stresses

We plot the maximum principal stress ( $S_1$ ), intermediate principal stress ( $S_2$ ), and minimum principal stress ( $S_3$ ) [MPa] versus coordinate system axes location [m] in 1D-diagrams and 3D-surface plots of the maximum principal stress  $S_1$  (Figs. 13 and 14). It is conspicuous for many 3D-numerical models that the stress magnitudes at the fault-zone unit contacts increase sharply. We assume that this is due to a boundary effect at strongly contrasting Young's moduli, since fault zones are limited by the given geometry and shape of the geometric entities and there is no possibility for the material to move freely. Thus, we discuss the findings on principal stresses within the fault damage zones only and not at the contacts to the host rocks.

In general, the fault-zone units damage zones and fault core show their own local stress field with principal stress magnitudes differing from those in the host rocks within hanging wall and footwall. In the majority of the 3D-numerical models principal stress magnitudes decrease within damage zones and in soft fault cores in particular. Further heterogeneities in the stress field are caused by the mechanical layering of the carbonate successions. At profile depth, layers with differing stiffness are displaced against each other. Since stiff layers take up most of the compressive stress, principal stress magnitudes in stiff layers are higher than in soft layers (Gudmundsson et al. 2010; Philipp et al. 2013).

There occur, however, pronounced differences in the local stress fields, depending on the fault-zone orientation and stress regime. To understand the impact of the fault-zone orientation on the local principal stress magnitudes, the applied horizontal stresses and  $S_H$  in particular are of great significance in the different stress regimes modeled.  $S_H$  is either  $S_2$  in the normal faulting regime ( $S_V > S_H > S_h$ ;  $S_H = 51$  MPa) or  $S_1$  in both the transitional regime ( $S_V = S_H > S_h$ ;  $S_H = 65$  MPa) and strike-slip regime ( $S_H > S_V > S_h$ ;  $S_H = 133$  MPa). In addition, also the applied vertical stress  $S_V$  ( $S_1$  in the normal faulting

regime and transitional regime; 65 MPa) is affected by varying fault-zone orientations. These effects are described in the following subsections.

#### 6.1.1 Principal stresses within the large-scale models

In addition to the general development of local stress fields within the fault zones in the large-scale 3D-numerical models we pay particular attention to the heterogeneous fault core (Fig. 13). Mineralizations in the fault core at contact to the hanging wall, modeled as higher Young's modulus, induce additional heterogeneities in the stress field. In this unit a local increase in the principal stress magnitudes in all 3D-numerical models, i.e., stress concentration, occurs regardless of the modeled stress regime and fault-zone orientation.

Principal stresses in *normal faulting regime* ( $S_V > S_H > S_h$ ;  $S_V = 65$  MPa,  $S_H = 51$  MPa,  $S_h = 36$  MPa) are quite similar throughout all modeled fault zones, but minor differences occur: The decrease of all principal stresses within the soft fault core is largest and most uniform for the parallel-fault-zone. In contrast, the decrease of  $S_1$  within the soft fault core is significantly reduced towards the 90°-fault zone.

In general, fault-zone local stress fields within *normal faulting* and *transitional regimes* ( $S_V = S_H > S_h$ ;  $S_V = S_H = 65$  MPa,  $S_h = 36$  MPa) have some similarities, particularly in the magnitudes of  $S_2$  and  $S_3$ . In the *transitional regime*, results show different trends for  $S_1$  and  $S_2$ . Although they are equal in magnitudes, they are acting in different directions (horizontal vs. vertical) and are therefore affected by different contacts (mechanical fault-zone units vs. mechanical layering). The magnitude of  $S_1$  depends on fault-zone orientation: no decrease of  $S_1$  within the soft fault core occurs in the 60°- and 90°-fault zone. The magnitude of  $S_1$  within the fault damage zone and fault core is higher compared with the normal faulting regime, becomes more homogeneous, and reflects the stress magnitude of  $S_1$  in the host rock.

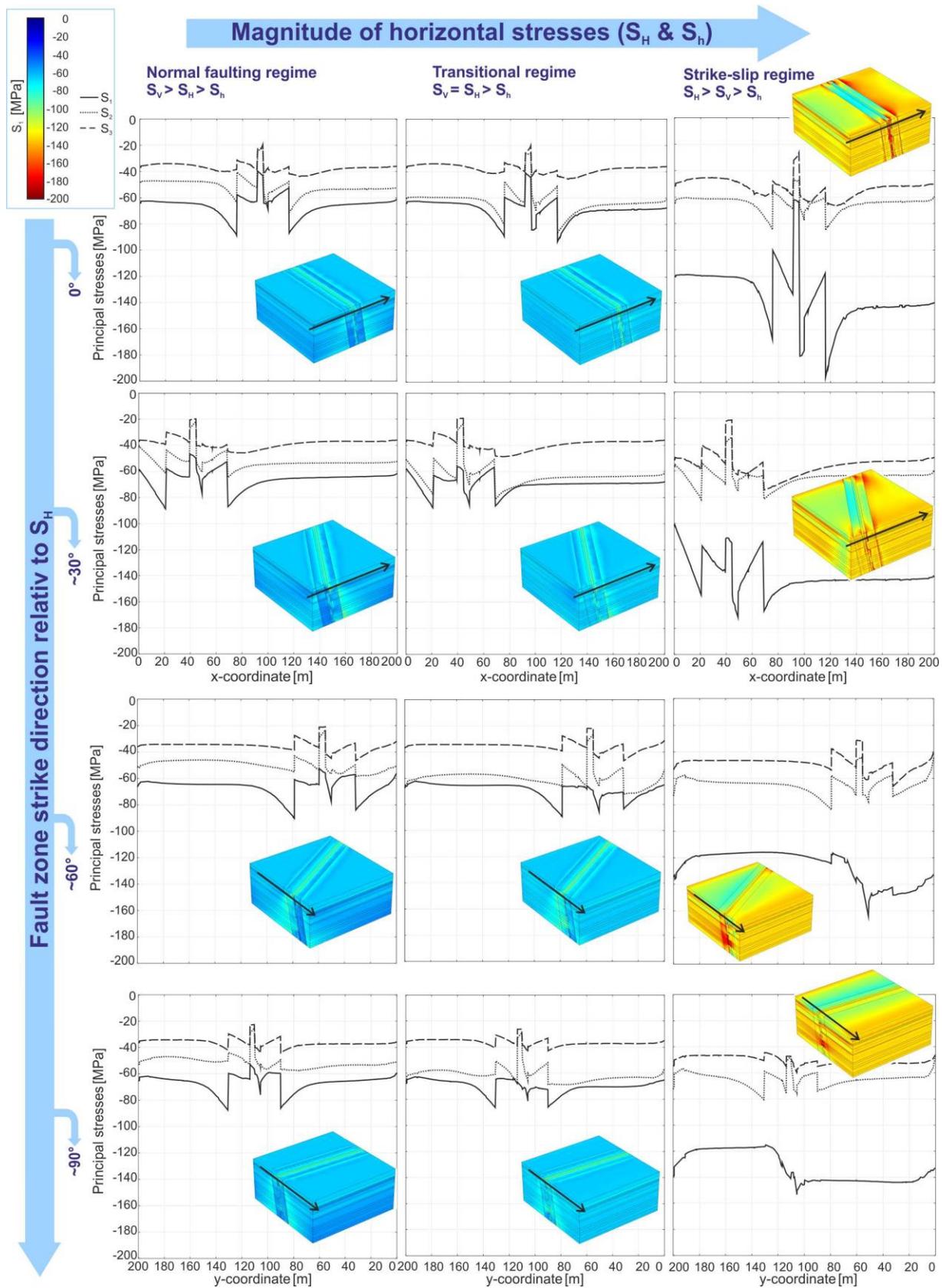


**Fig. 13 (previous page)** Principal stress magnitudes [MPa] within a total of 12 numerical models of the large-scale fault zone crosscutting the entire Upper Muschelkalk. Models of three stress regimes normal faulting (left), transitional (center) and strike-slip faulting (right) vary horizontally and applied magnitudes of horizontal stresses and  $S_H$  in particular increase rightwards. Models of four fault-zone orientations vary vertically and the fault-zone orientation in relation to  $S_H$  increases downwards ( $0^\circ$ ,  $30^\circ$ ,  $60^\circ$ , and  $90^\circ$ ). Since COMSOL Multiphysics® is an engineering software, computed principal stresses are negative and the magnitudes of principal stresses increase with decreasing values. The 1D-plots show magnitudes of the maximum principal stress  $S_1$ , intermediate principal stress  $S_2$ , and minimum principal stress  $S_3$  versus coordinate of the x-axis ( $0^\circ$ ,  $30^\circ$ ) or y-axis ( $60^\circ$ ,  $90^\circ$ ) respectively depending on the fault-zone orientation. The 3D-surface plots show the magnitudes of  $S_1$  in the entire 3D-numerical model. See key in the upper left for signature of  $S_1$ ,  $S_2$ , and  $S_3$  in the 1D-plots and color scale for magnitudes of  $S_1$  in the 3D-surface plots. The results are discussed in the text

Magnitudes of principal stresses within a modeled *strike-slip regime* ( $S_H > S_V > S_h$ ;  $S_H = 133$  MPa,  $S_V = 65$  MPa,  $S_h = 50$  MPa) are significantly different since  $S_H$  is by far the largest stress. First it is conspicuous that the mechanical layering in this stress regime, characterized by horizontal compression, obviously has the strongest impact. This results in a vertically very heterogeneous stress field and the formation of barriers for fracture propagation (cf. section 2). Due to fault-zone displacement different stress magnitudes of  $S_1$  occur between the fault-zone hanging wall and footwall with higher magnitudes of  $S_1$  in the stiffer layer (hanging wall) than in the softer layer (footwall).

A larger impact on principal stress magnitudes, however, is caused by the fault-zone orientation. Even though a significant decrease of the principal stresses occurs in particular in the parallel-fault zone, the aforementioned smaller decrease of  $S_1$  (or put vice versa: proportional increase of  $S_1$  within fault damage zones and fault core towards the  $90^\circ$ -fault-zone) is most apparent in this stress regime. The transition between lower principal stresses in the fault-zone footwall and higher principal stresses in the hanging wall becomes more gradual. Thus, the effects of horizontal mechanical fault-zone units decrease with increasing impact of  $S_H$  and with increasing angle to  $S_H$ . As a consequence, comparatively high magnitudes of  $S_1$  occur within the  $90^\circ$ -fault zone.

To sum up, fault zones parallel to and with  $30^\circ$  to  $S_H$  show lower principal stresses within the fault damage zones and fault core compared with both other fault zones, since  $S_1$  acts parallel and  $S_3$  normal to the fault zone in a strike-slip regime. They also show higher  $T_D$  or  $T_S$  (cf. Chapter 4.2) and may act as zones of weakness more easily. In contrast, a high horizontal stress ( $S_1$ ) acts normal to the  $90^\circ$ -fault-zone and therefore also normal to the mechanical unit contacts. Softer fault damage zones and the fault core are compressed (low  $T_D$ ). Thus, the transition between footwall and hanging wall across damage zones and fault core is more gradual.

### 6.1.2 Principal stresses within the medium-scale models

The characteristics of principal stresses in the medium-scale models are to a large extent comparable to those described in context with the large-scale models (section 6.1.1). However, differences occur due to the modeled homogeneous fault core which has equal  $E$  throughout the carbonate succession (Fig. 14). This fault-zone unit thus lacks additional heterogeneities so that principal stress magnitude distributions are more symmetric. Furthermore, the local stress field disturbances are more limited since incorporated fault zones have a smaller width.

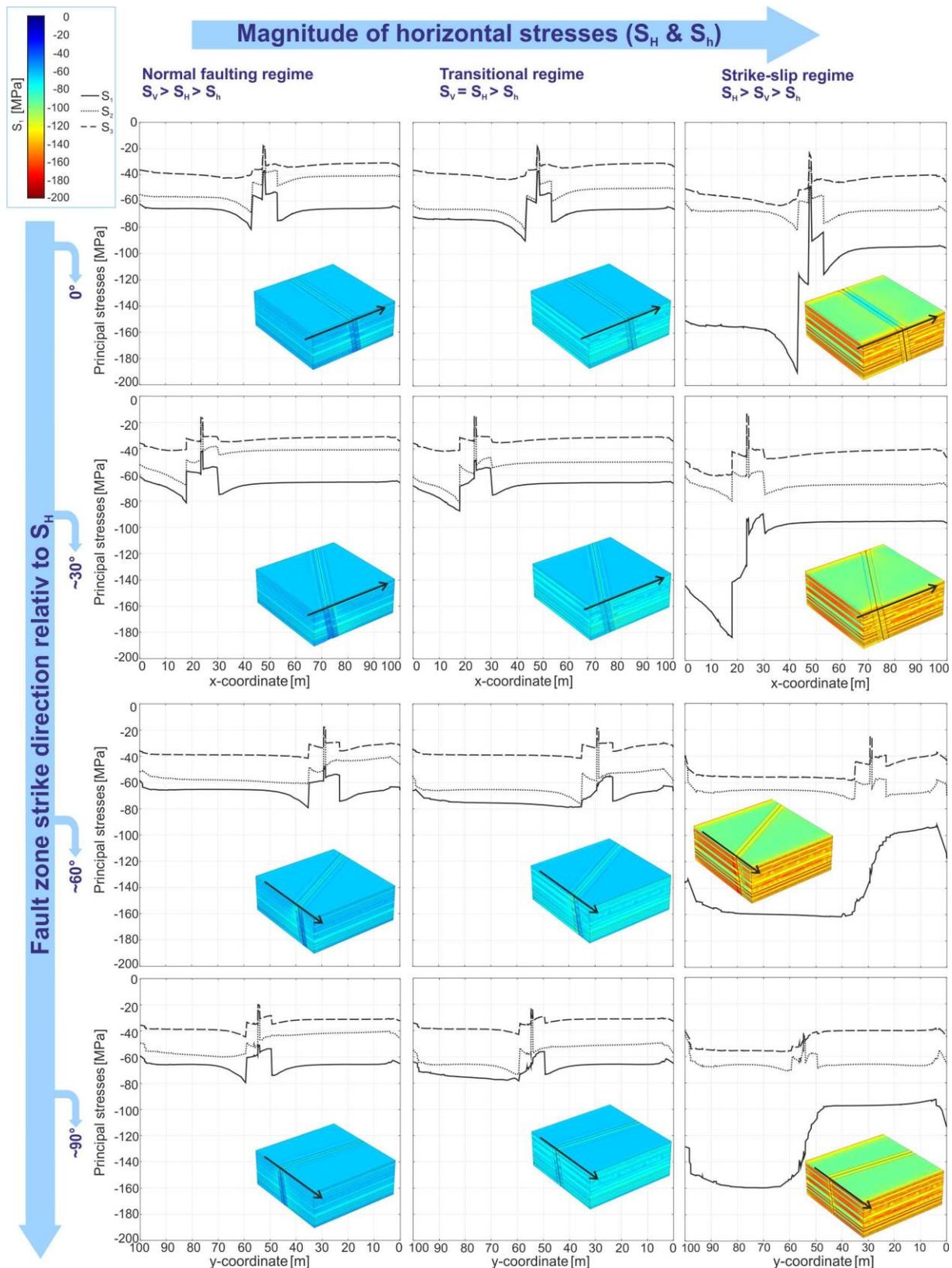


**Fig. 14** Principal stress magnitudes [MPa] within a total of 12 numerical models of the medium-scale fault zone crosscutting the Nodosus-Schichten (mo2) (cf. Fig. 13 captions and text for details)

Major differences, however, are caused by the mechanical properties of the carbonate succession. The Nodosus-Schichten (mo2) are modeled in high resolution and are characterized by high Young's modulus contrasts of mechanical layers. Stiff limestone beds alternate with soft clay zones and are displaced against each other (cf. section 5.3).

In all modeled stress regimes, contrasting to the large-scale models, this strong mechanical layering leads to different stress magnitudes of  $S_H$  ( $S_2$  in the *normal faulting regime*;  $S_1$  in the *transitional* and *strike-slip regime*) and  $S_h$  ( $S_3$  in all stress regimes) in host-rock footwall and hanging wall. This difference in principal stress magnitudes increases towards the *strike-slip regime* and is most conspicuous in fault zones oriented at high angle to  $S_H$ , particularly in the 90°-fault zone.

Thus, the results show distinct heterogeneities of principal stresses in the Nodosus-Schichten across the fault zone in horizontal direction comparable to those in the large-scale models and, in addition, within the carbonate succession in vertical direction. Therefore, the characteristics and principal stress magnitudes depend on the stiffness contrasts in the carbonate succession, the fault-zone orientation and the given stress regime.

## 6.2 Shear stresses

We present shear stresses [MPa] as equivalent stresses. 3D-surface plots are shown as *von Mises stress* as determined by the maximum-distortion-energy hypothesis (calculated from all principal stresses). The 1D-diagrams plot von Mises stress and additionally the simpler *Tresca stress* as the maximum shear stress (i.e., calculated from maximum and minimum principal stress only) versus coordinate system axes location [m]. Since the two equivalent stresses are determined in different ways, the stress magnitudes show slight differences in their magnitudes.

As mentioned in context with the results of principal stress magnitudes (section 6.1) we interpret significant increases of shear stress magnitudes at contacts between units with different Young's moduli mainly as boundary effects. These could, however, also represent results of planes of weakness, i.e., slip planes that occur in natural fault zones, particularly at the fault core.

Results show that, similarly to principal stress magnitudes, shear stress magnitudes differ within fault damage zones and fault core from those in the host rock. Furthermore, fault-zone local shear stresses are also affected by fault-zone orientation, stress regimes, fault-zone characteristics, and mechanical layering within the carbonate succession.

### 6.2.1 Shear stresses within the large-scale models

Results of the large-scale models show two contrasting trends of shear stress magnitudes across the fault zone from the *normal faulting regime* to the *strike-slip regime*, clearly depending on the fault-zone orientation, i.e., fault zones at a minor angle to  $S_H$  (parallel-fault-zone and 30°-fault-zone) show a different trend than fault zones oriented with high angle to  $S_H$  (60°-fault-zone and 90°-fault-zone (Fig. 15)). With regard to fault-core stiffness heterogeneities the trend is as follows. Stiff mineralizations at contact to the hanging-wall damage zone take up comparatively high amounts of shear stress in the parallel-fault-zone and 30°-fault-zone. Towards the 90°-fault-zone, in contrast, the soft fault core unit at contact to the footwall damage zone leads to higher shear stress concentration. This trend is more pronounced towards the *strike-slip regime* so that is likely to be caused by an increased horizontal compression on the 60°-and 90°-fault zone. This shear stress increase may be due to high impact of  $S_h$  which acts at 30° on the 60°-fault-zone and parallel to the 90°-fault-zone.

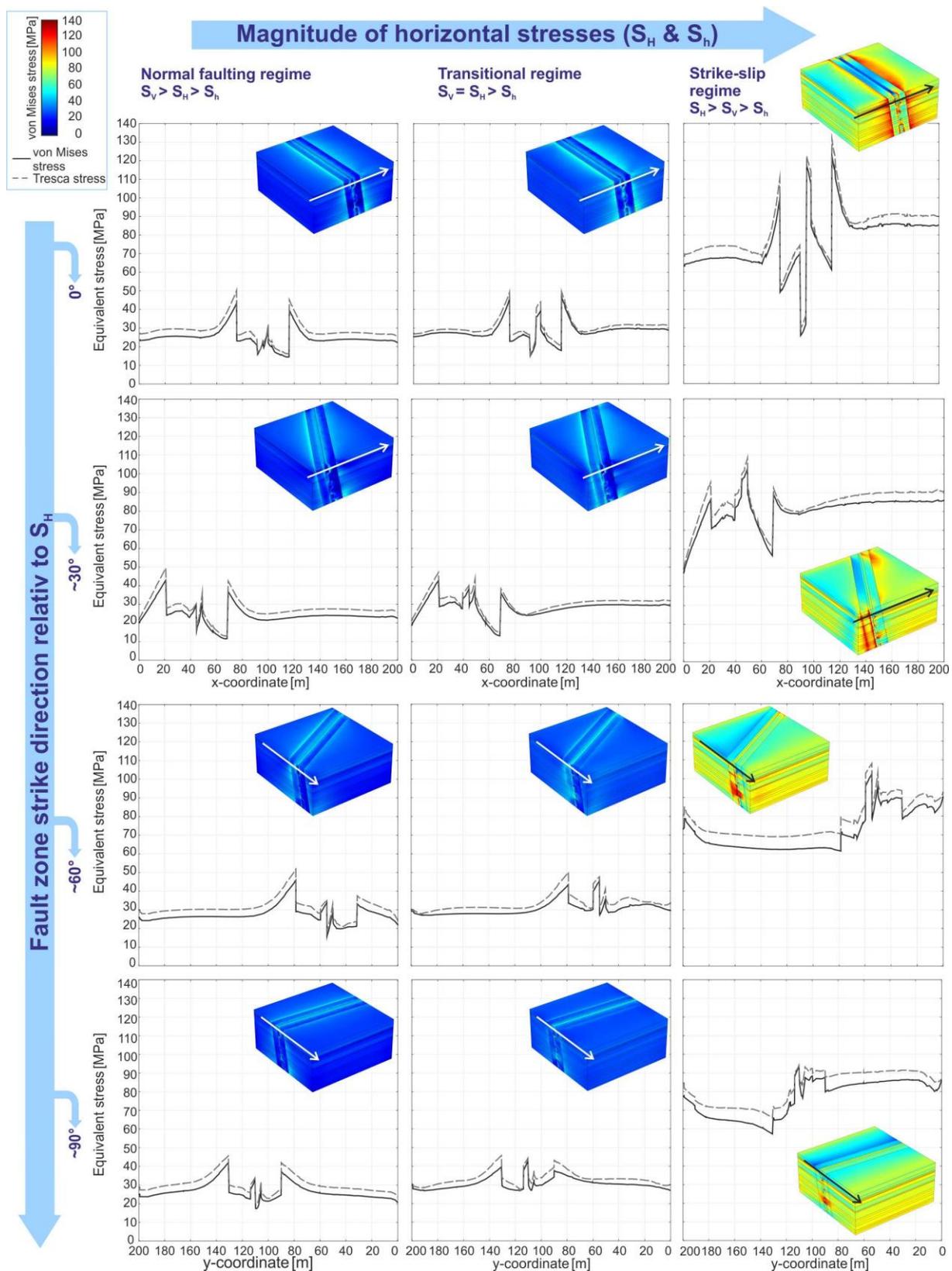


**Fig. 15** Shear stress magnitudes computed as equivalent stresses von Mises stress and Tresca stress [MPa] within a total of 12 numerical models of the large-scale fault zone crosscutting the entire Upper Muschelkalk (cf. Fig. 13 captions and text for details). The 1D-plots show magnitudes of von Mises stress and Tresca stress versus coordinate of the x-axis ( $0^\circ$ ,  $30^\circ$ ) or y-axis ( $60^\circ$ ,  $90^\circ$ ), respectively, depending on the fault-zone orientation. The stress magnitudes show slight differences since the equivalent stresses are computed in different ways. The 3D-surface plots show the magnitudes of von Mises stress in the entire 3D-numerical model. See key in the upper left for signature of von Mises stress and Tresca stress in the 1D-plots and color scale for magnitude of von Mises stress in the 3D-surface plots

A similar trend occurs in the damage zones. In the *normal faulting regime* results show a trend of slightly lower shear stress magnitudes compared with the host rock, particularly in the damage zone at contact to the hanging wall host rock. This trend, however, is less pronounced towards the 90°-fault-zone. With increasing impact of  $S_H$ , that is towards the strike-slip regime, the local shear stresses within fault-damage zones become more complex and the contrasting trends of fault zones with differing orientations (fault zones at a minor angle to  $S_H$  vs. fault zones at a high angle to  $S_H$ ) are more significant. Thus, there is a more gradual transition of local shear stresses between hanging wall host rock and damage zone.

Within the *strike-slip regime* and towards the 90°-fault zone the fault damage zones generally concentrate higher shear stresses. Comparatively high shear stresses occur not only in the footwall damage zone of the 30°-fault zone, but also in the hanging wall damage zone in the 60°-fault-zone and 90°-fault zone in particular. In the latter cases, results show higher shear stresses within the fault zone compared with the adjacent host rocks in both footwall and hanging wall whereby shear stresses increase from the footwall towards the hanging wall.

#### 6.2.2 Shear stresses within the medium-scale models

Results of medium-scale models (Fig. 16) show in most cases a partially significant increase of shear stresses within the soft fault core, particularly towards the 90°-fault zone. Exceptions occur for the parallel-fault-zone, showing decreasing shear stresses within the fault core. These results suggest that thinner fault cores take up higher shear stresses more easily than large-scale fault cores. High shear stresses within fault cores are in accordance with many field observations in which the strain is localized within the fault core (e.g., Caine et al. 1996; Faulkner et al. 2010). However, this could also be the cause of the fault core width in the medium scale models being too small to compensate the boundary effects characterized by a significant increase of shear stresses at geometric entity contacts.

In contrast to the *normal faulting regime* where relatively uniform local shear stress magnitudes occur within fault damage zone and fault core for all four fault-zone orientations, the local stress field becomes more heterogeneous towards the *strike-slip regime*. In both the transitional regime and the strike-slip regime, stiff limestone beds in the footwall fault damage zone concentrate higher shear stresses than the adjacent soft clay zones in the hanging wall damage zone. In the *transitional regime* and towards the 90°-fault-zone, further heterogeneities are most visible as a more gradual transition of shear stress magnitudes within the footwall at contact of host rock and damage zone. In contrast, there is a sharp decrease of shear stress magnitudes at the contact of hanging wall host rock and damage zone for all modeled fault-zone orientations.

The effect of a more gradual transition is more significant in the *strike-slip regime*, in which the fault damage zones and fault core clearly form a transition zone between high shear stress within the footwall host rock and lower shear stress within the hanging wall host rock with, again, a more pronounced gradual transition towards the 90°-fault zone.

An exception showing low shear stress magnitudes within the fault damage zone and fault core is the parallel-fault zone. However, also shear stresses within the 30°-fault zone and 60°-fault-zone are affected by mechanical fault-zone units. This is observable, for example, as a sharp increase of shear stresses at damage-zone-host rock contacts in the 30°-fault zone and a local increase of shear stresses within the fault core in the 60°-fault zone.

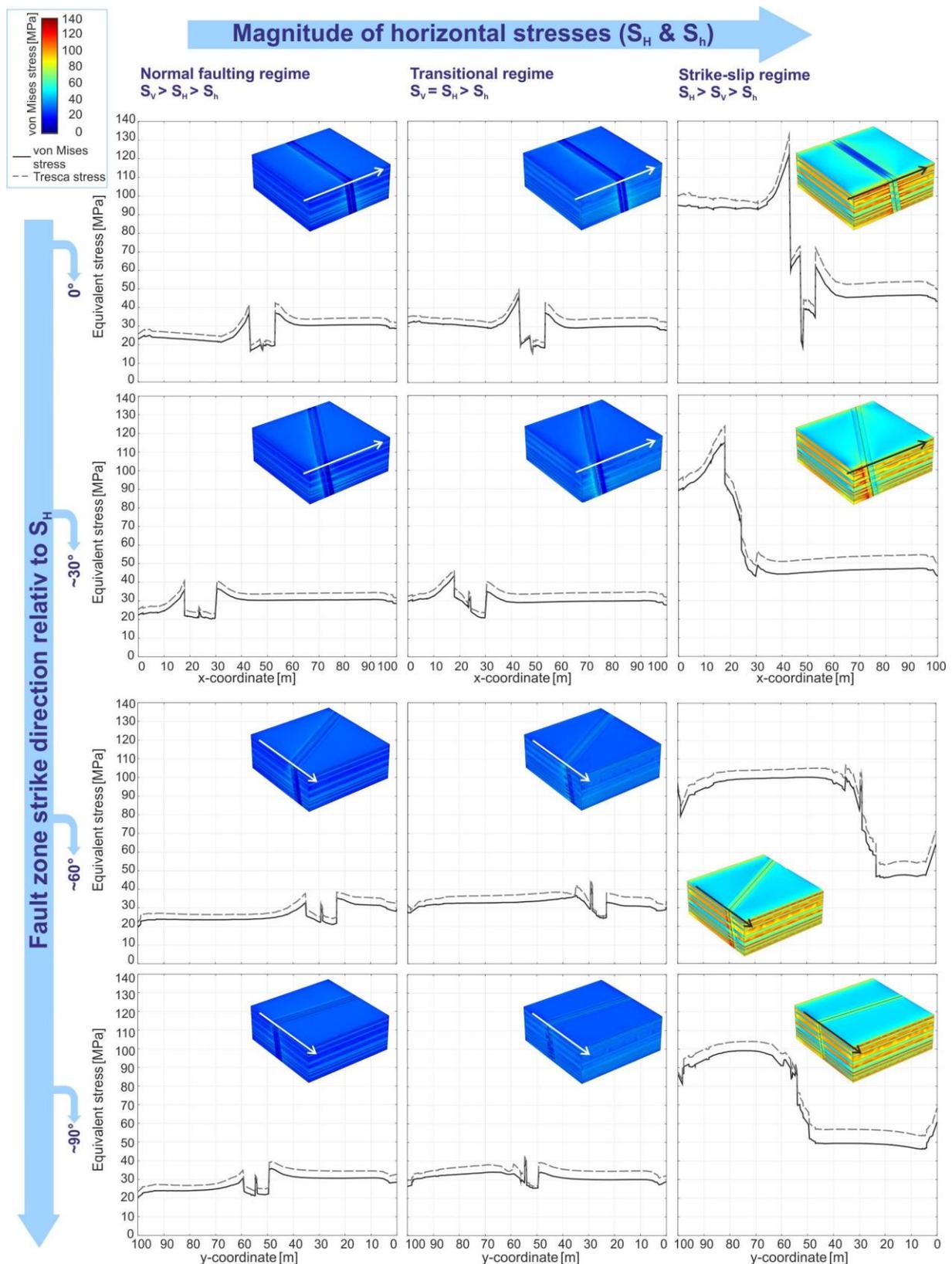


**Fig. 16** Shear stress magnitudes computed as equivalent stresses von Mises stress and Tresca stress [MPa] within a total of 12 numerical models of the medium-scale fault zone crosscutting the Nodosus-Schichten (mo2) (cf. Figs. 13 and 15 captions and text for details)

### 6.3 Displacements within fault zones

We present displacements along the coordinate system axes, in which applied magnitudes of  $S_V$  are acting parallel to the z-axis (positive upwards), magnitudes of  $S_H$  parallel to the y-axis (positive leftwards), and magnitudes of  $S_h$  parallel to the x-axis (positive rightwards). We show 1D-diagrams in which we plot the total displacement [m] (black) and displacements along the x-axis (blue), y-axis (red) and z-axis (orange) [m] versus coordinate system axis location [m]. Furthermore, we show 3D-surface plots of the total displacement [m]. Horizontal compression of the 3D-numerical models is indicated by negative displacement values along the x-axis or y-axis, respectively.

Displacements of both model series show that fault zones in the large-scale 3D-numerical models represent larger zones of weakness that provide opportunities to either displace the rocks or compress the modeled fault damage zones and fault core. Displacement values are generally higher and displacement trends induced by the fault-zone orientation are more pronounced than in the medium-scale 3D-numerical models.

#### 6.3.1 Displacements within the large-scale models

Majority of displacements in the *normal faulting regime* ( $S_V = S_1$ ) can be assigned to a downward movement of the entire 3D-numerical model geometry and of the softer fault-zone units in particular. This is indicated by continuous negative values of displacements in z-direction (Fig. 17), which increases within damage zone and fault core in particular with nearly identical values for all modeled fault-zone orientations. However, horizontal compression induced by  $S_H$  and  $S_h$  and heterogeneities in displacements within fault damage zone and fault core also occurs. For example, the results show an enhanced displacement in y-direction within the parallel-fault-zone and 30°-fault-zone caused by  $S_H$ . The impact of  $S_h$  on the 60°-fault-zone and 90°-fault-zone becomes obvious through an enhanced horizontal displacement in x-direction. The impact of fault-zone orientation on the displacement field for this stress regime in which  $S_H$  and  $S_h$  have only a secondary impact is thus clear.

We conclude, that within the *transitional regime* and *strike-slip regime* the total displacement along the 1D-profile is progressively related to displacement along the y-axis and, in contrast, amounts of displacements in z-direction and x-direction decrease in proportion. Towards the *strike-slip regime* with an increasing impact of  $S_H$ , results show significant differences in the distribution of the maximum total displacement for the four fault-zone orientations. We therefore discuss their impacts on the displacement fields within the modeled *strike-slip-regime* in the next paragraphs in more detail.

Fault zones oriented at a minor angle to  $S_H$  (0° and 30°) show a maximum total displacement within the fault core and the fault damage zones. In the parallel-fault zone the increasing displacement in y-direction (parallel to  $S_H$ ) is thereby symmetrical and gradual because the soft fault core and damage zones are pressed into the modeled block parallel to the mechanical unit contacts. The impact of  $S_H$  is therefore concentrated in soft damage zone and fault core. However, particularly the 30°-fault-zone seems to be favorably oriented for  $S_H$ -induced horizontal displacement within the fault-zone units fault core and damage zone since occurrence of the highest total displacement. In both hanging wall and footwall, horizontal compression causes a zone of maximum displacement within the soft fault-zone units that continues along the fault core towards the center of the 3D-numerical model. In the opposite fault block, that is the footwall or hanging wall, respectively, significantly lower displacements occur. We assume that these results indicate a high slip tendency  $T_S$  and shear movements particularly along the fault core and within the soft fault-zone units of this fault zone at an angle of 30° to  $S_H$ .

In contrast, within both other modeled fault zones, oriented at high angle to  $S_H$  (60°-fault-zone and 90°-fault-zone), the total displacement is highest at the model margins and decreases towards the fault core. Both fault zones, in particular the 90°-fault-zone, are compressed. In addition, solely within the 60°-fault-zone an enhanced impact of  $S_H$  becomes clear as an increased horizontal displacement in x-direction in the fault zone at an angle of 30° to the minimum horizontal stress  $S_h$ .

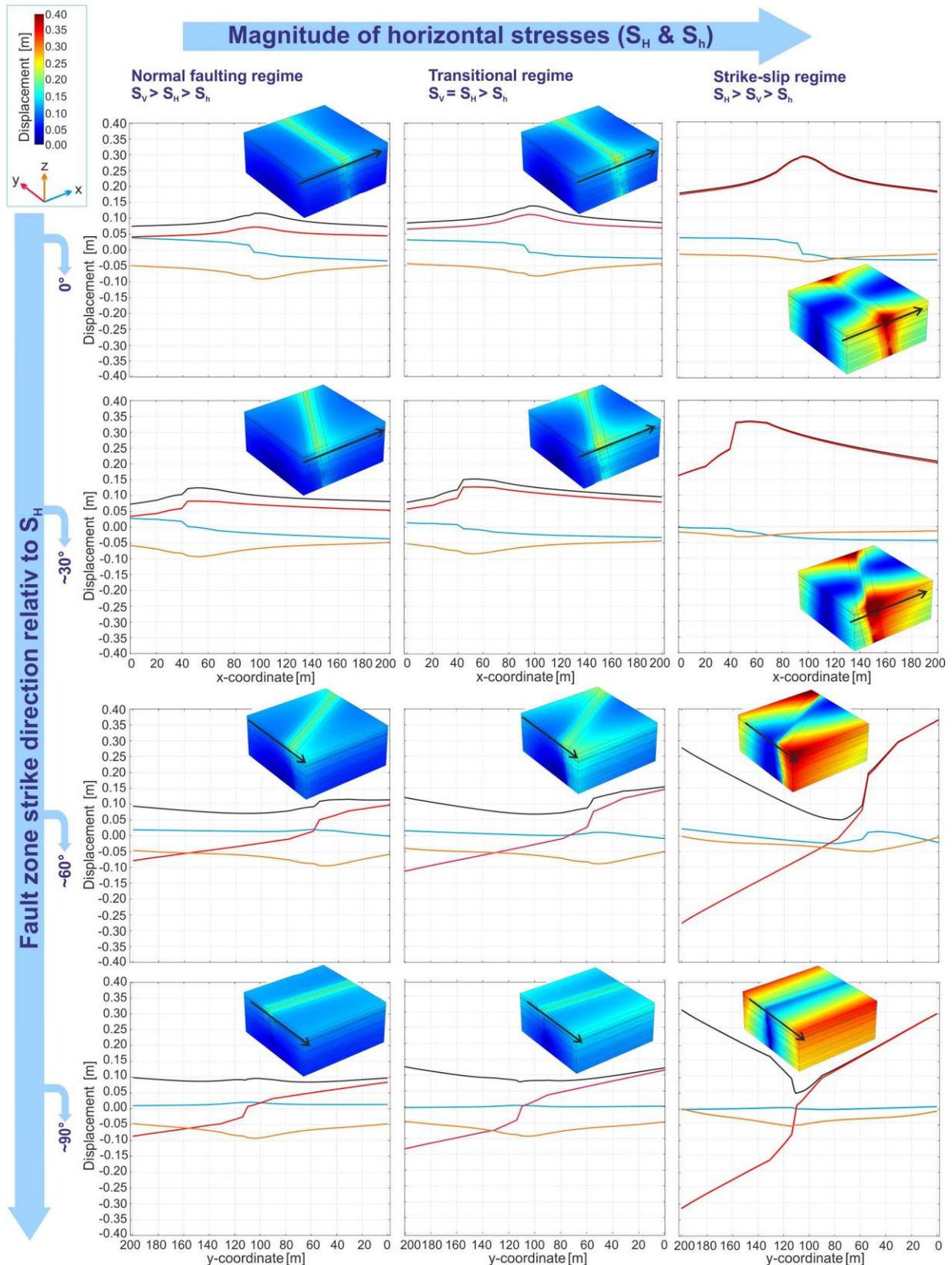


**Fig. 17 (previous page)** Displacements along the given coordinate system axes [m] within a total of 12 numerical models of the large-scale fault zone crosscutting the entire Upper Muschelkalk (cf. Fig. 13 captions and text for details). The 1D-plots show the total displacement and the displacements along the x-axis, y-axis, and z-axis versus coordinate of the x-axis (0°, 30°) or y-axis (60°, 90°), respectively, depending on the fault-zone orientation. Negative displacement values along the z-axis indicate a downward movement of the geometry. Horizontal stresses are applied on two opposite boundaries to model three-dimensional stress regimes. This horizontal compression results in negative displacement values along the x-axis or y-axis, respectively. The 3D-surface plots show the total displacement in the entire 3D-numerical model. See key in the upper left for signature of displacement along the coordinate system axes in the 1D-plots and color scale for magnitude of total displacement in the 3D-surface plots

---

### 6.3.2 Displacements within the medium-scale models

Due to similarities in displacement trends to the large-scale-models in section 6.3.1 only a brief comparison to the medium-scale-models is drawn. For the *normal faulting regime* a relatively uniform downwards movement of the geometry occurs comparable to the downwards movement of the host rock at the model margins of the large-scale models. However, results of the medium-scale-models show consistently smaller vertical displacements within damage zone and fault core. This shows that displacements in the numerical models are only to a minor degree affected by the incorporated fault zones (Fig. 18). Due to minor effects of  $S_H$  and  $S_h$  in this stress regime and the comparatively thin fault zones hardly any horizontal displacements occur within fault damage zones and fault core.

Due to increasing horizontal stresses the horizontal displacements increase consequently towards the *strike-slip regime*. In contrast to the large-scale models, however, where displacements are concentrated within well oriented fault zones (cf. section 6.3.1), the medium-scale models show displacement particularly at the model margins and only to a minor degree within the modeled fault damage zone and fault core in the *transitional regime*. In the *strike-slip regime*, finally, increased impact of the soft fault-zone units and fault-zone orientation is visible resulting in a similar displacement trend as described for the large-scale models above (section 6.3.1).

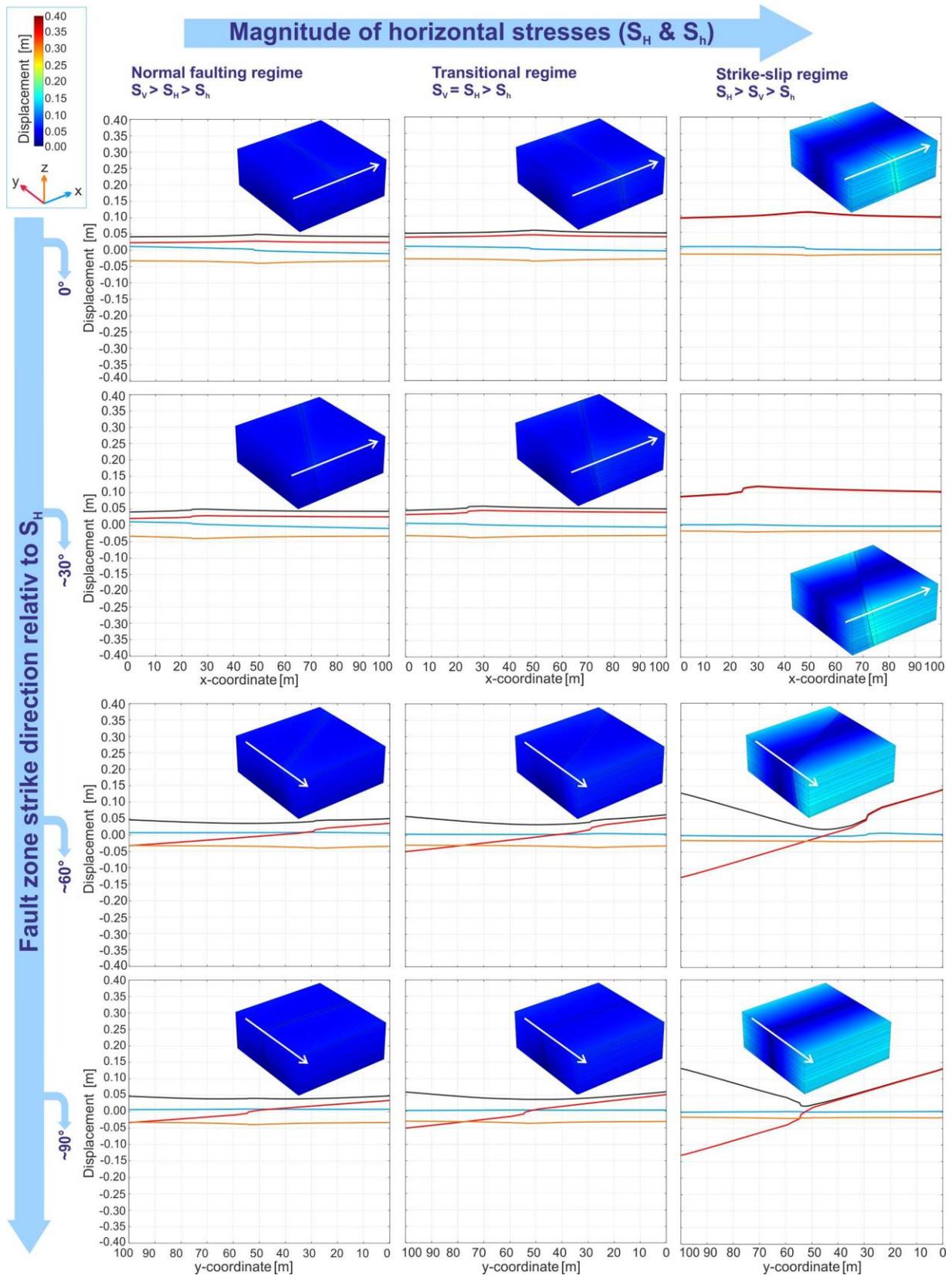


**Fig. 18** Displacements along the given coordinate system axes [m] within a total of 12 numerical models of the medium-scale fault zone crosscutting the Nodosus-Schichten (mo2) (cf. Figs. 13 and 17 captions and text for details)

## 7 Discussion and conclusions

This paper presents a field-study based workflow to develop 3D-numerical models on local stress fields within fault zones hosted in layered rocks at reservoir depths. The workflow includes three main steps to receive input data and boundary conditions: (A) characterization of fault-zone units and mechanical layering, (B) estimations of rock mechanical properties and (C) assumptions on the in-situ stress regime.

Definition of input data and boundary conditions for the numerical models worked well. Estimations on the material property Young's modulus  $E$ , received by laboratory tests of field samples and analytical models using rock hardness measurements in the field, provide solid results regarding its variations and reflect relative mechanical contrasts. However, stiffness contrasts decrease with increasing depth (cf., section 5.1; stiffness homogenization; Gudmundsson 2011; Philipp et al. 2013) and thus, at geothermally relevant depths, probably do not exist in the same scale. Analytical estimations on in-situ stress magnitudes in fault-related geothermal reservoirs (stress polygon; frictional equilibrium theory) are a powerful way to make assumptions on the in-situ stress regime if no measurements on stress magnitudes at depth are available.

The findings of presented 3D-numerical models suggest the general need of improvements regarding geometry setup which is based on characteristics of fault-zone units and mechanical layering. To avoid boundary effects, future numerical models could include zones of gradually changing Young's moduli between damage zone and host rock equivalent to the gradual decrease in fracture density towards the damage-zone-host-rock boundary in nature. Such a gradual transition, however, is difficult to model for varying fault-zone orientations and resulting various shapes and sizes of geometric entities. In contrast, the fault-core-damage-zone boundary is sharp in natural fault zones that are reflected realistically in the contrasting Young's moduli.

Moreover, it should be tested in future numerical models whether the assignment of contact-boundary conditions between adjacent boundaries, possible in COMSOL Multiphysics®, provide an improvement. The implementation is rather complicated, has to be set up carefully regarding the mesh at contact interface, friction, load etc. and therefore was omitted in these basic models.

Presented 3D-numerical models supported by analytical estimations on the in-situ stress field and fault-zone stress state are, despite their limitations, powerful tools to provide significant insights on fault-zone local stress fields in layered rocks at reservoir depths:

- Local stress fields of fault zones hosted in layered carbonate successions show pronounced heterogeneities. Their characteristics as well as principal stress magnitudes depend on stiffness contrasts in the carbonate succession, stiffness contrasts between softer fault damage zones and host rock, fault-zone orientation and the given stress regime. The decrease of stress magnitudes in soft rocks diminishes towards fault zones oriented at high angles to  $S_H$ . Changes in stress magnitudes become more gradual across fault-zone units in fault zones oriented at higher angles to  $S_H$  ( $60^\circ$ ,  $90^\circ$ ), particularly in horizontal compression (strike-slip regime). Comparatively high local stress magnitudes (e.g., high compressive stress) are the consequence in those fault zones, resulting in potential fracture closure or prevention of hydrofracture formation, respectively.
- Effects of mechanical layering increase from normal to strike-slip regime resulting in a vertically very heterogeneous local stress field. The fault damage zone and fault core form a transition zone between differing stress magnitudes in footwall and hanging wall if rocks with differing stiffness are displaced against each other, particularly in

fault zones oriented at a high angle to  $S_H$ . Effects of mechanical layering may, for example, result in formation of barriers to fracture propagation (stiff layers tend to concentrate compressive stresses) and thus lower probability of forming interconnected fracture networks necessary for fluid flow in reservoirs, induced for example by hydraulic stimulation. Furthermore, this vertically heterogeneous stress field may lead to wellbore instabilities in this succession characterized by rocks with varying failure behavior (development of compressive-stress-induced borehole breakouts if the stress concentration reaches the rock strengths; e.g., Zoback 2007). Mud weight cannot be adapted at such short distances but must be chosen carefully as to stay within the safe window between fracture gradient and pore pressure gradient.

- Fault damage zones in the Upper Muschelkalk-subunit Trochiten-Kalk (mo1) may be preferred potential drilling targets since this unit is per se characterized by a more homogeneous succession which is, as mentioned above, further homogenized towards geothermally relevant depths. Thin marl layers are common over large sections in the succession, but have only little effects on fracture propagation in these partially thick mechanical units. If necessary, it would easily be possible to improve the vertical hydraulic connectivity of the natural fracture network by stimulation.
- In contrast, the Upper Muschelkalk-subunit Nodosus-Schichten (mo2), characterized by strong mechanical layering, appears to be a rather unsuitable drilling target for a geothermal project in the URG, in particular towards a strike-slip regime (higher horizontal compression). Even though stiffness contrasts may be lower at depths, the formation or improvement of a vertical hydraulically active fracture network, for example by hydraulic stimulation, is challenging and may still be prevented within a vertically very heterogeneous stress field. Since the initial stiffness contrasts are significantly high, such a local stress field may still include various stress barriers for fracture propagation. Thus, an increased risk for the development of too small fractures, resulting in hydraulically non-active fracture systems, is stated for the mo2.
- Another goal of hydraulic stimulation is to expand pre-existing natural fractures, i.e., to increase fracture apertures and lengths. Previous research shows that fracture expansion can be ascribed to shearing processes (Zimmermann et al. 2011). Results of the presented 3D-numerical models show that stiff limestone beds concentrate shear stresses and could thus, to improve the horizontal permeability, be targeted for hydraulic stimulation treatments. These layers are hence preferable for shear failure of pre-existing fractures (fractures with high slip tendency). These shear movements along rough fracture planes may increase fracture aperture (self-propping effect) and thus permeability.
- In general, potential hydraulic stimulation of the fracture system within the described carbonate succession has to be planned with care for each particular unit of the Upper Muschelkalk (e.g., adjustment of fluid overpressure for hydrofracture formation). Variations of Young's modulus and thus stiffness contrasts at reservoir depth can be determined for example by acoustic logs, i.e., by wireline logging in an existing wellbore or by the usage of logging while drilling tools. Afterwards, 3D-numerical models of local stresses at reservoir depth can be adapted accordingly.
- Predicting the stress state of fault zones and associated potential fluid pathways in the URG is difficult due to the varying impact of  $S_H$  in the given stress regime, which is transitional between normal faulting and strike-slip faulting. In addition, varying  $S_H$ -orientations across the URG determine that fault zones of similar orientations located at different sites in the URG show contrasting tendencies to dilate or slip.

However, a detailed structural model of the subsurface, provided beforehand based on 2D or 3D seismic data, is in general part of a geothermal exploration concept (e.g.,

Huenges 2010). These data ideally give information on the stress regime and the structural inventory (fault-zone pattern, orientations) at a geothermal site. Subsequent to the drilling operation of a deep wellbore, in-situ magnitudes and orientations of horizontal stresses have to be determined, for example, by borehole breakouts or drilling-induced tensile fractures, respectively (e.g., Zoback 2007).

## **Acknowledgments**

The authors appreciate the support of the German Federal Ministry for Economic Affairs and Energy (BMWi), previously of the German Federal Ministry for the Environment, Nature Conservation and Nuclear Safety (BMU) as part of the Research and Development Project AuGE (Outcrop Analogue Studies in Geothermal Exploration) within the framework of the 5<sup>th</sup> Energy Research Program (FKZ 0325302C). Thanks to the owners of the quarries for the permission to perform the field studies, namely Sämann Stein- und Kieswerke GmbH & Co. KG and HeidelbergCement.

## **References**

- Agosta F, Alessandrini M, Antonellini M, Tondi E, Giorgioni M (2010) From fractures to flow: A field-based quantitative analysis of an outcropping carbonate reservoir. *Tectonophysics* 490: 197-213.
- Anderson EM (1951) The dynamic of faulting and dyke formation with application to Britain. Edinburgh. Oliver and Boyd, Edinburgh.
- Aydin A, Basu A (2005) The Schmidt hammer in rock material characterization. *Engineering Geology* 81: 1–14. <http://dx.doi.org/10.1016/j.enggeo.2005.06.006>.
- Barton CA, Zoback MD, Moos D (1995) Fluid flow along potentially active faults in crystalline rock. *Geology* 23: 683–686.
- Bastesen E, Braathen A (2010) Extensional faults in fine grained carbonates – analysis of fault core lithology and thickness-displacement relationships. *Journal of Structural Geology* 32: 1609-1628.
- Bastesen E, Braathen A, Nøttveit H, Gabrielsen RH, Skar T (2009) Extensional fault cores in micritic carbonate – Case studies from the Gulf of Corinth, Greece. *Journal of Structural Geology* 31: 403-420.
- Bastesen E, Braathen A, Skar T (2013) Comparison of scaling relationships of extensional fault cores in tight carbonate and porous sandstone reservoirs. *Petroleum Geoscience* 19: 385-398.
- Bauer JF, Meier S, Philipp SL (2015) Architecture, fracture system, mechanical properties and permeability structure of a fault zone in Lower Triassic sandstone, Upper Rhine Graben. *Tectonophysics* 647–648: 132–145. doi:10.1016/j.tecto. 2015.02.014.
- Bense VF, Gleeson T, Loveless SE, Bour O, Scibek J (2013) Fault zone hydrogeology. *Earth-Science Reviews* 127: 171-192.
- Brun JP, Wenzel F (1991) Crustal-scale structure of the southern Rhinegraben from ECORS-DEKORP seismic reflection data. *Geology* 19: 758–762. [http://dx.doi.org/10.1130/0091-7613\(1991\)019b0758:CSSOTSN2.3.CO;2](http://dx.doi.org/10.1130/0091-7613(1991)019b0758:CSSOTSN2.3.CO;2).
- Byerlee JD (1978). Friction of Rocks. *Pure Applied Geophysics* 116: 615-626.

- Engesser W, Leiber J (1991) Geologischer Bau und Landschaftsgeschichte. In: Schütz, J. (Ed.), Der Rhein-Neckar-Kreis. Theiss, Stuttgart: 17-49.
- Caine JS, Forster CB (1999) Fault zone architecture and fluid flow: insights from field data and numerical modeling. In: Haneberg WC, Mozley PS, Moore JC, Goodwin LB (Eds.), Faults and Sub-surface Fluid Flow in the Shallow Crust. AGU Geophysical Monograph 113: 101-127.
- Caine JS, Evans JP, Forster CB (1996) Fault zone architecture and permeability structure. *Geology* 24: 1025-1028.
- Chester FM, Logan JM (1986) Implications for mechanical properties of brittle faults from observations of the punchbowl fault zone, California. *Pure and Applied Geophysics* 124: 79-106.
- Childs C, Manzocchi T, Walsh JJ, Bonson CG, Nicol A, Schöpfer MPJ (2009) A geometric model of fault zone and fault rock thickness variations. *Journal of Structural Geology* 31: 117-127.
- Faulkner DR, Jackson CAL, Lunn RJ, Schlische RW, Shipton ZK, Wibberley CAJ, Withjack MO (2010) A review of recent developments concerning the structure, mechanics and fluid flow properties of fault zones. *Journal of Structural Geology* 32: 1557-1575.
- Faulkner DR, Mitchell TM, Jensen E, Cembrano J (2011) Scaling of fault damage zones with displacement and the implications for fault growth processes. *Journal of Geophysical Research* 116: B05403. <http://dx.doi.org/10.1029/2010JB007788>.
- Ferrill DA, Winterle J, Wittmeyer G, Sims D, Colton S, Armstrong A, Morris AP (1999) Stressed rock strains groundwater at Yucca Mountain, Nevada. *GSA Today* 9 (5): 1-8.
- Fossen H, Schultz RA, Shipton ZK, Mair K (2007) Deformation bands in sandstone: a review. *Journal of the Geological Society* 164: 755–769.
- Gross MR, Eyal Y (2007) Throughgoing fractures in layered carbonate rocks. *GSA Bulletin* 119: 1387-1404.
- Gross MR, Fischer MP, Engelder T, Greenfield RJ (1995) Factors controlling joint spacing in interbedded sedimentary rocks: Integrating numerical models with field observations from the Monterey Formation, USA. In: Ameen MS, (Ed.), *Fractography: Fracture topography as a tool in fracture mechanics and stress analysis*. Geological Society Special Publication 92: 215–233.
- Gudmundsson A (2000) Active fault zones and groundwater flow. *Geophysical Research Letters* 27: 2993-2996.
- Gudmundsson A (2011) *Rock Fractures in Geological Processes*. Cambridge University Press, Cambridge, UK.
- Gudmundsson A, Simmenes TH, Larsen B, Philipp SL (2010) Effects of internal structure and local stresses on fracture propagation, deflection, and arrest in fault zones. *Journal of Structural Geology* 32: 1643-1655.
- Heidbach O, Tingay M, Barth A, Reinecker J, Kurfess D, Müller B (2008) The World Stress Map database release 2008, doi:10.1594/GFZ.WSM.Rel2008.
- Heuze FE (1980) Scale effects in the determination of rock mass strength and deformability. *Rock Mechanics* 12: 167-192.

- Hobbs DW (1967) The formation of tension joints in sedimentary rocks: An explanation. *Geological Magazine* 104: 550-556.
- Homuth B, Rümpler G, Deckert H, Kracht M (2014) Seismicity of the northern Upper Rhine Graben – Constraints on the present-day stress field from focal mechanisms. *Tectonophysics* 632: 8-20.
- Huenges E (2010) *Geothermal Energy Systems: Exploration, Development, and Utilization*. Wiley-VCH Verlag GmbH & Co. KGaA, Weinheim, Germany.
- Illies JH (1972) The Rhine Graben Rift System – Plate tectonics and transform faulting. *Geophysical Surveys* 1: 27-60.
- Illies JH (1977) Ancient and recent rifting in the Rhinegraben. *Geologie En Mijnbouw* 56: 329–350.
- ISRM (2007) The complete ISRM suggested methods for rock characterization, testing and monitoring: 1974-2006. In: Ulusay R, Hudson JA (eds): *Suggested Methods Prepared by the Commission on Testing Methods, International Society for Rock Mechanics*. Compilation ISRM Turkish National Group, Ankara, Turkey.
- Jaeger C (1979) *Rock Mechanics and Engineering*. Cambridge University Press, Cambridge, UK.
- Jaeger JC, Cook NGW, Zimmermann RW (2007) *Fundamentals of Rock Mechanics* (4<sup>th</sup> edn.). Blackwell Publishing, Oxford, UK.
- Jeanne P, Guglielmi Y, Lamarche J, Cappa F, Marié L (2012) Architectural characteristics and petrophysical properties evolution of a strike-slip fault zone in a fractured porous carbonate reservoir. *Journal of Structural Geology* 44: 93-109.
- Jodocy M, Stober I (2010) Geologisch-geothermische Tiefenprofile für den baden-württembergischen Teil des nördlichen und mittleren Oberrheingrabens. *Erdöl Erdgas Kohle* 126: 68–76.
- Katz O, Reches Z, Roegiers J-C (2000) Evaluation of mechanical rock properties using a Schmidt Hammer. *International Journal of Rock Mechanics and Mining Sciences* 37: 723–728.
- Larsen B, Grunnaleite I, Gudmundsson A (2010) How fracture systems affect permeability development in shallow-water carbonate rocks: An example from the Gargano Peninsula, Italy. *Journal of Structural Geology* 32: 1212-1230.
- Logan DL (2002) *A First Course in the Finite Element Method*. Brooks/Cole, Pacific Grove, USA.
- Meier S, Bauer JF, Philipp SL (2015) Fault zone characteristics, fracture systems and permeability implications of Middle Triassic Muschelkalk in Southwest Germany. *Journal of Structural Geology* 70: 170-189. doi: 10.1016/j.jsg.2014.12.005.
- Moeck I, Schandelmeier H, Holl HG (2009) The stress regime in a Rotliegend reservoir of the Northeast German Basin. *International Journal of Earth Sciences* 98: 1643-1654.
- Morris A, Ferrill DA, Henderson DB (1996) Slip-tendency analysis and fault reactivation. *Geology* 24 (3): 275–278.
- Mutschler T (2004) Einaxiale Druckversuche an zylindrischen Gesteinsprüfkörpern Neufassung der Empfehlung Nr. 1 des Arbeitskreises “Versuchstechnik Fels” der Deutschen Gesellschaft für Geotechnik e.V.

- Narr W, Suppe J (1991) Joint spacing in sedimentary rocks. *Journal of Structural Geology* 13: 1037-1048.
- Nelson RA (1985) *Geologic Analysis of Naturally Fractured Rocks*. Gulf Publishing Company, Houston, Texas.
- Odling NE, Gillespie P, Bourguin B, Castaing C, Chiles JP, Christensen NP, Fillion E, Genter A, Olsen C, Thrane L, Trice R, Aarseth E, Walsh JJ, Watterson J (1999) Variations in fracture system geometry and their implications for fluid flow in fractured hydrocarbon reservoirs. *Petroleum Geoscience* 5: 373-384
- Paschen H, Oertel D, Grünwald R (2003) Möglichkeiten geothermischer Stromerzeugung in Deutschland. TAB Arbeitsbericht 84.
- Péška P, Zoback MD (1995) Compressive and tensile failure of inclined wellbores and determination of in situ stress and rock strength. *Journal of Geophysical Research* 100 (B7): 12791-12811.
- Philipp SL, Afşar F, Gudmundsson A (2013) Effects of mechanical layering on hydrofracture emplacement and fluid transport in reservoirs. *Frontiers in Earth Science* 1(4): 1-19. doi: 10.3389/feart.2013.00004.
- Plenefisch T, Bonjer K-P (1997) The stress field in the Rhine Graben area inferred from earthquake focal mechanisms and estimation of frictional parameters. *Tectonophysics* 275: 71-97.
- Priest SD (1993) *Discontinuity Analysis for Rock Engineering*. Chapman and Hall, London.
- Ramsay JG, Lisle RJ (2000) *Modern Structural Geology, Volume 3: Applications of Continuum Mechanics in Structural Geology*. Academic Press, London.
- Reyer D, Bauer JF, Philipp SL (2012) Fracture systems in normal fault zones crosscutting sedimentary rocks, Northwest German Basin. *Journal of Structural Geology* 45: 38-51.
- Rotstein Y, Edel J-B, Gabriel G, Boulanger D, Schaming M, Munsch M (2006) Insight into the structure of the Upper Rhine Graben and its basement from a new compilation of Bouguer Gravity. *Tectonophysics* 425: 55-70.
- Rousset D, Bayer R, Guillon D, Edel JB (1993) Structure of the southern Rhine Graben from gravity and reflection seismic data (ECORS-DEKORP program). *Tectonophysics* 221: 135-153.
- Sachpazis CI (1990) Correlating Schmidt hardness with compressive strength and Young's modulus of carbonate rocks. *Bulletin of the International Association of Engineering Geology* 42: 75-83.
- Schumacher ME (2002) Upper Rhine Graben: Role of preexisting structures during rift evolution. *Tectonics* 21, doi: 10.1029/2001TC900022.
- Schweizer V, Kraatz R (1982) Kraichgau und südlicher Odenwald. In: Gwinner, M.P. (Ed.), *Sammlung geologischer Führer* 72. Gebr. Borntraeger, Berlin-Stuttgart.
- Sibson RH (1994) Crustal stress, faulting and fluid flow. In Parnell, J. (Ed.), *Geofluids: Origin, Migration, and Evolution of Fluids in Sedimentary Basins*. Geological Society Special Publications 78: 69-84.
- Stober I, Jodocy M (2009) Eigenschaften geothermischer Nutzhorizonte im baden-württembergischen und französischen Teil des Oberrheingrabens. *Grundwasser* 14(2): 127-137.

- Stober I, Bucher K (2015) Hydraulic and hydrochemical properties of deep sedimentary reservoirs of the Upper Rhine Graben, Europe. *Geofluids* 15: 464-482.
- Tondi E, Antonellini M, Aydin A, Marchegiani L, Cello G (2006) The role of deformation bands, stylolites and sheared stylolites in fault development in carbonate grainstones of Majella Mountain, Italy. *Journal of Structural Geology* 28: 376-391.
- Twiss RJ, Moores EM (1992) *Structural Geology*. W.H. Freeman and Company, New York.
- Viles H, Goudie A, Grab S, Lalley J (2011) The use of the Schmidt Hammer and Equotip for rock hardness assessment in geomorphology and heritage science: a comparative analysis. *Earth Surface Processes and Landforms* 36: 320–333. <http://dx.doi.org/10.1002/esp.2040>.
- Yagiz S (2009) Predicting uniaxial compressive strength, modulus of elasticity and index properties of rocks using the Schmidt hammer. *Bull. Eng. Geol. Environ.* 68: 55–63.
- Ziegler PA (1992) European Cenozoic rift system. *Tectonophysics* 208: 91-111.
- Ziegler PA, Dèzes P (2005) Evolution of the lithosphere in the area of the Rhine Rift System. *International Journal of Earth Science (Geol. Rundschau)* 94: 594-614.
- Zimmermann G, Blöcher G, Reinicke A, Brandt W (2011) Rock specific hydraulic fracturing and matrix acidizing to enhance a geothermal system – concepts and field results. *Tectonophysics* 503: 146-154.
- Zoback MD (2007) *Reservoir Geomechanics*. Cambridge University Press, Cambridge.

#### **4 Architecture, fracture system, mechanical properties and permeability structure of a fault zone in Lower Triassic sandstone, Upper Rhine Graben**

Johanna F. Bauer, Silke Meier, Sonja L. Philipp

Published in *Tectonophysics* 647-648 (2015) 132-145. doi:  
10.1016/j.tecto.2015.02.014

##### **Abstract**

Close to the western Upper Rhine Graben Main Fault, Alsace, a NNE-SSW-striking fault zone, crosscutting porous, thick bedded Lower Triassic Bunter sandstone was investigated in detail, including its architecture, discontinuity system, mechanical rock properties and implications on its permeability structure and fault zone type. Field observations indicate a three-part fault zone structure including core-, transition- and damage zone. The at least 14 m thick fault core is composed of various slip surfaces and deformation bands, which encompass fractured host rock lenses. When connected, host rock lenses may transport fluids through the core zone. Adjacent transition zones are highly fractured in  $R_1$ -orientation, show folded beds and contain  $P_1$ -oriented deformation bands.  $R_1$  and  $P_1$ - fractures are synthetic shear fractures and project with an acute angle (10-20°) towards the fault plane. Only in the damage zone, fault-parallel striking fractures occur. Here, increasing fracture apertures and connectivity may increase the permeability towards the fault core. Mechanical rock properties from 12 rock samples (Young's modulus, uniaxial compressive strength, tensile strength) measured in all the parts of the fault zone, show highest values within the transition zone. In-situ measurements of rebound-hardnesses with a Schmidt-Hammer and analytical approaches, however, indicate that effective Young's moduli are two to sixteen times lower than the Young's moduli of intact rock. Values clearly decrease towards the fault core, even in the transition zone and are in average lower than effective Young's moduli in the damage zone. Although many fault zones in sandstone are sealing structures these field study show, that fault zones in porous sandstone may allow fluid flow.

# 1 Introduction

Fault zones are of particular importance to estimate reservoir permeability because they, depending on their architecture, enhance or impede permeability of the rock (Agosta et al., 2007; Caine et al., 1996; Caine and Forster, 1999; Gudmundsson et al., 2010). In that connection, outcrop analogue studies are useful to analyze the fault zone architecture and thereby increase the predictability of fluid flow behavior through and across fault zones in the corresponding deep reservoir (Chesnaux et al., 2009; Reyer et al., 2012).

Based on outcrop studies of consolidated brittle rocks, Caine et al. (1996) developed a conceptual fault zone model comprising core zone and surrounding damage zones with different properties and thicknesses. The fault core accommodates most of the strain and displacement of the fault zone and is formed by gouge and cataclasite, which cause a low permeability. The damage zone consists of minor faults and an increased fracture density (as fracture count per meter) compared to the host rock and therefore exhibits an enhanced permeability. Fracture induced permeability depends mainly on fracture aperture and connectivity. The fracture connectivity itself depends on fracture lengths, orientations and densities (De Dreuzy et al., 2001; De Marsily, 1986; Hestir and Long, 1990). In the fault zone model after Caine et al. (1996), the ratio between damage zone and total fault zone thickness contributes to the overall fluid flow behavior of the entire fault zone.

Although this conceptual model is widely accepted, it does not apply to all rock types, in particular not to porous sandstone (Caine and Minor, 2009; Heynekamp et al., 1999; Rawling and Goodwin 2006; Rawling et al., 2001). Therefore, two additional fault zone models have been proposed for different rock types (Fig. 1).

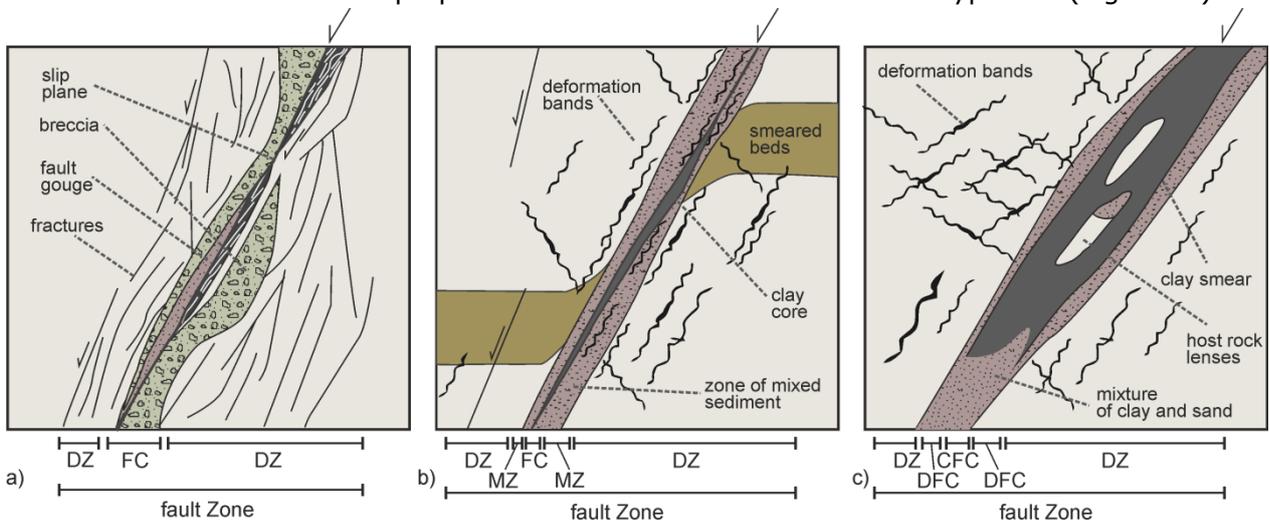


Fig. 1. Different architectures and structural elements of fault zones in a) crystalline rocks with fault core (FC) composed of breccia and fault gouge and damage zone (DZ) with increased fracture density (Caine et al., 1996), b) in porous sandstones with fault core (FC) composed of clay and a damage zone (DZ) with deformation bands. As a third fault zone part mixed zones (MZ) with deformed and mixed sediments where established (Heynekamp et al., 1999; Rawling and Goodwin, 2006) and in c) in un lithified to poorly lithified sediments with structured fault core into a central part (CFC) with clay membranes and host rock lenses and the distal part (DFC) composed of a mixture of sand and clay or clay lenses in a matrix of sand. The damage zone includes clusters of or single deformation bands. (Figure 1a, b modified after Loveless et al., 2011; Fig. 1c modified after Clausen et al., 2003).

They also separate a central core zone and surrounding damage zones with different mechanical, hydrological and structural characteristics. For porous rocks Heynekamp et al. (1999) found that there are mixed zones between the core and damage zone (Fig. 1b). In this model the damage zone includes deformation bands or zones of deformation

bands. The main impact of deformation bands, referred as zones with grain deformation, is the porosity reduction and therefore they also commonly involve a permeability reduction (Antonellini and Aydin, 1994; Rawling et al., 2001). The adjacent mixed zones are composed of deformed sediments, or zones with destroyed bedding. Within the mixed zone host rock lenses (elongated rock bodies originating from the damage zones) are common. In the center a clayey core occurs and is often reported as a low permeability zone (Caine and Minor, 2009; Heynekamp et al., 1999). In contrast, the fault zone model developed by Clausen et al. (2003) for unconsolidated to poorly consolidated sediments, divides the core zone into a central and a distal part instead of mixed zones (Fig. 1c). The central part is composed of host rock lenses, enveloped by clay membranes, and is surrounded by the distal fault core: a mixture of sand and clay. The damage zone also includes mostly deformation bands. In the latter two fault zone models in porous sandstone permeability decreases because of fault-related processes such as cataclasis or the formation of deformation bands rather than fractures. Thus, fault zones in clastic reservoirs may have a high sealing capacity (Antonellini and Aydin, 1994). In cases, however, where highly permeable beds juxtapose across the fault zone strike, the formation of host rock lenses in the core zone may allow fluid flow across the reservoir (Lindanger et al., 2007). Fault zone architecture does not only vary due to different lithology, but also along fault zone strike, down dip and time (e.g., Faulkner et al., 2010).

Beside the different effects of fractures and deformation bands on rock permeability they have contrary effects on effective rock mechanical properties. While fractures reduce the effective mechanical rock properties, such as uniaxial compressive strength (Kemeny and Cook, 1986), Young's modulus (Priest, 1993) or the brittle strain of a fault zone (Schultz, 2003) and increase permeability of the rock mass, mainly compaction deformation bands reduce the permeability and mechanical rock properties increase within the band (Fossen et al., 2007). These differences in the mechanical evolution in turn modify the mode of failure within the fault zone and therefore the permeability structure (Aydin and Johnson, 1978; Fossen et al., 2007). Thus, good constraints on the effective material properties are needed to investigate and to model the permeability structure of the faulted lithology (Loveless et al., 2011; Renshaw, 1996).

In this paper we present a detailed study of one outcrop exposing a fault zone at the western graben shoulder of the Upper Rhine Graben near Cleebourg (France). The study has two main objectives: First, we present the architecture of the fault zone. We examine, whether the described fault zone models (cf., Fig. 1) can be used and are focused on a highly deformed transition zone between the core and the damage zone. In particular, we discuss the permeability structure of the fault zone, including its fracture system within the different parts of the fault zone. Second, we present results of mechanical laboratory measurements of 12 intact outcrop rock samples. We examine the effects of fractures on the effective mechanical properties using the measured fracture data and mechanical rock properties in an analytical approach (Priest, 1993). To compliment these calculations, we also estimate effective mechanical properties with in-situ Schmidt-Hammer measurements.

## **2 Geological setting**

The European Cenozoic Rift System is a system of NNE-SSW- to N-S-trending grabens (Fig. 2a). Most prominent part of the system is the Upper Rhine Graben that extends about 300 km from the Rhenish Massiv (Frankfurt) in the north to the Jura Mountains (near Basel) in the south (Fig. 2b).

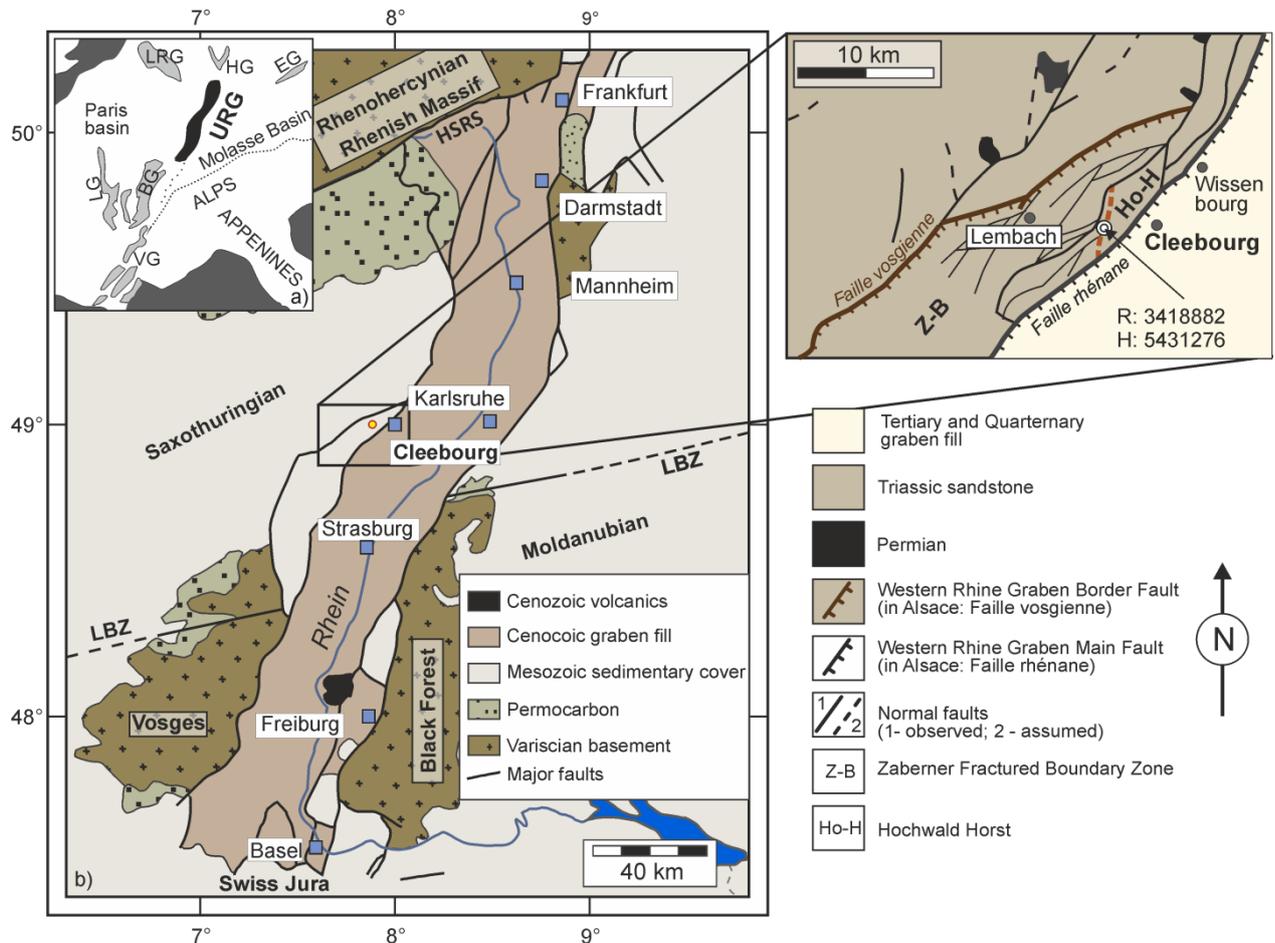


Fig. 2. a) The European Cenocoic Rift System with N-S- to NNE-SSW-oriented graben systems (light grey; LRG: Lower Rhine graben; HG: Hessian grabens; EG: Eger graben; BG: Bresse graben; LG: Limagne graben; VG: Vistrenque graben); in black the study area; URG: Upper Rhine Graben simplified after Ziegler and Dèzes, 2007). b) Simplified tectonic map of the Upper Rhine Graben. Black lines represent the main fault systems with Variscan terrain boundaries (LBZ, Lalaye-Lubine-Baden-Baden fault; HSRS, South Hunsrück-Taunus border fault (modified after Ziegler and Dezes (2007)). c) Zoom into the tectonic details of the studied outcrop area (white dot) at the Zaberner Fractured Boundary Zone with the western Rhine Graben Border Fault (in Alsace: Faille vosgienne) in the west and the Rhine Graben Main Fault (in Alsace: Faille rhénane) in the east (modified after Stapf, 1996, 1988). The GPS-coordinates give the location of the outcrop and the red dashed line indicates the studied fault zone.

Thereby the Upper Rhine Graben crosses the tectonostratigraphic units of the Variscan internides (Illies, 1977; Schumacher, 2002; Ziegler, 1992). Traditionally, the graben has been geomorphologically divided into a southern, central and a northern part, because the section between Strasbourg and Karlsruhe has more NE-SW-orientation (Schumacher, 2002). Its initiation started during the middle Eocene to early Miocene as an extensional rift valley in consequence of orogenic activity in the Alps and Pyrenees (Illies and Greiner, 1978; Ziegler, 1992; Ziegler and Dèzes, 2006). First climax of subsidence took place from Eocene to Early Oligocene and was interrupted during Miocene to Lower Pliocene and started again in Pliocene until recent time (Illies, 1977). The development of the Upper Rhine Graben was partly controlled by mantle diapirism, different stress fields and structures inherited from Variscan orogeny (Bergerat, 1987; Edel et al., 2007; Schumacher, 2002; Ziegler and Cloetingh, 2004). The evolution of the Upper Rhine Graben included four different stress regimes from its initiation until today. In the late Eocene rifting episode the Upper Rhine Graben was affected by an N-S-oriented compressional regime, alternated by an E-W-oriented extension in Oligocene and renewed compression with NE-SW-orientation during Early Eocene. The most significant change in the stress field took place in Miocene at which the maximum stress

field shifts to a horizontal position with a new NW-SE- to NNW-SSE-orientation (Bergerat, 1987; Schumacher, 2002). Under these conditions the Upper Rhine Graben is characterized by a continental transform zone with an N-S-trending sinistral motion (Illies and Greiner, 1978; Schumacher, 2002).

The Upper Rhine Graben is limited by prominent eastern and western boundary fault systems (Fig. 2b), which separate the sediment-filled graben and the uplifted graben shoulders. Along large parts of its boundary the Upper Rhine Graben has two sets of dominant fault zones (Brun and Wenzel, 1991; Schumacher, 2002).

The studied outcrop at Cleebourg is located between those nearly NE-SW-striking distinct fault zones at the Zaberner Fractured Boundary Zone, namely the western Rhine Graben Border Fault (in Alsace: Faille vosgienne) in the west and the western Rhine Graben Main Fault (in Alsace: Faille rhénane) in the east (Eisbacher and Fielitz, 2010). The 10 km thick Zaberner Fractured Boundary Zone exposes roughly 1 km thick Triassic sediments. The NE-SW-striking faulted blocks are separated and offset by N- to NNE-striking faults of younger ages (Fig. 2c) (Eisbacher and Fielitz, 2010). The studied NNE-SSW-striking fault zone is located in the Hochwald-Horst, a flexure with dip of around 30° in direction to the near western Upper Rhine Graben Main Fault (in Alsace: Faille rhénane; Eisbacher and Fielitz, 2010). The outcrop is located close to the western graben margin. In this area the Upper Rhine Graben Main Fault has a normal offset of 1.2 km (Eisbacher and Fielitz, 2010).

### **3 Outcrop characterization and methodology**

The outcrop is located in Alsace (north-east France; cf., section 2), exposing porous, thick bedded Trifels sandstones belonging to the Triassic Middle Bunter (Eisbacher and Fielitz, 2010; Ménillet et al. 1989). The exposure allows a 3D-view, including quarry floors, on the northwestern fault block and core zone of one fault zone (Fig. 3). Fault zone type and displacement are difficult to obtain and discussed in detail below.

Fault zone characteristics and fracture system parameters were examined by using cross section and window survey measurements. The maximum length of the cross sections is limited by outcrop size. The following fracture system parameters were recorded: fracture density, orientation (strike direction and dip angle), aperture, length, mineralization and connectivity. The length is measured linearly between fracture ends. If either one or both fracture tips extend beyond the outcrop we measured the fracture's minimum length. The aperture is measured perpendicular to fracture walls at its maximum value. As an indication for fracture connectivity and thus for a potential hydraulically active fracture network we measured fracture terminations in three different categories: fracture tips free, one tip connected, and both tips connected. Paleo-fluid transport is derived by fracture mineralization in five different categories: open, colored or discolored, incrustation, clay filled and mineralized.

Within the fault core zone deformation bands, slip surfaces (layers composed of fault gouge with some displacement), host rock lenses and lithological content were reported. To avoid cross section orientation bias recording fractures with parallel strike to one surface, cross sections were placed parallel and perpendicular to the strike of the fault zone (cf., Caine and Tomasiak, 2003; Terzaghi, 1965). Cross section measurements perpendicular to the fault plane started at the fault core margin. To get three-dimensional data of the fracture sets and to analyze the variations in horizontal connectivity, window survey measurements on four locations on the quarry floors with different distances to the main fault zone were used.

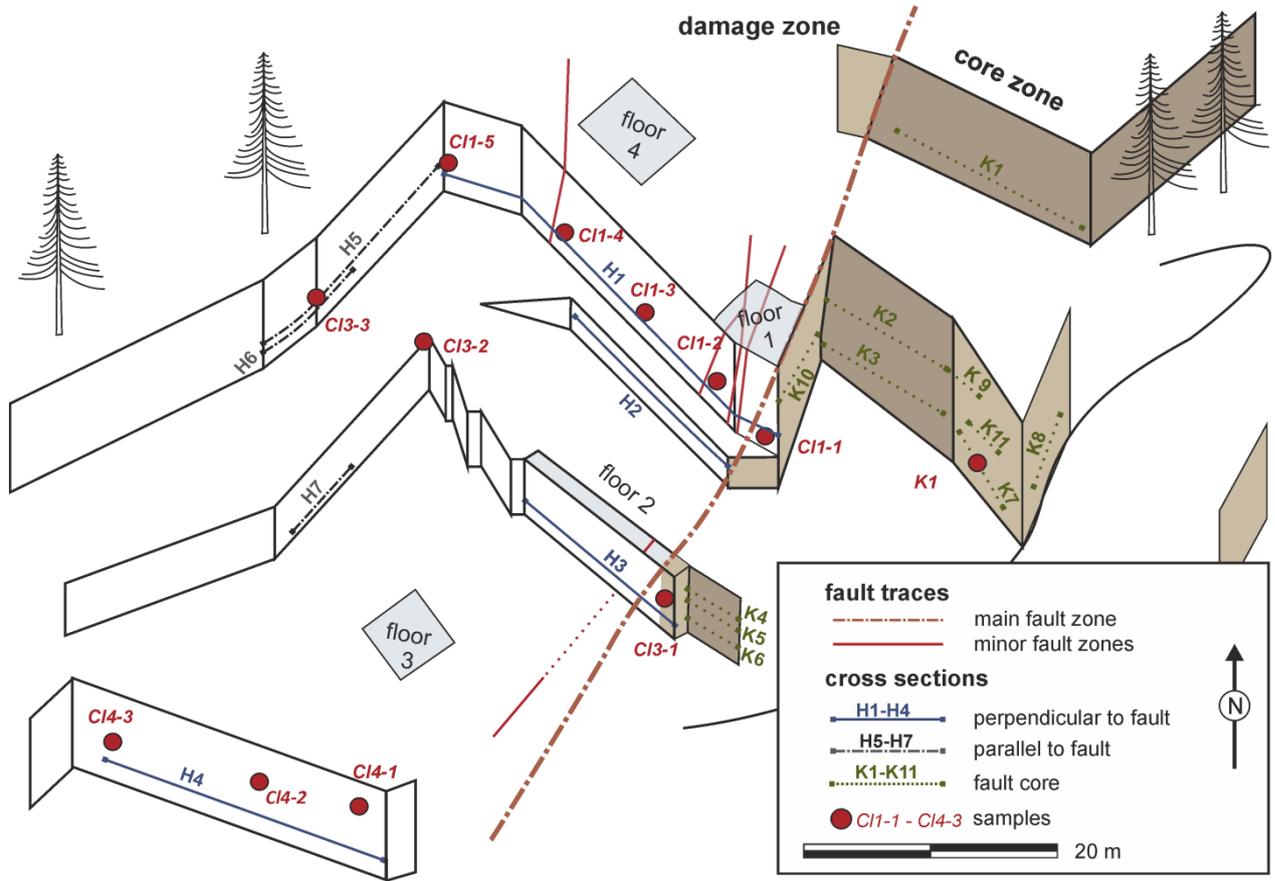


Fig. 3. Schematic 3D-view of the studied outcrop with marked cross sections, as well as the four recorded quarry floors (rectangles) on different outcrop levels and distances to the main fault zone and sample points C11-1 to C14-3 and K1 for mechanical laboratory measurements (red dots).

To characterize the mechanical effects of fractures on rock mass properties, laboratory experiments, analytical approaches, and in-situ experiments were performed. In the different parts of the fault zone cylindrical rock samples were drilled out (Fig. 3) with a coring-machine to enforce compression tests (Mutschler, 2004) and Brazilian tests (ISRM 1981; diametral compressive strength test) to investigate the uniaxial compressive strength UCS [MPa], static Young's modulus  $E_i$  [GPa] and indirect tensile strength  $T_o$  [MPa] of unfractured rock mass. Where possible, the specimens were taken parallel and perpendicular to bedding or parallel and across fault zone strike, respectively. Differing from Fairhurst and Hudson (1999) specimen diameters for  $E_i$  and  $T_o$  measurements was 35 mm and for UCS 45 mm. The specimen ends are flat to  $\pm 0.05$  mm. In advance of compression tests we determined the specimen's volumes and weights to calculate their bulk densities  $\rho_0$  [kg/m<sup>3</sup>].

Since fractures reduce the stiffness of in-situ intact rock masses we use an inverse correlation of the number of discontinuities to calculate effective Young's moduli  $E_e$  to get the distribution of mechanical rock properties along fault zone parts after Priest (1993; Eq. 1).

$$E_e = \frac{\sigma_n L}{\Delta L} = \left( \frac{1}{E_i} + \frac{1}{\bar{s} k_n} \right)^{-1} \quad (\text{Eq. 1})$$

When a fractured rock cube with a length  $L$  [m] gets compressed normal to fracture plane with a normal stress  $\sigma_n$  [MPa] the change in length  $\Delta L$  [m] (or strain) depends on the Young's modulus  $E_i$  [GPa] of the intact rock mass, on the fracture normal stiffness  $k_n$  [MPa/m] (normal stress per unit closure of the fracture) and  $\bar{s}$  [m] the average,

inverse discontinuity density. The first part of Eq. 1 corresponds to Hooke's Law, but includes the strain through fracture closure (Gudmundsson, 2011).

In the following calculation of  $E_e$  perpendicular and parallel to the fault plane, with the second part of Eq. (2), parameters  $E_i$  and  $\bar{\epsilon}$  were used as obtained in the field at different positions at the cross sections. For  $k_{nr}$ , which is very difficult to obtain in the field (Zangerl et al., 2008), published data and empirical relations to UCS were used (e.g., Chang et al., 2006; Reyer & Philipp, 2014).

An L-Type Schmidt-Hammer (impact energy: 0.735 Nm, USC range: 18-70 MPa) was used to estimate the effective uniaxial compressive strength and Young's modulus along the cross sections as well as at the rock sample positions before drilling (Aydin and Basu, 2005; Deere and Miller, 1966; Torabi et al., 2010; Viles et al., 2010; Yagiz, 2009). In a Schmidt-Hammer, a hammer released by a spring, indirectly impacts against the rock surface through a plunger. Part of the energy released by the spring is consumed by plastic deformation on the rock surface. The remaining elastic energy determines the rebound distance of the hammer. The travelled distance corresponds to the rebound-hardness  $R$  [-], expressed as a dimensionless scale on the device. Thereby, higher rebound-distances indicate a higher stiffness of the tested rock mass. Each measured rebound-hardness ( $R$ ) is a mean value determined from 10 impacts, applied at different points spaced at minimum 20 mm apart from each other. For mean value calculations the minimal and maximal  $R$ -value remains unaccounted to eliminate outliers. That instrument allows a detailed map of mechanical property variations, but no detailed absolute values, within the different fault zone parts (Viles et al., 2010). Correlations between  $R$  with  $E$  and USC are commonly used; see Yagiz (2009) for a summary. Included constants in those relationships, however, mainly depend on lithological characteristics, making it difficult to find one relationship for all rock types. Therefore, we use the  $R$ -value only for rough estimations on the effective mechanical property variations.

#### 4 Fault zone architecture

In the damage zone of the NNE-SSW-striking fault zone four normal faults (FZ1-4) with displacements of 2 to 6 cm and one oblique slip fault are formed (FZ5, Fig. 4a, c, d).

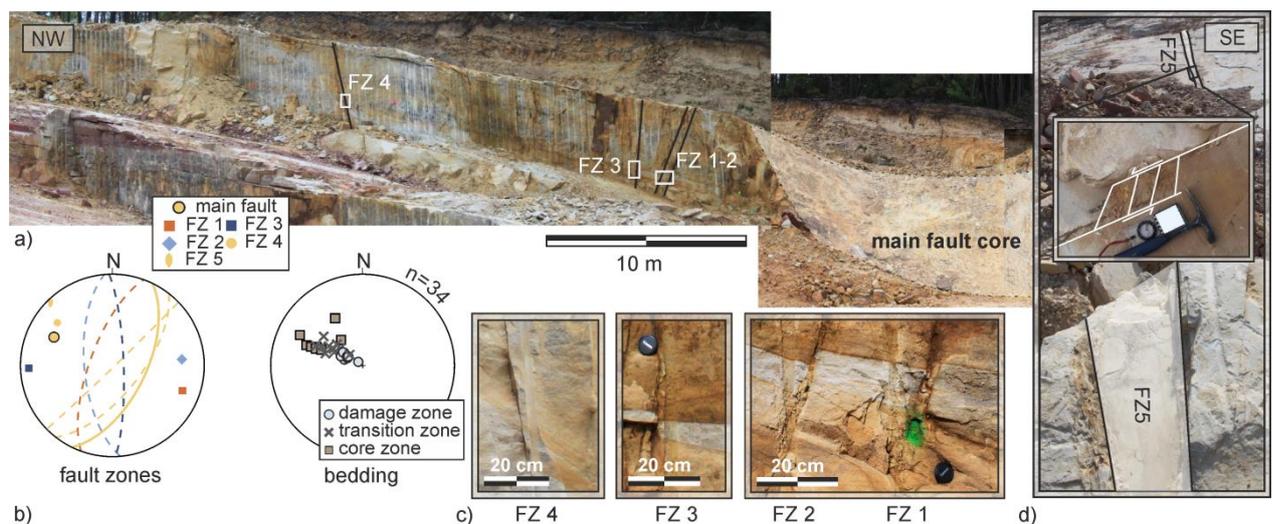


Fig. 4. a) Photograph of the main fault zone with highlighted fault core and minor fault zone locations (FZ1-4, cross section H1). b) Fault zone orientations of the minor faults (dashed lines) and the main fault zone strike (bold line) as well as the dip of bedding (equal area, lower hemisphere). c) Detailed photographs of the minor normal fault zones (FZ1-4) in the damage zone. d) Top view on oblique-slip fault FZ5 at quarry floor 2 (cf., Fig. 3).

The displacement and the fault zone type of the main fault zone are unknown because only the northwestern fault block and no slickensides are exposed and therefore part of the discussion. The bedding dips 15-65° towards the southeast, gets steeper, and is sometimes folded towards the fault core (Fig. 4b). The main fault zone and all minor faults strike sub-parallel to the main fault trends (N-S to NNE-SSW and NE-SW) of the Zaberner Fractured Boundary zone. Two minor faults (FZ1, 2) are antithetic and three (FZ3-5) synthetic with respect to the observed main fault zone strike within this outcrop (Figs. 2, 4b).

#### 4.1 Core zone

The partly exposed fault core shows an internally segregated zone with a minimum thickness of 14 m. Most common features are slip surfaces (sometimes transport water) and deformation bands, which encompass host rock lenses. Also common are Fe-Mn-concretions and sand pebbles or patchy clay (Fig. 5). Most of these slip surfaces strike parallel to the main fault zone, others in N-S-direction, are unpolished and not silicified but oftentimes iron-stained (Fig. 5a). They can be detected easily, due to separation of lithological distinct components on each side. They merge with each other but are most discontinuous. Lower strained host rock lenses are fractured and range from consolidated or unconsolidated material composed of clay, silt or sand.

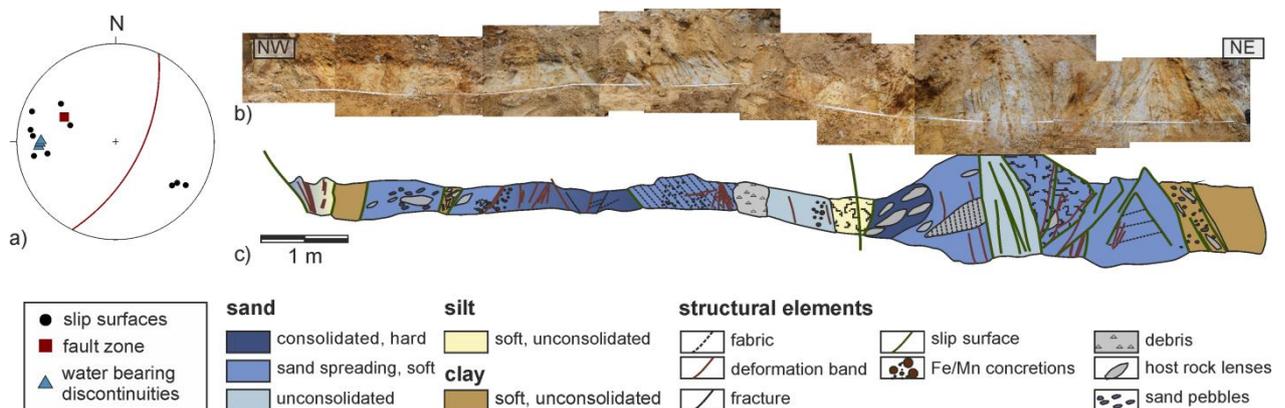


Fig. 5. a) Orientations of slip surfaces (black dots), main fault zone (red rectangle) and discontinuities which transport water (blue triangle) within the core zone (lower hemisphere, equal area) b) Photograph of the central fault core at cross section K3. c) Sketch of the architecture of the central core zone.

#### 4.2 Transition zone

According to Heynekamp et al. (1999), there is a transition zone between the fault core and the damage zone with different deformation characteristics. This zone can be characterized either as distal fault core (Fig. 6a, b) (Clausen et al., 2003) or as mixed zone (Fig. 6c, d) (Heynekamp et al., 1999). In both cases, this fault zone part combines characteristics from the central fault core and the damage zone. The transition zone includes mostly fractures and to minor degree deformation bands, which separate small host rock lenses, bedding is more continuous and the rock is more compact than in the fault core. In some cases there are small clay lenses in a sandy matrix as well as beds that can be traced from the damage zone into the transition zone. At cross section K4 to K6 occurs a clear slip surface between the damage zone and the aforementioned transition zone, relating this part to a unit of the fault core (distal fault core), but at cross sections K1 to K3 a clear slip surface separates the central fault core from this transition zone, making it comparable to the mixed zones after Heynekamp et al. (1999).

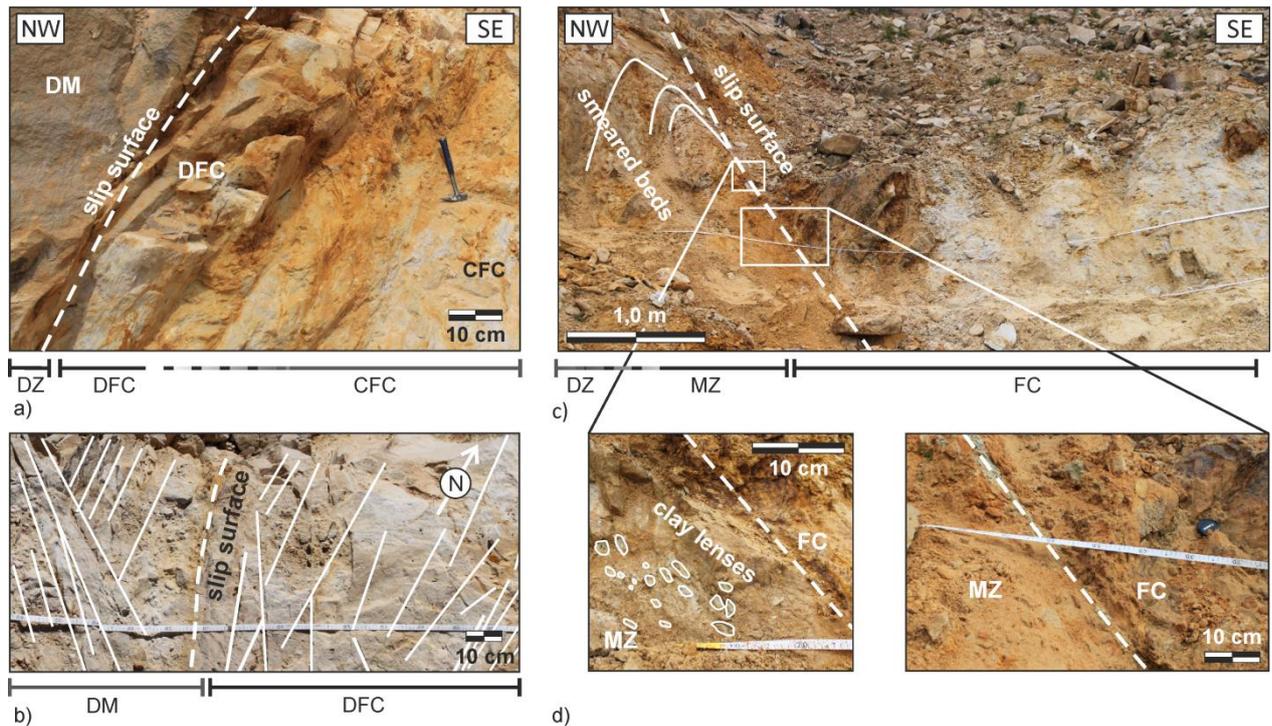


Fig. 6. a) Transition between the damage zone and the core zone at cross sections K4-K6. A clear slip surface between the damage zone (DZ) and the transition zone causes a distal fault core (DFC) with fault parallel host rock lenses and high fracture density. b) Top view on quarry floor 3 with the transition from the damage zone to distal fault core apparent through the reduced fracture density and their change in strike. c) Transition between the damage zone and the core zone at cross section K2. A clear slip surface between the transition zone and the core zone, characterizes this part as mixed zone (MZ). The mixed zone contains smeared beds, clay lenses, deformation bands as well as a high fracture density. d) Detailed photographs of the transition zone at cross section K2.

### 4.3 Damage zone

The damage zone is less affected by deformation than the core and transition zone. Most common structural elements in the damage zone are fractures. Deformation bands, common features in porous rocks or sands (Bruhn et al., 1994) are absent or invisible in this porous sandstone. Further, the damage zone also includes five minor fault zones. The lateral extension of the damage zone is vague and part of the discussion.

## 5 Fracture system parameters

### 5.1 Orientation of structural features

The most common discontinuities in the damage zone are fractures. Fracture orientations are plotted in symmetrical rose diagrams as well as normals to fracture planes in stereographic projection to get statistical fracture orientation data from the different parts of the fault zone (Fig. 7). In general four main different orientations occur, namely: NNE-SSW, NE-SW, E-W and N-S.

The main fracture set of the damage zone has a fault parallel (NNE-SSW) orientation with equal quantity of synthetic and antithetic fractures. Antithetic fractures show a wider scatter and become less frequent with larger distance to the core zone, whereas synthetic fractures are uniformly distributed in the northwestern faulted block (Fig. 8b).

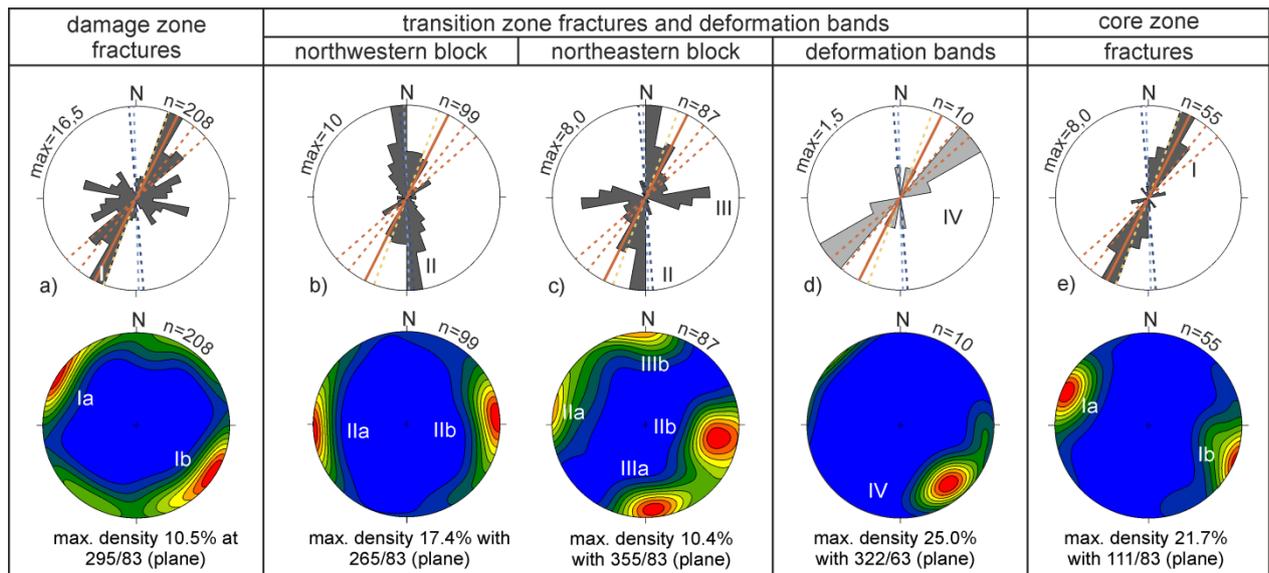


Fig. 7. Fracture and deformation band populations (marked with roman numerals: I-IV) in the different fault zone parts shown in symmetrical rose-diagrams and as contour plots of poles to fracture planes (equal area, lower hemisphere). The main fault strike is marked by a bold line and minor faults by dashed lines. a) NNE-SSW-striking fractures in the damage zone (population I). b) N-S-striking fractures in the transition zone of the northwestern faulted block (population II). c) N-S- and E-W-striking fractures within the transition zone of the northeastern faulted block (population II and III). d) NE-SW-striking deformation bands in the transition zones (population IV). e) NNE-SSW-striking fractures in host rock lenses in the core zone (population I). Fractures in host rock lenses (e) and damage zone fractures (a) have a fault parallel strike, whereby fractures in the transition zones (b, c) strike N-S and deformation bands (d) parallel to regional structures in NE-SW-direction.

In contrast to the fracture orientation in the damage zone reflecting the fault orientation, the main fracture set in the transition zones strikes N-S and forming a 20-30° angle to the main fault zone. Additionally there are E-W-striking fractures in the northeastern transition zone (Fig. 7a, b, c). Beside fractures, deformation bands are common in the transition zones and core zone. Most of the deformation bands in the transition zones strike parallel to the regional structures in NE-SW and consequently form a 26° angle to the main fault plane (Fig. 7d). Fractures in host rock lenses of the central core zone strike, similar to the uppermost slip surfaces, mostly parallel and synthetic to the main fault zone in NNE-SSW-direction (Fig. 7e).

## 5.2 Fracture density

To obtain the fracture density distribution across and along the fault we measured the density perpendicular and parallel to the main fault at cross sections and on quarry floors. The data of window surveys show an increasing fracture density towards the fault core. The density of parallel striking fractures is much higher compared with perpendicular striking fractures, but the relative enhancement of perpendicular striking fractures towards the fault core is 1.5 times higher.

Data from horizontal cross sections show a relation similar to measurements from window surveys, where fracture densities increase towards the major fault plane and at contacts to minor faults as well (Fig. 8a). The highest fracture density occurs in the northwestern transition zone, including mostly N-S-striking fractures (Fig. 8a, c). Fault parallel fractures are nearly absent in this transition zone and increase only in the damage zone (Fig. 8b, c).

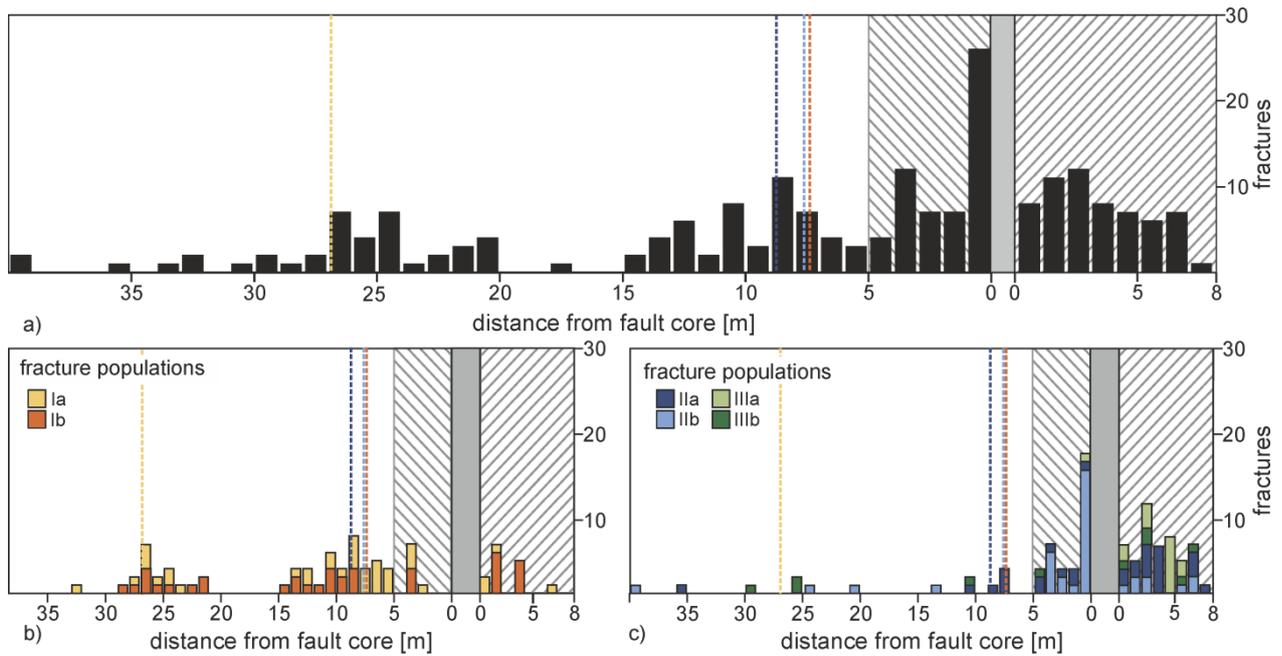


Fig. 8. Histograms showing the fracture density distribution perpendicular to the fault plane at cross section H1. Lines indicate the minor fault zone location, grey bars the fault core position and the dashed area the transition zone between the fault core and the damage zone. a) Fracture density distribution for all fractures. b) Fracture density distribution of fracture population I (strike-direction: NNE-SSW). Fracture population Ia is synthetic (dip ESE), Ib is antithetic to the fault (dip WNW). c) Fracture density distribution of fracture population II and III (strike direction: N-S and E-W). Fracture population IIa dip east, IIb dip west, IIIa dip N and IIIb in S-direction.

Within the transition zone at the northeastern faulted block E-W- and fault-parallel fractures are more frequent than in the northwestern transition zone (Fig. 8b, c), but this zone is still dominated by N-S-striking fractures.

### 5.3 Fracture length and aperture

Fracture length and aperture data were plotted against the distance from fault core and strike direction. Because fracture lengths and apertures are specific for different fracture populations, they are separated according to orientation data (Fig. 9). In general, longer fractures have higher fracture apertures. The ratio of aperture ( $b$ ) and length ( $l$ ) is defined as the fracture aspect ratio ( $b/l$ ). It follows that the shorter the fracture in relation to its aperture the higher is its aspect ratio.

The widest apertures occur in the transition zone of the northwestern faulted block and decline with increasing distance from the core zone and increase again around the minor faults. However, in the damage zone ESE-dipping fractures (synthetic to the main fault zone) show the highest and WNW-dipping (antithetic fractures) the lowest values of apertures (Fig. 9a, b).

The fracture length distributions show contrary relations. The lowest values occur in the distal zone and show an abrupt increase in the damage zone, where the longest fractures are mostly antithetic to the main fault zone (Fig. 9c, d).

In contrast to the cross sections, fracture apertures measured on the quarry floors get wider with increasing distance from the fault core. Comparable is, that NNE-SSW striking fractures (fracture population I) are longer compared with other orientations. However, fracture lengths do not change clearly with increasing distance from fault core, neither perpendicular nor parallel to the main fault zone.

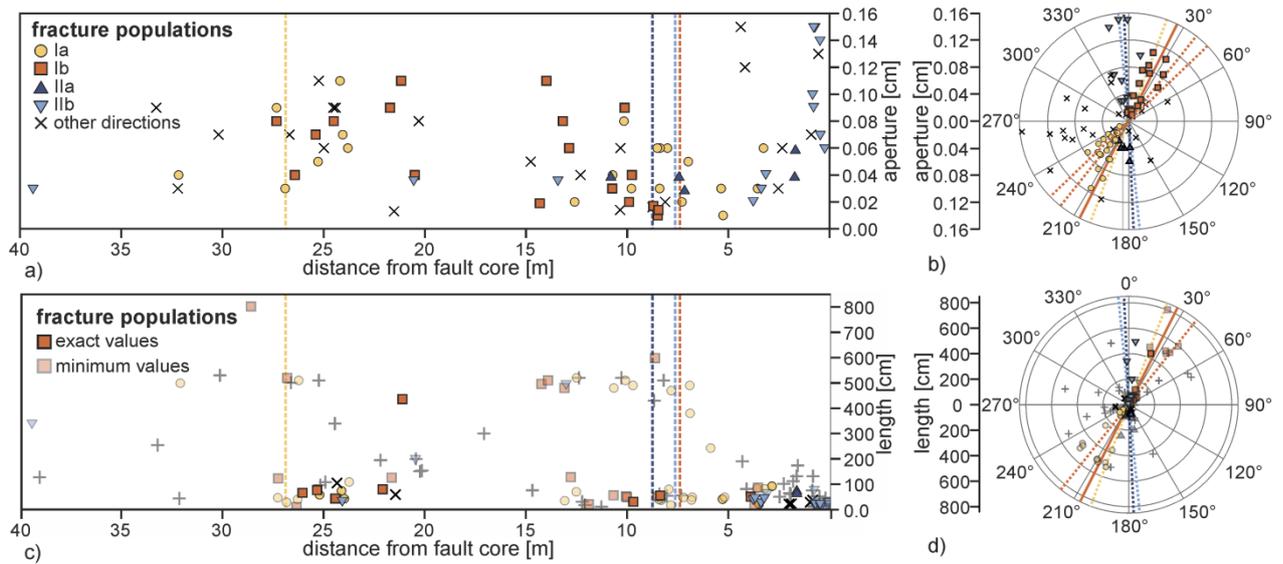


Fig. 9. Diagrams showing the variations of fracture aperture [mm] and fracture length [m]. a) Apertures against distance from fault core separated after their dip direction (Ia: dip ESE, Ib: dip WNW, IIa: dip E and IIb: dip S). Lines indicate the minor fault zone positions. b) Apertures in a circular diagram versus strike direction. c) Fracture length against distance from fault core with marked minimum length values. Lines indicate the minor fault zone positions. d) length in a circular diagram versus strike direction.

The relation between fracture length and fracture aperture shows that they are negatively correlated within the outcrop (Fig. 10). In most cases fractures with high apertures have short lengths.

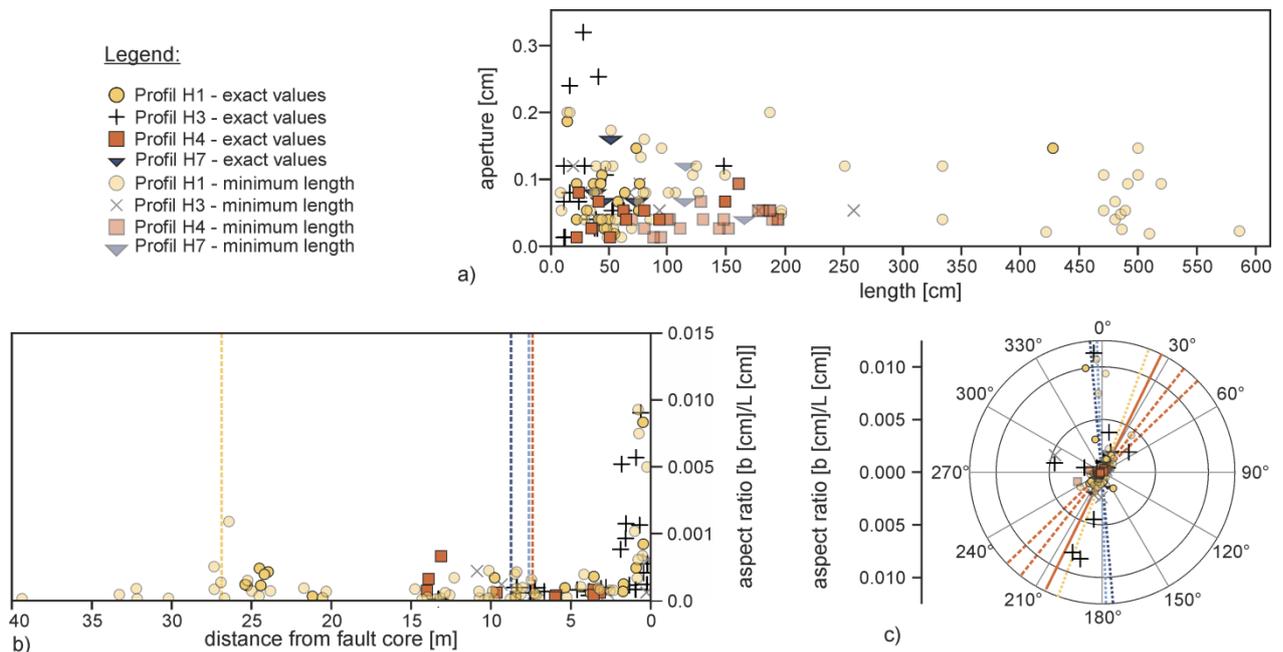


Fig. 10. a) Relation between fracture length (cm) and aperture (cm). b) The aspect ratio (aperture [cm] /length [cm]) with increasing distance from fault core at cross section H1. A high aspect ratio indicates a short fracture in relation to its aperture.

#### 5.4 Fracture connectivity and mineralization

The fracture connectivity in the outcrop is low with 51% unconnected and just 14% fractures connected at both tips. In general, the connectivity increases with proximity to the core zone. In detail, 86% of all fractures connected at both tips and 49% of fractures connected at one tip are located in the transition zones and get less frequent with increasing distance from the fault core (Fig. 11a, b). The highest fracture connectivity is

given for N-S-striking fractures and the lowest for fractures striking sub-parallel to the main fault plane.

Most fractures are open (71%) and only 7% are mineralized. 95% of all mineralized fractures are located in the transition zones (Fig. 11c, d).

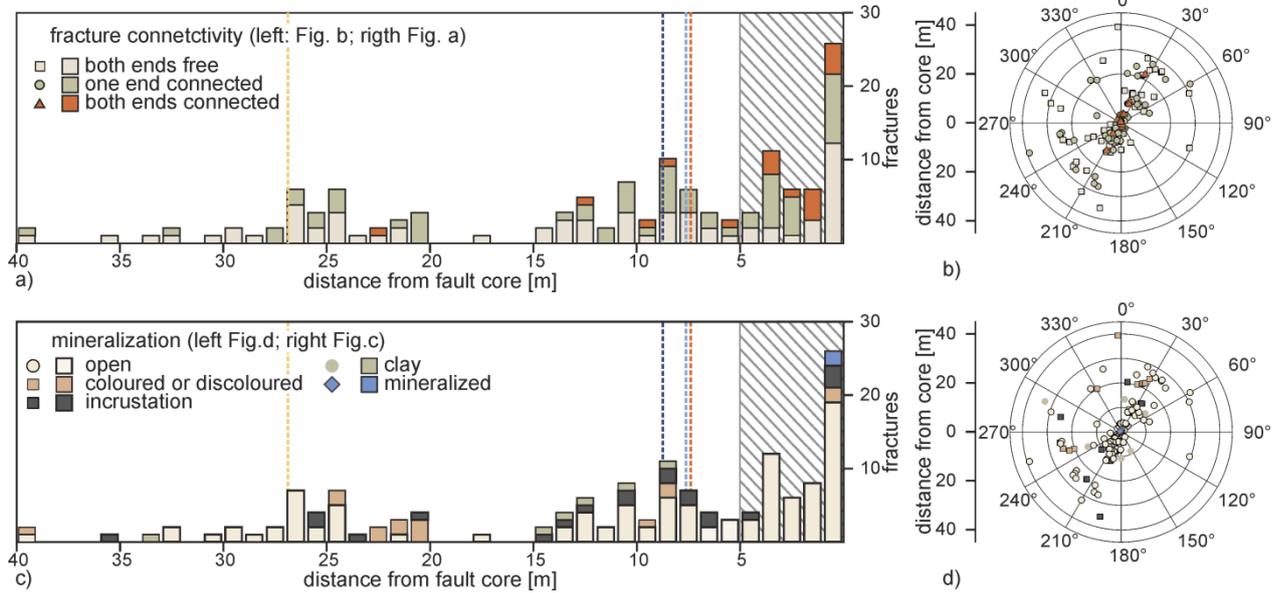


Fig. 11. Histograms show the variations of fracture connectivity (a) and fracture mineralization (b) across the fault zone at cross section H1. Lines indicate the minor fault zone positions, the dashed area the transition zone. Circular diagrams showing the fracture connectivity (c) and mineralization (d) versus strike direction and distance from core zone of all fractures measured in the outcrop.

## 6 Mechanical rock properties

### 6.1 Laboratory measurements

The measured mechanical rock properties are listed in table 1. For the 12 measured rock samples the uniaxial compressive strength (UCS) values range between 33.4 MPa and 60.8 MPa within the damage zone, 53.4 MPa and 66.6 MPa within the transition zone and the one sample taken in the core zone has a UCS of 15.0 MPa parallel to bedding. Values measured perpendicular to bedding range between 36.7 MPa and 60.1 MPa inside the damage zone and between 48.6 MPa and 73.9 MPa inside the transition zone.

Young's moduli ( $E_i$ ) parallel to bedding range between 7.6 GPa and 17.0 GPa within the damage zone, 8.2 GPa and 15.6 GPa within the transition zone and the value taken in the core zone is 4.2 GPa. The values perpendicular to bedding are 9.2 GPa and 18.4 GPa within the damage zone, 9.5 GPa and 18.6 GPa inside the transition zone.

Indirect tensile strength ( $T_0$ ) measurements amount about 1.7 MPa to 3.5 MPa inside the damage zone and within the transition zone about 2.3 MPa and 2.8 MPa, the core zone sample gives 0.6 MPa parallel to bedding. The values perpendicular to bedding range between 1.2 MPa and 2.0 MPa within the damage zone and between 1.7 MPa and 2.7 MPa within the transition zone. The core sample amounts to 0.6 MPa.

Table 1. Summarized mean values of the mechanical rock properties: UCS, E<sub>i</sub> and T<sub>0</sub> parallel and perpendicular to bedding. Grey marked samples are located in the transition zone, K1 in the core zone. All other samples are located in the damage zone.

Sample	parallel to bedding			perpendicular to bedding		
	UCS [MPa]	E <sub>i</sub> [GPa]	To [MPa]	UCS [MPa]	E <sub>i</sub> [GPa]	To [MPa]
CI 1-1	53.4 ±0.4	8.2 ±2.2	2.3 ±0.6	48.6 ±6.2	9.5 ±1.1	1.7 ±0.4
CI 1-2	33.4 ±1.5	8.6 ±1.0	1.9 ±0.1	40.5 ±2.8	11.4 ±1.1	1.7 ±0.3
CI 1-3	33.4 ±6.1	10.5 ±2.0	1.7 ±0.4	36.7 ±7.6	9.3 ±1.2	1.7 ±0.3
CI 1-4	46.7 ±6.7	11.9 ±4.3	2.6 ±0.7			2.0 ±0.1
CI 1-5	36.7 ±6.2	7.6 ±1.0	2.2 ±0.3	44.5 ±1.1	14.5 ±3.3	1.2 ±0.3
CI 3-1	61.1 ±1.0	13.6 ±1.4	2.5 ±0.3	58.7 ±0.8	14.7 ±1.1	2.5 ±0.4
CI 3-2	40.5 ±6.8	8.9 ±2.9	3.0 ±0.4	49.6 ±2.2	9.2 ±0.3	2.0 ±0.2
CI 3-3	35.9 ±2.2	11.4 ±0.6	2.2 ±0.1	39.8 ±11.0	10.0 ±1.7	1.3 ±0.3
CI 4-1	66.6 ±6.8	15.6 ±1.8	2.8 ±1.1	73.9 ±3.1	18.6 ±2.9	2.7 ±0.4
CI 4-2	60.8 ±12.4	17.0 ±0.3	3.5 ±0.3	56.6 ±15	18.4 ±3.4	3.3 ±0.9
CI 4-3	46.6 ±5.6	13.2 ±0.7	3.4 ±0.4	60.1 ±2.6	11.0 ±1.1	1.7 ±0.2
K1	15.0 ±1.6	4.2 ±0.8	0.6 ±0.2			0.6 ±0.1

Measured UCS and E<sub>i</sub> values with compression parallel to bedding are mostly 1 to 1.9 times lower than values perpendicular to bedding. T<sub>0</sub> is however 1 to 1.7 times lower with compression perpendicular to bedding planes than values parallel to bedding (Table 1).

That means the highest UCS values, perpendicular and parallel to bedding, occur within the transition zone and the lowest within the core zone. The distribution of the highest E<sub>i</sub> is differing from the UCS values. At cross section H3 the highest E<sub>i</sub> values occur in the transition zone, at cross section H1 albeit in the damage zone and at cross section H4 the values are nearly similar for the transition and damage zone. T<sub>0</sub> reaches the highest values inside the damage zone, followed by the transition and core zone. The lowest values always occur in the core zone. Generally the mechanical properties are the highest at cross section H4, followed from cross section H3. The lowest values occur at cross section H1. Also the bulk rock density ρ<sub>0</sub> increases from cross section H4 to H3 to H1 with 2146 to 2183 to 2188 kg/m<sup>3</sup>.

## 6.2 Schmidt-Hammer Rebound-hardness

Values from cross section surveys H1, H2 and H3 were taken under wet conditions and are therefore much lower than sample values at the corresponding position (measured in the laboratory) and cross sections H4 and K7 which are taken under dry conditions. Previous studies have shown that moisture reduces rock hardness about 10 to 30% (Barton and Choubey, 1977; Viles et al., 2010). This implies that these data cannot be compared directly. At any rate, the in-situ rebound-hardness tests exhibit higher R-values with increasing distance from the fault core (Fig. 12).

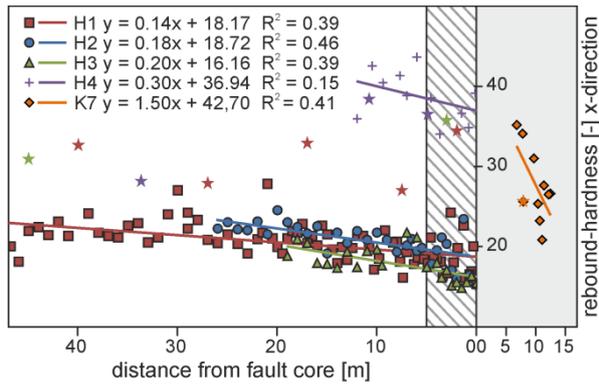


Fig. 12. Closely spaced rebound-hardness measurements against the distance from fault core at different cross sections. Rebound-hardnesses from the rock samples are marked with stars. The dashed area show the transition zone between the fault core and the damage zone and the grey area show the core zone.

Measurements within the fault core were not possible in large parts, meaning that the rebound-hardness must be lower than 15, which is the lowest measured value inside the outcrop. The only measurements at cross section K7<sub>dry</sub> range between 26 and 32 [-] in x-direction. The sample value in that cross section averages 26 [-]. The highest R-values occur at cross section H4<sub>dry</sub> (34-44), followed by cross section H1<sub>wet</sub> (15-28), H2<sub>wet</sub> (16-25) and H3<sub>wet</sub> (15-22).

### 6.3 Effective Young's moduli

Using the determined fracture densities along the damage zone,  $E_i$  [GPa] and UCS [MPa] of the rock samples (Table 1), the effective Young's moduli  $E_e$  [GPa] were calculated with equation 1 (cf., section 3; Fig. 13).

The increased fracture densities near the fault core clearly decrease  $E_e$ .  $E_e$ -values range between 1 and 7 GPa compared with the laboratory values ( $E_i$ ) between 8 to 17 GPa. In particular  $E_e$  is two to sixteen times lower than  $E_i$ . The decrease of  $E_e$  is highest near the fault core as well as around the minor fault zones.

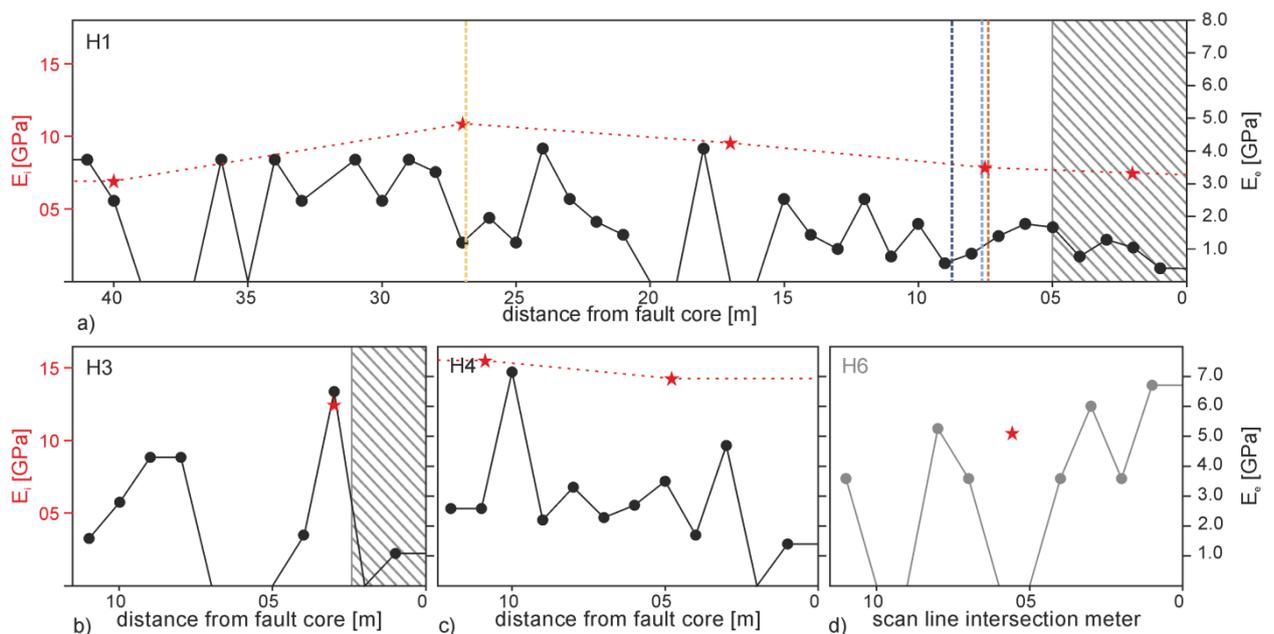


Fig. 13. Calculated effective and intact Young's moduli [GPa] perpendicular to the fault zone at cross section a) H1, b) H3 c) H4 and d) parallel to the fault zone at cross section H6 (cf., Fig. 3). The dashed areas show the transition zone between the fault core and the damage zone and dashed lines in a) the position of the minor fault zones.

## 7 Discussion

### 7.1 Fault zone architecture

The studied fault zone, crosscutting porous, thick bedded sandstones, can be divided into three different parts: damage zone, transition zone and core zone. The at least 14 m thick central fault core contains high strain zones (slip surfaces), separated by low strain zones with different grain sizes, porosities and consolidation states (host rock lenses). Similar heterogeneous fault core characteristics have been described by Faulkner et al. (2003; Carboneras strike slip fault – mica shists – southeastern Spain) and Foxford et al. (1998; salt related normal Bartlett fault zone – sandstone – SE Utah), where individual high strain zones encompass less strained host rock lenses. Such distributed fault cores were explained with the aid of varying mechanical rock properties and the transition of stress to strain or rather strain hardening and strain softening processes (Faulkner et al., 2010, 2003).

Strain softening, or reduced load bearing capacity in the stress-strain curve after failure, leads to strain concentration on fractures, which develop into fault zones. Strain softening is induced through e.g., intense fracturing, incorporated weak rocks into the slip surface forming clay smear, breccia or gouge. Particularly, clays are mechanically weak (Byerlee, 1978) and clayey fault cores with low shear resistance would localize deformation and form weak narrow fault cores like the five minor fault zones within the damage zone. Thus, strain softening would prevent the building of the observed 14 m thick fault core structure. In contrast, strain hardening is an increased load bearing capacity after failure, where the rock gets stronger with increasing strain. Strain hardening causes, for example by the formation of deformation bands, porosity reduction or generic increasing grain contact area and increased shear resistance. In cases where a slip surface strain hardens, a self-locking effect, new slip planes in weaker rocks may generate. Strain hardening processes may be an explanation regarding the large thickness of the observed fault core, consisting of various slip surfaces (Childs et al., 1996; Foxford et al., 1998). The development and incorporation of host rock lenses further increase the fault core thickness and may result in the observed 14 m thick fault core.

The fault core is surrounded by a 1-5 m thick transition zone. We observed that this architectural fault zone part combines characteristics from the core and the damage zone. This comes apparent through the change in fracture orientations, degree of deformation and occurrence of deformation bands within the transition zone. There is a sharp contact either distal or proximal to the central fault core and thus, the transition zone is not just a part of the core or the damage zone.

Our observations, concerning the structural characteristics of the transition zone, show some similarities with those described by Heynekamp et al. (1999) and Clausen (2003). The former authors characterize this zone as a "mixed zone", which is also observed in poorly lithified sediments by Rawling et al. (2001, 2006; Sand Hill Fault – Rio Grande Rift), Caine and Minor (2009; San Ysidro Fault – Albuquerque Basin) and Minor and Hudson (2006; various faults – northern Albuquerque Basin). Mixed zones range from intact, friable sediments to mixtures of clay, sand and gravel with relicts of sedimentary bedding. Bedding is mostly rotated in direction towards the fault zone strike. Further, they observed a sharp contact between the mixed zone and the core zone. This description is consistent with our observation in the upper part of the outcrop. The transition in the middle part of the outcrop coincides to a larger extent with the model by Clausen et al. (2003). Based on extensional faults in unconsolidated silt to fine-grained

sand (Northwestern Bornholm, Denmark), they distinguished between a distal and a central fault core. The distal fault core has similar characteristics as the mixed zones, but is in sharp contact towards the damage zone and is thus comparable to our observation in the middle part of the outcrop. Divergent to the descriptions above, we observed the highest fracture densities within the entire fault zone in the transition zone and lower incidence of deformation bands.

The transition zone is encompassed by the damage zone and is composed of mostly open fractures and minor faults. Fractures within the damage zone are mostly sub-parallel to the fault zone strike. Estimation of the lateral extent of the damage zone is not possible. Due to the minimum fault core thickness of 14 m, however, the damage zone thickness is presumably larger than the outcrop dilation (>40 m).

## 7.2 Fracture system parameters

For all exposed fault zone parts we observed differing fracture system parameters. As already mentioned, the most obvious distinction between the damage zone and the transition zone comes apparent by changing fracture orientations. Within the damage zone mostly fault parallel fractures occur (NNE-SSW) as well as an orthogonal-oriented fracture set, which is shifted toward an N-S-orientation within the transition zone and then rotated back within the core zone (Fig. 8). We conclude that these fractures are shear fractures in an  $R_1$ -orientation after Petit (1987). This observation has an important effect on the interpretation of the fault zone type (see below).

Fracture density, aperture and connectivity control the hydraulic connectivity of the fracture network (De Dreuzy et al., 2001; De Marsily, 1986; Hestir and Long, 1990). Previous studies of fault zones show an increased fracture density towards the fault core (Caine et al., 1996; Reyer et al., 2012). Similarly we observe that the relative enhancement of fractures oriented perpendicular to the fault strike is higher than for parallel striking fractures. This may play an important role concerning the fracture connectivity, because the probability of interconnected fractures increases with (i) density and (ii) fracture orientations. Therefore the fracture connectivity increases with proximity from the fault core and is highest for  $R_1$ -fractures (N-S-orientation) within the transition zone.

We observed slightly increased fracture apertures with decreasing distance from the fault core, whereby the fracture length clearly decreases. In particular, N-S-striking fractures within the transition zone have the widest apertures and shortest length. Fracture aperture partly depends on the local stress field (cf., Philipp et al., 2007): Fractures perpendicular to  $\sigma_1$  get closed and parallel striking fractures tend to open. Due to the recent stress field (active since Miocene;  $\sigma_1$  NW-SE; Schumacher, 2002) NNE-SSW-striking damage zone fractures are rather closed than N-S-striking transition zone shear fractures. It is also known that even small shearing leads to twisted fracture walls (self-propping effect) and lead to a sustained increase of the fracture aperture even under unfavorable stress fields (Häring, 2007).

We propose two main reasons to explain that most of the transition zone fractures remain short. First, the phenomenon is explainable by mechanical layering and related changes in rock stiffness (Young's modulus). A propagating fracture is arrested, when it reaches a mechanically weak contact such as an open bedding contact or a fracture (Economides and Nolte, 2000; Gudmundsson, 2011). Mechanical layering does not necessarily coincide with sedimentary bedding, but rather coincides with changes in grain size, porosity or mineralization in one bed and thus induced changes in mechanical rock properties. In particular, due to changes of Young's modulus within and around the

transition zone (see below), the stress field may change locally and form an inhomogeneous or unfavorable stress field for a propagating fracture. Second, the short fractures are mostly interconnected and their high density implies that these beds are saturated with fractures resulting in stress shadows. Therefore these fractures get linked to each other and remain consequently short (cf., Van der Pluijm and Marshak, 2004).

Consistent with the described fracture network the only mineralized fractures occur within the transition zone. Also common are Fe-Mn-oxide incrustations or staining within the entire fault zone, mostly in NE-SW-orientation. These features indicate a hydraulically active fracture network in the past. Our observations correspond to the description by Eisbacher and Fielitz (2010). They found mineralizations mostly in NNW- to WNW-striking or locally in N-S-striking faults or fractured zones. Near the western Rhine Graben Main Fault they further describe NE-striking Fe-Mn-ore (sometimes Pb-Zn) mineralization. Most fractures within the outcrop, however, remain open and enable a potentially enriched recent fluid transport.

### *7.3 Fault zone type and displacement*

The type, displacement and thickness of the described fault zone are unknown. Various indications, however, allow us to characterize it as an ESE-dipping, sinistral oblique-slip fault (see below).

The orientation of structural components (fractures, deformation bands, minor faults, slip surfaces), are used to define the fault slip direction. The slip direction is defined as the bisecting plane between  $R_1$ - and  $P_1$ -fractures. Riedel shear fractures ( $R_1$ -fractures) are synthetic towards the fault zone, project into and form mostly 10-20° angles towards the fault plane.  $P_1$ -fractures are likewise synthetic (Katz et al., 2004; Petit, 1987). With respect to the main fault zone orientation, transition zone fractures occur predominantly in the  $R_1$ -shear orientation with left lateral motions.  $P_1$ -orientation is in particular marked at the minor fault FZ5 (NE-SW-orientation), which also shows a sinistral motion. Also deformation bands within the core zone are in  $P_1$ -orientation. This indicates a sinistral movement caused by a NNW-SSE-oriented  $\sigma_1$  during fault zone formation. That may relate the fault zone formation to Miocene with a NW-SE- to NNW-SSE-oriented stress field (including a sinistral slip regime; Bergerat, 1987, Schumacher, 2002; cf., section 2). This assumption also fits with the general description of the Zaberger Fractured Boundary Zone with mostly N- to NNE-striking faults that cut and offset the graben parallel (NE-SW) faults (Fig. 2; Eisbacher and Fielitz, 2010). Because the southeastern terrain clearly cut downwards in direction to the graben center and the closeness to the graben center an ESE-dipping normal component is likely. All these assumptions define the exposed fault block as the footwall.

Scaling relationships of the displacement have often been performed based on the damage zone thickness (Faulkner et al., 2011), core zone thickness (Bastesen et al., 2013; Scholz, 1987) or the trace length of the fault zone (Dawers and Anders 1995). They exhibit mostly a wide scatter (even in log-log plots), because of different host rocks, tectonic regimes or different methods defining damage or core zone thickness (Faulkner et al., 2010). Most of these scaling relationships show increasing displacement with increasing damage zone or core zone thicknesses. In our study, however, such relations are not applicable, since the thickness of the different fault zone parts and the trace length are unknown. In general the at least 14 m thick core zone and the proximity to the Rhine Graben border lead to the assumption of a high displacement fault.

#### 7.4 Permeability structure

The fault zone model after Caine et al. (1996) gives four end members for the overall permeability structure of brittle fault zones. The fault core is outlined as a barrier to fluid flow and the damage zone enhances the permeability due to a high fracture density. Depending on the thickness of the different zones, distributed conduits, localized conduit, localized barriers and combined conduit-barrier systems were identified (Caine et al., 1996). Small-scale normal fault zones in sandstones, described by Reyer et al. (2012), tend to be localized barriers. They further observed that higher displacement faults more likely are combined conduit-barrier systems. In those cases, the damage zone contains deformation bands. Rawling et al. (2001) classified large displacement faults in poorly lithified sediments (Sand Hill Fault) with deformation band dominated damage zones, as barriers to fluid flow.

Both fault zone models, however, are not applicable on the presented fault zone, because the transition zone is not taken into account, the presented fault core is not just a sealing structure and the damage zone does not contain deformation bands.

An exact determination of the fluid flow category after Caine et al. (1996) is not possible because of the unknown fault zone thickness, but it best corresponds into the combined conduit-barrier classification. The fracture dominated damage zone increases the permeability. The structure of the fracture system indicates an increased permeability towards the fault core in NE-SW direction and orthogonal to it, because of increasing apertures and densities of such striking fractures.

Mixed zones are referred to have a reduced permeability compared with the host rock (Rawling and Goodwin, 2006; Rawling et al., 2001). But within the studied transition zone, besides deformation bands, also the highest fracture density, aperture and connectivity occur. Thus the fracture induced permeability may even be higher in comparison with the damage zone and shifted towards N-S and E-W.

The central core zone, which contains permeability reducing structures like narrow slip surfaces composed of fault gouge as well as deformation bands, also includes areas with more consolidated, porous and fractured rock. This means that the core zone itself represents a combined conduit-barrier system. Fluid flow across the fault zone could be possible when the fractured lenses within the core zone are interconnected or rather allow fluids to pass through the low-permeability high strain zones. Such processes are, for example, observed by hydraulic pumping tests within a deformation band dominated fault zone in sandstone, where a mostly uninterrupted fluid communication occurs between both fault walls (Medeiros et al., 2010). Furthermore we observed some areas which transport water around slip surfaces within the core zone, which also imply a fault core parallel fluid transport. Otherwise some water storage within the porous sands between the in permeable fault gouges may be possible.

Under high fluid pressure, the slip tendency reaches twice the tensile strength of the rock ( $2T_0$ , Gudmundsson et al., 2010). The low tensile strength of the core zone (cf., section 7.5) may facilitate, even under low shear stresses, slip events within the fault core (Gudmundsson et al., 2010).

#### 7.5 Mechanical properties of the fault rock

Knowing the mechanical rock properties is a key issue to understand and predict fault zone formation, architectural components and therefore fluid flow conditions. We determined that UCS-values are higher in the transition zone than in the damage zone. In comparison to the damage zone also  $E_i$  values are sometimes higher within the

transition zone and  $T_0$  does not clearly change. Obviously, mechanical rock properties within the core zone are by far the lowest. All measured values are particularly comparable with the lower end from normal values of sandstones ( $E_i$ : 0.4-84.3 GPa, UCS: 6-170 MPa,  $T_0$ : 0.4-25 MPa; Gudmundsson, 2011).

Normally, it is easier for fractures to propagate along bedding planes, than to pass through it and accordingly mechanical rock properties measured perpendicular to bedding are higher than parallel values (Hoek and Brown, 1997). Within this sandstone there is just a slight anisotropy between the mechanical rock properties of bedding parallel and bedding perpendicular measurements (Table 1). That means beddings planes within this sandstone have little impact on mechanical rock properties. Further it is possible that microfractures reduce the mechanical rock properties perpendicular to bedding in comparison to values parallel to bedding planes.

However, laboratory data are higher than in-situ values due to smaller amounts of fractures (Priest, 1993). These variations were measured by using a Schmidt-Hammer and calculated by analytical approaches after Priest (1993). Both methods do not reflect increased UCS or  $E_i$  within the transition zone. First, the R-values taken from rock samples do not show clearly increased values within the transition zone. Second, the closely spaced taken in-situ R-values (which are effective values) rather indicates gradually increasing mechanical rock parameters, with decreasing fracture densities (Fig. 13). Also, our calculations regarding  $E_e$  show that the Young's modulus in particular is reduced around the minor faults and within the transition zone, where the highest fracture density occurs (Fig. 9, 14). From that we derive that the mechanical parameters of intact rock are highest in the transition zone, but effective values are in average lower than in the damage zone. These variations in effective Young's moduli lead to stress concentrations within the outer part of the damage zone or in the host rock, where  $E_e$  is higher because of lower fracture densities. However, although the core zone rather tends to form a stress shadow, most strain remains within this zone, for example because of already existing weak fault planes (Gudmundsson 2011, Gudmundsson et al. 2010).

## 8 Conclusions

1. Detailed field studies of a fault zone crosscutting Lower Triassic sandstones in Alsace (north-east France) show that previous conceptual fault zone models are not applicable to the observed fault zone in porous sandstone because of a thick fault core and a fracture dominated transition zone and damage zone.
2. Fault zones in porous rocks are often deformation band dominated, but here these are less common within the transition and core zone so that the sealing effect of these structures is less developed within the described fault zone. Also the fault core, consisting of highly strained slip surfaces and lower strained fractured host rock lenses, may allow fluid flow across the fault induced by linked fractured host rock lenses.
3. Within the damage zone the aperture and density of fault parallel striking fractures as well as fault perpendicular striking fractures increase towards the fault core. This may lead to an increased fracture connectivity and enhance the possibility of a hydraulically active fracture network.
4. Compared with the damage zone larger fracture apertures and connectivity on fracture tips occur within the transition zone. This may enhance the fracture induced permeability in N-S-direction to a greater extent compared with other directions and fault zone parts.

5. Mechanical laboratory measurements of intact rock specimens display the highest uniaxial compressive strength and Young's modulus within the transition zone. But fracture affected effective Young's moduli (determined with a Schmidt-Hammer and analytical approaches) are smaller in the transition zone and increase with increasing distance from the fault core.
6. Fault zones in the Lower Triassic Bunter, and possibly other porous sandstones, not always are sealing structures. Even a thick fault core is not inevitably a barrier for fluid flow. Low tensile strength within the core enhances the risk for slip events during ongoing reservoir production. The damage zone, with mostly open fractures, may be potentially drilling targets for geothermal projects in the Upper Rhine Graben system. But because the connectivity decreases clearly with increasing distance from the fault core hydraulic stimulations may be needed.

### **Acknowledgments**

The authors appreciate the support of the German Federal Ministry for Economic Affairs and Energy (BMWi), previously of the German Federal Ministry for the Environment, Nature Conservation and Nuclear Safety (BMU) as part of the Research and Development Project AuGE (Outcrop Analogue Studies in Geothermal Exploration) within the framework of the 5th Energy Research Program (FKZ 0325302). Thanks to the company RAUSCHER for the permission to perform the field studies in the outcrop. Comments from Agust Gudmundsson and an anonymous reviewer helped improving the manuscript. We also acknowledge the editor Laurent Jolivet and the Tectonophysics team for publishing our work.

### **References**

- Agosta, F., Prasad, M., Aydin, A., 2007. Physical properties of carbonate fault rocks, fucino basin (Central Italy): Implications for fault seal in platform carbonates. *Geofluids* 7, 19-32. [dx.doi.org/10.1111/j.1468-8123.2006.00158.x](https://doi.org/10.1111/j.1468-8123.2006.00158.x).
- Antonellini, M., Aydin, A., 1994. Effect of faulting on fluid-flow in porous sandstones - Petrophysical properties. *American Association of Petroleum Geologists Bulletin* 78, 355-377.
- Aydin, A., Basu, A., 2005. The Schmidt hammer in rock material characterization. *Engineering Geology* 81, 1-14. [dx.doi.org/10.1016/j.enggeo.2005.06.006](https://doi.org/10.1016/j.enggeo.2005.06.006).
- Aydin, A., Johnson, A.M., 1978. Development of faults as zones of deformation bands and as slip surfaces in sandstone. *Pure and Applied Geophysics* 116, 931-942. [dx.doi.org/10.1007/BF00876547](https://doi.org/10.1007/BF00876547).
- Barton, N., Choubey, V., 1977. The Shear Strength of Rock Joints in Theory and Practice. *Rock Mechanics* 10, 1-54. [dx.doi.org/10.1007/BF01261801](https://doi.org/10.1007/BF01261801).
- Bastesen, E., Braathen, A., Skar, T., 2013. Comparison of scaling relationships of extensional fault cores in tight carbonate and porous sandstone reservoirs. *Petroleum Geoscience* 19, 385-398. [dx.doi.org/10.1144/petgeo2011-020](https://doi.org/10.1144/petgeo2011-020).
- Bergerat, F., 1987. Stress fields in the European platform at the time of Africa-Eurasia collision. *Tectonics* 6, 99-132. [dx.doi.org/10.1029/TC006i002p00099](https://doi.org/10.1029/TC006i002p00099).
- Bruhn, R.L., Parry, W.T., Yonkee, W.A., Thompson, T., 1994. Fracturing and hydrothermal alteration in normal-fault zones. *Pure and Applied Geophysics* 142, 609-644. [dx.doi.org/10.1007/BF00876057](https://doi.org/10.1007/BF00876057).

- Brun, J.P., Wenzel, F., 1991. Crustal-scale structure of the southern Rhinegraben from ECORS-DEKORP seismic reflection data. *Geology* 19, 758-762. [dx.doi.org/10.1130/0091-7613\(1991\)019<0758:CSSOTS>2.3.CO;2](https://doi.org/10.1130/0091-7613(1991)019<0758:CSSOTS>2.3.CO;2).
- Byerlee, J., 1978. Friction of Rocks. *Pure and applied geophysics* 116, 615-626. [dx.doi.org/10.1007/BF00876528](https://doi.org/10.1007/BF00876528).
- Caine, J.S., Evans, J.P., Forster, C.B., 1996. Fault zone architecture and permeability structure. *Geology* 24, 1025-1028. [dx.doi.org/10.1130/0091-7613\(1996\)024<1025:FZAAPS>2.3.CO;2](https://doi.org/10.1130/0091-7613(1996)024<1025:FZAAPS>2.3.CO;2).
- Caine, J.S., Forster, C.B., 1999. Fault zone architecture and fluid flow: Insights from field data and numerical modeling, in: Haneberg, W.C., Mozley, P.S., Moore, J.C., Goodwin, L.B. (Eds.), *Faults and Subsurface Fluid Flow in the Shallow Crust*. American Geophysical Monograph 113, 101-127. [dx.doi.org/10.1029/GM113p0101](https://doi.org/10.1029/GM113p0101).
- Caine, J.S., Minor, S.A., 2009. Structural and geochemical characteristics of faulted sediments and inferences on the role of water in deformation, Rio Grande Rift, New Mexico. *Geological Society of America Bulletin* 121, 1325-1340. [dx.doi.org/10.1130/b26164.1](https://doi.org/10.1130/b26164.1).
- Caine, J.S., Tomusiak, S.R.A., 2003. Brittle structures and their role in controlling porosity and permeability in a complex Precambrian crystalline-rock aquifer system in the Colorado Rocky Mountain Front Range. *Geological Society of America Bulletin* 115, 1410-1424. [dx.doi.org/10.1130/B25088.1](https://doi.org/10.1130/B25088.1).
- Chang, C.D., Zoback, M.D., Khaksar, A., 2006. Empirical relations between rock strength and physical properties in sedimentary rocks. *Journal of Petroleum Science and Engineering* 51, 223-237. [dx.doi.org/10.1016/j.petrol.2006.01.003](https://doi.org/10.1016/j.petrol.2006.01.003).
- Chesnaux, R., Allen, D.M., Jenni, S., 2009. Regional fracture network permeability using outcrop scale measurements. *Engineering Geology* 108, 259-271. [dx.doi.org/10.1016/j.enggeo.2009.06.024](https://doi.org/10.1016/j.enggeo.2009.06.024).
- Childs, C., Watterson, J., Walsh, J.J., 1996. A model for the structure and development of fault zones. *Journal of the Geological Society* 153, 337-340. [dx.doi.org/10.1144/gsjgs.153.3.0337](https://doi.org/10.1144/gsjgs.153.3.0337).
- Clausen, J.A., Gabrielsen, R.H., Johnsen, E., Korstgard, J.A., 2003. Fault architecture and clay smear distribution. Examples from field studies and drained ring-shear experiments. *Norwegian Journal of Geology* 83, 131-146.
- Dawers, N.H., Anders, M.H., 1995. Displacement-length scaling and fault linkage. *Journal of Structural Geology* 17, 607-614. [dx.doi.org/10.1016/0191-8141\(94\)00091-D](https://doi.org/10.1016/0191-8141(94)00091-D).
- De Dreuzy, J.R., Davy, P., Bour, O., 2001. Hydraulic properties of two-dimensional random fracture networks following a power law length distribution 1. Effective connectivity. *Water Resources Research* 37, 2065-2078. [dx.doi.org/10.1029/2001WR900010](https://doi.org/10.1029/2001WR900010).
- De Marsily, G., 1986. *Quantitative Hydrogeology: Groundwater Hydrology for Engineers*. Academic Press, New York.
- Deere, D.U., Miller, R.P., 1966. *Engineering Classification and Index Properties for Intact Rock*. Air Force Weapons Laboratory, Kirtland Air Force Base, New Mexico.
- Economides, M.J., Nolte, K.G., 2000. *Reservoir Stimulation*. Wiley, New York.

- Edel, J.B., Schulmann, K., Rotstein, Y., 2007. The Variscan tectonic inheritance of the Upper Rhine Graben: evidence of reactivations in the Lias, Late Eocene–Oligocene up to the recent. *International Journal of Earth Sciences* 96, 305-325. [dx.doi.org/10.1007/s00531-006-0092-8](https://doi.org/10.1007/s00531-006-0092-8).
- Eisbacher, G.H., Fielitz, W., 2010. Karlsruhe und seine Region Nordschwarzwald, Kraichgau, Neckartal, südlicher Odenwald, Oberrhein-Graben, Pfälzerwald und westliche Schwäbische Alb. In: Rothe, P. (Ed.), *Sammlung geologischer Führer* 103. Gebr. Borntraeger, Stuttgart.
- Fairhurst, C.E., Hudson, J.A., 1999. Draft ISRM suggested method for the complete stress-strain curve for intact rock in uniaxial compression. *International Journal of Rock Mechanics and Mining Sciences* 36, 281-289.
- Faulkner, D.R., Jackson, C.A.L., Lunn, R.J., Schlische, R.W., Shipton, Z.K., Wibberley, C.A.J., Withjack, M.O., 2010. A review of recent developments concerning the structure, mechanics and fluid flow properties of fault zones. *Journal of Structural Geology* 32, 1557-1575. [dx.doi.org/10.1016/j.jsg.2010.06.009](https://doi.org/10.1016/j.jsg.2010.06.009).
- Faulkner, D.R., Lewis, A.C., Rutter, E.H., 2003. On the internal structure and mechanics of large strike-slip fault zones: field observations of the Carboneras fault in southeastern Spain. *Tectonophysics* 367, 235-251. [dx.doi.org/10.1016/S0040-1951\(03\)00134-3](https://doi.org/10.1016/S0040-1951(03)00134-3).
- Faulkner, D.R., Mitchell, T.M., Jensen, E., Cembrano, J., 2011. Scaling of fault damage zones with displacement and the implications for fault growth processes. *Journal of Geophysical Research-Solid Earth* 116, B05403. [dx.doi.org/10.1029/2010JB007788](https://doi.org/10.1029/2010JB007788).
- Fossen, H., Schultz, R.A., Shipton, Z.K., Mair, K., 2007. Deformation bands in sandstone: a review. *Journal of the Geological Society* 164, 755-769. [dx.doi.org/10.1144/0016-76492006-036](https://doi.org/10.1144/0016-76492006-036).
- Foxford, K.A., Walsh, J.J., Watterson, J., Garden I.R., Guscott, S.C., Burley, S.D., 1998. Structure and content of the Moab Fault Zone, Utah, USA, and its implications for fault seal prediction. In: Jones, G., Fisher, Q.J., Knipe, R.J. (Eds), *Faulting, Fault Sealing and Fluid Flow in Hydrocarbon Reservoirs*. Geological Society, London, Special Publications 147, 87-103. [dx.doi.org/10.1144/GSL.SP.1998.147.01.06](https://doi.org/10.1144/GSL.SP.1998.147.01.06).
- Gudmundsson, A., 2011. *Rock Fractures in Geological Processes*. Cambridge University Press, Cambridge.
- Gudmundsson, A., Simmenes, T.H., Larsen, B., Philipp, S.L., 2010. Effects of internal structure and local stresses on fracture propagation, deflection, and arrest in fault zones. *Journal of Structural Geology* 32, 1643-1655. [dx.doi.org/10.1016/j.jsg.2009.08.013](https://doi.org/10.1016/j.jsg.2009.08.013).
- Häring, M. O., 2007. *Geothermische Stromproduktion aus Enhanced Geothermal Systems (EGS): Stand der Technik*. Geothermal Explorers Ltd, CH-4133, Pratteln.
- Hestir, K., Long, J.C.S., 1990. Analytical expressions for the permeability of random two-dimensional Poisson fracture network based on regular lattice percolation and equivalent media theories. *Journal of Geophysical Research: Solid Earth and Planets* 95, 21565-21581. [dx.doi.org/10.1029/JB095iB13p21565](https://doi.org/10.1029/JB095iB13p21565).
- Heynekamp, M.R., Goodwin, L.B., Mozley, P.S., Haneberg, W.C., 1999. Controls on faultzone architecture in poorly lithified sediments, Rio Grande Rift, New Mexico: implications for fault-zone permeability and fluid flow. In: Haneberg, W.C., Mozley, P.S., Casey Moore, J., Goodwin, L.B. (Eds.), *Faults and Subsurface Fluid Flow in the Shallow Crust*. AGU Geophysical Monograph 113, DC, 27-51. [dx.doi.org/10.1029/GM113p0027](https://doi.org/10.1029/GM113p0027)

- Hoek, E., Brown, E.T., 1997. Practical estimates of rock mass strength. *International Journal of Rock Mechanics and Mining Sciences* 34, 1165-1186. [dx.doi.org/10.1016/S0148-9062\(97\)00305-7](https://doi.org/10.1016/S0148-9062(97)00305-7).
- Illies, J.H., 1977. Ancient and Recent Rifting in the Rhinegraben. *Geologie En Mijnbouw-Netherlands Journal of Geosciences* 56, 329-350.
- Illies, J.H., Greiner, G., 1978. Rhinegraben and Alpine System. *Geological Society of America Bulletin* 89, 770-782. [dx.doi.org/10.1130/0016-7606\(1978\)89<770:RATAS>2.0.CO;2](https://doi.org/10.1130/0016-7606(1978)89<770:RATAS>2.0.CO;2).
- International Society for Rock Mechanics, 1981. *Rock Characterization, Testing and Monitoring – ISRM Suggested Methods*. Pergamon, London.
- Katz, Y., Weinberger, R., Aydin, A., 2004. Geometry and kinematic evolution of Riedel shear structures, Capitol Reef National Park, Utah. *Journal of Structural Geology* 26, 491-501. [dx.doi.org/10.1016/j.jsg.2003.08.003](https://doi.org/10.1016/j.jsg.2003.08.003).
- Kemeny, J., Cook, N.G.W., 1986. Effective moduli, nonlinear deformation and strength of cracked elastic solid. *International Journal of Rock Mechanics and Mining Sciences* 23, 107-118. [dx.doi.org/10.1016/0148-9062\(86\)90337-2](https://doi.org/10.1016/0148-9062(86)90337-2).
- Lindanger, M., Gabrielsen, R.H., Braathen, A., 2007. Analysis of rock lenses in extensional faults. *Norwegian Journal of Geology* 87, 361-372.
- Loveless, S., Bense, V., Turner, J., 2011. Fault architecture and deformation processes within poorly lithified rift sediments, Central Greece. *Journal of Structural Geology* 33, 1554-1568. [dx.doi.org/10.1016/j.jsg.2011.09.008](https://doi.org/10.1016/j.jsg.2011.09.008).
- Medeiros, W.E., do Nascimento, A.F., Alves da Silva, F.C., Destro, N., Demetrio, J.G.A., 2010. Evidence of hydraulic connectivity across deformation bands from field pumping tests: Two examples from Tucano Basin, NE Brazil. *Journal of Structural Geology* 32, 1783-1791. [dx.doi.org/10.1016/j.jsg.2009.08.019](https://doi.org/10.1016/j.jsg.2009.08.019).
- Ménillet, F., Benecke, W., Schumacher, E., Van Werveke, L., Leppia, A., Thürach, H., Konrad, H.J., Illies, H., Rinck, G., Schwoerer, P., 1989. Carte géol. France (1/50 000), feuille LEMBACH (168) - Orléans: Bureau de recherches géologiques et minières. Notice explicative par MÉNILLET F. et coll. (1989), 91 p.
- Minor, S.A., Hudson, M.R., 2006. Regional Survey of Structural Properties and Cementation Patterns of Fault Zones in the Northern Part of the Albuquerque Basin, New Mexico – Implications for Ground- Water Flow. U.S. Geological Survey Professional Paper 1719.
- Mutschler, T., 2004. Einaxiale Druckversuche an zylindrischen Gesteinsprüfkörpern Neufassung der Empfehlung Nr. 1 des Arbeitskreises "Versuchstechnik Fels" der Deutschen Gesellschaft für Geotechnik e.V..
- Petit, J.P., 1987. Criteria for the sense of movement on fault surfaces in brittle rocks. *Journal of Structural Geology* 9, 597-608. [dx.doi.org/10.1016/0191-8141\(87\)90145-3](https://doi.org/10.1016/0191-8141(87)90145-3).
- Philipp, S.L., Gudmundsson, A., Oelrich, A.R.I., 2007. How structural geology can contribute to make geothermal projects successful, European Geothermal Congress, Unterhaching.
- Priest, S.D., 1993. *Discontinuity Analysis for Rock Engineering*. Chapman and Hall, London.

- Rawling, G.C., Goodwin, L.B., 2006. Structural record of the mechanical evolution of mixed zones in faulted poorly lithified sediments, Rio Grande rift, New Mexico, USA. *Journal of Structural Geology* 28, 1623-1639. [dx.doi.org/10.1016/j.jsg.2006.06.008](https://doi.org/10.1016/j.jsg.2006.06.008).
- Rawling, G.C., Goodwin, L.B., Wilson, J.L., 2001. Internal architecture, permeability structure, and hydrologic significance of contrasting fault-zone types. *Geology* 29, 43-46. [dx.doi.org/10.1130/0091-7613\(2001\)029<0043:IAPSAH>2.0.CO;2](https://doi.org/10.1130/0091-7613(2001)029<0043:IAPSAH>2.0.CO;2).
- Renshaw, C.E., 1996. Estimation of fracture zone geometry from steady-state hydraulic head data using iterative sequential cokriging. *Geophysical Research Letters* 23, 2685-2688. [dx.doi.org/10.1029/96GL02415](https://doi.org/10.1029/96GL02415).
- Reyer, D., Bauer, J., Philipp, S.L., 2012. Fracture systems in normal fault zones crosscutting sedimentary rocks, Northwest German Basin. *Journal of Structural Geology* 45, 38-51. [dx.doi.org/10.1016/j.jsg.2012.06.002](https://doi.org/10.1016/j.jsg.2012.06.002).
- Reyer, D., Philipp, S.L., 2014. Empirical relations of rock properties of outcrop and core samples from the Northwest German Basin for geothermal drilling. *Geothermal Energy Science* 2, 21-37. [dx.doi.org/10.5194/gtes-2-21-2014](https://doi.org/10.5194/gtes-2-21-2014).
- Scholz, C.H., 1987. Wear and Gouge Formation in Brittle Faulting. *Geology* 15, 493-495. [dx.doi.org/10.1130/0091-7613\(1987\)15<493:WAGFIB>2.0.CO;2](https://doi.org/10.1130/0091-7613(1987)15<493:WAGFIB>2.0.CO;2).
- Schultz, R.A., 2003. A method to relate initial elastic stress to fault population strains. *Geophysical Research Letters* 30, 1593. [dx.doi.org/10.1029/2002GL016681](https://doi.org/10.1029/2002GL016681).
- Schumacher, M.E., 2002. Upper Rhine Graben: Role of preexisting structures during rift evolution. *Tectonics* 21, 1-17. [dx.doi.org/10.1029/2001TC900022](https://doi.org/10.1029/2001TC900022).
- Stapf, K.R.G., 1988. Zur Tektonik des westlichen Rheingrabenrandes zwischen Nierstein am Rhein und Wissembourg (Elsaß). *Jahresberichte und Mitteilungen / Oberrheinischer Geologischer Verein* 70, 399-410.
- Stapf, K.R.G., 1996. Neue Erkenntnisse zur Tektonik des pfälzischen Rheingrabenrandes, in: Geiger, M. (Ed.), *Haardt und Weinstraße: Beiträge zur Landeskunde*, Pfälzische Gesellschaft zur Förderung der Wissenschaften, Speyer, pp. 60-96.
- Terzaghi, R.D., 1965. Sources of error in joint surveys. *Geotechnique* 15, 287-304. [dx.doi.org/10.1680/geot.1965.15.3.287](https://doi.org/10.1680/geot.1965.15.3.287).
- Torabi, S.R., Ataei, M., Javanshir, M., 2010. Application of Schmidt rebound number for estimating rock strength under specific geological conditions. *Journal of Mining & Environment* 1, 1-8.
- Van Der Pluijm, B.A., Marshak, S., 2004. *Earth Structure*, second ed.. W.W. Norton & Company Inc., New York.
- Viles, H., Goudie, A., Grab, S., Lalley, J., 2010. The use of the Schmidt Hammer and Equotip for rock hardness assessment in geomorphology and heritage science: a comparative analysis. *Earth Surface Processes and Landforms* 36, 320-333. [dx.doi.org/10.1002/esp.2040](https://doi.org/10.1002/esp.2040).
- Yagiz, S., 2009. Predicting uniaxial compressive strength, modulus of elasticity and index properties of rocks using the Schmidt hammer. *Bulletin of Engineering Geology and the Environment* 68, 55-63. [dx.doi.org/10.1007/s10064-008-0172-z](https://doi.org/10.1007/s10064-008-0172-z).
- Zangerl, C., Evans, K.F., Eberhardt, E., Loew, S., 2008. Normal stiffness of fractures in granitic rock: A compilation of laboratory and in-situ experiments. *International Journal*

of Rock Mechanics and Mining Sciences 45, 1500-1507.  
*dx.doi.org/10.1016/j.ijrmms.2008.02.001.*

Ziegler, P.A., 1992. European Cenozoic rift system. Tectonophysics 208, 91-111.  
*dx.doi.org/10.1016/0040-1951(92)90338-7.*

Ziegler, P.A., Cloetingh, S., 2004. Dynamic processes controlling evolution of rifted basins. Earth-Science Reviews 64, 1-50. *dx.doi.org/10.1016/S0012-8252(03)00041-2.*

Ziegler, P.A., Dèzes, P., 2006. Crustal evolution of Western and Central Europe. Geological Society, London, Memoirs 32, 43-56.  
*dx.doi.org/10.1144/gsl.mem.2006.032.01.03.*

## 5 Rock samples of the Muschelkalk: Facies and diagenesis

Samples of limestone beds within the Muschelkalk successions were taken in outcrop analogues (cf. Chapters 2 and 3). In Chapter 3, laboratory measurements on rock mechanical properties were presented for samples NL-mo (named NL in Chapter 3; Nussloch), KN (Knittlingen), and IL (Illingen). Here, in addition, thin sections are presented for the samples NL-mu (Nussloch, Lower Muschelkalk) and NGO1 (Nussloch, Upper Muschelkalk). Thin-section analyses were performed with a transmitted-light microscope (Leica DM LP) to gain insights in Muschelkalk facies and diagenetic processes. Classification according to Dunham (1962) and brief description based on representative figure tables of each thin section are presented in this Chapter.

Sample NGO1 is classified as bioclastic packstone (Fig. 5.1). This sample contains abundant shell debris, for example bivalves and brachiopods, as well as cephalopods in micritic to microsparitic matrix. Neomorphism is common, for instance, in ooids. Neomorphism indicates diagenetic processes, i.e., alteration and recrystallization of crystals and thus changes in their shape and size (e.g., Flügel, 2004). Furthermore, some bivalve shells reveal dissolution and recrystallization processes (blocky cement, bladed cement). Stylolites are indicated by black clay seams (indicators of pressure solution; e.g., Tondi et al., 2006). Fracture porosity is mainly sealed by calcite cement. Crosscutting relationships of fractures and stylolites include one fracture terminating at a stylolite, thus being younger; thickness increase is observable at contact of fracture and stylolite. Moreover, fracture offset occurs at another stylolite.

Sample NL-mo is classified as bioclastic packstone/wackestone (Fig. 5.2.). The matrix is mainly formed by micrite and microspar. Some sectors, however, show pronounced recrystallization (blocky cement or drusy cement). Abundant shell debris is present (bivalves, gastropods, cephalopods). Neomorphic and diagenetic processes are indicated by recrystallization of bivalve shells and gastropods. Stylolites are evident by dark clay seams. Fractures are mainly sealed by ferrous calcite cement. However, some fractures are partially open.

Sample NL-mu is classified as bioclastic packstone (Fig. 5.3). Bivalve shells are very common in a micritic to sparitic matrix. Bladed calcite cement and blocky calcite cement, respectively, replaced those shells. Stylolites are indicated by dark clay seams, even though less frequent than in samples NGO1 and NL-mo. Fractures are presumably sealed by calcite cement of two generations (blocky cement replaced bladed cement).

Sample IL is classified as interbedded bioclastic packstone/wackestone and mudstone (Fig. 5.4). Thin-bedded packstones/wackestones, comprising in particular bivalve shells, are separated by thin layers of mudstone. Diagenesis is represented as recrystallization of bivalve shells and gastropods. Few stylolites occur and also few micro-fractures, sealed by calcite cement.

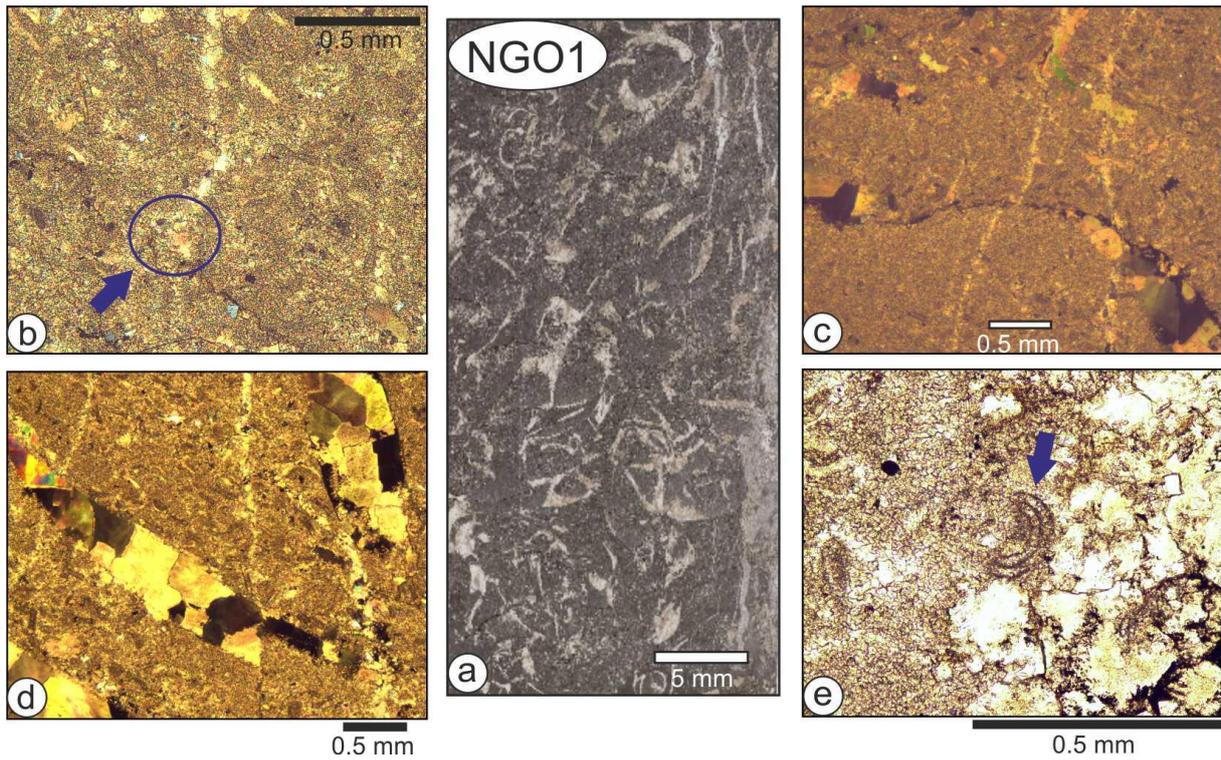


Fig. 5.1. Thin section images with transmitted light of sample NGO1. Scales of 0.5 mm and 5 mm are displayed. a) Scan of the entire thin-section. b) Fracture terminating at a stylolite (see arrow). c) Fracture offset at a stylolite. d) Blocky cement within bivalve shells. e) Neomorphism of an ooid (see arrow).

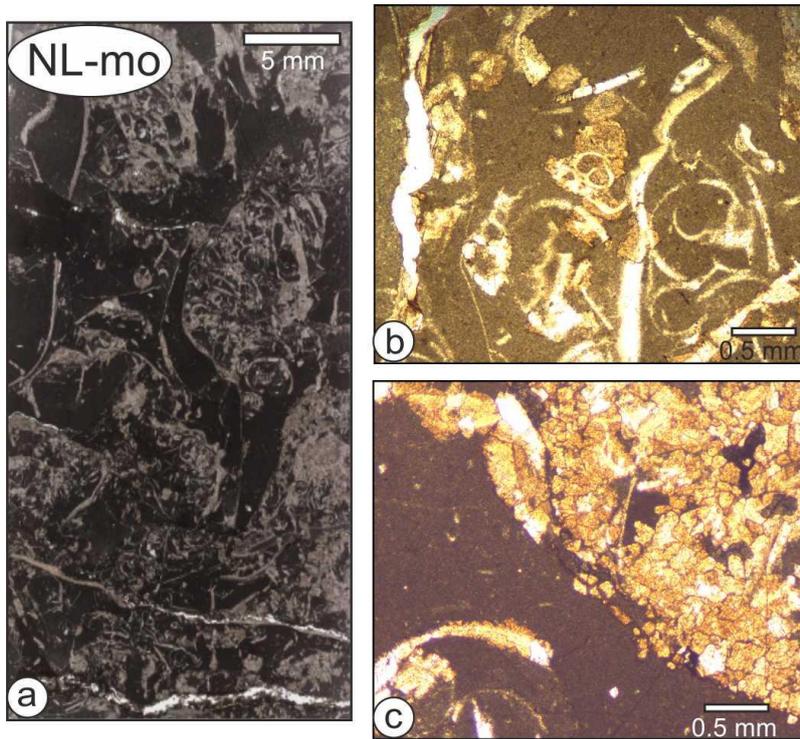


Fig. 5.2. Thin section images with transmitted light of sample NL-mo. Scales of 0.5 mm and 5 mm are displayed. a) Scan of the entire thin-section. b) Recrystallization of gastropod shells. c) Area showing significant cementation (blocky cement and drusy cement).

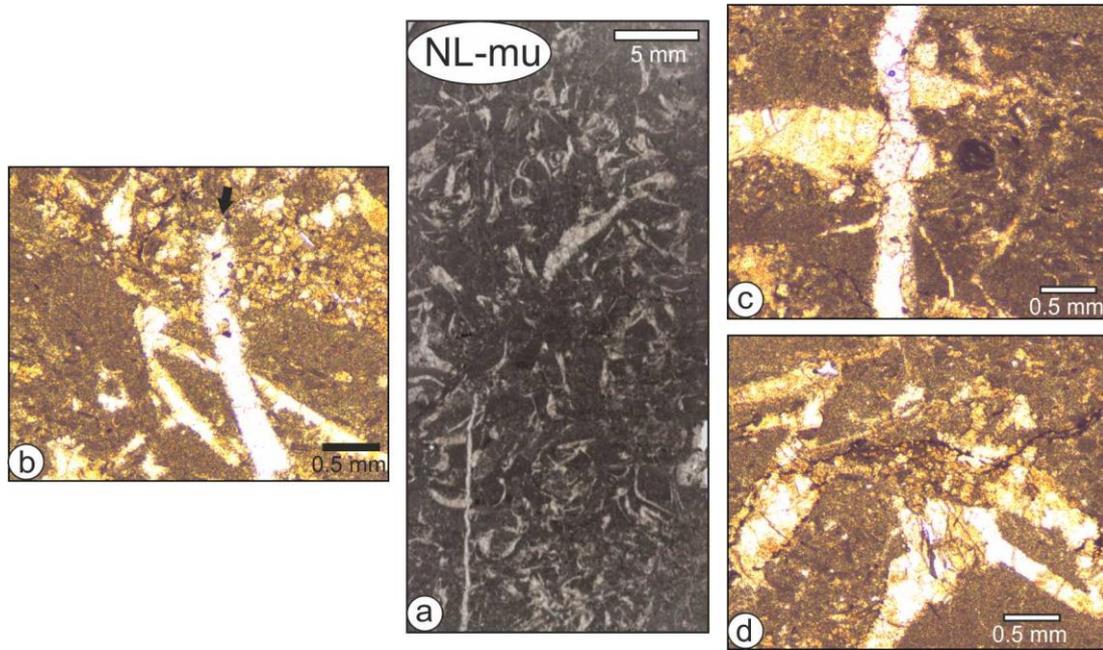


Fig. 5.3. Thin section images with transmitted light of sample NL-mu. Scales of 0.5 mm and 5 mm are displayed. a) Scan of the entire thin-section. b) - d) Bladed and blocky calcite cement replaced shells. Calcite of two generations is cementing fracture porosity.

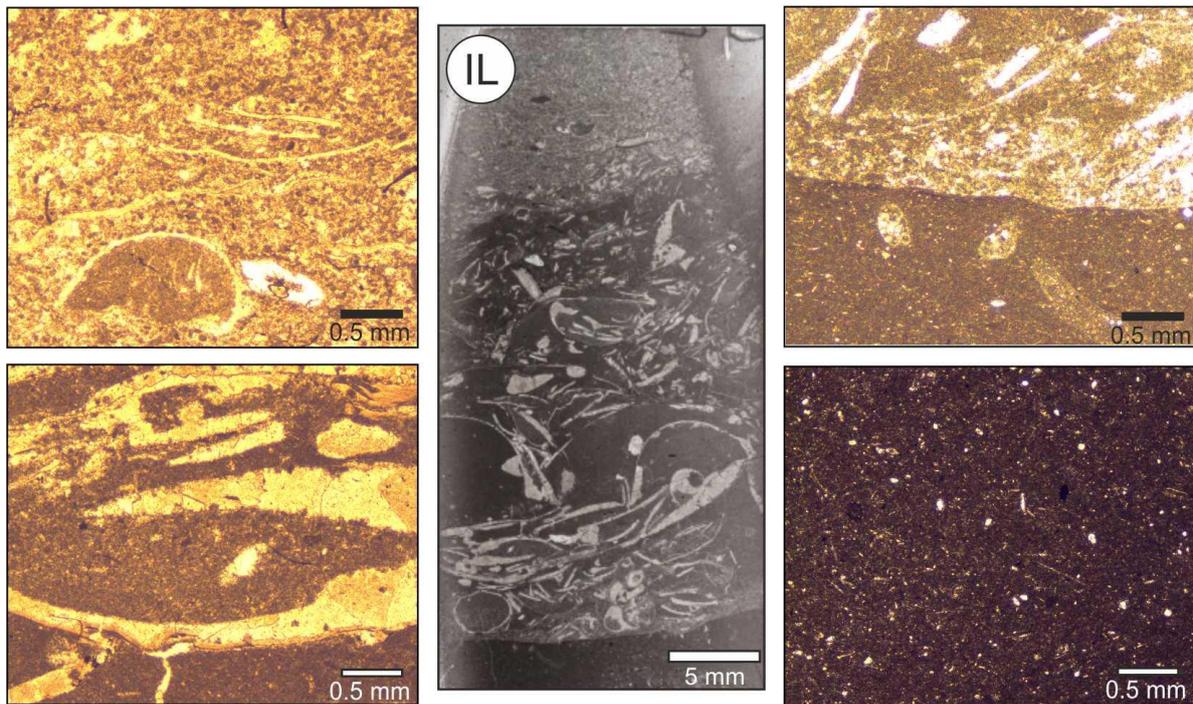


Fig. 5.4. Thin section images with transmitted light of sample IL. Scales of 0.5 mm and 5 mm are displayed. A scan of the entire thin-section is presented in the center. Thin layers of mudstone are clearly visible.

Sample KN is classified as bioclastic packstone (Fig. 5.5). The matrix is formed by microspar to micrite, some parts by sparite. The sample contains abundant shell debris, in particular bivalve shells, and some cephalopods. At least two generations of calcite cement are formed within bivalve shells (bladed cement and blocky cement replacing bivalve shells), indicating neomorphism. Some stylolites occur. Microfractures are rare, sealed by calcite cement.

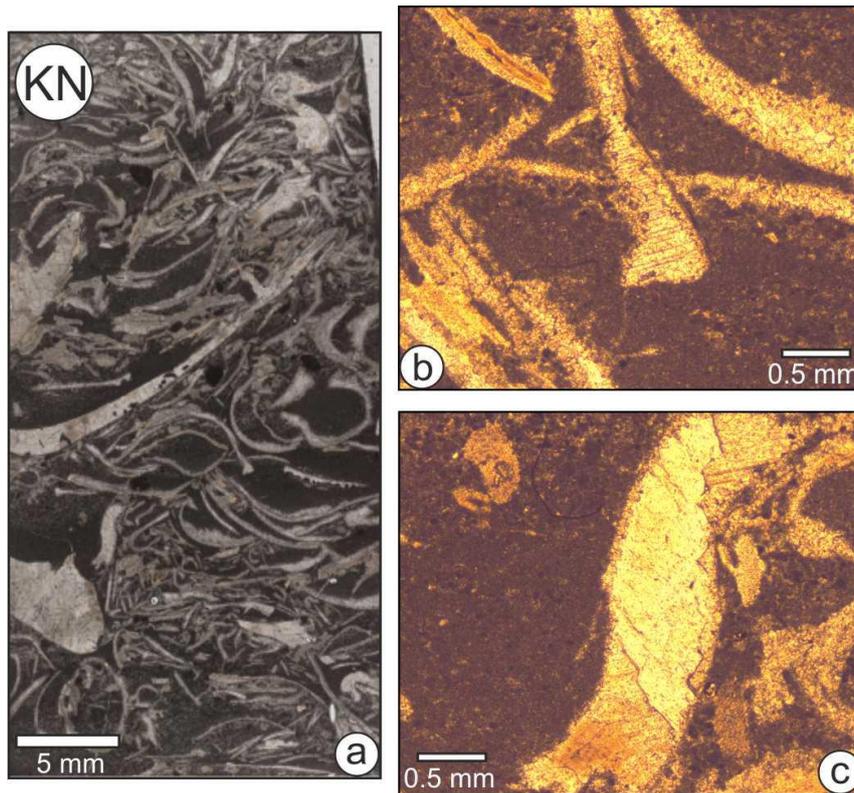


Fig. 5.5. Thin section images with transmitted light of sample KN. Scales of 0.5 mm and 5 mm are displayed. a) Scan of the entire thin-section. b) and c) Bladed and blocky cement replacing bivalve shells.

The diagenetic evolution of the Middle Triassic Muschelkalk in Southwest Germany was described in detail by Geng (1997). This study is based on samples taken inside the URG (core samples) and in quarries on both graben shoulders. Geng (1997) proposed complex diagenetic processes of Muschelkalk rocks in the URG area that started syn-sedimentary and continued through burial of the sediments. Subsequent processes were either characterized by uplift (flanks) or by deep burial (inside the graben). Six generations of calcite cement and two stages of dolomite cement were specified in chronological order by Geng (1997): (1) aragonite and Mg-calcite cement, (2) bladed and prismatic-columnar calcite, (3) non-zoned equant calcite and saddle dolomite cement 1, (4) zoned blocky calcite in uplifted areas and (5) non-zoned calcite and siderite in the URG, (6) saddle dolomite 2.

Samples analyzed in this thesis reflect these complex diagenetic processes: early diagenetic cements, cements representing deeper-burial, and late diagenetic cements indicating uplift were observed. According to Geng (1997) bladed calcite, now replacing shells, was formed under submarine to shallow burial conditions and is thus early diagenetic (temperatures 25-40°C). Saddle dolomite cement 1 (Sd1) replacing shells (Soyk, pers. comm.) also occurs in the rock samples. This cement represents a deeper-burial, pre-Tertiary diagenetic stage (temperatures 75-105°C; Geng, 1997). Blocky (ferrous) calcite, cementing for example fracture porosity and replacing Sd1 (e.g., sample NL-mo; Soyk, pers. comm.), was formed post-Tertiary. This cement is only found outside the graben in uplifted areas (blocky calcite cement E1; Geng, 1997), and is common in samples analyzed in this thesis. According to Geng (1997) this cement was precipitated from a mixture of meteoric waters and hydrothermal waters (fluid temperatures: 62-92°C). It occurs in fractures, solution induced vugs, and other secondary pores.

## References

Dunham, R.J., 1962. Classification of carbonate rocks according to depositional texture. In: Ham W.E. (Ed.). Classification of Carbonate Rocks. American Association of Petroleum Geologists Memoir, 108-121.

Flügel, E., 2004. Microfacies of Carbonate Rocks – Analysis, Interpretation and Application. Springer, Heidelberg.

Geng, A., 1997. Diagenesis of the Middle Triassic Muschelkalk, Southwestern Germany. PhD-thesis, Ruprecht-Karls-University Heidelberg, 85 pp.

Tondi, E., Antonellini, M., Aydin, A., Marchegiani, L., Cello, G., 2006. The role of deformation bands, stylolites and sheared stylolites in fault development in carbonate grainstones of Majella Mountain, Italy. Journal of Structural Geology 28, 376-391.

## 6 Summarizing Discussion

Can typical permeability structures be defined for differently-scaled fault zones in layered carbonate successions of Muschelkalk age (URG)? Can knowledge about fault-zone local stress fields at reservoir depths be improved for such fault zones? Are there fault-zone orientations preferable for fluid flow in the URG? What are the differences and similarities of Muschelkalk fault zones compared with fault zones in porous and thick-bedded sandstones of Bunter age? To resolve these questions, this thesis applies a mixed-method approach, comprising outcrop analogue studies, analytical models, and numerical models.

Main findings for (1) layered carbonate successions and (2) thick-bedded sandstones in the URG (Chapters 2 and 4) reveal that this approach provides characterization of fault-zone structural inventories at high resolution. Moreover, 3D-numerical models give significant insights on fault-zone local stress fields in layered carbonate successions at reservoir depth (Chapter 3). Results also indicate, however, limitations and challenges regarding application to reservoir depths, in particular for reservoir exploitation.

Here I present a summarizing discussion of the key results in context with exploration and exploitation of aforementioned potential geothermal reservoirs in the URG.

### 6.1 Fault-zone related permeability in potential hydrothermal reservoirs of the Upper Rhine Graben

Chapters 2 and 4 discuss characteristics of fault zones hosted in rocks of either Muschelkalk or Bunter age. Here, main results are synthesized and discussed to propose suitable targets of geothermal wellbores in the URG:

As mentioned in Chapter 1, Caine et al. (1996) distinguish (1) localized conduits, (2) distributed conduits, (3) localized barriers, and (4) combined conduit-barriers. Results on fault-zone characteristics (Chapters 2 and 4) show a slight difficulty in defining numerical indices  $F_a$  (fault-zone architectural index),  $F_m$  (mean of  $F_a$ -values for a single fault zone), and  $F_s$  (spatial variability index) stated by Caine et al. (1996) that are based on the relative width of a high-permeability damage zone and a low-permeability fault core. This is because thicknesses of analyzed fault damage zones are unknown in the present study since outer damage-zone boundaries are either not exposed (in case of large-scale fault zones) or diffuse due to strong deformation of fault blocks (repeated slip events on the fault plane). However, detailed descriptions on characteristics of fault damage-zone fracture systems and fault cores allow well-founded assumptions on fault-zone permeability structures in Muschelkalk and Bunter that are discussed in the following sections.

#### 6.1.1 *Fault-zone permeability structures in Muschelkalk rocks*

Fault zones in carbonate successions of the Muschelkalk analyzed in this thesis show distinct damage zones that may act as conduits for fluid flow. This is in accordance with previous studies which described well-developed damage zones in carbonates acting as conduits due to an enhanced fracture density and fracture connectivity (cf. Chapter 2; e.g., Micarelli et al., 2006a; Agosta et al., 2010; Reyer et al., 2012). Because the carbonate succession considered here, however, is particularly heterogeneous, the damage-zone characteristics vary significantly (Chapter 2): Damage zones in the more homogeneous mo1 are characterized by comparatively well-connected fracture systems and non-stratabound fractures, providing hydraulic pathways across several beds. Thus, such fracture systems may provide significant increases in permeability. In contrast,

damage-zone fracture systems in the mo2 are only to a minor degree affected by faulting processes (poor fracture connectivity, high amount of stratabound fractures). Even though an increase in fracture density exists, comparatively short fractures within the stiff limestone beds may increase the reservoir permeability only to a very limited degree because of their limited vertical extent. Thus, the lithology and in particular the mechanical layering has great impact on the fracture-system's hydraulic behavior in fault damage zones hosted in the Muschelkalk of the URG. Such impact of mechanical layering on fracture vertical extension and fracture connectivity was also observed by Reyer et al. (2012). They proposed, for rocks with strong mechanical layering (many layer-parallel heterogeneities) such as some parts of the Lower Muschelkalk in the Northwest German Basin, poor fracture connectivity despite potentially high fracture density.

Several studies dealing with fault zones in carbonates describe clay smear that is sheared or dragged into the core, acting as sealing material (e.g., Bastesen and Braathen, 2010; Bense et al., 2010; Bastesen et al., 2013). Fault cores analyzed in this thesis show similarities (Chapter 2): Fault zones hosted in units with a high amount of marl layers (marl-rich units), such as the mo2, comprise fault cores into which partially thick marl layers were dragged, acting as clay smear. However, this is certainly not the only fault core material. Fault cores are, regardless of fault-zone scale, very complex and may be characterized by varying hydraulic behavior. Medium-scale fault zones in Knittlingen show a huge variety in fault-core characteristics (fault breccia, lenses, tilted bedding, both marl and limestone dragged into the fault core, mineralizations) indicating both potential sealing (e.g., marl, mineralization) and potential conductive structures (e.g., lenses, coarse breccia) (e.g., Bense et al., 2010; Faulkner et al., 2010). Fault-core sections characterized by pronounced complexity are comparatively thick (e.g., Chapter 2 Fig. 9). Such fault-core complexity and also fault core width increases for large-scale fault zones comprising minor slip surfaces, host rock lenses, and partially thick mineralizations (Chapter 2 Figs. 6 and 8). The findings are thus comparable to the study of Bastesen et al. (2013) who describe a greater fault-core thickness in faults of greater complexity than in planar faults. In complex fault cores, such as those described in the large-scale fault zones in Nussloch and Illingen (Chapter 2), there is in particular the possibility that host rock lenses or minor slip surfaces provide paths for fluid flow (e.g., Faulkner et al., 2010).

Fault-zone permeability structures in carbonate successions of the Muschelkalk may be defined as follows (Fig. 6.1): Medium-scale fault zones may act either as combined conduit-barriers or distributed conduits. Fault damage zones may behave as conductive structures if they comprise a well-connected system of open fractures. In contrast, very complex fault cores may be barriers for fault-zone-orthogonal fluid flow, but conduits for fault-parallel flow (lenses, coarse breccia). Fault zones with a thin and more homogeneous fault core, in contrast, may behave as distributed conduits and may allow fluid flow across the fault core in sections with low marl content. This is partly consistent with the study of Reyer et al. (2012) who proposed a distributed conduit structure for normal fault zones in carbonates in the Northwest German Basin. Due to the complex tectonic history of the URG, however, this thesis deals not only with pure extension structures. The Knittlingen fault zones, for example show compressional and inversion structures (e.g., footwall short-cut, folds; cf. Chapter 2 Fig. 9.). Since such structures are caused by high horizontal stress, reduced permeability and formation of barriers are likely (reduced fracture apertures; e.g., Sibson, 1995, Bense et al., 2010).

Large-scale fault zones in carbonate successions of the Muschelkalk, i.e., fault zones at reservoir scale, may correspond to combined conduit-barrier systems which are,

however, more complex than those in medium-scale fault zones. The permeability structure within the same fault zone may vary vertically across the Muschelkalk succession. This is particularly due to fault cores with a high complexity and mechanical layering of the Muschelkalk, affecting fracture vertical extension (mo1 vs. mo2; see above). In general, a positive effect of damage zones on reservoir permeability is not likely from all subunits of the Muschelkalk. A combined conduit-barrier structure of fault zones in carbonates, however, was proposed in previous studies that also discuss the difficulty to make general assumptions on fault-zone permeability structures therein (e.g., Micarelli et al., 2006a; Micarelli et al., 2006b; Agosta et al., 2007; Bense et al., 2010; Agosta et al., 2012).

A limitation in applying the Caine et al. (1996) model was also described in the review paper by Faulkner et al. (2010) who name permeability heterogeneities and -anisotropies which clearly depend on the fault-zone three-dimensional structure and fault-zone growth. In general, this thesis supports the proposal that fault-zone permeability structures depend on various variables such as host-rock lithology, stress regime, fault-segment linkage, potential reactivation of the fault plane, and displacement as described in previous studies (Graham et al., 2003; Childs et al., 2009; Lunn et al., 2009; Bense et al., 2010; Faulkner et al., 2010; Torabi and Berg, 2011; Bastesen et al., 2013). For fault zones considered in thesis, in particular former changes in the stress regime and the probability of fault-zone inversion as well as fault growth, i.e., linkage of fault segments in adjacent mechanical layers, may have the greatest impact on fault-zone permeability structure.

Following from this discussion, the most promising drilling targets for geothermal wells are presumably damage-zone fracture systems in the mo1. The well paths in such a reservoir with comparatively low thickness have to be planned with care. At least one deviated well in a geothermal doublet could intersect as many fractures as possible and would connect them to the respective well (e.g., Huenges, 2010).

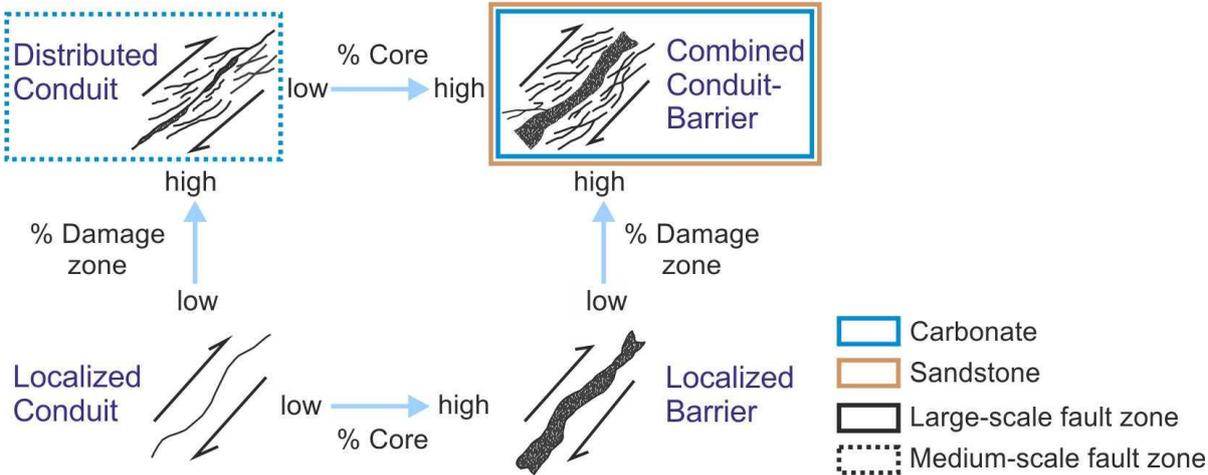


Fig. 6.1. Definition of four endmembers for a fault-zone permeability structure based on the relative percentage of fault core and damage zone (cf. Chapter 1; modified from Caine et al., 1996). Permeability structures proposed for fault zones analyzed in this thesis are highlighted (color code indicating lithology and fault-zone scale see key). Large-scale fault zones in both carbonates and sandstones are characterized as combined conduit-barriers. Medium-scale fault zones may be either characterized as distributed conduits or combined conduit-barriers.

6.1.2 Fault-zone permeability structure in Lower Bunter – A comparison

As mentioned in Chapter 4, the permeability structure of the fault zone hosted in thick bedded sandstones of Bunter age corresponds best to the endmember of a combined conduit-barrier system (Fig. 6.1). A conduit behavior is particularly stated for the fracture

system in damage zone and transition zone. The wide and very complex central core zone, however, should be highlighted due to a mixture of sealing (e.g., fault gouge, deformation bands) and conductive structures (porous and fractured rock), indicating its own combined conduit-barrier structure. However, this outcrop provides only a small window in relation to the fault-zone vertical extent. Thus, there is the possibility that the permeability structure may also change vertically within the Bunter sandstone succession. Clastic rocks of Bunter age comprise, similarly to the Muschelkalk, also parts with strong mechanical layering (e.g., alternations of claystone and sandstone). This mechanical layering leads, as well, to low fracture connectivity as described in the study by Reyer et al. (2012). Furthermore, fault-zone permeability structures in sandstones depend, for example, on variations of sandstone cementation and porosity and the probability whether potential low-permeability zones of deformation bands will form rather than fractures (localized barrier; e.g., Antonellini and Aydin, 1994; Rawling et al., 2001; Reyer et al., 2012). Nevertheless, certain hydraulic conductivities of a deformation-band dominated fault damage zone in reservoir-scale, indicated by field pumping tests, have been stated by Medeiros et al. (2010).

Regarding fault-zone related permeability of Lower Bunter sandstones it is furthermore possible to draw a link to current geothermal exploration in the URG: Fault-zone-related significant fluid paths at reservoir depth in sandstones of Bunter age have been found in the geothermal well Brühl GT1. This well targets the damage zone of a reservoir-scale fault zone. A high hydraulic conductivity at reservoir depth is indicated by (1) significant mud loss at reservoir depth while drilling and (2) first pumping tests from this geothermal well (Reinecker et al., 2015). Although the targeted fault zone crosscuts also the Muschelkalk, significant mud losses in the well Brühl GT1 were not observed until reaching the Upper Bunter (Reinecker et al., 2015). Thus, significant fluid paths in the Muschelkalk are not indicated.

### 6.1.3 *Mineralizations within the fault damage zones*

Both permeability structures in Muschelkalk and Bunter proposed above are based on the assumption that open fractures exist at reservoir depth. Here, the effect of mineralization within the fracture system shall shortly be discussed since fault-zone related fracture systems in both Muschelkalk (e.g., calcite, dolomite) and Bunter (e.g., barite, Fe-oxides) are possibly sealed at depth.

Mineralization of the fracture network is common in carbonates and it is well known that such mineralization reduces fracture-related permeability and thus induces permeability anisotropies (e.g., Micarelli et al., 2006a; Bense et al., 2010). Although the majority of fractures analyzed in outcrop analogues of the Muschelkalk are open, data show that the amount of mineralized fractures increases towards the fault cores (Chapter 2 Fig. 14). These mineralizations indicate previous hydrothermal activities in the fracture system, mainly parallel to the fault-zone strike. However, due to their potential present-day sealing capacity they may form barriers for fault-zone parallel fluid flow within a geothermal reservoir.

That most of the fractures are open can also be stated for the fault zone crosscutting the Lower Bunter: Data for the Cleebourg fault zone show only very few mineralized fractures, limited to the transition zone (Chapter 4 Fig. 11) that could, however, also result in sealing behavior. Field studies by Soyk (2015) in a nearby outcrop on the western URG graben shoulder (Leistadt quarry) reveal significant fracture mineralizations in the periphery of a main fault zone (presumably the western main graben boundary

fault zone) indicating former hydrothermal activity in the related fracture system. Thus, similar mineralization at reservoir depth is possible.

The degree of mineralization in both Muschelkalk and Bunter, however, may be different at reservoir depths. To detect potentially open or potentially sealed fractures in deep wellbores, geophysical tools such as wellbore imaging (Formation Micro Imager FMI – electrical imaging; Ultrasonic Borehole Imager UBI – acoustic imaging) are commonly used (e.g., Huenges, 2010, Zoback, 2007). Results of those tools used in the wellbore Brühl GT1 indicate a section of open fractures that correlates with the zone of partially significant mud loss (Reinecker et al., 2015). Wireline-logging data for the Muschelkalk reservoir are not available. This is due to wellbore instabilities in the related wellbore section.

## **6.2 Stress state and fault-zone permeability**

This thesis presents analytical estimations on fault-zone stress states at Muschelkalk-reservoir depth in the URG (Chapter 3). Stress state-dependent hydraulic behavior of fault zones at reservoir depth should, of course, be further evaluated in context with small-scale damage-zone fractures providing potential fluid paths in the reservoir. Previous studies proposed that open fractures in damage zones that are preferably oriented in the present-day stress field (high slip tendency and high dilation tendency) show an increased hydraulic conductivity (e.g., Barton et al., 1995; Zoback, 2007; Faulkner et al., 2010). Investigations on the orientation of main fracture sets associated with fault damage zones in outcrop analogues of Muschelkalk and Bunter reveal that main fracture sets and fractures with largest apertures are formed parallel or subparallel to fault-zone strike (Chapters 2 and 4). Thus, hydraulic activity of the fracture system is directly linked to fault-zone stress state in the present-day stress field.

However, analytical estimations on fault-zone stress states highlight the problem that general statements on slip and dilation tendencies of fault zones in the URG are difficult to make (Chapter 3 – transitional stress regime and variations in orientations of horizontal stresses; Chapter 3 Figs. 4 and 5). Moreover, in this thesis only fault-zone orientations determined in the outcrop analogue are available and used for analytical estimations (poles of the fault zones). Thus, these estimations reflect one selective fault-zone stress state for each fault zone only. In nature, a greater complexity is caused by the fact that fault planes may show slight strike variations and rather have an undulating than a planar geometry. This is visible for example in the Illingen quarry exposing the slip surface of the large-scale oblique-slip fault zone presented in Chapter 2. An undulating slip surface results in deviating stress states along a single fault zone or slip surface, respectively.

To estimate in-situ stress states in a geothermal reservoir, it is preferred to develop 3D-structural models with fault-plane geometries received by interpretation of 2D and 3D seismic data, respectively. If such seismic data are available, it is a common procedure to visualize slip and dilation tendencies of fault planes and related potential reactivations of individual fault-plane sections (e.g., Moeck et al., 2009 - Northeast German Basin, Germany; Jolie et al., 2015 – Basin-and-Range Province, Nevada, USA; Meixner et al., 2016 - Upper Rhine Graben, Germany), for example by using the software 3Dstress® (SwRI) (Morris et al., 1996). As an example, Fig. 6.2 shows slip and dilation tendencies of the fault pattern around the geothermal site of Bruchsal (URG) by Meixner et al. (2016).

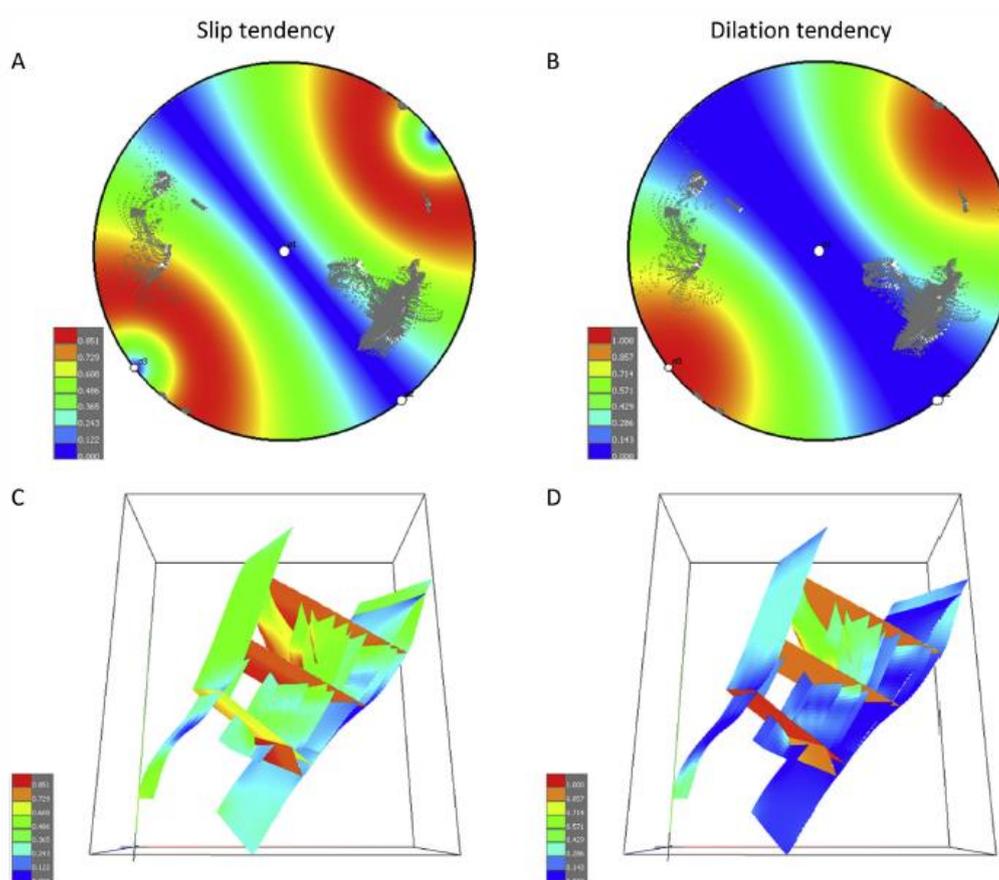


Fig. 6.2. Deviating slip tendencies (left) and dilation tendencies (right) under a transitional regime (normal to strike-slip faulting) for the Bruchsal geothermal site at a depth of 2.000 m, URG (Meixner et al., 2016). The top row shows stereonet projections of the tendency values and poles of the fault-zone pattern. The base row shows the tendency distribution over the fault pattern in Bruchsal in 3D views.

### 6.3 Enhancing hydrothermal reservoirs – Stimulation treatments in sedimentary successions

The lessons learned from established geothermal projects show that the natural permeability in hydrothermal reservoirs must be enhanced to achieve economic viability. Results on fracture-system characteristics within fault damage zones compiled in this thesis also show that stimulation treatments to improve the fracture-system hydraulic activity may be needed (Chapters 2 and 4), in particular in the mo2 (high amount of stratabound pre-existing fractures, even very close to the slip surface). Thus, the necessity of enhancing the geothermal-well-productivity becomes clear (Enhanced Geothermal Systems; EGS). Enhancement of fluid-flow rates in low-enthalpy reservoirs can be provided by well-established stimulation tools such as hydraulic stimulation and chemical stimulation (e.g., Zimmermann et al., 2011).

Hydraulic stimulation is caused by high-pressure fluid injection into the geothermal reservoir and, in particular, applied in low-porous rocks (e.g., Zimmermann et al., 2011). In hydrothermal reservoirs, comprising a natural fracture system, it is intended either to extent pre-existing natural fractures or to increase the connectivity by linkage of fractures. Reactivation and opening processes of pre-existing fractures are caused by tensile or shear failure, respectively (Zimmermann et al., 2011; Zang et al., 2014; Xie and Min, 2016). In particular, shear movements along the fracture plane may result in persistent fracture opening (self-propping effect) (e.g., Huenges, 2010; Jung et al., 2005).

In context with 3D-numerical models (Chapter 3), vertical heterogeneous stress fields and the formation of stress barriers affecting vertical fracture propagation in the Muschelkalk succession, in particular towards the strike-slip regime, have been discussed in detail; they correspond to results of previous studies (e.g., Larsen and Gudmundsson, 2010; Philipp et al., 2013). An increased risk of non-effective hydraulic stimulation (too small fracture extensions) was stated to occur in the entire Muschelkalk succession and in particular in units with strong mechanical layering (e.g., the mo2). Here, potential hydraulic stimulations in the Bunter reservoir shall briefly be considered: Thick-bedded sandstones exposed in the outcrop analogue Cleebourg are, at first glance, relatively homogeneous (Chapter 4). However, variations in this thick sandstone beds are common in particular as changes in grain size and porosity. In contrast to the analyzed Muschelkalk succession, shale interbeds are rare and, if present, thin. Thus, in comparable Bunter successions uncertainties are present as changes in porosity and cementation rather than as mechanical layering: In poorly cemented units showing high porosity one problem could be to reach the fluid pressure needed to create or expand fractures since the injected water may infiltrate the pore volume. The Bunter also comprises, however, mechanically layered units consisting of low-porous sandstone and shale interbeds. For such units, results of 3D-numerical models described in Chapter 3 should be transferable to the potential Bunter reservoir, i.e., there occurs a similar risk of non-effective hydraulic stimulation of the pre-existing fracture system at reservoir depth.

Chemical stimulation is another appropriate tool and, for instance, well-established in carbonate rocks, but also used in sandstones. The stimulation process is provided by chemical dissolution or acidization respectively, and caused by a combination of hydraulic fracturing and acid injection. This tool is primarily used to remove damage material near the wellbore, but also to enhance the fracture-system conductivity (acid etching; Economides and Nolte, 2000; Zimmermann et al., 2011). Since this method is intended to produce conductive fractures (Zimmermann et al., 2011), it may be possible to acidize mineralizations within the existing fracture system to create fluid flow paths. In case of strong fracture-system mineralization, hydraulic stimulation may thus be replaced by chemical stimulation to enhance fracture-related permeability in both hydrothermal reservoirs considered in this thesis.

## References

- Agosta, F., Prasad, M., Aydin, A., 2007. Physical properties of carbonate fault rocks, Fucino basin (Central Italy): implications for fault seal in platform carbonates. *Geofluids* 7, 19–32.
- Agosta, F., Alessandroni, M., Antonellini, M., Tondi, E., Giorgioni, M., 2010. From fractures to flow: A field-based quantitative analysis of an outcropping carbonate reservoir. *Tectonophysics* 490, 197-213.
- Agosta, F., Ruano, P., Rustichelli, A., Tondi, E., Galindo-Zaldívar, J., Sanz de Galdeano, C., 2012. Inner structure and deformation mechanisms of normal faults in conglomerates and carbonate grainstones (Granada Basin, Betic Cordillera, Spain): Inferences on fault permeability. *Journal of Structural Geology* 45, 4-20.
- Antonellini, M., Aydin, A., 1994. Effect of faulting on fluid-flow in porous sandstones: Petrophysical properties. *American Association of Petroleum Geologists Bulletin* 78, 355-377.
- Barton, C.A., Zoback, M.D., Moos, D., 1995. Fluid flow along potentially active faults in crystalline rock. *Geology* 23, 683–686.

- Bastesen, E., Braathen, A., 2010. Extensional faults in fine grained carbonates – analysis of fault core lithology and thickness-displacement relationships. *Journal of Structural Geology* 32, 1609-1628.
- Bastesen, E., Braathen, A., Skar, T., 2013. Comparison of scaling relationships of extensional fault cores in tight carbonate and porous sandstone reservoirs. *Petroleum Geoscience* 19, 385-398.
- Bense, V.F., Gleeson, T., Loveless, S.E., Bour, O., Scibek, J., 2013. Fault zone hydrogeology. *Earth-Science Reviews* 127, 171-192.
- Caine, J.S., Evans J.P., Forster, C.B., 1996. Fault zone architecture and permeability structure. *Geology* 24, 1025-1028.
- Childs, C., Manzocchi, T., Walsh, J.J., Bonson, C.G., Nicol, A., Schöpfer, M.P.J., 2009. A geometric model of fault zone and fault rock thickness variations. *Journal of Structural Geology* 31, 117-127.
- Economides, M.J., Nolte, K.G., 2000. *Reservoir Stimulation*, 3rd Edition. Wiley and Sons Ltd., United Kingdom.
- Faulkner, D.R., Jackson, C.A.L., Lunn, R.J., Schlische, R.W., Shipton, Z.K., Wibberley, C.A.J., Withjack, M.O., 2010. A review of recent developments concerning the structure, mechanics and fluid flow properties of fault zones. *Journal of Structural Geology* 32, 1557-1575.
- Graham, B., Antonellini, M., Aydin, A., 2003. Formation and growth of normal faults in carbonates within a compressive environment. *Geology* 31, 11-14.
- Gudmundsson, A., Simmenes, T.H., Larsen, B., Philipp, S.L., 2010. Effects of internal structure and local stresses on fracture propagation, deflection, and arrest in fault zones. *Journal of Structural Geology* 32, 1643-1655.
- Huenges, E., 2010. *Geothermal Energy Systems: Exploration, Development, and Utilization*. Wiley-VCH Verlag GmbH & Co. KGaA, Weinheim, Germany.
- Jolie, E., Moeck, I., Faulds, J.E., 2015. Quantitative structural-geological exploration of fault-controlled geothermal systems - A case study from the Basin-and-Range Province, Nevada (USA). *Geothermics* 54, 54-67.
- Jung, R., Orzol, J., Jatho, R., Kehrer, P., Tischner, T., 2005. The GeneSys-Project: Extraction of geothermal heat from tight sediments. Proc 30. Workshop on Geothermal Reservoir Engineering, SGP-TR-176.
- King, G., 1983. The accommodation of large strains in the upper lithosphere of the earth and other solids by self-similar fault systems - the geometrical origin of b-Value. *Pure and Applied Geophysics* 121, 761-815.
- Larsen, B., Gudmundsson, A., 2010. Linking of fractures in layered rocks: Implications for permeability. *Tectonophysics* 492, 108-120.
- Lunn, R.J., Willson, J.P., Shipton, Z.K., Moir, H., 2008. Simulating brittle fault growth from linkage of preexisting structures. *Journal of Geophysical Research* 113, B07403, doi:10.1029/2007JB005388.
- Medeiros, W.E., do Nascimento, A.F., Alves da Silva, F.C., Destro, N., Demétrio, J.G.A., 2010. Evidence of hydraulic connectivity across deformation bands from field pumping tests: Two examples from Tucano Basin, NE Brazil. *Journal of Structural Geology* 32, 1783-1791.

- Meixner, J., Schill, E., Grimmer, J.C., Gaucher, E., Kohl, T., Klingler, P., 2016. Structural control of geothermal reservoirs in extensional tectonic settings: An example from the Upper Rhine Graben. *Journal of Structural Geology* 82, 1-15.
- Micarelli, L., Moretti, I., Jaubert, M., Moulouel, H., 2006a. Fracture analysis in the southwestern Corinth rift (Greece) and implications on fault hydraulic behavior. *Tectonophysics* 426, 31-59.
- Micarelli, L., Benedicto, A., Wibberley, C.A.J., 2006b. Structural evolution and permeability of normal fault zones in highly porous carbonate rocks. *Journal of Structural Geology* 28, 1214-1227.
- Moeck, I., Kwiatek, G., Zimmermann, G., 2009. Slip tendency analysis, fault reactivation potential and induced seismicity in a deep geothermal reservoir. *Journal of Structural Geology* 31, 1174-1182).
- Morris, A., Ferrill, D.A., Henderson, D.B., 1996. Slip-tendency analysis and fault reactivation. *Geology* 24 (3), 275-278.
- Philipp, S.L., Afşar, F., Gudmundsson, A., 2013. Effects of mechanical layering on hydrofracture emplacement and fluid transport in reservoirs. *Frontiers in Earth Science* 1(4), 1-19, doi: 10.3389/feart.2013.00004.
- Reinecker, J., Bauer, J.F., Bechstädt, T., Drews, T., Filomena, M., Grobe, R., Hochschild, T., Meier, S., Melchert, B., Miernik, G., Philipp, S.L., Soyk, D., Stollhofen, H., 2015. Verbundprojekt AuGE: Aufschlussanalogstudien und ihre Anwendbarkeit in der geothermischen Exploration - Entwicklung von Methoden zur Ermittlung von Permeabilitäten und Transmissivitäten aus Reservoir-Informationen des Oberrheingrabens. AuGE – Outcrop analogue studies in geothermal exploration. Schlussbericht Teilprojekt A. TIBKAT.
- Reyer, D., Bauer, J.F., Philipp, S.L., 2012. Fracture systems in normal fault zones crosscutting sedimentary rocks, Northwest German Basin. *Journal of Structural Geology* 45, 38-51.
- Sibson, R.H., 1995. Selective fault reactivation during basin inversion: potential for fluid redistribution through fault-valve action. In: *Geological Society Special Publications* 88, 3-19.
- Soyk, D., 2015. Diagenesis and reservoir quality of the Lower and Middle Buntsandstein (Lower Triassic), SW Germany. Dissertation, 181 pp., Ruprecht-Karls-University Heidelberg. <http://www.ub.uni-heidelberg.de/archiv/18871>.
- Torabi, A., Berg, S.S., 2011. Scaling of fault attributes: A review. *Marine and Petroleum Geology* 28, 1444-1460.
- Xie, L., Min, K.-B., 2016. Initiation and propagation of fracture shearing during hydraulic stimulation in enhanced geothermal system. *Geothermics* 59, 107-120.
- Zimmermann, G., Blöcher, G., Reinicke, A., Brandt, W., 2011. Rock specific hydraulic fracturing and matrix acidizing to enhance a geothermal system – concepts and field results. *Tectonophysics* 503, 146-154.
- Zang, A., Oye, V., Jousset, P., Deichmann, N., Gritto, R., McGarr, A., Majer, E., Bruhn, D., 2014. Analysis of induced seismicity in geothermal reservoirs - an overview. *Geothermics* 52, 6-21.
- Zoback, M.D. 2007. *Reservoir Geomechanics*. Cambridge University Press, Cambridge.

## 7 Conclusions and Outlook

Fault zones in sedimentary hydrothermal reservoirs of Muschelkalk and Bunter age are potential target structures of geothermal projects in the URG. This thesis contributes to their exploration. In Chapter 1 four main aims are introduced. Here, main conclusions revealed by a mixed-method approach are stated. Afterwards, some possible improvements regarding the approach and further investigations are briefly described.

### *(1) Defining fault-zone characteristics and estimating their permeability structure at different fault-zone scales:*

Medium-scale (displacement 1-10 m) and large-scale fault zones (displacement >10 m) in layered carbonate successions may behave as combined conduit-barrier systems. Medium-scale fault zones may, in case of a thin and homogeneous fault core comprising breccia, also act as distributed conduits. Potential conductive and potential sealing structures, however, change across the Muschelkalk succession, in particular in large-scale fault zones. Descriptions reveal that both damage-zone fracture-system characteristics (e.g., connectivity, vertical extension) and fault-core characteristics show pronounced differences across the Muschelkalk:

Damage-zone fracture systems in rather homogeneous units such as parts of the mo1 have a more positive impact on reservoir permeability than those in heterogeneous units (strong small-scale mechanical layering; e.g., parts of the mo2): First-mentioned fracture systems (e.g., fracture in parts of the mo1) are characterized by a relatively high hydraulic connectivity between multiple layers and high fracture connectivity of shorter fractures. These properties are more pronounced in proximity to the fault cores. Latter fracture systems (e.g., fracture systems in parts of the mo2) show, in contrast, limited vertical extent and poor fracture connectivity. Thus, damage zones formed in the mo1 may be preferable target structures of geothermal wells. In contrast, fault damage zones in the mo2 are less suitable for geothermal exploitation.

Enhanced fracture-induced permeabilities can be expected parallel and subparallel to fault zones and to prominent regional structures, if favorably oriented in the present-day stress field (cf. Chapter 6.2). Fracture-system data show largest fracture apertures in these directions and comparatively high fracture apertures around the fault core.

Fault cores in both reactivated medium-scale fault zones and large-scale fault zones are mainly very complex structures. They comprise manifold material, either with sealing behavior (e.g., marl, mineralizations) or potentially conductive behavior (e.g., breccia, host rock lenses, minor slip surfaces). Fault cores in marl-rich successions are particularly characterized by sealing behavior (clay smear). In general, many uncertainties exist and potential sealing materials within the fault cores are very likely. Thus, fault cores should be avoided as drilling targets.

### *(2) Improving knowledge of fault-zone local stress field within the hydrothermal potential Muschelkalk reservoir in the Upper Rhine Graben:*

3D-numerical models on fault-zone local stress field at stress conditions similar to those at reservoir depth were developed. Considerable differences in local stress fields were found, depending on (1) fault-zone orientation (angles at 0°, 30°, 60°, or 90° to the maximum horizontal stress  $S_H$ ), (2) stress regime (normal faulting regime, transitional

regime normal to strike-slip faulting, strike-slip faulting regime), (3) fault-zone scale (medium-scale vs. large-scale) and (4) contrasts in mechanical properties.

In a normal faulting regime, soft fault rocks consequently concentrate less principal stresses than the host rock, facilitating hydraulic stimulation in these units. Clear fault-zone-orientation dependency of stress magnitudes is concluded with increasing horizontal compression (transitional and strike-slip regime). Soft fault damage zones and fault cores at angles of 60° or 90° to  $S_H$  form a gradual transition zone between differently stressed layers in footwall and hanging wall. They concentrate higher principal stresses than comparable units oriented at 0° or 30° to  $S_H$ . High compressive stress concentrations may, for example, result in fracture closure of pre-existing fractures and prevention of hydro-fracture development. In contrast, fault zones trending parallel to  $S_H$  concentrate, independent of stress regime, less stresses than the host rock. Hence, they are more promising for hydro-fracture development.

3D-numerical models show increasing impact of mechanical layering from normal faulting regime to strike-slip regime. In a strike-slip regime, local stress fields become vertically heterogeneous, affecting hydraulic stimulation and wellbore stability. Regarding hydraulic stimulation of the natural fracture system in Muschelkalk rocks, the following is thus concluded. Vertical fracture propagation induced by hydraulic stimulation in the mechanically layered mo2, comprising clay zones  $\alpha$ - $\zeta$  and thus a very heterogeneous stress field, is very challenging, in particular by high horizontal compression. Improvement of the fracture-system connectivity is difficult and stimulations treatments have to be planned with care. In contrast, further improvement of the fracture-system connectivity in more homogeneous units such as the mo1 appears to be more feasible. Stiff limestone beds concentrate shear stresses and can thus be targeted for shear-failure of pre-existing fractures (increase of fracture aperture, self-propping effect).

Regarding drilling operation, rapidly changing stress concentrations across the Muschelkalk must be expected, leading to wellbore instabilities. Mud weights must be chosen carefully to prevent breakouts or formation of drilling induced tensile fractures.

### *(3) Identifying fault zones with preferable orientation for fluid flow in the Upper Rhine Graben:*

Analytical models of fault-zone stress states at stress conditions similar to those at geothermally relevant depth were presented for fault-zone orientations determined in outcrop analogues. They reveal significant stress state variations of each fault zone. This is particularly due to the well-known uncertainties in the URG, i.e., transitional stress regime and common changes in orientation of the maximum horizontal stress  $S_H$  (NW-SE to NNW-SSE). Analytical models only reflect selective stress states. Precise fault-zone slip and dilation tendencies and thus the likelihood of being hydraulically conductive structures are thus difficult to propose. However, estimates are concluded: Fault zones oriented within the range of potential  $S_H$ -directions (NW-SE to NNW-SSE) are not likely to be subjected to high horizontal compressive stress. They may either have a comparatively high dilation tendency or comparatively high slip tendency.

The orientation of the maximum horizontal stress  $S_H$  varies in a certain range that can be narrowed with detailed surveys. 2D-seismic or 3D-seismic based structural models of the fault-zone patterns at reservoir depths are well-established tools to characterize the structural inventory at a geothermal site. Hence, profound knowledge on the stress state of the targeted fault zone can be expected within the scope of reservoir exploration.

*(4) Comparing fault zones within different potential hydrothermal reservoirs in the URG. Fault zones in layered carbonate successions versus fault zones in thick bedded sandstone:*

Similar to described fault zones hosted in Muschelkalk the analyzed fault zone hosted in sandstones of Bunter best corresponds to a combined conduit-barrier system. Damage zone and transition zone comprise a well-developed fracture system potentially behaving as a fluid conduit. The very complex fault core comprises a mixture of both sealing and conductive structures. Thus, the core does not necessarily act as a barrier. However, occurrence of brittle failure structures in Bunter sandstones is needed to form a well-pronounced fracture system. Units in which formation of deformation bands is likely should be determined beforehand.

In case of an open and well-connected fracture system fault damage zones in both Muschelkalk and Bunter are most promising targets. This is, in both sedimentary successions, more likely in more homogeneous units with a low degree of mechanical layering. When exploiting a potential geothermal reservoir in Muschelkalk or Bunter, respectively, the possibility of a mineralized fracture system has to be taken into account. Mineralization within the fracture system causes further permeability anisotropies. Data show that the majority of the fractures are open fractures. However, the amount of mineralization increases towards the fault cores. Considering this fact, geophysical tools such as wellbore imaging are required.

To conclude, fault zones in both the Muschelkalk carbonate succession and the Bunter thick-bedded sandstone may be promising target structures of geothermal projects in the URG. However, this thesis in general deals with fault zones showing high deformation grade and having undergone repeated slip events in the framework of the URG-evolution (e.g., oblique-slip fault zones, reactivated fault zones). Described fault-zone structures are very heterogeneous in both sedimentary successions since they were most likely formed by fault linkage (recognizable for example by complex fault cores). This leads to various uncertainties regarding their permeability structure and the possibility of their variation in both horizontal and vertical direction. In particular, uncertainties exist for large-scale fault zones (displacement >10 m) and thus reservoir-scale fault zones. General statements on fault-related permeabilities in hydrothermal reservoirs of the URG are difficult. The following issues arise if a fault zone is a possible target: Is the specific fault zone a pure normal fault? Is there the possibility of former fault-zone reactivation events? Was the fault zone, for instance, subjected to high horizontal stress (closure of the fracture system)? Does the geometry suggest formation by linkage of pre-existing fault segments resulting in a complex structure? Detailed fault-zone characterization prior to drilling is required.

The findings of this thesis show that the applied mixed-method approach provides profound assumptions on fault-related reservoir characteristics in the URG. The definition of preferable and, in contrast, unsuitable targets of deep geothermal wellbores in sedimentary successions of Muschelkalk and Bunter is possible. However, some uncertainties were also pointed out. To what extent these outcrop-based assumptions are applicable to deep reservoir conditions must be solved with further investigations. Comparisons should be made to data of the subsurface.

Such data are, for instance, high-resolution 2D- or 3D-seismic data reflecting the 3D-structure of the fault zone and thus fault-zone complexity. Furthermore, specific values

on potential permeability enhancement in proximity to a fault zone are needed. Whether and to what extent such enhancement arises, can only be determined correctly in the targeted reservoir during or subsequent to the drilling operation (e.g., in-situ pumping tests). Such pumping test data are available for the Bunter reservoir (Reinecker et al., 2015; wellbore Brühl GT1; cf. Chapter 6) and can thus be compared with outcrop analogue data. Corresponding results will be presented in the PhD-thesis of Johanna Bauer (in prep.).

Furthermore, some components of the presented approach need further improvements. Information on fault-zone stress states presented in this thesis are based on orientation data determined in limited fault-zone sections. Thus, those stress states are selective and do not reflect the fault-zone three-dimensional structure. Deviating slip and dilation tendencies of a fault zone can be analyzed by an outcrop-based structural model. A new technique, i.e., terrestrial laser scanning (LiDAR scanning), has been used to visualize large-scale surfaces in outcrop analogues (Wiatr, et al., 2013; Reinecker et al., 2015; Wilkinson et al., 2015). The fault plane exposed in the Illingen quarry, for instance, provides the opportunity for a LiDAR survey and development of a 3D-model. A slip- and dilation tendency distribution, as described in Chapter 6 (Fig. 6.2), can be visualized.

As mentioned in Chapter 3, future 3D-numerical models comprising damage zones with gradually changing Young's moduli between damage zone and host rock would offer a major opportunity to estimate more realistic local stress fields. With such models, the natural gradual decrease of fracture density towards the host rock would be reflected. In order to implement such numerical models it is necessary to ensure that these models can still be solved (risk of too high computing power). In order to reduce complexity, it is recommended to start with a smaller number of layers.

Moreover, further information on interaction between hydraulic stimulation (e.g., vertical fracture propagation) and mechanically layered rocks at reservoir depth is needed. Hydro-mechanical 3D-numerical models of fluid overpressure applied in a pre-existing fracture system and, for instance, external horizontal compression at reservoir depth would be a powerful tool to analyze this issue.

Young's moduli  $E$  assigned in presented 3D-numerical models are estimations and only reflect relative variations. They are based on correlations of Schmidt-hammer Rebound hardness measurements with  $E$  published in literature. Since those correlations are lithology dependent (facies, diagenesis), regression analyses specifically for Muschelkalk rocks need to be performed. Therefore, it is recommended to perform more laboratory measurements of rock samples taken in various limestone beds of the carbonate successions. Rebound hardness measurements in equal beds should provide the opportunity for correlations.

Young's moduli furthermore need to be adapted to reservoir conditions at depth. Results of rock mechanical properties presented in this thesis were determined by uniaxial compression tests only. Triaxial tests are well-established to simulate reservoir stress condition since they consider confining pressure (e.g., Jaeger et al., 2007; Zoback, 2007) and should be performed in further studies.

## References

Bauer, J.F., in preparation. Fault zones in geothermal exploration in the Upper Rhine Graben: Architecture and numerical assessed hydrogeological impact. PhD-thesis (preliminary title).

Jaeger, J.C., Cook, N.G.W., Zimmermann, R.W., 2007. Fundamentals of Rock Mechanics (4<sup>th</sup> edn.). Blackwell Publishing, Oxford, UK.

Reinecker, J., Bauer, J.F., Bechstädt, T., Drews, T., Filomena, M., Grobe, R., Hochschild, T., Meier, S., Melchert, B., Miernik, G., Philipp, S.L., Soyk, D., Stollhofen, H., 2015. Verbundprojekt AuGE: Aufschlussanalogstudien und ihre Anwendbarkeit in der geothermischen Exploration - Entwicklung von Methoden zur Ermittlung von Permeabilitäten und Transmissivitäten aus Reservoir-Informationen des Oberrheingrabens. AUGE – Outcrop analogue studies in geothermal exploration. Schlussbericht Teilprojekt A. TIBKAT.

Wiatr, T., Reicherter, K., Papanikolaou, I., Fernández-Steege, T., Mason, J., 2013. Slip vector analysis with high resolution t-LiDAR scanning. Tectonophysics 608, 947-957.

Wilkinson, M., Roberts, G.P., McCaffrey, K., Cowie, P.A., FaureWalker, J.P., Papanikolaou, I., Philips, R.J., Michetti, A.m., Vittori, E., Gregory, L., Wedmore, L., Watson, Z.K., 2015. Slip distributions on active normal faults measured from LiDAR and field mapping of geomorphic offsets: an example from L'Aquila, Italy, and implications for modelling seismic moment release. Geomorphology 237, 130-141.

Zoback, M.D. 2007. Reservoir Geomechanics. Cambridge University Press, Cambridge.

## Appendix

---

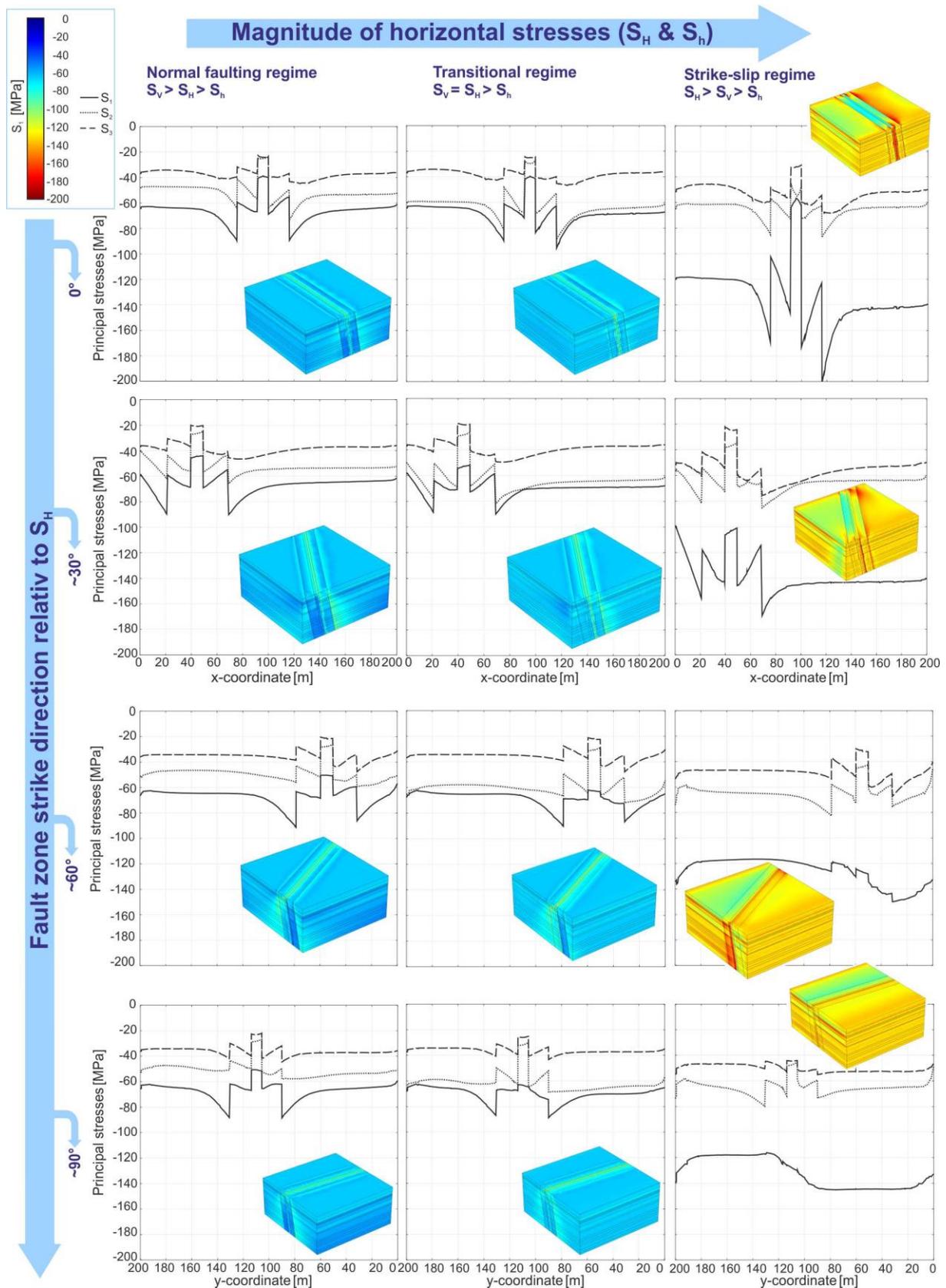


Fig. 1. Principal stress magnitudes [MPa] within a total of 12 numerical models of the large-scale fault zone crosscutting the entire Upper Muschelkalk, hosting a homogeneous fault core (homogeneous Young's modulus) instead of a heterogeneous fault core presented in Chapter 3 (cf. Fig. 13 captions and text in Chapter 3 for details).

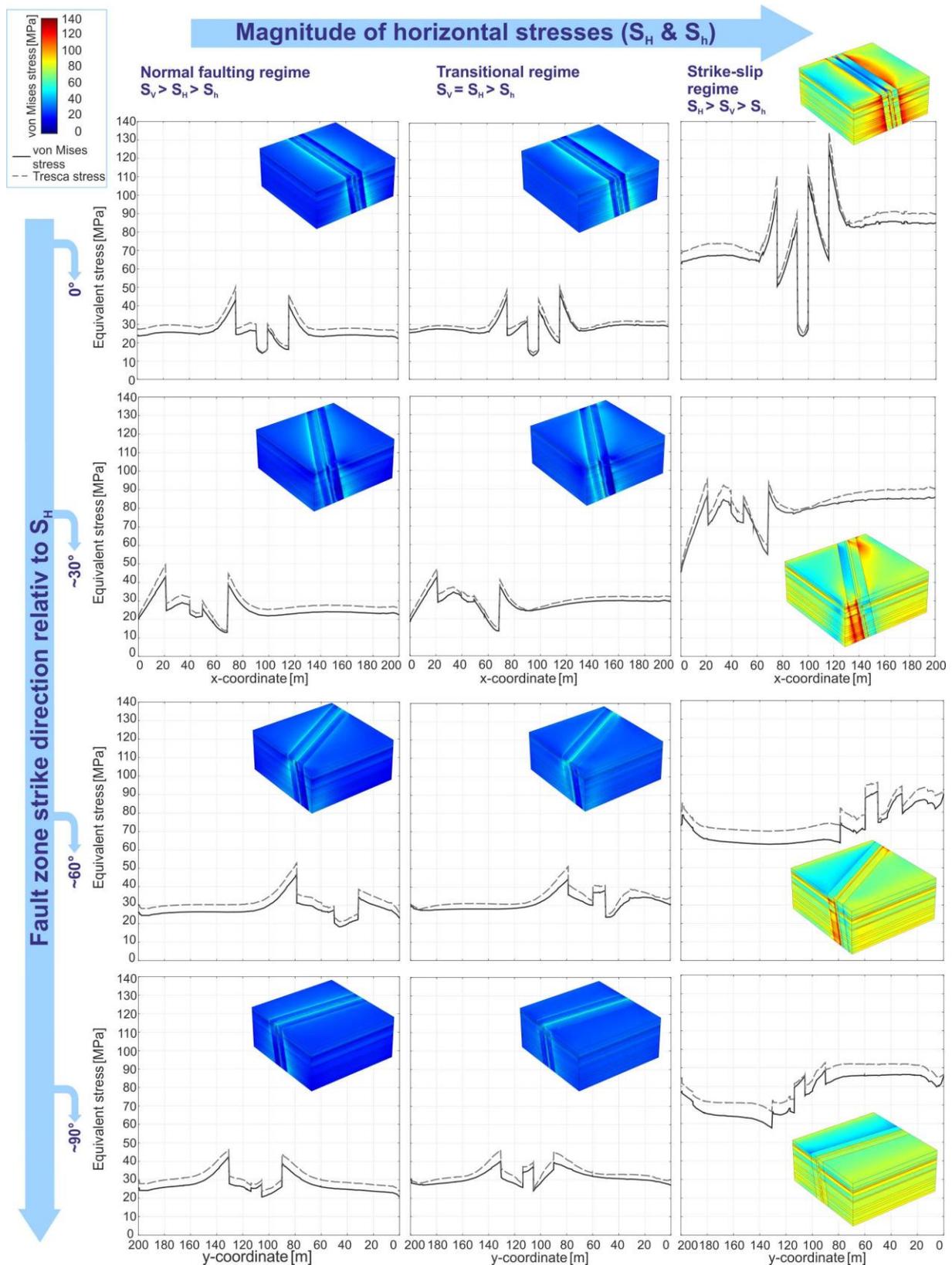


Fig. 2. Shear stress magnitudes computed as equivalent stresses von Mises stress and Tresca stress [MPa] within a total of 12 numerical models of the large-scale fault zone crosscutting the entire Upper Muschelkalk, hosting a homogeneous fault core (homogeneous Young's modulus) instead of a heterogeneous fault core presented in Chapter 3 (cf. Fig. 13 and 15 captions and text in Chapter 3 for details).



## **Acknowledgments / Danksagung**

Die vorliegende Arbeit entstand im Rahmen des Verbund-Forschungsprojekts AuGE. Ich danke daher vielmals meiner Doktormutter Sonja L. Philipp für die Möglichkeit, in diesem spannenden Forschungsprojekt mitzuwirken. Die gemeinsamen fachlichen Diskussionen, aber auch die Möglichkeit, die Arbeit frei und nach meinen Vorstellungen zu gestalten, haben mich an Erfahrung gewinnen lassen. Ich danke für das Vertrauen. Im gleichen Maße danke ich zudem für die entspannte Arbeitsatmosphäre und die zahlreichen auch fachfremden Gespräche, ob nun in Göttingen oder per Telefon zwischen Göttingen und Frankfurt.

Ein großer Dank geht weiterhin an Martin Sauter für die Übernahme des Korreferats sowie die zahlreichen konstruktiven Gespräche und Anregungen. Zudem danke ich Jonas Kley, Sharon Webb, John Reinecker und Kristian Bär für die Bereitschaft, in meiner Prüfungskommission zu sein.

Ich danke dem Bundesministerium für Wirtschaft und Energie, zuvor Bundesministerium für Umwelt, Naturschutz und Reaktorsicherheit (BMU), für die finanzielle Unterstützung im Rahmen des AuGE-Projekts.

Von ganzem Herzen danke ich Johanna für die gemeinsame Zusammenarbeit und für so viele weitere Dinge. Ob nun die gemeinsame erfolgreiche oder auch weniger erfolgreiche Zeit im Gelände, die spannenden fachlichen Diskussionen, die teilweise ernsten Gespräche und aufbauenden Worte. Nicht zuletzt seien aber die lustigen Stunden auf so mancher Dienstreise und Tagung erwähnt. Es war eine sehr schöne Zeit. Ebenso danke ich Doro für die tolle gemeinsame Zeit im Büro, die tolle Zusammenarbeit und viele hilfreiche Gespräche. Die gemeinsamen Tagungen und so vieles mehr machen die Zeit unvergesslich.

Für die schöne Zeit danke ich der Abteilung Strukturgeologie, allen wissenschaftlichen Mitarbeitern sowie ehemaligen und aktuellen Doktoranden. Ein besonderer Dank geht dabei an Marie-France Hesse, die mich in allen organisatorischen Dingen sehr unterstützt hat. Bedanken möchte ich mich zudem bei unseren Hiwis (u.a. Pascal, Torben, Augusto). Danke für die tatkräftige Unterstützung bei Probenahmen im Gelände und der Probenaufbereitung.

Danke an die Kollegen aus dem AuGE-Projekt. Insbesondere an die Koordinatoren John Reinecker, René Grobe, Axel Wenke sowie die Doktorand/innen Maria, Dominik, Georg, Till und Torben.

Meiner Familie danke ich für die Unterstützung über die letzten Jahre. Ihr seid mir auf jede erdenkliche Art und Weise eine große Stütze. Danke für Euer Interesse an meiner Arbeit und die aufmunternden Gespräche, besonders in der Endphase. Insbesondere danke ich, dass ihr mir über die letzten Monate den Rücken frei gehalten habt, so dass ich mich auf das Fertigstellen der Arbeit konzentrieren konnte.

## CV / Lebenslauf

### Persönliche Daten

Name	Silke Meier
Geburtsdatum	29.11.1982
Geburtsort	Hildesheim
Nationalität	Deutsch

---

### Hochschulstudium

10/2011 – 05/2016	Promotionsstudium Georg-August-Universität Göttingen - Geowissenschaftliches Zentrum; Abteilung Strukturgeologie und Geodynamik
WS 2003 – SS 2008	Geowissenschaften Georg-August-Universität Göttingen Abschluss: Diplom-Geowissenschaftlerin
<i>Diplomarbeit:</i>	<i>„Klüftung und Kluftgenese im Kraichgau, Baden-Württemberg – tektonische Entwicklung und regionale Kluftmuster auf der östlichen Grabenschulter des Oberrheingrabens“. In Kooperation mit der GeoEnergy Consulting GmbH, Karlsruhe</i>
<i>Studienschwerpunkte:</i>	Vertiefungsrichtung Geologie Nebenfächer Geophysik und Strukturgeologie
<i>Diplomkartierung:</i>	<i>„Geologische Kartierung im Leinetalgraben südlich der Ortschaft Hillerse“</i>
10/2006	Abschluss: Bachelor of Science
<i>Bachelorarbeit:</i>	<i>„Vulkanotektonik des Zentralvulkans Hekla in Südisland“</i>

---

### Lehrtätigkeit

Lehrbeauftragte am Geowissenschaftliches Zentrum, Göttingen	Übungen der Veranstaltungen: „Fluidtransport in Reservoirs“; Master-Studiengang „Geowissenschaften“ „Case Studies in Geothermics“; Internationaler Master-Studiengang „Hydrogeology and Environmental Geoscience“
---	---

---

### Beruflicher Werdegang

Seit 03/2016	Sachbearbeiterin Altlasten/Geotechnik Partnerschaftsgesellschaft Dr. Pelzer und Partner – Partnerschaft Diesing, Kumm, Dr. Pelzer, Dr. Türk
10/2011 – 01/2015	Wissenschaftliche Mitarbeiterin Geowissenschaftliches Zentrum, Göttingen Abteilung: Strukturgeologie und Geodynamik

09/2010 – 09/2011	Geowissenschaftlerin AWIA Umwelt GmbH, Göttingen
03/2010 – 09/2010	Wissenschaftliche Hilfskraft Geowissenschaftliches Zentrum, Göttingen Abteilungen: Strukturgeologie und Geodynamik; Angewandte Geologie
12/2008 – 11/2009	Geologin IGA TEC GmbH, Speyer

## Publikationen

### *Rezensierte Zeitschriftenartikel*

**Meier, S.**, Bauer, J.F., Philipp, S.L., 2015. Fault zone characteristics, fracture systems and permeability implications of Middle Triassic Muschelkalk in Southwest Germany. *Journal of Structural Geology* 70, 170-189.

Bauer, J.F., **Meier, S.**, Philipp, S.L., 2015. Architecture, fracture system, mechanical properties and permeability structure of a fault zone in Lower Triassic sandstone, Upper Rhine Graben. *Tectonophysics* 647-648, 132-145.

Philipp, S.L., Reyer, D., **Meier, S.**, 2010. Strukturgeologische Geländestudien in Aufschlussanaloga und Permeabilitätsentwicklung in geothermischen Reservoiren. In: R. Greiling and A. Kontny (Hrsg.), *Zeitschrift für Geologische Wissenschaften. Geologische Beiträge zur Geothermie des südwestlichen Mitteleuropas*, 49-59.

### *Eingereichte Zeitschriftenartikel und Artikel in Vorbereitung*

**Meier, S.**, Bauer, J.F., Philipp, S.L., submitted. Fault zones in layered carbonate successions: From field data to stress field models. Submitted to *Geomechanics and Geophysics for Geo-Energy and Geo-Resources*.

Bauer, J.F., **Meier, S.**, Philipp, S.L.. Outcrop based numerical models of the conduit-barrier system of fault zones in Lower Triassic sandstone of the Upper Rhine Graben.

### *Relevante Tagungsbeiträge (nur eigene Präsentationen)*

Meier, S., Bauer, J.F., Philipp, S.L. 2012. *Kurzfassung, Poster und Kurzvortrag*. Fault zone characterization in potential geothermal reservoirs in the Upper Rhine Graben area based on outcrop analogue studies. 3rd European Geothermal PhD-Day, Pisa, 29.-30. März.

Meier, S., Bauer, J.F., Philipp, S.L. 2012. *Kurzfassung und Poster*. Charakterisierung von Störungszonen in Aufschlussanaloga potentieller geothermischer Reservoire des Oberrheingrabens. In: Kümpel, H.-J., Röhling, H.-G., Steinbach, V. (Hrsg.) *GeoHannover 2012: GeoRohstoffe für das 21. Jahrhundert*. Hannover, Schriftenreihe der Deutschen Gesellschaft für Geowissenschaften, 80. ISBN 978-3-510-49228-2, 01.-03. Oktober.

Meier, S., Bauer, J.F., Philipp, S.L. 2012. *Erweiterte Kurzfassung und Poster*. Charakterisierung von Störungszonen im Muschelkalk des Oberrheingrabens - Aufschlussanalogstudien. In: *Geothermische Vereinigung (Hrsg.): Der Geothermiekongress 2012*. 13.-16. November, Karlsruhe, Kongressband CD-ROM, 5. S.

Meier, S., Bauer, J.F., Philipp, S.L. 2013. *Kurzfassung, Poster und Kurzvortrag*. Infrastructure of fault zones crosscutting the Muschelkalk limestones of the Upper Rhine Graben - Outcrop Analogue Studies. 4th European Geothermal PHD-Day 2013, Szeged, Ungarn, 05.-07. Mai.

Meier, S., Bauer, J.F., Philipp, S.L. 2013. *Kurzfassung und Vortrag*. Characterization of fault zones in Triassic Muschelkalk limestones of the Upper Rhine Graben with regard to geothermal exploration. In: Philipp, S.L., Acocella, V. (Hrsg.): *Rock Fractures in Geological Processes, Abstracts of the Presentations of the Symposium*, 37-40, Universitätsdrucke Göttingen, ISBN 978-3-86395-141-2, Universitätsverlag Göttingen, London, 26.-27. November.

Meier, S., Bauer, J.F., Philipp, S.L. 2013. *Kurzfassung und Poster*. Outcrop Analogue Studies in Geothermal Exploration – Characterization of fault zones in Triassic Muschelkalk limestones of the Upper Rhine Graben. AGU Fall Meeting, Abstract #H51D-1211, San Francisco, 09.-13. Dezember.

Meier, S., Bauer, J.F., Philipp, S.L. 2014. *Erweiterte Kurzfassung, Kurzvortrag und Poster*. Permeability analyses of fault-related geothermal reservoir rocks of the Upper Rhine Graben, Germany – Outcrop analogue studies in the Middle Triassic Muschelkalk. 5th European Geothermal PhD-Day, Darmstadt, 31. März -2. April.

Meier, S., Bauer, J.F., Philipp, S.L., 2014. *Kurzfassung und Poster*. Fault zones in Triassic Muschelkalk limestones of the Upper Rhine Graben: Infrastructure characterization and permeability structure analyses. EGU General Assembly, Geophysical Research Abstracts 16, EGU2014-1609, Wien, 27. April-02. Mai.

Meier, S., Bauer, J.F., Philipp, S.L. 2014. *Kurzfassung und Vortrag*. Fault zone characterization in Triassic Muschelkalk limestones relating to geothermal exploration in the Upper Rhine Graben. GeoFrankfurt2014, Dynamik des Systems Erde / Earth System Dynamics, Schriftenreihe der Deutschen Gesellschaft für Geowissenschaften 85, ISBN 978- 3-510-49234-3, Frankfurt, 22.-24. September.

Meier, S., Bauer, J.F., Philipp, S.L. 2014. *Kurzfassung und Poster*. Charakterisierung von Störungszonen für die geothermische Exploration anhand von Aufschlussanaloga in karbonatischen Gesteinen des Oberrheingrabens. „Science Bar“ auf dem Geothermiekongress 2014, Essen, 11.-13. November.